THREE DIMENSIONAL FLOW STRUCTURES AND TURBULENCE DISTRIBUTION IN AN URBAN ENVIRONMENT

BY

BRUNO MONNIER

Submitted in partial fulfillment of the
requirements for the degree of
Doctor of Philosophy in Mechanical and Aerospace Engineering
in the Graduate College of the
Illinois Institute of Technology

Approved 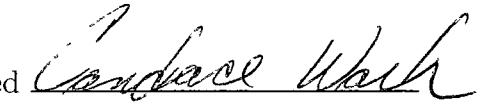
Advisor

Chicago, Illinois
December 2010

UMI Number: 3455032

ProQuest LLC
789 East Eisenhower Parkway
P.O. Box 1346
Ann Arbor, MI 48106-1346

ACKNOWLEDGMENT

"Une civilisation sans la Science, ce serait aussi absurde qu'un poisson sans bicyclette." Pierre Desproges

I would like to first thank very deeply my advisor, Dr. Candace Wark, who inspired me to work on my Ph.D. Her guidance, advice, and friendship have been essential in the completion of this degree. And her constant support of my desire to try new ideas gave me the opportunity to collaborate closely with Dr. Paritosh Mokhasi and Dr. Dietmar Rempfer from whom I have learned a lot.

I am very thankful to Dr. Hassan Nagib who originally gave me the opportunity to come to the Illinois Institute of Technology. His guidance and critical mind have helped strengthen this thesis. I am also very grateful to all the FDRC members, Professors, members of my committee who have commented on and suggested improvements to my work: Dr. David Williams, Dr. Sudhakar Nair, Dr. Ganesh Raman, Dr. Shawn Shadden, Dr. Kevin Cassel and Dr. Hamid Arastoopour. I would also like to acknowledge the contributions to this work from undergrad students Siddha Pimputkar, Aicha Thiam, Brian Neiswander, Minaz Virani, Seth Thomas, Stefan Stevanovic, and Jonathan Swanson. Additionally, the expertise of Craig Johnson in the machine shop was of great value.

Friends and family have played a central role during the most critical portion of this work. Their support, kind words, and understanding have helped tremendously. In no particular order, thanks go to: Betty, John, Tonton, Mimile, Moira, Ryan, Karen, Margie, Steffen, Nina, Ava, Wayne, Becca, Lola, Dawn, Sudeep, Paritosh, Bhavana, Brian, Ron, Sallie, Sarah, Jackson (the licker) and many others.

My parents and sister have always pushed me to do what I wanted and helped me reach my goals, even when these goals took me 4000 miles away from them. I am

very grateful for the time and effort that they have invested to provide me with the necessary tools to follow my own path.

A very special thanks goes to Rachel whose constant support and love have helped me remain afloat and finish the writing without losing a single hair. Her professional assistance in proof-reading this dissertation is also greatly appreciated.

I dedicate this thesis to my grand-mother. She has kept her faith intact that the day would come when I would finally be done chasing degrees. I swear I won't start another Ph.D. grandma.

TABLE OF CONTENTS

APPENDIX Page

LIST OF TABLES

LIST OF FIGURES

ABSTRACT

Understanding and controlling the dispersion of pollutants and contaminants in urban areas has become a major focus recently. Field measurements, numerical studies, and wind tunnel experiments have increased in number. Specifically, there is a growing need for a spatio-temporal description of such complex flow fields under well-controlled conditions, typically obtained in wind tunnel experiments. The reduced scale model of interest is a 4 by 3 array of cuboid blocks in an experimentally modeled, neutrally stratified, atmospheric boundary-layer. The use of Stereoscopic Particle Image Velocimetry (SPIV) allows for a three-dimensional description of this urban flow. A large amount of SPIV data is collected upstream and in each middle street of the urban environment allowing for a study of the flow evolution from street to street. Valuable information about the flow structures are presented along with the mechanisms responsible for contaminant transport and dispersion. The effects of small incidence angles of the incoming flow with respect to the urban array and the effects of streamwise spacing between streets on the flow characteristics are investigated. A major observation from this work is that a strong channeling effect is observed for incidence angles as small as 4.5° and is found to be comparable in strength to that observed in other investigations for much larger angles. A coupling between this channeling effect and the structures responsible for contaminant transport is revealed.

An innovative method using sparse measurements to estimate the continuous temporal evolution of the dominant structures in the flow is investigated. Proper Orthogonal Decomposition is used to obtain a reduced-order representation (ROR) of the flow field. Sparse velocity measurements within the domain serve as input to measurement models that provide an estimation of the ROR of the velocity field. This ROR of the flow field could be regarded as the first that provides a temporal

evolution of a spatially well-resolved flow field in a complex geometry. Finally, a linear state-space model is used to describe the continuous temporal evolution of the ROR of the velocity field which is of primary importance with respect to contaminant tracking at the urban scale.

CHAPTER 1
INTRODUCTION

1.1 Introductory comments

Urban flows have been increasingly studied during the past decade. Many challenges are yet to be fully addressed, with the understanding of contaminant dispersion being one of the critical issues. In the context of pollution dispersion in densely populated areas and the fear of chemical or biological attacks, more studies are addressing this type of flow. The physics involved are very complex since the flow is often strongly three-dimensional (3D) and dependent upon the temperature distribution, the turbulence induced by moving cars, the presence of obstacles such as trees in the streets, etc. Remote flow sensing, in particular, has become a very important field of research. Through the use of sparse sensors optimally distributed in an urban environment, the desire is to estimate the characteristics of the flow field and predict its evolution. This is especially important in the context of predicting the displacement of a plume of contaminants.

Another relatively recent area of interest relevant to this type of study is the desire to fly Micro Aerial Vehicles (MAVs) in urban areas. These MAVs, which are unmanned aerial vehicles with relatively small dimensions (10-20 cm wingspan), can be used for surveillance, data collection (remote sensing), and can be flown in areas that are hazardous to people. However, they are most often still limited to flying in relatively calm wind conditions (Watkins et al., 2009; Watkins, Ravi, & Loxton, 2010). Therefore, there is a growing need to characterize wind gusts and both the intensity and spatial distribution of turbulence at the urban scale so as to provide the flow fundamentals to design new generations of MAVs with enhanced maneuverability.

1.2 Advantages and limitations of field experiments and numerical simulations

While they are essential to verify results obtained both from numerical and wind tunnel experiments, direct field studies are extremely difficult and expensive to conduct. Many parameters are influencing the flow field and results are often difficult to interpret. In terms of practicality, the most common tools used to measure velocity in field experiments are sodars and anemometers installed on tall towers which usually results in a rather coarse spatial resolution. As a result, turbulence characterization is mostly carried out in 1D, usually along a vertical axis, see Nielsen (2000) and Christen, Vogt, and Rotach (2003) for example. Few field experiments have considered spatial variation of turbulence at the street level (e.g. Rotach, 1995; Eliasson, Offerle, & Grimmond, 2006). Other types of work in simplified field experiments can be found in Louka, Belcher, and Harrison (1998), who worked toward a better understanding of the ventilation of pollution from a street formed of two long buildings and its dependence on the shape of the roofs of the obstacles. They focused on the coupling of the turbulent airflow in a street canyon with the turbulent airflow above the roofs. Within the same field setting, Louka, Belcher, and Harrison (2000) performed experiments to study the air flow within the street and found that the recirculation region is highly unsteady and that the shear layer from the upstream roof is very unstable due to a Kelvin-Helmoltz instability. In a more realistic environment, Louka, Vachon, Sini, Mestayer, and Rosant (2002) looked at the thermal effects on the flow field in a street in Nantes, France, and compared their results to a 2D numerical simulation using a standard k-ϵ model. They found that the numerical simulations overestimate the thermal effects on the flow field. Dobre et al. (2005) showed the flow behavior in a few streets in London, UK. More specifically, their work illustrated the effect of the wind incidence angle with respect to the streets and the role of the street intersections on the wind direction switching phenomenon. Their measurements showed that the flow within the street can be viewed as the vector sum of a channeling in the streets and a recirculation vortex.

The work by S. Xie, Zhang, Qi, and Tang (2003) is very interesting in the sense that it would be extremely difficult to reproduce in a wind tunnel. They performed field tests with the measurements of the concentration of car exhaust in Guangzhou, China. They found that in the street, pollutants are carried from the windward to the leeward side of the street by a large recirculation region. One part of the pollutants gets trapped in the recirculation region, while the other is flushed out of the street at the roof level. One major finding is that photochemical reactions involving O_3 take place at the roof level and is therefore less of a threat to pedestrians.

Recently, there has been an increased effort in developing and improving computational and numerical models. Camelli, Lohner, and Hanna (2006) have used very large-eddy simulation (VLES) to study the release of a passive scalar contaminant in realistic urban areas. This technique is equivalent to standard large-eddy simulation (LES), but the largest scales are on the order of a few kilometers. Krajnovic and Davidson (2000) have used LES on a single cube while Baik and Kim (1999) have used a 2D k-ϵ turbulence model for a 2D street.

Kim and Baik (2004) used a 3D numerical simulation, renormalized group k-ϵ scheme, to solve the flow within an array of cubes. They investigated the dependence of the vortical structures on the wind incidence angle and then classifed the flow in three regimes depending on this incidence angle.

More recently, Coceal, Thomas, Castro, and Belcher (2006) performed a direct numerical simulation of the turbulent flow within an array of cubes and found very good agreement with experimental data. Only numerical studies can provide information with excellent spatio-temporal resolution, but unless DNS is used, the main drawback is their limited ability to capture accurately the range of turbulence scales. The use of DNS is however very costly in terms of computation. And even with recent progress in computing, numerical simulations need validation through

experimental studies for such complex flow fields. Therefore, there is a very specific need for reliable 3D data in a more realistic urban model.

The study of Kim and Baik (2003) is interesting in the sense that by using a 2D numerical model to solve the flow within a single street, it allowed them to vary the inflow turbulence intensity easily. Such a study in an experimental setting would be more challenging. They found that as the inflow turbulence increases, both turbulent kinetic energy and turbulent diffusivity increase. Similarly, the magnitude of the mean speed increases and the vortical regions are strengthened. An increase in turbulent intensity is directly linked to an enhanced pollutant dispersion within the street.

As mentioned previously, thermal stratification of the atmospheric boundary layer is very difficult to simulate in a wind tunnel although some have been successful in doing so as will be seen in the following section. However, there is no such constraint for numerical simulations, and researchers have started looking into the effects of solar radiation on the flow field at the street level. By simulating ground-level heating through various numerical models, X. Xie, Liu, Leung, and Leung (2006) were able to show that thermal effects could enhance vertical diffusion especially for low mean wind speeds. In another work by X. Xie, Huang, Wang, and Xie (2005), the study of step-up and step-down configurations for the street geometry was carried out as well as the heating of either the windward or leeward side of the street. The thermal effects in these cases could then either strengthen or weaken the main vortex within the street. Similar results were obtained independently by Mestayer, Sini, and Jobert (1995). Uehara, Murakami, Oikawa, and Wakamatsu (2000) looked at the effect of flow stratification on the flow field within the street over a range of Richardson numbers (defining stable, neutral, or unstable atmospheres). Kim and Baik (2001) performed a numerical simulation of a street with bottom heating. They were able

to observe significant changes in the flow structure for large temperature gradients with the generation of a second vortical structure within the street, located directly underneath the vortical structure found for no temperature gradients.

1.3 Wind tunnel experiments

Unlike field experiments, wind tunnel experiments allow for a good control over the parameters driving the flow field of interest. It also allows for investigating independently the effect of the key parameters.

Most past wind tunnel studies have focused their interest on two-dimensional (2D) configurations (i.e. spanning the width of the wind tunnel) and have considered the neutrally stratified atmospheric boundary layer since it is extremely difficult to simulate a temperature distribution in a wind tunnel. A seminal study of flow patterns in an urban environment was performed by Oke (1988). This work, which is relevant to street design and contaminant dispersion, described the effect of streamwise spacing on street canyons. Although his results were 2D, he identified three different regimes directly dependent on the streamwise spacing of the street canyon. Li, Leung, Liu, and Lam (2008) performed experiments in a water channel, investigating the different flow regimes using Laser Doppler Anemometry. Similar regimes have been found in 3D configurations (i.e. finite size of the streets). Martinuzzi and Havel (2000) investigated the effect of the streamwise spacing between two cubic blocks mounted in tandem in a thin boundary layer and found three distinct regimes for different streamwise spacings. Other parameters such as the span-to-width ratio of the obstacles or the spanwise spacing for obstacle arrays are believed to have an effect on the transition between regimes. Few wind tunnel experiments have investigated more realistic geometries (e.g. Rafailidis, 1997; Kastner-Klein & Rotach, 2004). While these studies are considering more complex geometries, the amount of information about the mean flow field and the turbulence within the model is limited spatially.

Recently, researchers have begun investigating the effect of three-dimensionality; but again, there are very few measurements offering full 3D sets of data. Becker et al. (2002) with Laser Doppler Anemometry (LDA) and Sousa (2002) with 2D - three component particle image velocimetry (2D-3C PIV) measurements were among the first to have looked at three-dimensional flow fields around a single cuboid obstacle. Becker et al. (2002) described the effect of the angle of attack, the aspect ratio, the Reynolds number and the boundary-layer type on the flow structures around a single obstacle. They found no fundamental changes in the vortex structure for the various boundary layers investigated, and determined that an increase in the power-law coefficient n in

$$\frac{U}{U(h)} = \left(\frac{z}{h}\right)^n \tag{1.1}$$

caused a reduction in the size of the recirculation region downstream of the obstacle. Here, U is the time-averaged velocity at the wall-normal coordinate z, and h is a wall-normal location in the upper part of the inertial sublayer at which the velocity $U(h)$ is known. They also found that increasing the incidence angle created and subsequently amplified a dislocation of one leg of the arch vortex behind the single block until it attached to its top for incidence angles larger than 60°. Sousa (2002), using conservation of mass to extract the third velocity component from 2D PIV data around a cube, focused his interest on the identification and localization of large-scale vortical structures. He found that swirling strength and normalized angular momentum techniques were more advantageous for identifying coherent structures as compared with a vorticity-based method. Similarly, Martinuzzi and Tropea (1993) using various flow visualization techniques, as well as static pressure measurements on the surface of the obstacle, showed the effect of the width-to-height ratio on the three dimensionality of the flow past a single 3D obstacle. They found that, for an obstacle with a width-to-height ratio, $W/H > 6$, the flow downstream of the block is largely 2D with alternating saddle and nodal points on the windward face of the obstacle.

They concluded that cellular structures were created upstream of the obstacle and that the flow was following preferred paths over the top.

Hussein and Martinuzzi (1996) investigated the turbulence dissipation rate, the production, convection and transport terms and the balance of the turbulent kinetic energy transport equation for a three-dimensional flow around a cube mounted in a channel using LDA. They identified various scales relevant to different features of the flow around the cube (e.g. wake, shear layer, horseshoe vortex). These different scales characterizing the turbulence production and dissipation are a good indication that the flow field within an urban area is a multi-scale problem.

Belcher and Coceal (2001) and Coceal and Belcher (2004) developed an urban canopy model for mean winds in urban areas that compares well with data from wind tunnel experiments. Interestingly, they could model the minimal distance within an array of buildings that is required to reach an adjustment to the inhomogeneous canopies.

Many researchers have investigated the flow within an array of obstacles, for example, regular and staggered arrays of cubes (Castro et al., 2006; Cheng & Castro, 2002; Reynolds & Castro, 2008). Their primary goal was to understand the features of urban-like boundary layers, what influenced them and how to parameterize them. With the same objective in mind, MacDonald, Schofield, and Slawson (2002) performed experiments with a regular array of cubes and measured characteristic mean flow and turbulence statistics for urban areas.

Robins and Castro (1977) investigated the plume dispersion in the vicinity of a wall mounted cube by releasing propane for different configurations (porous cube, release from a point source at different locations, release from a stack, etc...) The concentration of propane was measured downstream of the cube and it was found

that an effective source height concept could be applied to estimate the concentration field beyond two cube heights. A fundamental difference was found in the behavior of the flow dispersion phenomenon between high and low level release with the authors underlining a possible effect of surface geometry on dispersion.

Castro and Robins (1977) investigated the pressure distribution on the surface of a wall-mounted cube in a turbulent boundary layer and the flow field in its wake. Two incidence angles of the incoming flow were studied. They showed that an increase of turbulence intensity and shear would reduce the size of the recirculation region downstream of the cube. Reattachment on the top surface of the obstacle is observed for the urban type boundary layer (as opposed to the cube being placed in a uniform flow). This reattachment occurs for different cube sizes, but may be intermittent for the larger obstacles (as the height approaches the boundary layer thickness). For a 45° incidence angle, the cube placed in a uniform flow sheds vortices from its top edges, similar to a delta wing, that have a strong effect on the axial velocity for a distance of about six times the cube length, then this effect diminishes quickly. When turbulence intensity is raised in the case of the urban type boundary layer, this effect tends to disappear. Garbero, Salizzoni, and Soulhac (2010) performed an experimental study of pollutant dispersion within a street network, measuring the mass exchange between the streets and the flow above the roofs for various geometrical configurations as well as various wind directions.

An interesting experimental study at a larger scale was carried out by Richards, Hoxey, and Short (2001) where they measured the surface pressure on a 6 m cube sitting on the ground in an open country. They found good agreement with wind tunnel data for the windward face of the cube, but the pressure distribution in the field experiment was more sensitive to incoming velocity profiles, turbulence and Reynolds number on the other faces than the pressure distribution obtained in the

wind tunnel experiment. Richards, Hoxey, Connell, and Lander (2007) carried out a 1:40 scaled-down wind tunnel experiment of this cube and compared their results to the field experiments. They found similar behavior but identified various sources of discrepancies between the wind tunnel and field experiments. These included a Reynolds number effect and the difficulty to reproduce varying wind directions to match the field experiment, affecting the mean and amplitude of pressure observed during the measurements.

Mostly during the last decade, researchers have begun to investigate other effects on the flow field within urban-like environments. The addition of thermal effects, presence of obstacles such as trees, and extra turbulence generated by moving cars are more and more investigated experimentally. In a first study, Kovar-Panskus, Moulinneuf, et al. (2002) looked at the streamwise aspect ratio effect of the street on the flow pattern, followed by a study where Kovar-Panskus, Louka, et al. (2002) investigated thermal effects in a wind tunnel experiment. They investigated the flow field within a street for conditions where a single recirculation region is the dominant flow structure. Under low speed wind conditions, as the heating of the windward wall is increased, the reverse flow speed magnitude is reduced. Upon further heating, the flow pattern significantly changed.

Some researchers have started to look into added turbulence generated by moving cars. For example, Eskridge and Rao (1986) focused specifically on the turbulence levels created by moving objects. More recently, Kastner-Klein, Fedorovich, and Rotach (2001) studied the high concentration levels of car exhaust encountered when the incoming flow was normal to the street, and looked at the effects of one-way and two-way traffic on this concentration. In another study, Kastner-Klein, Berkowicz, and Plate (2000) found that dispersion of pollutants could be enhanced by the motion of vehicles, especially at low wind speeds. Ahmad, Khare, and Chaudhry

(2002) implemented multi-lane traffic for simulating road traffic and concluded that pollutant concentrations could be reduced significantly by moving cars, once again at low wind speeds.

In the last few years, the effect of still obstacles on the dispersion of pollutants has been investigated. More specifically, the effect of trees was highlighted in the work by Gromke and Ruck (2009), Gromke and Ruck (2007) and Gromke, Buccolieri, Sabatino, and Ruck (2008). It was found that, in some cases, the presence of trees actually lowers the dispersion of pollutants from the leeward side of the street, by weakening the large recirculation region. On the windward side of the street, pollutant concentrations were less than in the baseline case (with no trees), due to a larger amount of clean air moving into the street from the top. Gayev and Savory (1999) focused on trying to model the roughness associated with stationary obstacles in a single street-canyon model.

1.4 Remote Flow sensing

Remote flow sensing has become a major topic of investigation in the last few decades. A simple example of remote flow sensing is weather forecasting. Sensors are distributed around the Earth and provide various types of measurements to models that predict the weather. In terms of estimation of velocity field based on sparse measurements, work has been done in the past 25 years. Glauser and George (1992) provide a comprehensive review of conditional sampling, stochastic estimation, pseudo flow visualization (Tabatabai, Kawall, & Keffer, 1987) and Proper Orthogonal Decomposition (POD). The main focus of their paper is on multipoint measurements as it can provide a larger picture of the flow field when those techniques are used.

Adrian and Moin (1988) also used linear stochastic estimation to estimate "conditional eddies" $< u'|u >$ in a turbulent channel flow. Delville, Ukeiley, Cordier,

and Bonnet (1999) applied POD, to a two-stream plane mixing layer. The two-point correlation tensor serving as the kernel for the POD was calculated using cross-wire measurements.

Other examples of the use of Linear Stochastic Estimation, LSE, can be found in Hudy, Naguib, and Humphreys (2007) where they combine PIV measurements and surface pressure measurements to obtain the temporal evolution of the largest structures over a backward-facing step. Murray and Ukeiley (2006) and Ukeiley and Murray (2005) investigate the flow in open cavities at subsonic speed. Once again, combining pressure measurements and PIV realizations via stochastic estimation, it is possible to gain insight on the temporal evolution of dominant structures in the flow. Naguib, Wark, and Juckenhoefel (2001) investigated the stochastic estimation of the conditional streamwise velocity based on wall static pressure measurements beneath a turbulent boundary layer. It was shown that the inclusion of both the linear and quadratic terms of the stochastic estimation was necessary to obtain an accurate estimate of the conditional velocity field.

Taylor and Glauser (2004) used a combination of PIV measurements, pressure measurements, POD analysis and LSE to estimate the velocity field of the flow between a backward facing ramp and an adjustable flap. Different extensions of the LSE technique have been developed in the work of Hudy et al. (2007) and Tinney et al. (2006) with spectral LSE, Borée (2003) with an extension to LSE and POD called extended POD, Bonnet and Delville (2001) with various coherent structures identification techniques, Picard and Delville (2000) with a spectral and physical POD and LSE applied to the shear layer of a jet, and others.

1.5 Various approaches to the contaminant dispersion and transport problem

The established approach to predict the dispersion and transport of a contam-

inant in an urban environment is based on Gaussian plume models (Sykes, Parker, Henn, & Gabruk, 1996) which are only applicable to flat terrain and correctly resolve only the largest scales (Patnaik, Grinstein, Boris, Young, & Parmhed, 2007). Flow characteristics associated with separation and recirculation regions commonly found in urban areas are also not resolved using these models. The dispersion of a contaminant is handled by a diffusion term, and is again not captured adequately due to the complex geometries and wind gusts found in an urban environment.

In order to resolve complex geometries and a wider range of scales, standard CFD simulations have been performed, but they typically require a very large amount of computer power; see for example Aliabadi and Watts (2002). For the same reason, DNS is still inapplicable to high Reynolds number flows. Instead, many have looked into RANS simulations with various turbulence closure models. The primary drawback is of course that RANS models do not represent the temporal evolution of the flow field of interest.

A good alternative to DNS and RANS can be found in LES. Details about new advances made in CFD computations towards a better prediction of plume dispersion and transport are given in Patnaik et al. (2007). The use of Monotone Integrated Large Eddy Simulation (MILES) provides an improvement on the prediction of contaminant transport and dispersion over the standard plume models. However, the lack of three-dimensional data resolved in time in a well-controlled environment such as a wind tunnel is preventing a better validation of these predictive tools. Especially, careful studies of street geometry and the effect of the incidence angles of the incoming flow are needed to further refine and validate MILES (Patnaik et al., 2007).

A different approach was presented in the work by Mokhasi, Rempfer, and Kandala (2009) based on a reduced-order representation of the flow field. Instead of solving it numerically in both space and time, this approach focuses on decomposing

the flow field into a set of spatial basis functions and a set of temporal coefficients using POD. The spatial basis functions do not depend on time and can therefore be stored and reused at a later stage. The temporal prediction of the flow field is performed on the coefficients. By combining evolution models with measurement models through the use of unscented Kalman filters, they were able to obtain an improved prediction over linear stochastic estimation. An optimization of sensor placement for urban flows was studied in Mokhasi and Rempfer (2004) based on a POD representation of the flow field.

1.6 Need for 3D information about the urban flow field

To our knowledge, no wind tunnel study of urban flows utilizes Stereoscopic Particle Image Velocimetry, SPIV. Even though PIV has become a common measurement technique for evaluating flow structures and turbulence characteristics, its use in the standard 2D form is not very attractive for the study of urban flows. With SPIV, it is possible to gain a full 3D representation of the flow field. One of the primary reasons for the absence of SPIV measurements in the literature is the difficulty in the implementation and setup. In order to collect enough information to resolve 3D features in a turbulent flow, a very large number of data planes has to be collected which can be extremely time consuming. However, SPIV offers the ability to look more deeply into the structure of the flow field within the streets as well as the turbulence characteristics, and is therefore very appealing for the study of complex flows. This work addresses the lack of data describing the three dimensionality of the flow patterns and turbulence within a complex geometry. The goal is to provide a better knowledge of the fluid dynamics, such as flow patterns and turbulence statistics as functions of the aspect ratio of the streets, the incidence angle and speed of the incoming wind, etc. Eventually, the insight gained from a three-dimensional study can be very valuable for pollution control at the street level, for street design to enhance

ventilation, for optimized remote flow sensing, and for characterizing the turbulence evolution within an urban environment that is crucial to improving the performance of prediction in complex flows.

1.7 Origins of the selected experimental model

Gailis (2004) and Yee, Gailis, Hill, Hilderman, and Kiel (2006) investigated a reduced-scale model of the Mock Urban Setting Test (MUST) experiment, which was performed at the Dugway Proving Ground in Utah (see Biltoft (2001)). The work of Gailis (2004) serves as a complement to fill in the gaps between the field and reduced scale study, and emphasizes the scaling between the two experiments. Yee et al. (2006) compared the field experiment to both a wind-tunnel and water-channel reduced scale experiment, and found that the behavior of plume dispersion is qualitatively the same for all studies, but that with proper scaling it is also possible to obtain a satisfactory quantitative model of the field data using the water channel. Yee and Biltoft (2004) focused their work on the full-scale experiment, collecting measurements of the plume dispersion within the array of obstacles. The model used in our work is based on the MUST experiment, but we have used 12 blocks instead of 120; however, we have retained a similar aspect ratio. The motivation for selecting a simplified version of the MUST experiment is that it offers a more complex geometry than the typical single street or 2D channel found in the literature by simulating a small network of streets, yet is simple enough that it allows for optical access for our SPIV measurement technique. The network of streets allows for an in-depth investigation of turbulence characteristics from street to street and provides valuable information at the intersections of the streets where the three-dimensional effects are strongest.

1.8 Motivations

The main motivation for this work is to gain a better understanding of the flow field in complex urban environments through detailed three-dimensional measurements with a direct application to the problem of contaminant transport and dispersion in urban areas. These measurements will be beneficial in the understanding of the dominant three-dimensional flow structures related to transport and regions of large production of turbulence related to dispersion found in an urban setting.

Using some of the tools described in Mokhasi et al. (2009) and Mokhasi (2009b), an assessment of the feasibility of estimating a highly dimensional flow field is performed. This could provide a reference data set that is resolved in both space and time and that could be used as a test data set to compare various approaches to the problem of contaminant transport prediction.

The spatial description of the flow structures and, especially, turbulence mechanisms within an urban environment are of primary interest for characterizing wind gusts that are detrimental to flying MAVs. A better description of the flow unsteadiness and turbulence intensities could provide grounds for improving the maneuverability of MAVs.

Finally, the spatial description of the mean flow can provide valuable information in terms of optimal placement of wind turbines in urban areas so as to maximize their power output. The knowledge of spatial regions of high turbulence intensity is of interest here, as wind turbines should be placed away from these regions so as to avoid excessive fatigue.

1.9 Outline of the thesis

In Chapter 2, the experimental setup is described. The environmental wind tunnel at the Illinois Institute of Technology, IIT, is used for this study, with its advantages being a relatively large test section and the availability of the various

tools that have been implemented over the last three decades to simulate realistic neutrally stratified boundary layers. The selection of the urban model studied in this thesis is also discussed. Chapter 2 also introduces the various measurement techniques used for this work. Stereoscopic Particle Image Velocimetry and Hot-wire Anemometry are described relative to our needs for specific information about the flow field. Chapter 3 presents a three-dimensional description of the mean flow features. The use of SPIV allows for good spatial resolution and provides a rather thorough picture of the mean flow structures within the urban model. The mean streamlines and various techniques used to identify vortical structures and/or coherent structures are discussed and compared. The effect of various parameters, such as the incidence angle of the incoming flow field and the streamwise spacing between streets, are investigated. In Chapter 4, the three-dimensional turbulence characteristics of the flow field within an urban array are described. The turbulent kinetic energy field is investigated in detail along with the locations of high turbulence production. The SPIV data allow for the calculation of many terms in the turbulent kinetic energy equation allowing us to isolate the various mechanisms responsible for driving the turbulence production. Chapter 5 presents the work done to gain insight about the temporal evolution of the most energetic flow structures found in this complex flow field. A reduced-order representation of the velocity field utilizing POD and two measurement models providing an estimate of the temporal evolution of the flow field are discussed and compared. The accuracy of these measurement models is investigated and the amount of information that can be resolved is demonstrated. Chapter 6 presents a discussion of the results. Finally, Chapter 7 provides a summary of the main contributions of this thesis.

CHAPTER 2

EXPERIMENTAL SETUP AND METHODOLOGY

2.1 Wind Tunnel

2.1.1 Modelling of the Atmospheric Boundary Layer.

2.1.1.1 Definition. The first step in this investigation was to experimentally model the atmospheric boundary layer (ABL) for the conditions of interest (see Stull, 1988, for a comprehensive introduction to boundary-layer meteorology). The wind velocity profile of the ABL is often characterized by a log-law in the inertial sublayer. However, using a power law, see Equation 1.1, provides a simpler characterization of a neutrally stratified boundary layer (Plate, 1971) since only one parameter (the exponent) is needed to describe the wind velocity profile in the inertial sublayer. Typical exponents for various types of terrains can be found in the work by Davenport (1965), and range from 0.4 for large high-rises to 0.16 over a flat surface such as a lake. Three different ABLs with power-law exponents varying from 0.14 to 0.20, respectively corresponding to flow over vegetation and flow over lower suburban buildings, were used for this investigation.

2.1.1.2 Wind-Tunnel Modeling. The boundary layers are modeled in a closed-loop wind tunnel at IIT, based on the work done earlier by Nagib, Morkovin, Yung, and Tan-atichat (1974) and Gunnarsson (1974). The experiment is carried out in the low speed test section that is capable of mean free-stream speeds, U_0, up to 8 m/s. The test section is 1.2 m in span by 1.7 m in height by 0.635 m in length. For larger test sections such as this one, it is very important to consider the spanwise uniformity of the incoming boundary layer. Nagib et al. (1974) and Gunnarsson (1974) used roughness elements and a counter jet upstream of the test section to tune the characteristic parameters of the approaching boundary layer and ensure spanwise

uniformity. The counter jet, discussed both in Nagib et al. (1974) and Gunnarsson (1974), proved to be very useful in ensuring spanwise uniformity for the free-stream flow speeds of interest here. The configurations we chose for roughness elements and counter jet settings provide a spanwise uniform neutrally stratified atmospheric boundary layer for free-stream speeds ranging from $U_0 = 2.2$ m/s to 3.4 m/s.

The counter jet consists of a 60-mm diameter steel tube placed on the floor of the wind tunnel and spanning the entire width. The counter jet is placed at the upstream location of the roughness fetch (Figure 2.1) which is 3.48 m upstream of the test section. There are 38, 6.35-mm diameter holes drilled along the span of the steel tube, with the tube itself being connected to a compressed air supply. The orientation, θ_J, of the 38 jets can be varied from $-20°$ to $+20°$ with respect to the oncoming free stream by rotating the tube. The magnitude of the jet velocity, U_J, can also be varied by controlling the compressed air supply pressure. For our study, we found that $U_J/U_0 = 15$ with an upstream flow angle, θ_J of $+10°$ (see Fig. 2.1 for definition of θ_J) provides a spanwise uniform boundary layer in the test section. The reader is referred to Gunnarsson (1974) for a more comprehensive discussion of the counter jet technique. Directly downstream of the counter jet is the roughness element fetch. The roughness elements used are 30 mm cubes placed randomly on the floor (see Figure 2.1). The end of the roughness fetch is 2.08 m from the counter jet and 1.40 m from the upstream edge of the 1.22 m $\times$ 1.93 m test section. The roughness elements occupy 8% of the planform area of the entire roughness fetch. The test section, which begins 1.40 m after the downstream end of the roughness fetch, can be clearly seen in Figure 2.2.

2.1.1.3 Characteristics of the modelled ABL. The characteristics of the three atmospheric boundary layers are summarized in Table 2.1. Creation of boundary layers 2 and 3 was made possible by modifying the diverging section of the wind

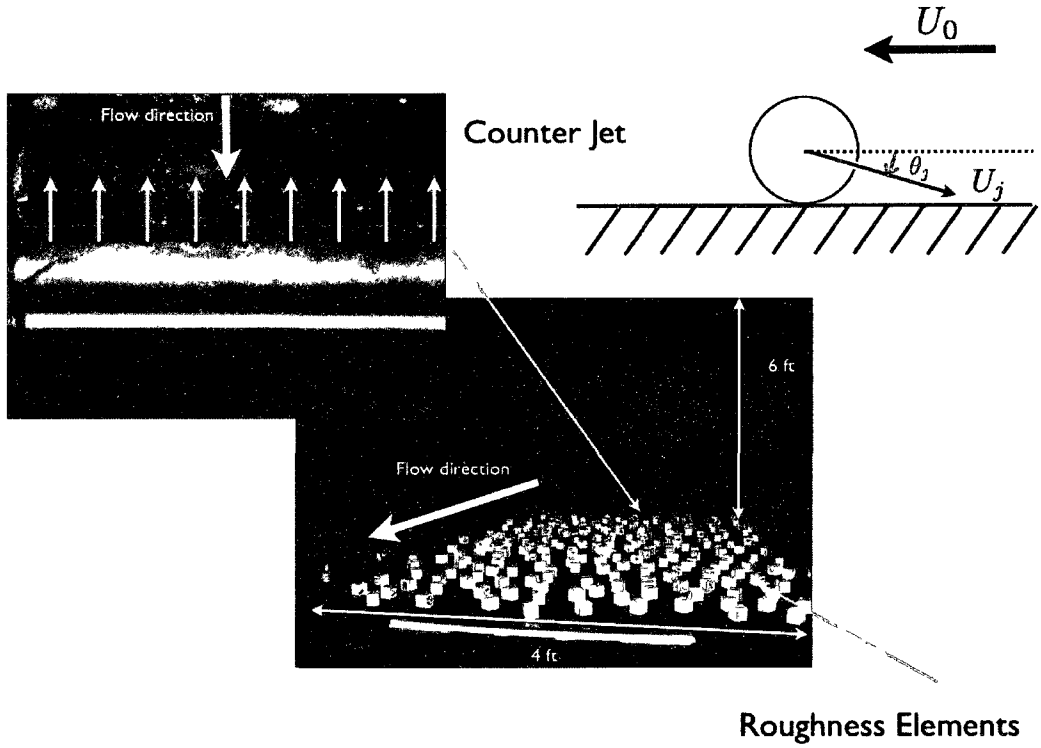

Figure 2.1. Photograph of counter jet and roughness elements upstream of the test section. Note: the test section is not shown here and is downstream of this image.

tunnel upstream of the test section. A honeycomb and a screen were added in order to specifically modify the mean velocity profiles and turbulence profiles in the near wall region. The modifications were made so as to conserve thick boundary layers that match realistic settings more closely.

The approach boundary layers are documented using a spanwise array of three hot wires. The rack is mounted on a vertical traverse system enabling measurement of the velocity profiles starting from a position in close proximity to the floor ($\approx$ 1 mm) and extending approximately 400 mm above it. The middle hot wire is located along the centerline of the wind tunnel while the two other hot wires are located 127 mm apart from the centerline. Note that for meteorological studies, x, y and z are the streamwise, spanwise and wall-normal coordinates, respectively.

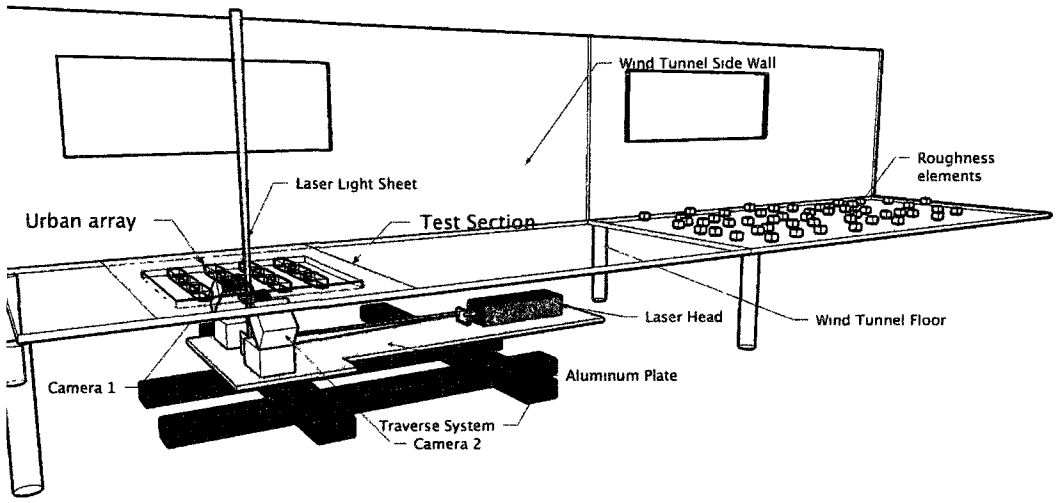

Figure 2.2. Schematic of the stereoscopic PIV setup, the roughness fetch and the test section.

Table 2.1. Boundary layers test matrix

ABL #	$\mathbf{U_0}$	δ	θ	$\mathbf{Re_\theta}$	$\mathbf{n}$
ABL1	3.1 m/s	$\approx$ 500 mm	$\approx$ 75 mm	$\approx$ 14800	0.20
ABL2	2.2 m/s	$\approx$ 400 mm	$\approx$ 40 mm	$\approx$ 5600	0.14
ABL3	3.4 m/s	$\approx$ 450 mm	$\approx$ 50 mm	$\approx$ 10800	0.17

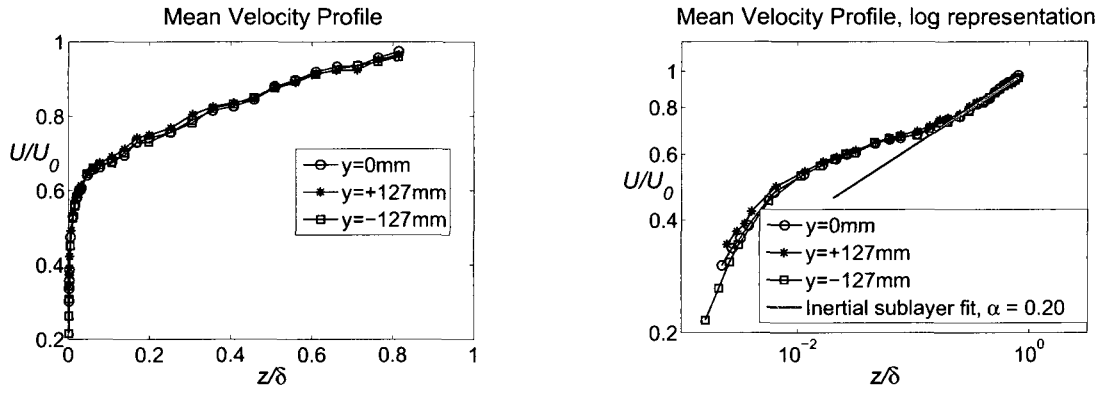

(a) Linear representation

(b) Logarithmic representation

Figure 2.3. Normalized velocity profiles for ABL1 at three spanwise positions taken 75 mm upwind of the urban array.

Figure 2.3 presents the velocity profiles for ABL1, obtained 75 mm upstream of the test section entrance without the experimental urban array in the test section. The results illustrate good spanwise uniformity. A power-law fit to these profiles in the inertial range yields a coefficient of 0.20, which is typical of atmospheric flow over suburban areas as described by Plate (1971). Since the hot-wire traverse is limited to 400 mm, a Pitot-static tube traverse is used to estimate the boundary-layer thickness δ, where δ is defined as the wall-normal (z) location where $U/U_0 = 0.99$ ($\delta \approx 500$ mm for ABL1). The momentum thickness θ is obtained from the profiles ($\theta \approx 75$ mm) and is computed as:

$$\theta = \int_0^{0.8m} \frac{U(z)}{U_0}\left(1 - \frac{U(z)}{U_0}\right) dz \tag{2.1}$$

where the integration is performed over the interval 0 to 0.8 m.

Similarly, Figure 2.4 presents the velocity profiles for ABL1, ABL2 and ABL3 so as to provide an easy comparison between the three boundary layers that are considered. The velocity profiles shown for ABL2 and ABL3 were obtained 100 mm upstream of the test section and the values for δ, θ and the power-law coefficient n

are presented in Table 2.1. Figures 2.5(a) and 2.5(b) present the logarithmic representation of the normalized velocity profiles for ABL2 and ABL3, respectively. With power-law coefficients of 0.14 and 0.17, ABL2 and ABL3 represent flows over lower roughness, such as vegetation, and exhibit again rather large boundary layer thicknesses, $\delta \approx 400mm$ and $\delta \approx 450mm$, respectively.

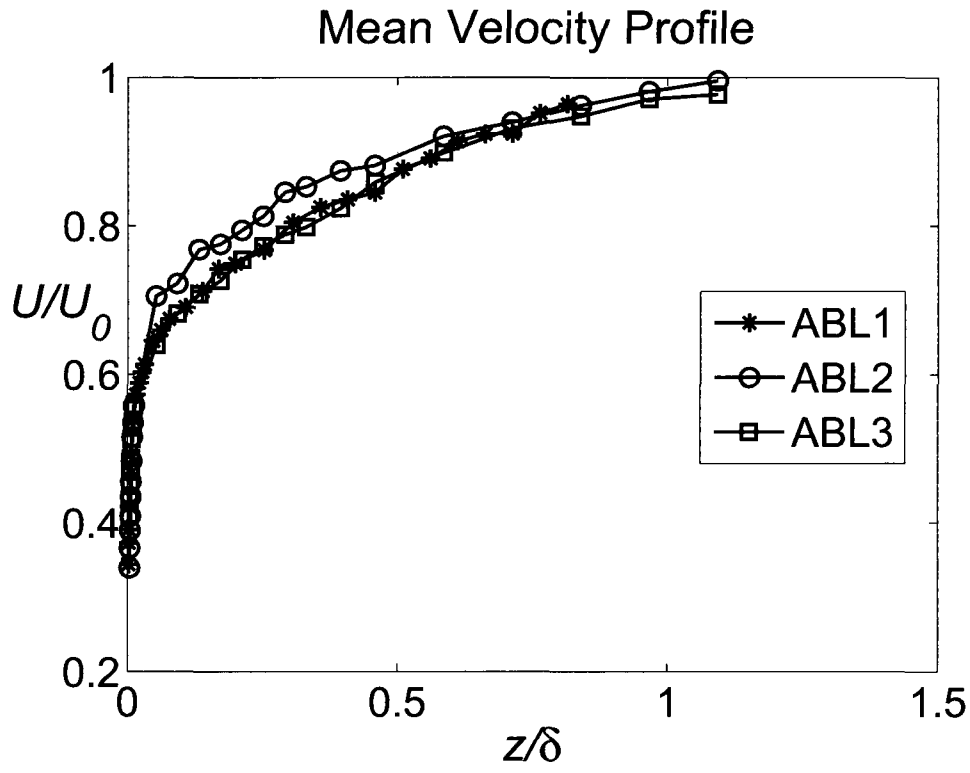

Figure 2.4. Normalized velocity profiles for all three ABLs upwind of the urban array.

2.1.2 Urban model.

2.1.2.1 Scaling considerations. The configuration we have chosen for this study is based on the MUST field experiment; see Brown et al. (2002) for details about the actual MUST field experiment and Gailis (2004) for a wind-tunnel study. The number of obstacles used in the MUST experiment was 120. For this investigation, only 12 obstacles are used, arranged in four rows and three columns as depicted in Figure 2.6. The aspect ratio of the obstacles is the same as in the MUST experiment;

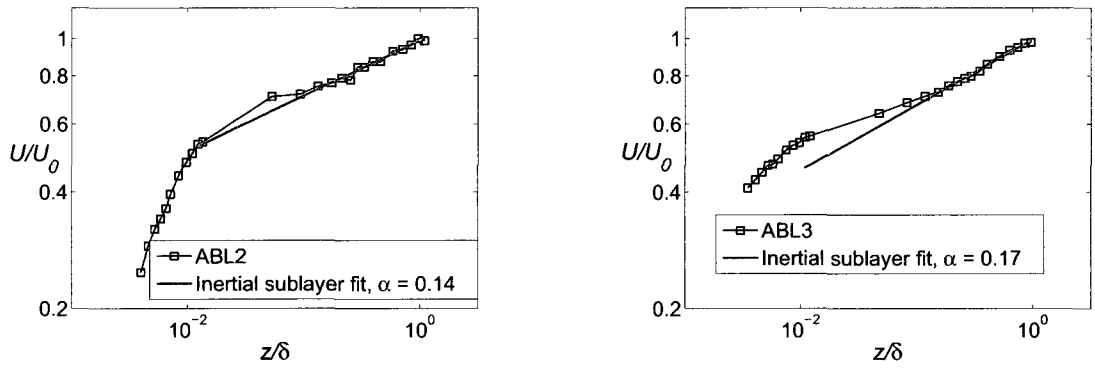

(a) ABL2 (b) ABL3

Figure 2.5. Logarithmic representation of Normalized velocity profiles for ABL2 and 3 upwind of the beginning of the urban array.

that is, $L/H = 5$ and $S/H = 1$, where L is the spanwise width ($L = 127$ mm), H is the wall-normal height and S is the streamwise length of the obstacles ($H = S = 25.4$ mm). D is the spanwise distance between the blocks and is kept at $D = 51$ mm, and W is the streamwise distance between the rows. In this investigation, two W/H values were studied: $W = 102$ mm and $W = 38$ mm, corresponding respectively to $W/H = 4$ and $W/H = 1.5$. Figure 2.6 also provides the coordinate system used herein. The origin, O, is located at the mid-span of the block on the floor next to the leeward wall of the upstream block. The x-axis is defined with respect to the model, and is orthogonal to the street axis. Three incidence angles, α, are investigated in this work, where α is defined as the angle of the x-axis with respect to the approach boundary layer mean flow direction. For $\alpha = 0°$, the incoming flow is aligned with the x-axis of the urban array and orthogonal to the urban array street axis. To achieve non-zero inclination angles, the entire urban array is rotated within the wind-tunnel test section. This then positions the x-axis of the urban array at an angle with respect to the incoming mean flow direction, and the urban array street axis is then no longer orthogonal to the incoming flow direction. When the array is rotated within the test

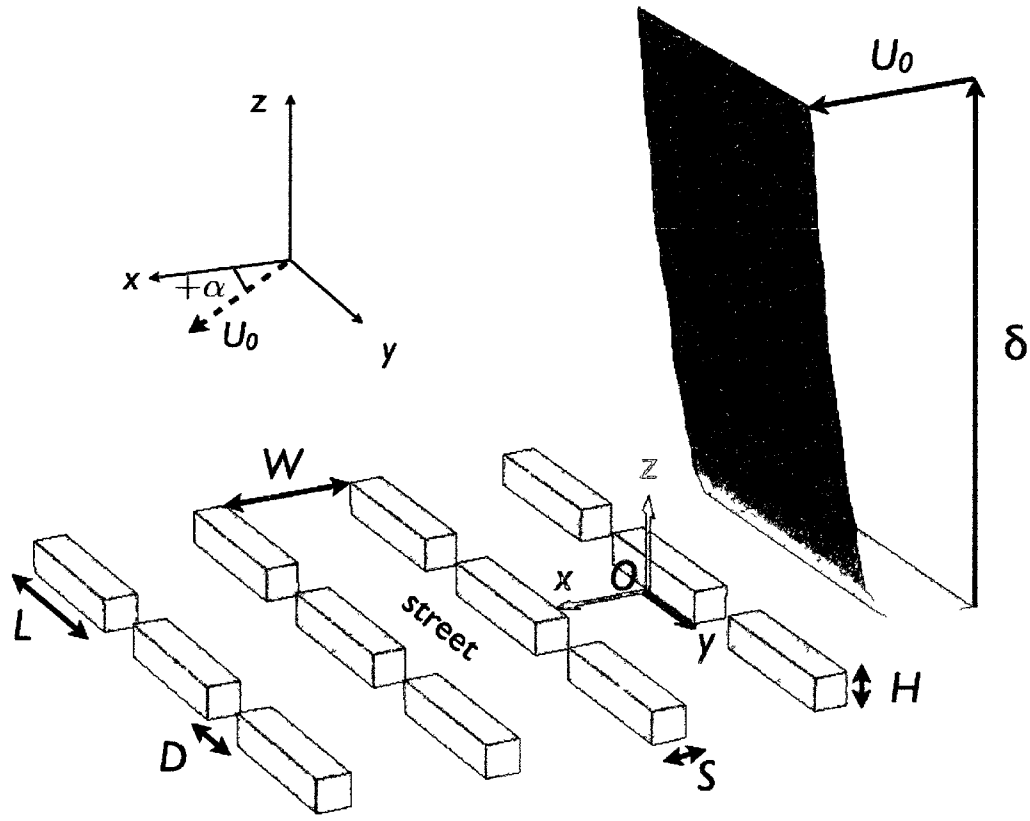

Figure 2.6. Schematic of the array, coordinate system and characteristic dimensions.

section, the x-y-z coordinate system also rotates with the array. That is, the y-axis is always aligned with the street axis and the z-axis is the wall-normal axis.

The height of the blocks used in this investigation is chosen such that adequate spatial resolution is obtained with the stereo PIV system. If the Jensen number ($J_e = \delta/z_0$) were to be matched, as suggested by Wang, Plate, Rau, and Keiser (1996), to the MUST field experiments ($J_{e_{MUST}} \approx 8000$), then an H of approximately 5 mm for our block would be required. In the J_e number, z_0 is the aerodynamic roughness length in the neutral log-law,

$$\frac{U}{u_*} = \frac{1}{\kappa} \ln\left(\frac{z-d}{z_0}\right) \tag{2.2}$$

κ is the Von Karman constant, d is the zero-displacement plane, and u_* is the friction

velocity. For the MUST experiment, the atmospheric boundary layer is approximately 400 m thick and the aerodynamic roughness length is about 0.05 m; therefore, we have $z_0 \approx 0.06$ mm. According to Fang and Sill (1992), we then have to match the ratio H/z_0 for both the full- and reduced-scale experiment yielding $H \approx 5$ mm. This is considered to be too small to achieve adequate spatial resolution for our stereo PIV measurements and we therefore chose $H = 25.4$ mm.

2.2 Apparatus and Data Processing

2.2.1 Hot-wire anemometry. The hot-wire probes used to characterize the three atmospheric boundary layers described earlier were operated by a Constant Temperature Anemometer, CTA, custom-made at IIT. The hot wires were built using a 3.8-μm diameter tungsten wire (Sigmund Cohn Co.). The sensing length of the wire was about 1 mm to ensure a length-to-diameter ratio of $l/d > 200$. The non-dimensional sensing length, $l^+ = lu_\tau/\nu$, is less than 20 as advised by Blackwelder and Haritonidis (1983) to satisfy the spatial resolution of the small-scale turbulence structures found in wall-bounded flows. The overheat ratio was set at 1.7. The hot wires were calibrated in situ against a Pitot static probe. Fourth-order polynomial curves were used to fit the calibration data. The temperature was also monitored using a thermocouple so as to correct for any drift in the measured signals of the hot wires according to the temperature correction formula provided by Drubka, Tan-atichat, and Nagib (1977). The output signals were low-pass filtered using an Ithaco filter with a 2 kHz cut-off frequency. The sampling frequency was set at 4 kHz and the acquisition time was set at 30 s per wall-normal position of the hot wire. A National Instruments data acquisition board (PCI-6251) was used to acquire the hot-wires measurements along with the LabVIEW interface.

2.2.2 Stereoscopic PIV system. Particle Image Velocimetry (PIV) is a measurement technique that was introduced in the early 80's (Adrian & Yao, 1985).

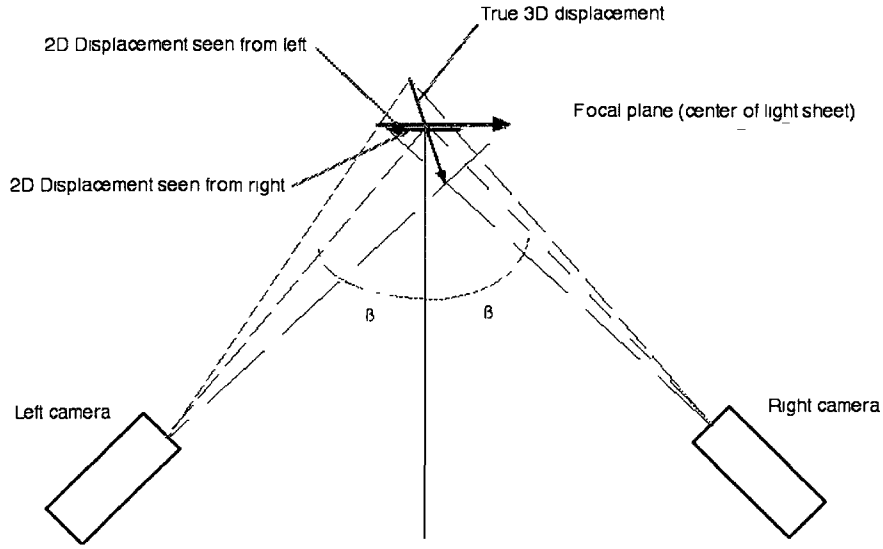

Figure 2.7. Stereoscopic principle.

Adrian (2005) defines PIV as "the accurate, quantitative measurement of fluid velocity vectors at a very large number of points simultaneously." An extension to this technique called Stereoscopic PIV (SPIV) (e.g. Soloff, Adrian, & Liu, 1997) is used in this study. Essentially, the addition of a second camera allows for determining the third component of the velocity field in the out-of-plane direction. Figure 2.7 presents a simple sketch of the two cameras pointing at the region of interest from different positions. The displacement of a particle is therefore seen differently from the two cameras. Through a calibration procedure that records known out-of-plane displacements of a calibration target from both cameras, the 3D velocity field can be estimated in the laser plane. The Scheimpflug condition (image plane, lens plane and object plane intersecting in one line) (see Louhichi, Fournel, Lavest, & Aissia, 2006) is also satisfied so as to improve the image quality when looking at the laser plane at an angle.

Figure 2.8 presents a photograph of the SPIV setup with the laser firing. In order to make SPIV measurements possible over a large domain, it is necessary to

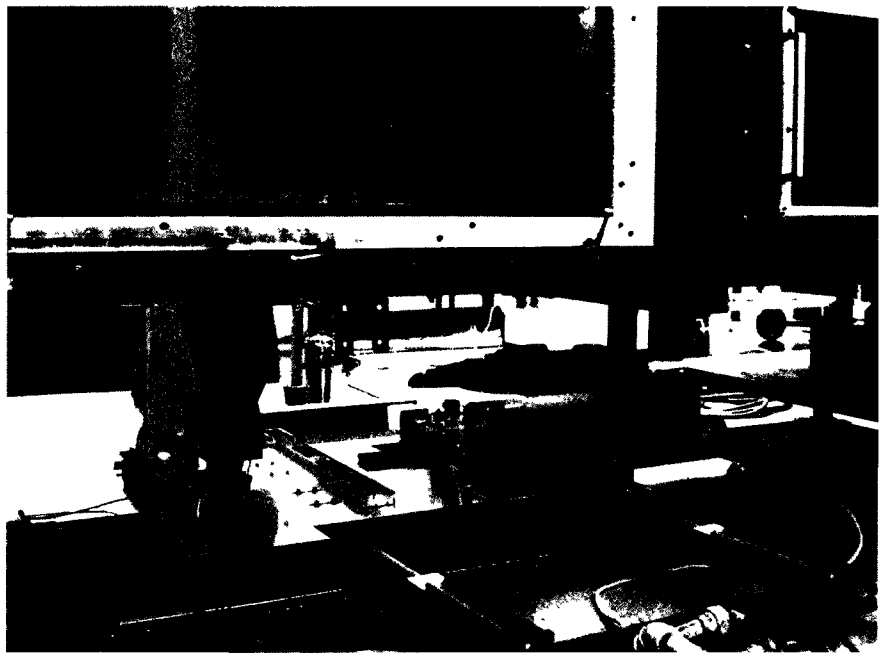

Figure 2.8. Picture of the Stereoscopic Particle Image Velocimetry system.

move the measurement system quickly and accurately. The calibration process for SPIV is tedious because a new calibration is usually required for each independent plane of data if any of the SPIV components are moved. However, in this work, a solution to overcome this limitation is implemented, where we set the entire SPIV system on a single plate sitting on a two-axis traverse system located under the wind tunnel. As can be seen in Figures 2.2 and 2.8, the laser head, the light sheet optics, and the two cameras are secured to that plate. The stereo configuration chosen is also shown in Figures 2.2 and 2.8, with the two cameras viewing the laser light sheet from opposite spanwise sides at an angle β of about 50° as defined in Figure 2.7. The light sheet enters the test section through a thin (3.18 mm) glass section of the floor. The advantages of this setup include the high accuracy of the computer-controlled two-axis traverse system, the ease of rotation of the entire PIV system to study different approach flow incidence angles, and most importantly, this system requires a single calibration per dataset (up to 224 planes). In addition, the calibration process is

greatly simplified by keeping the calibration target immobile and instead displacing the SPIV setup at various out-of-plane positions using the traverse system.

The traverse system is a two-axis traverse system manufactured by Velmex, and has a large traveling distance (635 mm along both axes) so that the entire test section can be covered if needed. The repeatability is typically 4 μm, which means that when the laser plane is returned to its initial position, there is no more than 4 μm of discrepancy due to backlash. The straight line accuracy is 0.076 mm over the entire travel distance and the screw lead accuracy is 0.076 mm per 250 mm (data provided by Velmex).

The SPIV system is from Integrated Design Tools, Inc (IDT); the laser is a pulsed dual-head Nd-Yag New Wave Research (200 mJ per pulse). The two cameras are X-Stream 5 with 1280x1024 pixels and IDT ProVision-XS software is used to acquire and process the raw images. The frequency of acquisition is always set at its maximum value of 15 Hz.

The seeding is done via three Trust Science Innovation (TSI) atomizers and consists of a mixture of polyethylene glycol (PEG) and distilled water. The atomizers produce a mean droplet diameter of 0.3 μm with a geometric standard deviation of less than 2.0 μm so that the particles will follow the flow accurately (see Raffel, Willert, & Kompenhans, 1998). The seeding particles are injected into the wind tunnel through three inlets at the floor just downstream of the roughness fetch. The injection speed is low enough so that it does not generate additional disturbances in the flow. This was confirmed by acquiring hot-wire velocity profiles just upstream of the urban array. The atomizers were emptied from the water and PEG mixture and run at the same compressed air pressure value as that used in the SPIV study to simulate the seeding. These velocity profiles agreed very well with those for no injection; therefore, the effect of the seeding on the boundary layer is considered to

be negligible.

2.2.3 SPIV data processing. The commercial software used to process the raw SPIV images is ProVision-XS by Integrated Design Tools (IDT) and lets us store a "flag matrix" that contains the status of each computed velocity vector. Namely, we know if the computation of the vector is successful; which means, a valid vector is one where all conditions to obtain an accurate estimation of the velocity are met. Conversely, a spurious vector is one where all conditions are not met. A common approach is to replace the spurious vectors with interpolated vectors using a least square estimation based on the nearest neighbors approximation. This is not the approach used for the current study. When considering turbulent flows such as the urban flow, it is very difficult to obtain a uniform seeding. Often, PIV images will present regions without any particles, and depending on the size of these regions, the nearest neighbors approximation can be highly inaccurate.

A more efficient way of recovering the missing information is to use gappy-POD (Gunes, Sirisup, & Karniadakis, 2006), which was successfully implemented by Murray and Ukeiley (2007) on PIV data. Details about the technique are provided in Appendix A. The amount of spurious velocity vectors in our data sets is on average 2% and the large amount of SPIV snapshots available to us for each vertical plane make gappy-POD an excellent alternative to standard interpolation (Gunes et al., 2006).

2.2.4 Notes on accuracy.

2.2.4.1 Accuracy of out-of-plane velocity component. For typical SPIV investigations, the accuracy for the in-plane components is usually given as 1-2%. Recently, many have looked into various techniques to improve the accuracy of the out-of-plane velocity component (e.g. Calluaud & David, 2004; Lecerf, Renou, Allano,

Boukhalfa, & Trinit, 1999; Prasad, 2000; Willert, 1997).

Prior to the collection of the SPIV data in the urban environment, a separate experiment was carried out to estimate the accuracy of our SPIV system. In order to estimate the accuracy of the out-of-plane component of the velocity field, SPIV measurements were taken in an axisymmetric jet. Figure 2.9 presents a photograph of the setup. The jet is shown on the right hand side in the picture and the cameras are mounted on the side and pointed at a calibration target, which is mounted perpendicular to the jet axis. In this configuration, the out-of-plane component captures the streamwise velocity of the jet. Several data sets were collected in this configuration by varying the calibration target type and the number of calibration images. The calibration target providing the best results for this jet flow is shown in Figure 2.10, as seen from both cameras. The target is made of aluminum to ensure its flatness. The grid nodes (with a 5-mm spacing in both the horizontal and vertical directions) are holes through the plate. In this example, the white mesh displayed on top of both views of the target is covering a 50×35-mm region. Each mesh node is aligned with a target grid node. The calibration process tracks the displacement of these grid nodes as the target is moved by a small amount in the out-of-plane direction. The best results in accuracy of the mean velocity measurements were obtained for 11 calibration images spanning the thickness of the laser light sheet ($\approx$ 2 mm). These calibration parameters were therefore used in the collection of the SPIV measurements in the urban environment.

The same velocity measurements were performed for a configuration where the calibration target was mounted parallel to the jet. As a result, the streamwise component of the jet was captured by an in-plane component of the SPIV data. Figure 2.11 illustrates the results for the streamwise velocity profile of the axisymmetric jet as measured using both configurations. It can be seen that the agreement in the mean

Figure 2.9. Picture of the axisymmetric jet and SPIV cameras.

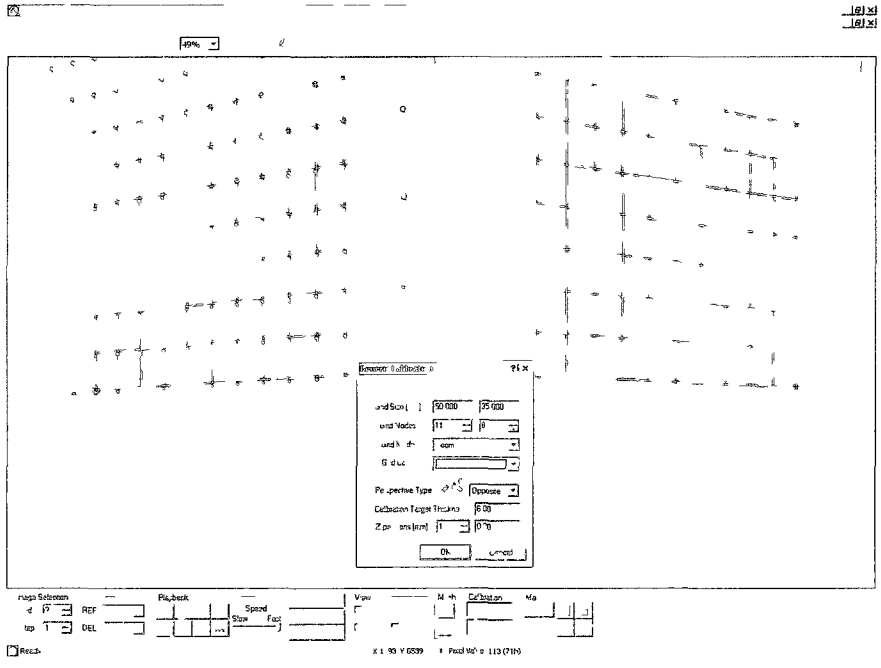

Figure 2.10 Calibration target as seen from both cameras

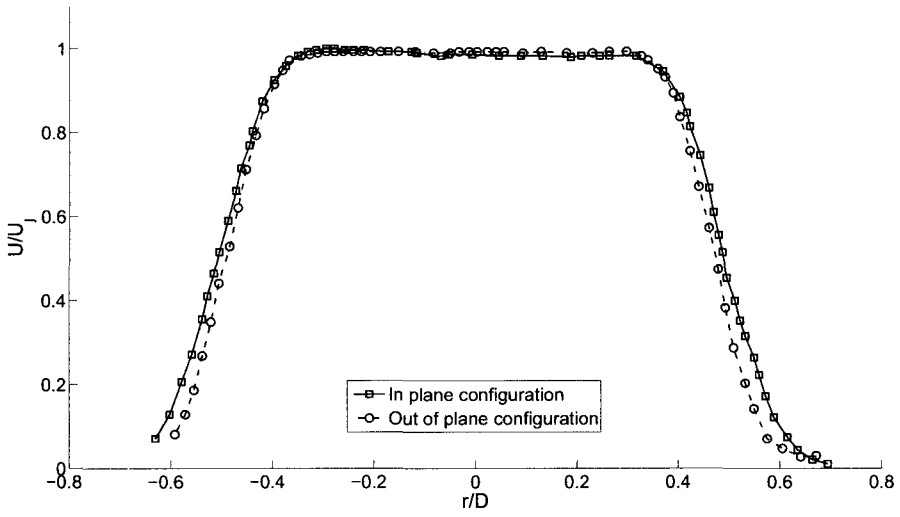

Figure 2.11. Comparison of streamwise velocity profiles for both measurement configurations.

velocity profile is very good in the core of the jet ($-0.4 < r/D < 0.4$). In this region, the difference in magnitude between the in- and out-of-plane configurations does not exceed 2% as shown in Figure 2.12 and is comparable to the accuracy obtained by Lecerf et al. (1999). Larger differences are observed in the shear layer where the seeding was non-uniform.

2.2.4.2 Error measurement within the 3D data sets. The non-uniform seeding problem mentioned above is one of the greatest challenges in performing SPIV measurements. The non-uniform seeding was more apparent for the ABL1 data set at a $W/H = 1.5$. When presenting the data for this condition (in Chapters 3 to 6), there will be some regions above the block close to the upstream edge where this noise is evident. The second major challenge is the inherent difficulty with PIV in providing good data close to walls. In order to estimate the accuracy of the measurement in our domain, we computed the divergence of the mean velocity field normalized by the ratio U_{rms}/L_x, where U_{rms} is the root-mean-square value of the streamwise velocity

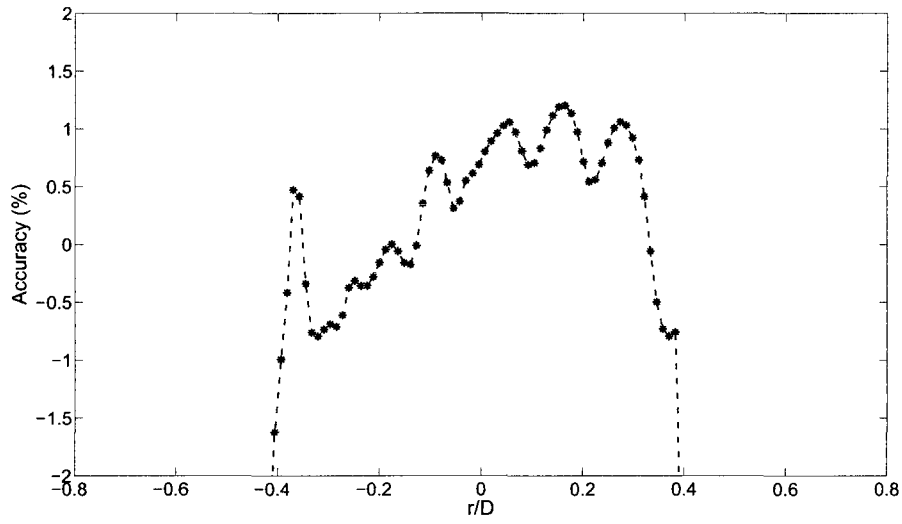

Figure 2.12. Deviation in % between the mean streamwise velocity measured in in-plane and out-of-plane configurations.

component and L_x is the characteristic distance between two consecutive data points in the streamwise direction. For an incompressible flow, the divergence is equal to zero, so the divergence of our measured velocity field will give us an idea of our SPIV accuracy. As expected, the divergence of the mean velocity field is farther from zero close to the walls and in areas where the seeding was insufficient.

The following quantity was computed to yield an estimation of the error:

$$err = 1 - \sqrt{\frac{\sum_{i=1}^{n} (\Delta_i - < \Delta_{comp} >)^2}{\sum_{i=1}^{n} (\Delta_i - \Delta)^2}} \tag{2.3}$$

where n is the number of data points in the region of interest, Δ is the true divergence of the velocity field (equal to 0 since the flow is incompressible), Δ_i is the value of the divergence computed at the i^{th} data point using the three components of velocity, and $< \Delta_{comp} >$ is the average of the computed divergence over the region of interest. For example, we find an $err = 2e^{-7}$ and $3e^{-4}$ for the data set ABL1 at $W/H = 4$

for $0°$ and $-4.5°$ respectively and $err = 0.006$ and 0.004 for the $W/H = 1.5$ case at $0°$ and $-4.5°$ respectively. Overall, all data sets present very low values of the mean velocity field divergence, except in a near-wall region (≈ 1 mm).

CHAPTER 3

SPATIAL DESCRIPTION OF MEAN FLOW AND COHERENT STRUCTURES

3.1 Introduction

Mean streamlines and coherent structures can provide very valuable information regarding the internal structure of the flow field within the urban environment. The mean flow represents a very large contribution to the kinetic energy ($\approx$ 80%). Thus, the knowledge of the mean flow will provide useful information regarding this urban flow field.

In this chapter, we will first focus our attention in Section 3.2 on the flow field as it evolves from upstream of the urban array to the downstream streets for an incidence angle of $\alpha = 0°$. This will be done for two different approach boundary layer profiles. The effect of the incidence angle on the urban flow will then be investigated in Section 3.3. First, we will look at the effect of three incidence angles (0°, $-4.5°$ and 15°) in street 2 in Section 3.3.1. In Section 3.3.2, the global effect on the urban environment for a single non-zero incidence angle (15°) will be discussed. The streamwise spacing effect on the flow field will be studied in Section 3.4 again for a single street (street 2) for two W/H conditions ($W/H = 1.5$ and 4). The flow regime associated with a wider street (Oke, 1988) will also be investigated under a non-zero incidence angle ($-4.5°$).

Table 3.1 summarizes the different tests that were performed for each of the Atmospheric Boundary Layers (ABLs) investigated and Figure 3.1 describes the location of the streets and the intersections. SPIV data have been acquired between the middle of intersections a and b, upstream of the array, and in each of the streets 1 to 3 for ABL2 and ABL3. SPIV data were collected in street 2 only for the ABL1 data set. The wall-normal domain in which we have 3D data extends to approximately

$2H$.

Table 3.1. Approach boundary layers characteristics.

ABL #	W/H	α	Street	U_0	δ	n
ABL1	1.5, 4	0°, ±4.5°	2	3.1 m/s	500 mm	0.20
ABL2	1.5	0°, 15°	upstream, 1, 2 and 3	2.2 m/s	400 mm	0.14
ABL3	1.5	0°	upstream, 1, 2 and 3	3.4 m/s	450 mm	0.17

For ABL1, SPIV images are recorded for 400 pairs of images per plane. 32 planes are used to cover the second street (see Fig. 3.1) in the spanwise direction. The spanwise spacing between the planes was varied from 3.625 mm ($0.14H$) near the edges of the block to 10 mm ($\approx 0.4H$) near the center. For the $W/H = 1.5$ case, each plane contains 39 × 51 ($x \times z$) data points. For the $W/H = 4$ case, each plane consists of 108 × 56 ($x \times z$) data points (three planes are combined in the x-z plane for each spanwise location). In both cases, the spatial resolution in both the streamwise and wall-normal directions is approximately 1 mm.

For ABL2 and ABL3, SPIV images are recorded for 1218 pairs of images per plane with 56 planes being used to cover the region of interest in the spanwise direction. The spanwise spacing between the planes for a given street is mostly kept constant at approximately 3 mm ($0.12H$). Each plane consists of 39 × 56 ($x \times z$) data points, yielding again a spatial resolution of about 1 mm in both the streamwise and wall-normal directions. Figure 3.2 presents a few planes per street along the spanwise direction (13 out of 56 for clarity) to show in more detail where the data are collected. Each data plane is collected independently of the others. By combining the mean quantities from each plane into a 3D matrix, we can then construct mean flow structures.

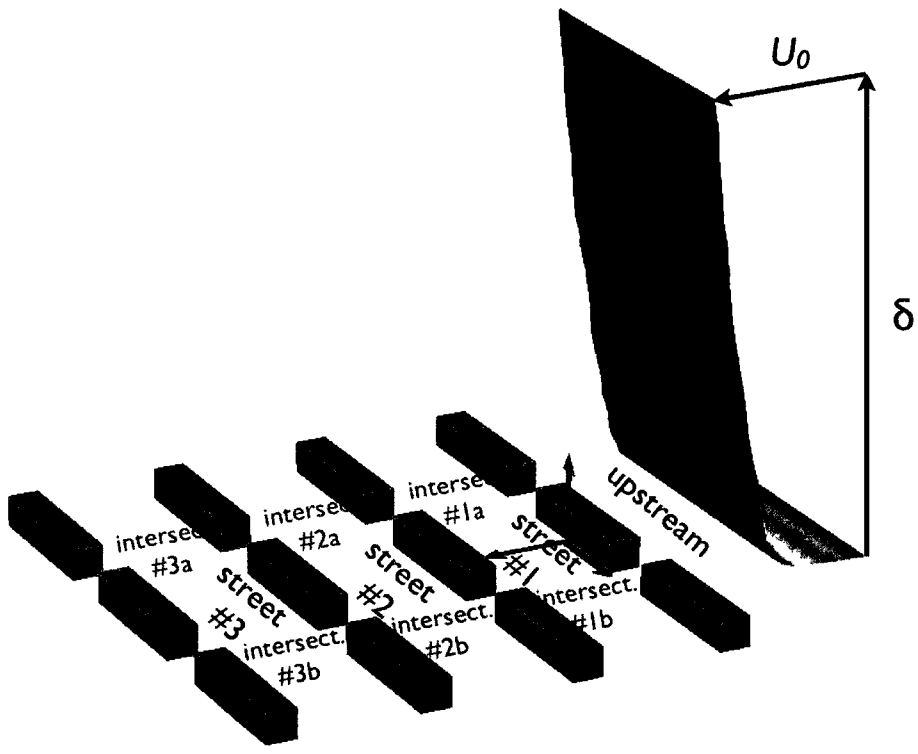

Figure 3.1. Schematic of the urban array, description of streets and intersections.

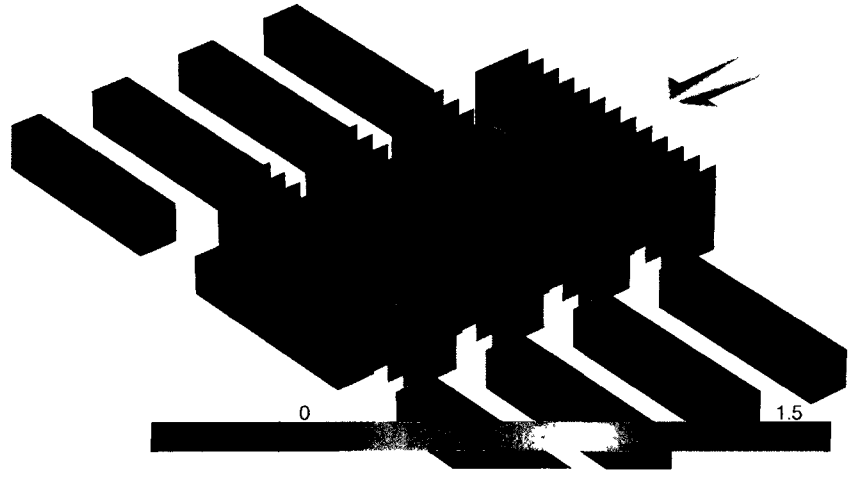

Figure 3.2. Schematic illustrating a few of the SPIV planes for ABL2 and ABL3 data sets. Coloring represents the streamwise component of velocity U normalized by the mean velocity at $z/H = 1$ obtained upstream of the urban array.

3.2 Street to street evolution of flow structures: $W/H = 1.5$ and $\alpha = 0°$

3.2.1 Mean streamlines. It should be noted that in this and the following sections, when streamlines are presented, we are actually presenting streamtubes as defined in the Matlab® environment. The reason for using streamtubes over streamlines is the ability to color the tubes based on a variable of interest in the flow field. We are interested in the Turbulent Kinetic Energy (TKE) normalized by a squared velocity scale. The flow field within a complex urban geometry has multiple scales and is difficult to characterize universally. This scaling characterization is not the focus of this work, therefore we selected the mean velocity obtained from the boundary layer profiles upstream of the array at a vertical position of $z/H = 1$, U_H, as our velocity scale. This is a simple scaling parameter that is relevant to the turbulence generated near the roofs of the buildings. The normalized Turbulent Kinetic Energy will from now on be referred to as TKE_H. The TKE is calculated as

$$\mathrm{TKE} = \frac{1}{2}\left(\overline{u'^2} + \overline{v'^2} + \overline{w'^2}\right),$$

where u', v', and w' are the fluctuating components of the velocity as defined using the classic Reynolds decomposition with the overbar representing time averaging. TKE_H is therefore:

$$\mathrm{TKE}_H = \frac{\mathrm{TKE}}{U_H^2},$$

The Matlab® streamtube function allows the diameter of the tube to represent the local divergence of the flow field. However, we are only considering an incompressible flow field, so the diameter must therefore remain constant. From this point forward, we refer to these streamtubes as streamlines. In order to plot the streamlines, we need to specify the location of the starting points. Table 3.2 summarizes this information for the various figures presented in this section. The location of the starting points are presented as normalized coordinates with respect to an in-

dependent origin in each street for easy comparison. In other words, the streamlines have the same relative starting points from street to street.

Table 3.2. Starting locations for mean streamlines for both ABL2 and ABL3.

Figure	ABL #	α	x/W	y/L	z/H
3.3	ABL2	0°	0.15	0, ±0.22, ±0.44, ±0.66	0.20, 0.60
3.5	ABL3	0°	0.15	0, ±0.22, ±0.44, ±0.66	0.20, 0.60
3.6	ABL3	0°	0.25	0, ±0.07, ±0.15, ±0.22, ±0.30, ±0.37, ±0.44, ±0.51, ±0.59, ±0.66	0.08, 0.16
3.7(a)	ABL2	0°	0.15	0	0.12, 0.20
3.7(b)	ABL3	0°	0.15	0	0.12, 0.20

3.2.1.1 Mean flow structure dependence on ABL characteristics. For our baseline case, we consider the ABL2 data set with a fixed incidence angle of $\alpha = 0°$. As shown in Table 3.1, the mean free-stream speed is $U_0 = 2.2$ m/s and the power-law exponent is $n = 0.14$. Figure 3.3 presents a general view of representative streamlines colored with TKE_H within the array for this data set. In addition to Table 3.2, where the starting locations of the streamlines are given, Figure 3.4 provides a visual representation of these starting points within the urban array. In order to make the comparison relevant between streets, the starting points are selected so as to have the same position with respect to the streets. Figure 3.3 shows a few representative mean streamlines that capture the recirculation region trapped in each street, and the

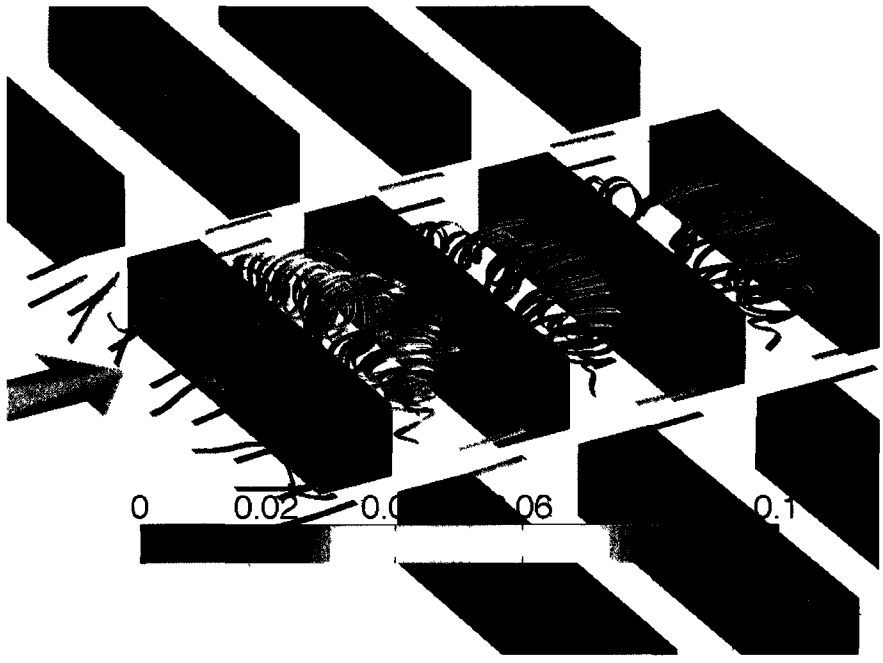

Figure 3.3. Representative mean streamlines for ABL2 at $\alpha = 0°$. The starting locations for the streamlines are given in Table 3.2 and displayed in Figure 3.4. Color represents local TKE_H.

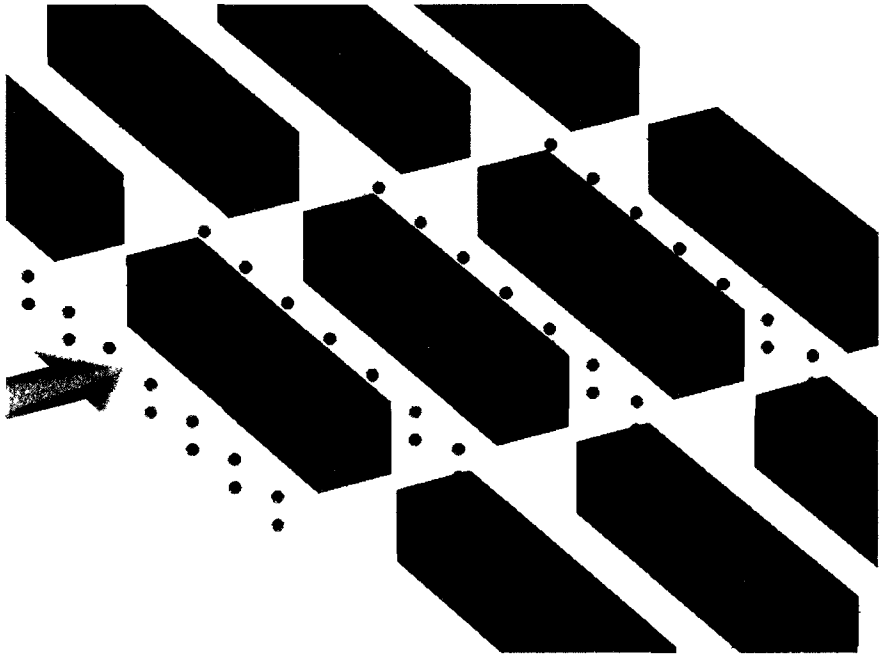

Figure 3.4. The starting locations for the streamlines shown in Figures 3.3, 3.5 and 3.23.

mean streamlines upstream of the urban array indicate the presence of a portion of the classic horseshoe vortex. From this figure, it appears that the structures trapped in each street are very similar in shape. That is to say they all present a large single recirculation region. The largest difference from street to street that can be observed from this Figure is in the TKE_H distribution. The TKE_H levels found in the first street are much larger than those found in streets 2 and 3. The drop of TKE_H from street 2 to 3 is not nearly as significant as that from 1 to 2, indicating that the flow is starting to converge towards an equilibrium state. Work by Martinuzzi and Havel (2000), for two wall-mounted cubes in tandem in a turbulent flow, shows that above the roof of the upstream block, the flow separates at the leading edge and reattaches to the top of the block forming a recirculation region. This recirculation region which is not resolved for our configuration participates in an acceleration of the flow directly above the array and in the enhancement of TKE_H. They found that this separation and reattachment regions are not observed on top of the downstream blocks, explaining the lower and more uniform levels of TKE_H found in streets 2 and 3. The mean streamlines displayed in Figure 3.3 also show the high three dimensionality of the mean flow field near the ends of the streets. Some differences in the level of symmetry of the recirculation regions can be identified in the mean streamline pattern between streets 2 and 3. As the flow is evolving deeper in the array, its three dimensionality actually increases. This phenomenon will be investigated in more detail when discussing the coherent structures calculated for this data set.

The ABL3 data set provides information about the flow structures for a faster mean free-stream speed of $U_0 = 3.4$ m/s and a larger power-law exponent $n = 0.17$. Figure 3.5 presents the mean streamlines associated with this data set. The starting points are identical to the ones used in Figure 3.3 for the ABL2 case. A comparison of Figures 3.3 and 3.5 shows that the structures in the flow field do not seem to be affected by the increase in mean free-stream speed and power-law exponent. In

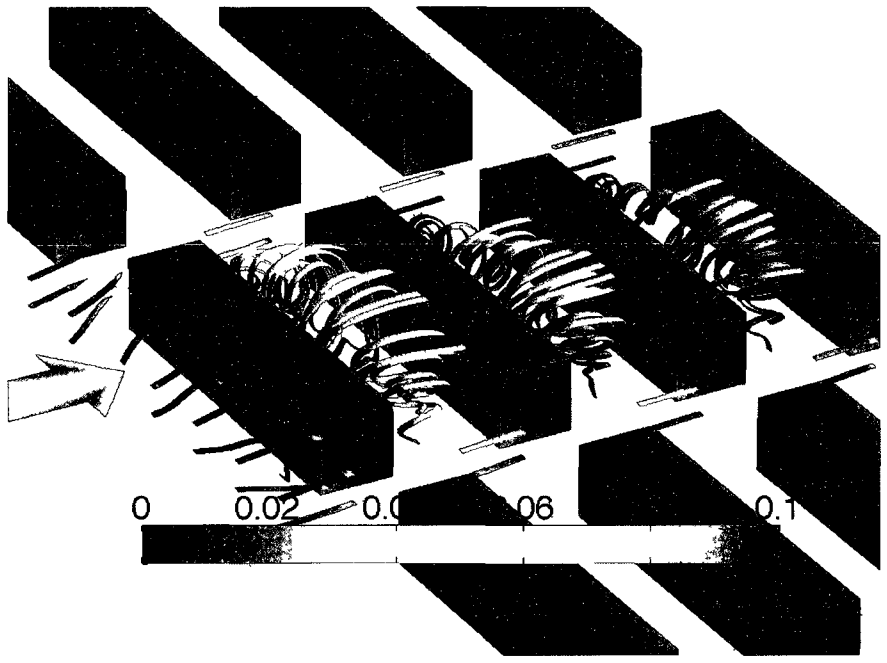

Figure 3.5. Representative mean streamlines for ABL3 at $\alpha = 0°$. The starting locations for the streamlines are given in Table 3.2 and displayed in Figure 3.4. Color represents local TKE_H.

terms of flow regime, we are still looking at a single recirculation region within each street. The only apparent difference between the two cases is the increased value of TKE_H in street 2 and 3 for the ABL3 data. This would seem to indicate that the turbulence distribution is still strongly evolving from street to street and that the rate at which equilibrium can be reached may be dependent on the incoming boundary layer characteristics. This aspect will be investigated in more detail when looking at the turbulence distribution and production mechanisms in Chapter 4.

Figure 3.6 shows in more detail the structure of the upstream recirculation region, the so-called horseshoe vortex. It is interesting to note that the TKE_H levels associated with this recirculation region are low as compared with the TKE_H levels observed in Figure 3.5 for street 1. This indicates that the horseshoe vortex is a fairly stable structure sitting upstream of the urban array. Figures 3.7(a) and 3.7(b) show streamlines starting mid-span ($y/L = 0$) for data sets ABL2 and ABL3, respectively.

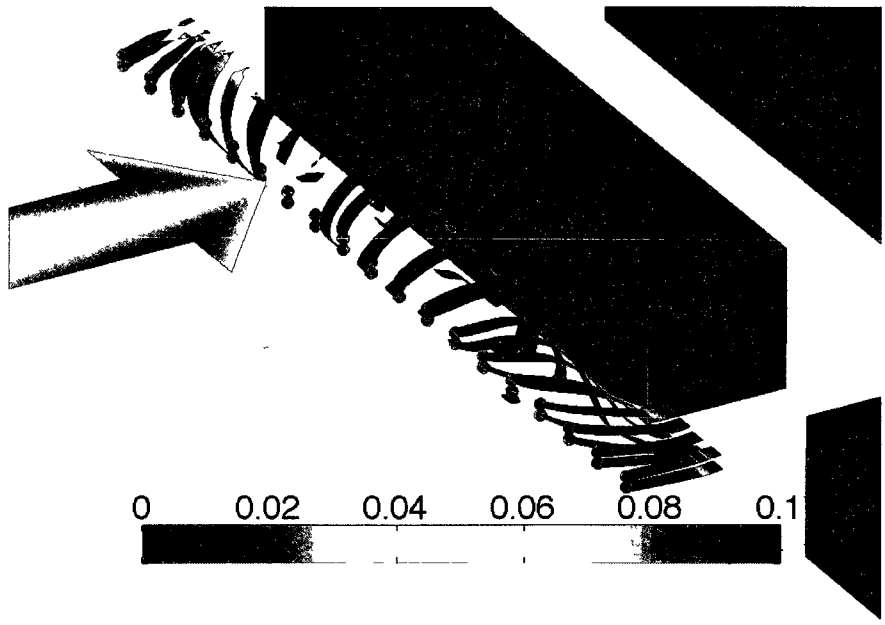

Figure 3.6. Representative mean streamlines for ABL3 at $\alpha = 0°$. The starting locations for the streamlines are given in Table 3.2 and displayed as red dots. Color represents local TKE_H.

From these figures, it is apparent that there are differences when comparing street 1 with streets 2 and 3 for the location of the recirculation region, both for ABL2 and ABL3. Street 1 exhibits a recirculation region that is located higher in the street, closer to the roof level, while streets 2 and 3 both show that the location of the recirculation region is lower in the street. In the region upstream of the array, the two streamlines depicted for both boundary layers identify a stagnation line on the windward surface of the first block at $z/H \approx 1/3$. The streamlines above the stagnation line go above the block, while the streamlines below the stagnation line form the horseshoe vortex. These observations, valid both for ABL2 and ABL3, are again in agreement with the work by Martinuzzi and Havel (2000).

3.2.2 Coherent Structures. Defining a coherent structure has been a challenge for many years. Researchers have tried to find a measurable or computable quantity that could characterize a coherent structure, and originally vorticity was the quantity

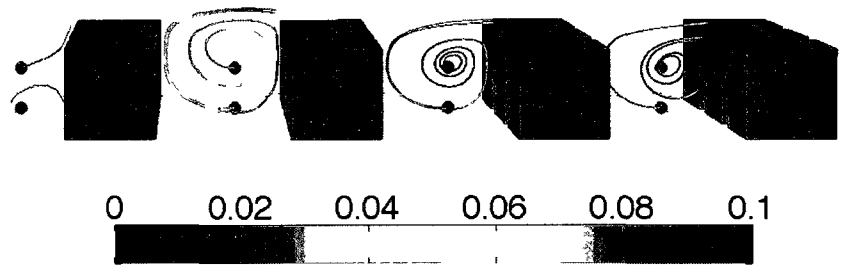

(a) ABL2

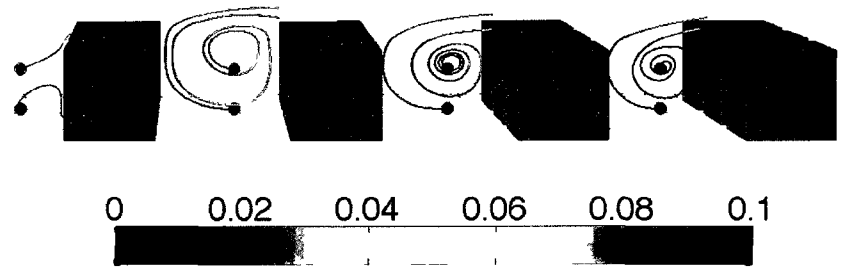

(b) ABL3

Figure 3.7. Representative mean streamlines at mid-span for ABL2 and ABL3 at $\alpha = 0°$. The starting locations for the streamlines are given in Table 3.2 and displayed as red dots. Color represents local TKE_H.

of choice. Over the years, many have proposed various definitions of a coherent structure, using vorticity contours, the Q-criterion (Hunt, Wray, & Moin, 1988), the λ_2 criterion, the λ_{ci}^2 criterion or the normalized angular momentum (Sousa, 2002) among others. All of these techniques have drawbacks. It was found in Monnier, Neiswander, and Wark (2010) that a combination of normalized angular momentum and the Q-criterion could yield relevant information about the extent, shape and core location of vortical structures for this urban array. Recently, with the work by Haller (2005), Haller (2001), Green, Rowley, and Haller (2007) and Shadden, Lekien, and Marsden (2005), Lagrangian coherent structures have been increasingly studied and they have proven to represent very well coherent structures in many cases.

In the first part of this section, we apply some of these techniques to our three-dimensional data sets to study the coherent structures in this urban environment. Vorticity contours, Q-criterion contours, and normalized angular momentum contours will be presented both for ABL2 and ABL3. The λ_2 and λ_{ci}^2 techniques were also investigated, but they provide very similar information to the Q-criterion and are therefore only shown in Appendix B.

3.2.2.1 Vorticity Magnitude. Figure 3.8 shows a sketch of the well documented arch vortex downstream of a single obstacle (Sakamoto & Arie, 1983). It is a vortical structure that has two "legs" and a roof. Each leg is composed of fluid rotating about the vertical axis and the roof is composed of fluid rotating about the spanwise axis. The sense of rotation is illustrated in Figure 3.8.

In order to investigate similar structures in the present flow field, isosurfaces of the mean vorticity components are computed. The mean vorticity components are

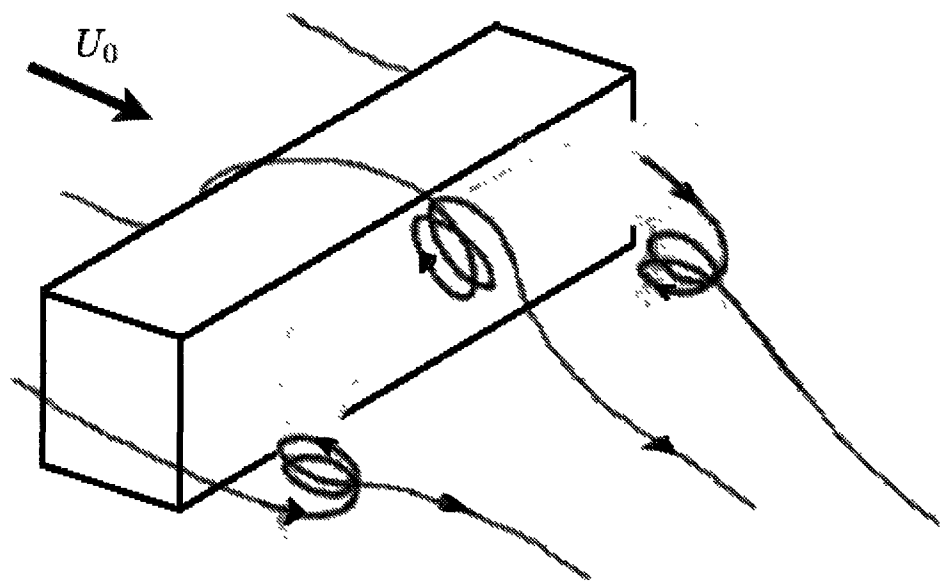

Figure 3.8. Schematic of the arch vortex downstream of a bluff body.

derived using:

$$\omega_x(x,y,z) = \frac{\partial W}{\partial y} - \frac{\partial V}{\partial z} \tag{3.1}$$

$$\omega_y(x,y,z) = \frac{\partial U}{\partial z} - \frac{\partial W}{\partial x} \tag{3.2}$$

$$\omega_z(x,y,z) = \frac{\partial V}{\partial x} - \frac{\partial U}{\partial y} \tag{3.3}$$

where U, V, and W are the mean components of the velocity field. We present isocontours of the absolute value of the mean vorticity components ($|\omega_x|$ in red, $|\omega_y|$ in blue and $|\omega_z|$ in green), so similar structures that are rotating in opposite directions will appear with the same color. For example, the two legs of the arch vortex which have opposite sign vorticity (ω_z) along the vertical axis will both be shown in green. These isocontours are normalized by the spatially averaged mean vorticity magnitude, $< \omega >= \left\langle \sqrt{\omega_x^2 + \omega_y^2 + \omega_z^2} \right\rangle$, in the domain that is resolved with our SPIV data.

Figure 3.9 presents an isocontour of $\frac{|\omega_x|}{<\omega>} = 1$ (streamwise vorticity) for the

ABL2 data set at an incidence angle of $\alpha = 0°$. Directly upstream of the array near the ground, two zones with larger $|\omega_x|$ are captured close to the sides of the block ($y/L \approx \pm 0.52$). These zones correspond to the legs of the horseshoe vortex identified with the mean streamline representation depicted in Figure 3.6. This feature is not observed directly upstream of the windward wall of the following streets for this $W/H = 1.5$ spacing. The large recirculation region is the driving flow structure in the street, and this streamwise spacing of $W/H = 1.5$ does not allow for a secondary recirculation region (Oke, 1988). However, as we go downstream, zones of larger $|\omega_x|$ are found closer to the sides of streets 2 and 3 (i.e. the intersections) ($y/L = \pm 0.4$), near the roof level ($z/H = 0.9$). The isocontours become larger in size from street 2 to 3, indicating that the magnitude of the streamwise vorticity in this region may actually increase as the flow evolves downstream. The asymmetry mentioned earlier is also directly observable in the streamwise vorticity distribution and could also contribute to the increase of streamwise vorticity between street 2 and 3.

Figure 3.10 displays an isocontour of $\frac{|\omega_z|}{<\omega>} = 1$ (wall-normal vorticity) for this same ABL2 data set. This component of vorticity is mainly due to the shear layer formed from the sides of the blocks and represents the legs of the arch vortex quite well.

Figure 3.11 presents three isocontours of spanwise vorticity for levels of $\frac{|\omega_y|}{<\omega>} = 1, 2, 3$ to highlight different features. This component of vorticity is mainly due to the shear layer formed from the top surface of the blocks. Figure 3.11(a) presents the largest threshold for the spanwise vorticity and therefore captures the strongest vortical regions. The head of the horseshoe vortex begins to appear just upstream of the array. In street 1, structures with vorticity levels of $\frac{|\omega_y|}{<\omega>} = 3$ are not observed. Those levels are observed, however, in streets 2 and 3 nearer the intersections indicating that the vorticity is increasing as the flow evolves farther downstream. The $|\omega_y|$

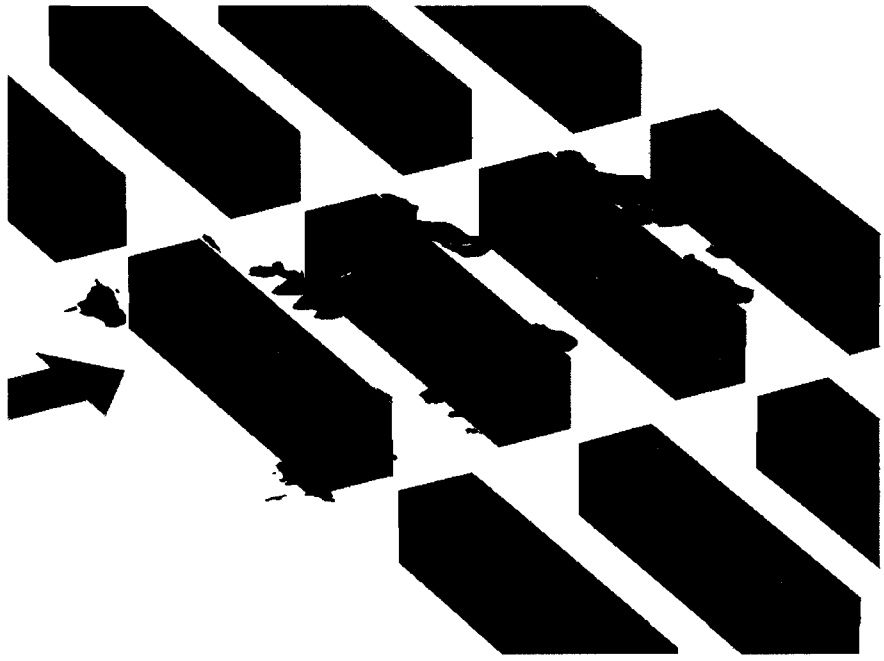

Figure 3.9. Isocontour of $\frac{|\omega_x|}{<\omega>} = 1$ for ABL2 at $\alpha = 0°$ and $W/H = 1.5$.

levels in street 3 are larger than for street 2, again showing an increase in $|\omega_y|$ with downstream location. Similar levels of spanwise vorticity start to appear in streets 2 and 3 with an increase in size of the isocontours, see Figure 3.11(a), suggesting that the vorticity is increasing as the flow evolves further downstream. This is similar to the behavior of the streamwise vorticity shown in Figure 3.9. This increase in vorticity magnitude is postulated to be related to an increase in three-dimensionality with increasing street number. This will be discussed further in regards to the bending of the arch vortex as the flow evolves within the array. As the threshold is lowered, the spanwise vorticity associated with the large recirculation region in each street becomes more apparent.

Finally, for ABL3 with an incidence angle of $\alpha = 0°$, the conclusions are very similar to the ABL2 case. The data are shown in Appendix B, in Figures B.4 to B.6.

3.2.2.2 Second invariant of the velocity gradient tensor Q. The second

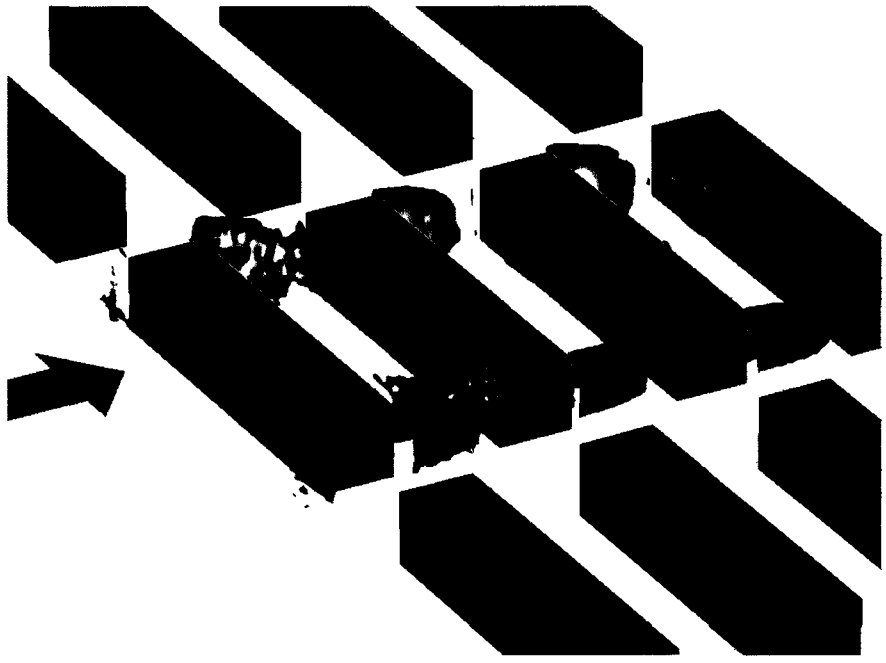

Figure 3.10. Isocontour of $\frac{|\omega_z|}{<\omega>} = 1$ for ABL2 at $\alpha = 0°$ and $W/H = 1.5$.

invariant of the velocity gradient tensor, Q, as presented in Hunt et al. (1988) is used to identify "eddy zones." Such a zone is defined according to two criteria: first, the irrotational straining is small as compared with the vorticity (corresponding to setting a threshold Q_E); and second, if the pressure tends to a minimum somewhere in the zone, there is a pressure gradient across the streamline. The second invariant of the velocity gradient tensor was used in Krajnovic and Davidson (2000) and Chong, Perry, and Cantwell (1990). They preferred this method over vorticity magnitude to identify coherent structures because it better captures rotation even when the shear effects are important since vorticity generated by the shear effects is "subtracted." This technique involves the use of spatial derivatives and is therefore commonly used for numerical data sets. However, our experimental data sets are unique in the sense that we have a fairly well-resolved mean velocity field to compute this criterion and estimate its potential for characterizing coherent structures. The application of such a technique is bound to be noisier for experimental data since the spatial resolution,

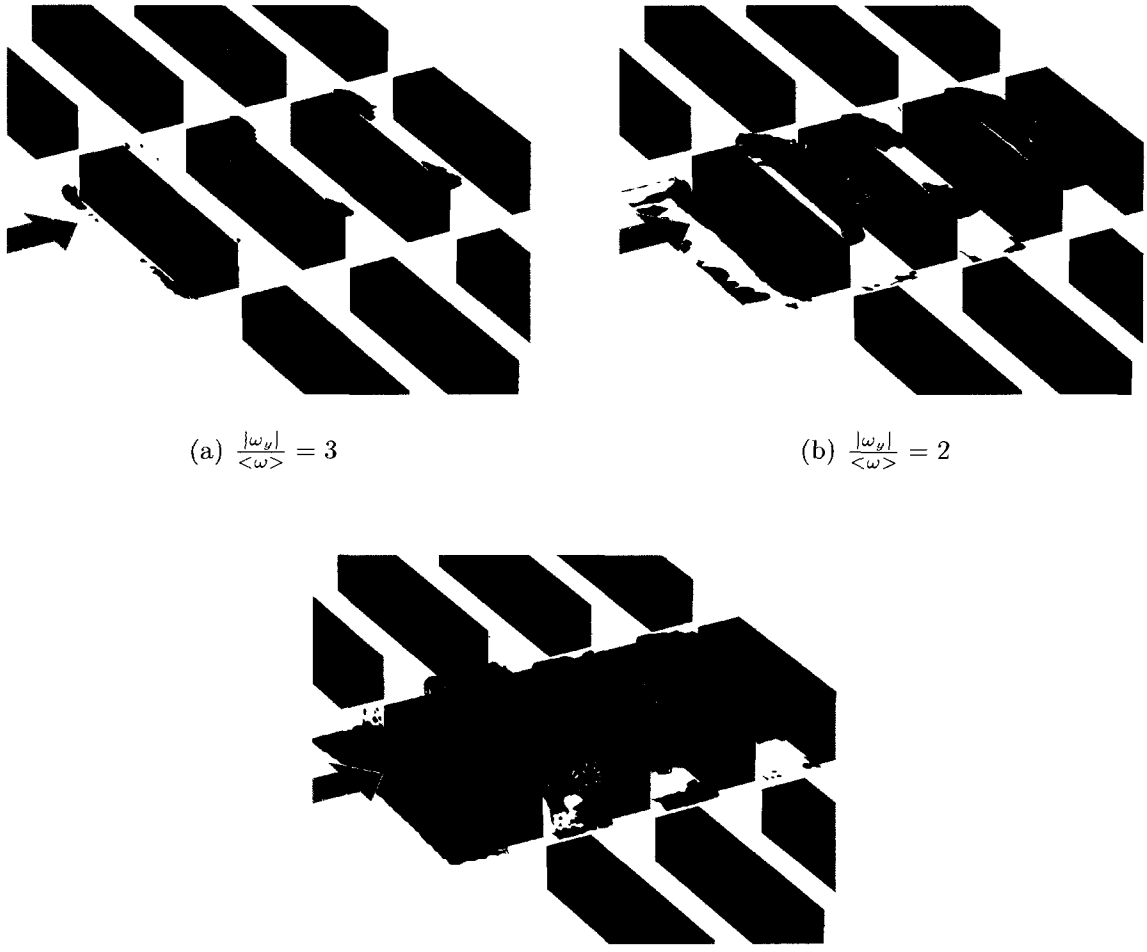

(a) $\frac{|\omega_y|}{<\omega>} = 3$

(b) $\frac{|\omega_y|}{<\omega>} = 2$

(c) $\frac{|\omega_y|}{<\omega>} = 1$

Figure 3.11. Isocontour of $\frac{|\omega_y|}{<\omega>}$ for ABL2 at $\alpha = 0°$ and $W/H = 1.5$ for three threshold levels.

especially in the spanwise direction, is still limited. However, an important advantage of this technique is to provide closed isosurfaces that follow more closely the mean streamline pattern. For incompressible flow, we can write the second invariant of the mean velocity gradient tensor as:

$$Q = -\frac{1}{2}\frac{\partial U_i}{\partial x_j}\frac{\partial U_j}{\partial x_i} = -\frac{1}{2}\left(S_{ij}S_{ij} - \Omega_{ij}\Omega_{ij}\right) \tag{3.4}$$

where S_{ij} is the rate of strain tensor $\left(S_{ij} = \frac{1}{2}\left(\frac{\partial U_i}{\partial x_j} + \frac{\partial U_j}{\partial x_i}\right)\right)$ and Ω_{ij} is the rate of rotation tensor $\left(\Omega_{ij} = \frac{1}{2}\left(\frac{\partial U_i}{\partial x_j} - \frac{\partial U_j}{\partial x_i}\right)\right)$. Ω_{ij} is related to vorticity as defined earlier by $\omega_i = \epsilon_{ijk}\Omega_{kj}$, where ϵ_{ijk} is the Levi-Civita symbol.

We first investigate the data set ABL2 using isocontours of the Q-criterion normalized by its spatial average, $< Q >$, in the domain that is resolved with our SPIV data. To do so, we present four different thresholds to give an indication of the zones that are most dominated by the recirculation regions. These four thresholds are presented in decreasing order. This means that more and more detail will be added to the figures, showing weaker and weaker levels of the Q-criterion. Figure 3.12 presents this evolution for ABL2 at a 0° incidence angle. Interestingly, the strongest recirculation region is found directly upstream of the array which corresponds to the classic horseshoe vortex. In Figure 3.12(a), it is possible to see the horseshoe vortex bending slightly around the edges of the blocks indicating the presence of the horseshoe vortex legs. However, this threshold does not show any features in streets 1 to 3 meaning that the vorticity captured in the horseshoe vortex is the largest. Upon decrease of the threshold, see Figure 3.12(b), some features start to show in street 3. With further decrease to a threshold of 2, some features show in street 2. As expected from the vorticity contours shown earlier, vortical structures appear stronger in street 3 than in street 2. This phenomenon may be related to a flow field that is becoming more and more three-dimensional as it evolves downstream and may be related to the flow converging towards an equilibrium state as the flow

turbulence is getting more uniformly distributed from street to street. Upon further decrease in the threshold, we can now see the outline of the arch vortex in the different streets. It is interesting to note that the horseshoe vortex upstream of the array does not grow excessively in size with decreasing threshold, indicating that it is very well defined by the Q-criterion. The strength of the vortical structures within street 3 is larger than those in streets 1 and 2. But the vortical structures are larger in size in streets 1 and 2 as compared with street 3 (Fig. 3.12(d)). It is also of interest to note the asymmetry in the vortical structures in streets 2 and 3. It appears that one side shows a stronger Q-criterion. This is better captured with this technique than with the mean streamline description. As will be emphasized when investigating the effect of the incidence angle of the incoming flow, the urban flow field is sensitive to asymmetries in the wind direction or in the array.

Finally, for ABL3 with an incidence angle of $\alpha = 0°$, the conclusions are again very similar to those for the ABL2 case. Therefore, the data for ABL3 are shown in Appendix B, in Figure B.1 for the same four thresholds.

3.2.2.3 Normalized angular momentum. As opposed to the identification tools discussed above which rely on velocity gradients and hence derivatives of the experimental data, the Normalized Angular Momentum, NAM, is based on an integration of the velocity field and is therefore less noisy. It was used by Sousa (2002) on 2D-3C PIV data. In that investigation, the third component of the velocity field was determined from the continuity equation as he did not have a direct measurement for it. The Normalized Angular Momentum is defined as:

$$\boldsymbol{f}(\boldsymbol{x}_P) = \frac{1}{R}\int_{\boldsymbol{x}\in R} \frac{(\boldsymbol{x}-\boldsymbol{x}_P)\times \boldsymbol{V}(\boldsymbol{x})}{|\boldsymbol{x}-\boldsymbol{x}_P||\boldsymbol{V}(\boldsymbol{x})|} d\boldsymbol{x} \tag{3.5}$$

where $\boldsymbol{x}$ is the spatial vector in the domain R, $\boldsymbol{V}(\boldsymbol{x})$ is the velocity vector at $\boldsymbol{x}$ and $\boldsymbol{x}_P$ is the spatial location where $\boldsymbol{f}$ is computed. This equation is discretized for the present study and the magnitude of $\boldsymbol{f}$, denoted as f, is computed for each node. The

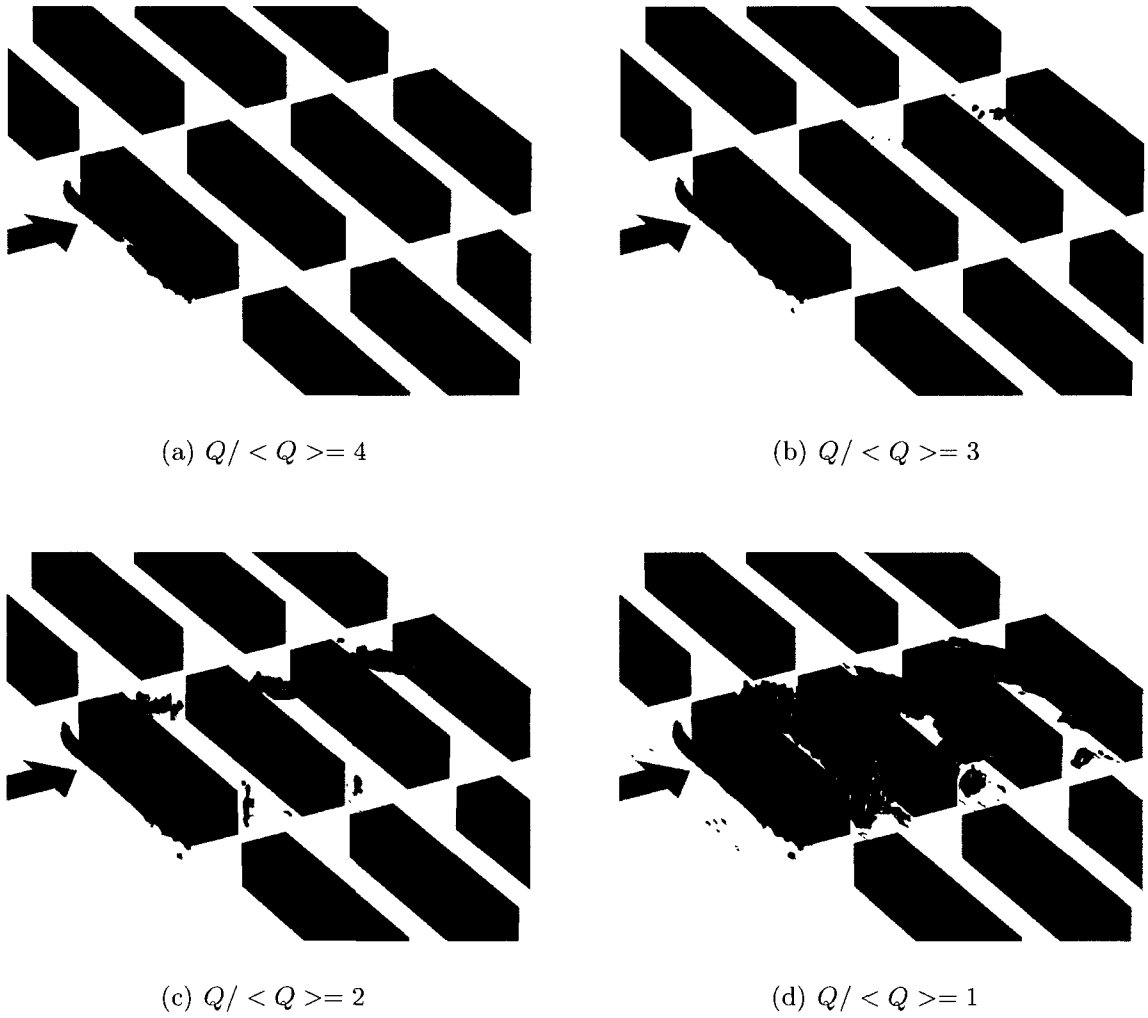

(a) $Q/ < Q >= 4$

(b) $Q/ < Q >= 3$

(c) $Q/ < Q >= 2$

(d) $Q/ < Q >= 1$

Figure 3.12. Isocontours of Q-criterion normalized by $< Q >$ for ABL2 at $\alpha = 0°$ for four threshold levels.

NAM method is a very powerful way of accurately finding the core location of the vortical structures. However, as it is not measuring the vorticity associated with the flow, no relevant information on the local strength of the structure can be gained. This explains why this technique should be used in conjunction with the Q-criterion that provides complementary information on the shape and strength of vortical structures (e.g. Monnier et al., 2010). To demonstrate this, we present once again four different levels of f in Figure 3.13 for ABL2 at an incidence angle of $\alpha = 0°$. $\boldsymbol{f}$ is normalized so that a threshold value close to 1 provides more accuracy on the core location of vortical structures. Therefore, as we decrease the value of the threshold from 0.80 to 0.35 in increments of 0.15, the NAM structures increase in size. The usefulness of the NAM structure is in its ability to provide a clearer picture of the core location of the vortical structures. Again, looking at higher levels of NAM narrows the core location.

Figure 3.14 presents the isocontours of NAM for the ABL3 at an $\alpha = 0°$ incidence angle. These contours provide an accurate way of comparing the location of flow structures for the different incoming boundary layer characteristics. The features depicted by the isocontours of NAM for the ABL3 data set are nearly identical to those displayed for ABL2 in Figure 3.13.

3.3 Effect of the incidence angle on the urban flow field

In this section, we focus on the effect of small incidence angles, $\alpha = -4.5°$ and $\alpha = 15°$ for the flow through this urban array, while past studies (Yee & Biltoft, 2004; Zhou & Stathopoulos, 1997; Santiago, Dejoan, Martilli, Martín, & Pinelli, 2009; Niachou, Livada, & Santamouris, 2008; Crowther, Galeil, & Hassan, 2002; Nakamura, Igarashi, & Tsutsui, 2003; Becker et al., 2002) investigated primarily large incidence angles (30°, 45°, 60°, 90°).

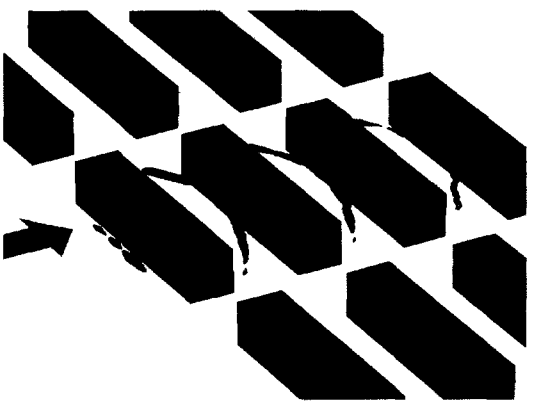

(a) $f = 0.80$

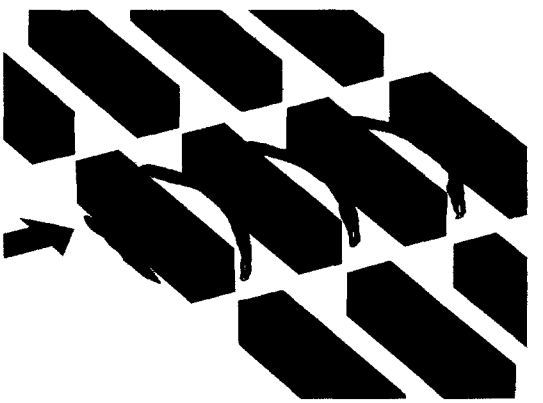

(b) $f = 0.65$

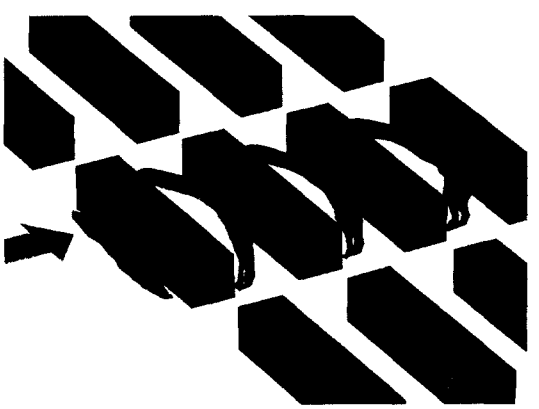

(c) $f = 0.50$

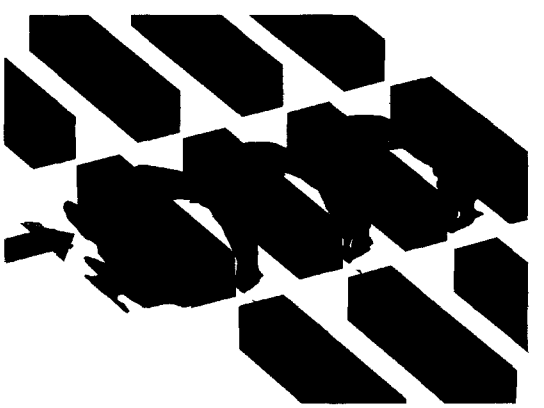

(d) $f = 0.35$

Figure 3.13. Isocontours of NAM for ABL2 at $\alpha = 0°$ for four threshold levels.

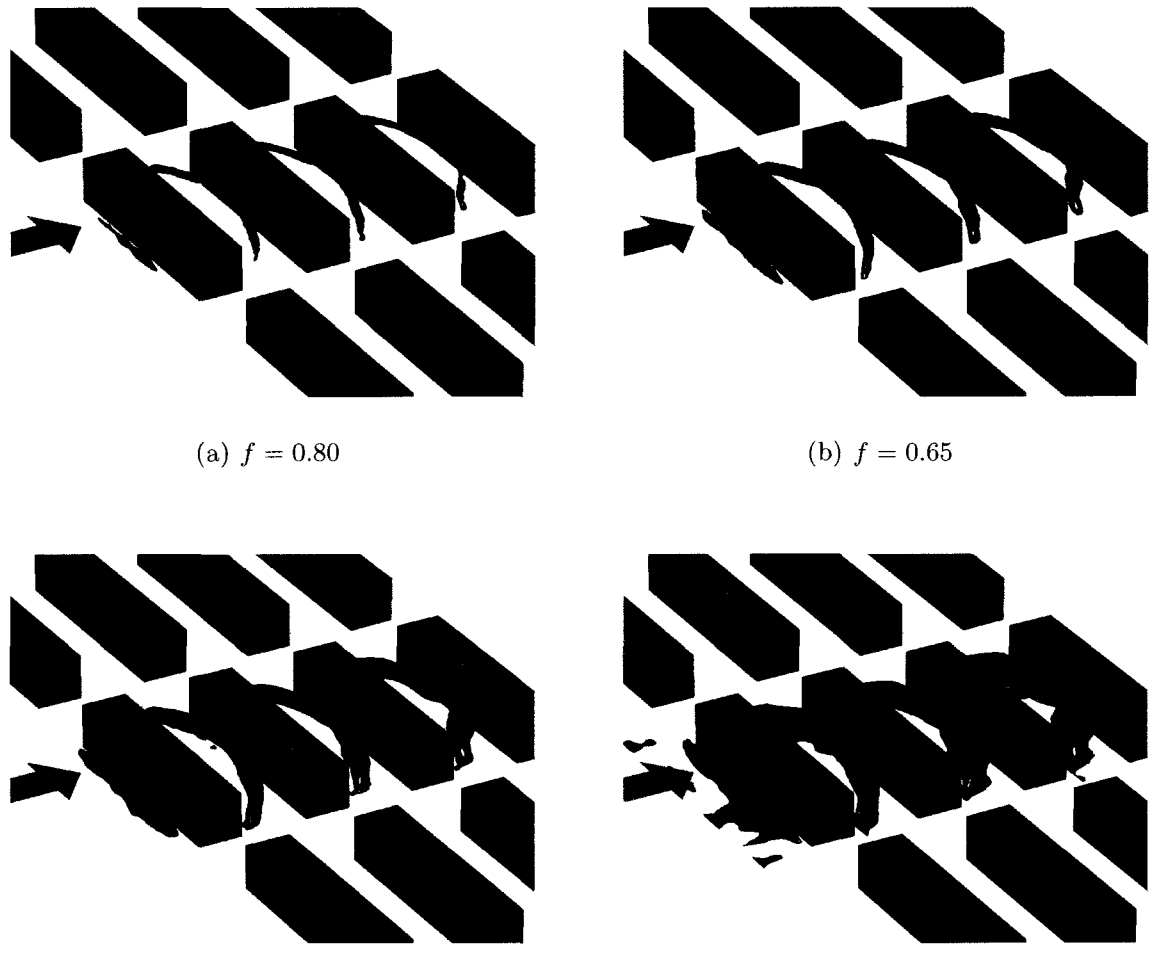

(a) $f = 0.80$ (b) $f = 0.65$

(c) $f = 0.50$ (d) $f = 0.35$

Figure 3.14. Isocontours of NAM for ABL3 at $\alpha = 0°$ for four threshold levels.

3.3.1 Incidence angle effect in street 2. In this section, we will focus our interest on street 2 as defined in Figure 3.1 for $W/H = 1.5$.

3.3.1.1 Mean streamlines. The mean streamlines presented in this section are computed in a similar manner as previously explained and the color mapping corresponds again to the TKE_H levels. Table 3.3 summarizes the location of the starting points for the calculation of the streamlines presented in this section. The viewpoint used in this section (direction from which we are looking at the three dimensional representation of the data) is selected so as to highlight the effect of the various incidence angles presented. That is, we look at the three-dimensional mean streamlines from an upstream position. Figure 3.15 presents the baseline case at a zero-incidence angle for the ABL1 case. Figure 3.16 presents the mean streamlines for the ABL1 case at an $\alpha = -4.5°$ incidence angle. Finally, Figure 3.17 presents similar mean streamlines for the ABL2 case at the $\alpha = 15°$ incidence angle. From Figure 3.15, it can be seen that the symmetry of the streamlines is fairly high in street 2. The effect of the incidence angle on the mean streamlines displayed in Figure 3.16 for $\alpha = -4.5°$ is quite dramatic. These streamlines follow a helicoidal path down the street, indicating a "channeling" of the flow down the street. Upon further increase of the incidence angle to 15° (Figure 3.17), the mean streamlines appear to be even more aligned along the spanwise direction with fewer revolutions in the "helicoidal" path. This channeling effect of the flow along the street axis has been observed by others (e.g. Louka et al., 1998; Yee et al., 2006) for larger incidence angles.

3.3.1.2 Coherent structures. In this section, we will investigate the effect of the incidence angle in street 2 using the coherent structure identification tools discussed earlier. The well-known arch vortex observed earlier in the general description of the urban array for a zero-incidence angle is again shown in Figure 3.18 (with the upstream viewpoint) at $\alpha = 0°$ and serves as a baseline case. Figure 3.19 presents

Table 3.3. Starting locations for mean streamlines for $W/H = 1.5$ in street 2.

Figure	α	x/W	y/L	z/H
3.15	0°	0.15	0, ±0.22, ±0.44, ±0.66	0.20, 0.60
3.16	−4.5°	0.15	0, ±0.22, ±0.44, ±0.66	0.20, 0.60
3.17	15°	0.15	0, ±0.22, ±0.44, ±0.66	0.20, 0.60

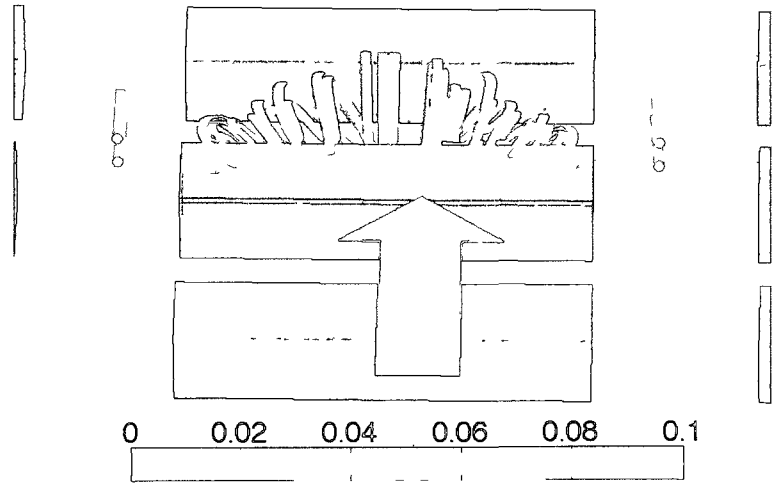

Figure 3.15. Representative mean streamlines for ABL1 at $W/H = 1.5$ and $\alpha = 0°$. The starting locations for the streamlines are given in Table 3.3 and displayed as red dots. Color represents local TKE_H.

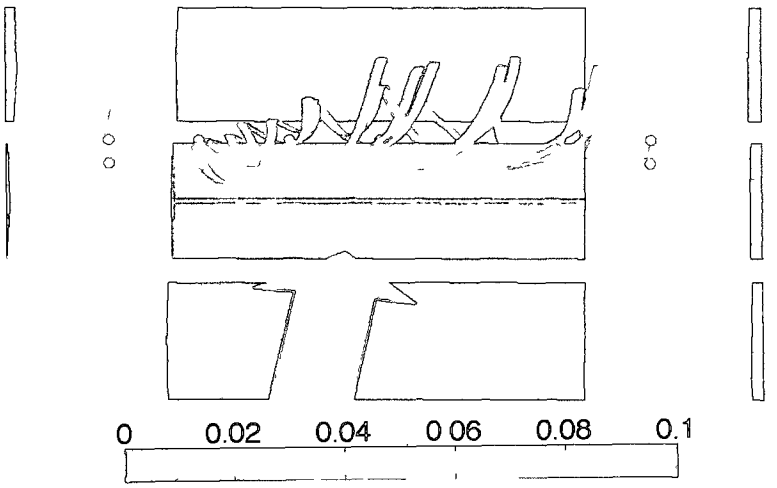

Figure 3.16. Representative mean streamlines for the ABL1 at $W/H = 1.5$ and $\alpha = -4.5°$. The starting locations for the streamlines are given in Table 3.3 and displayed as red dots. Color represents local TKE_H.

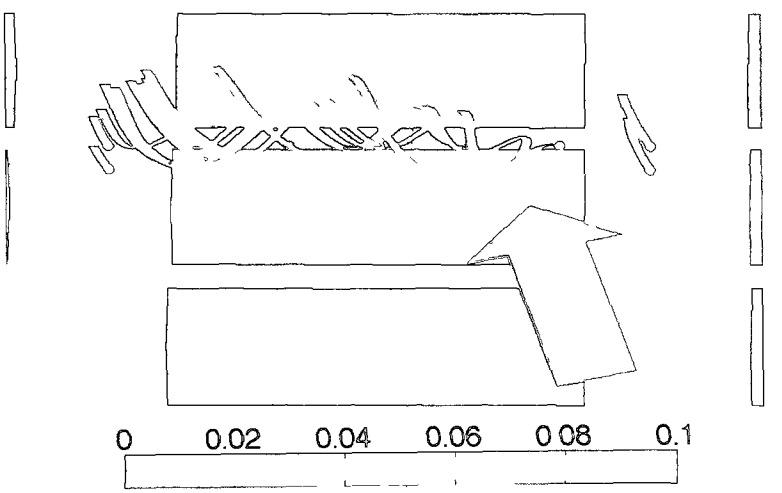

Figure 3.17. Representative mean streamlines for the ABL2 at $W/H = 1.5$ and $\alpha = 15°$. The starting locations for the streamlines are given in Table 3.3 and displayed as red dots. Color represents local TKE_H.

the same isocontour for the $\alpha = -4.5°$ incidence angle. It can be seen that the core location of the arch vortex has been shifted deeper in the street on the side that is not directly exposed to the incoming flow. The right leg has moved downstream and closer to the intersection and in Figure 3.20, we can see this effect due to a further increase in the incidence angle. For the $\alpha = 15°$ case, the leg of the arch vortex is not within our field of view, meaning that it has moved out of the street and is a direct consequence of the channeling effect. This can be related to results obtained by Becker et al. (2002) on the flow around a single obstacle where they observed a shift in position of the footprint of the vortical structure for incidence angles from 0° to 90° in increments of 30°. However, the results presented here are different in terms of topology: the fact that there are interactions between streets and intersections in our study changes the pattern observed in Becker et al. (2002). Indeed, instead of converging towards a state where the shifted footprint reattaches on top of the building, it is actually clearly leaving the street for our configuration. For our building, Figure 3.21 describes the mechanism associated with the displacement of the arch vortex as the incidence angle is increased as proposed in the work by Becker et al. (2002). For incidence angles sufficiently large in this urban array, the channeling effect is driving the flow field within the street.

Figure 3.22 presents an isocontour of the Q-criterion for the ABL2 case in street 2 at an $\alpha = 15°$ incidence angle. As mentioned before, in order to get a more complete representation of the vortical structure, it is best to use the NAM and Q-criterion in conjunction as the latter method provides information about the extent, shape and strength of the vortical structure. Similar features, as observed with the NAM isocontour, are observed in Figure 3.22 for the Q-criterion. The absence of the second leg of the arch vortex is emphasized. In addition, it appears that the strength of the vortical structure is less on the left side of the street where the flow is exiting the street since it is not captured by the isocontour level selected to display

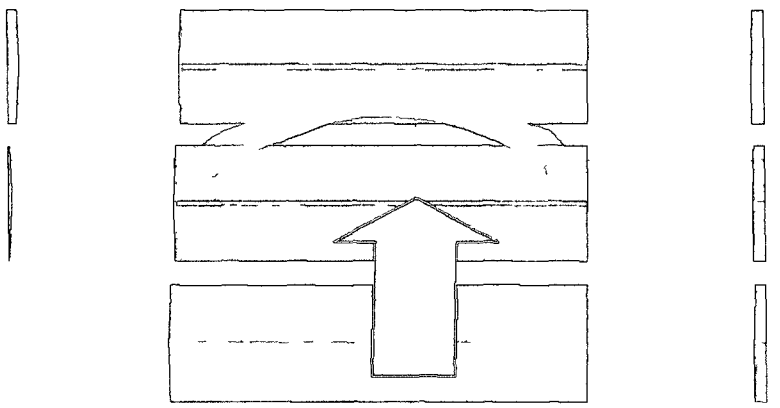

Figure 3.18. Isocontour of NAM ($f = 0.55$) for ABL1 at $\alpha = 0°$ and $W/H = 1.5$ in street 2.

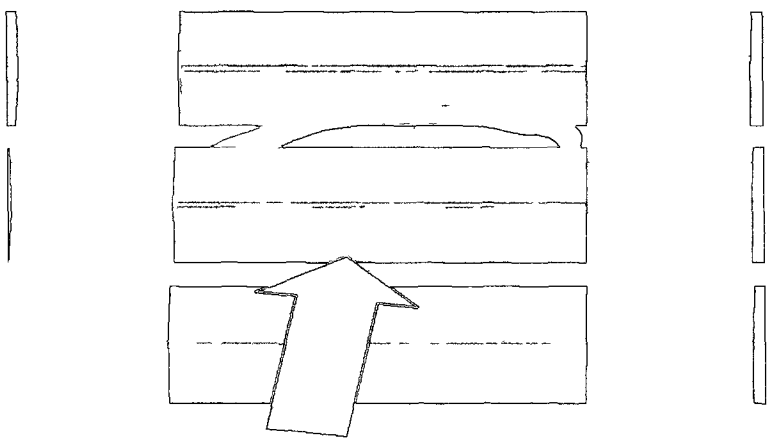

Figure 3.19. Isocontour of NAM ($f = 0.55$) for ABL1 at $\alpha = -4\,5°$ and $W/H = 1.5$ in street 2.

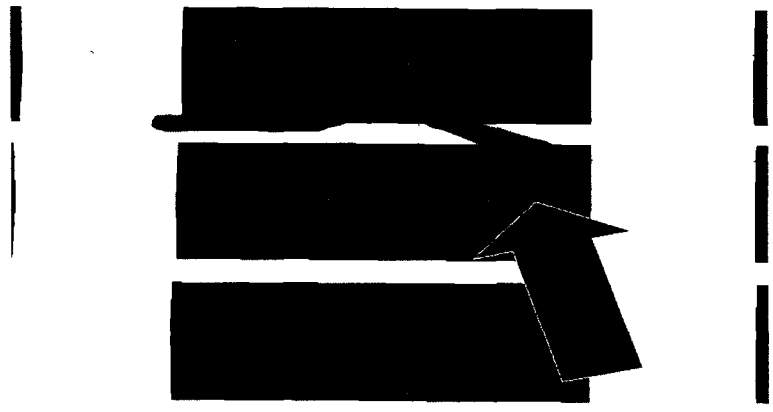

Figure 3.20. Isocontour of NAM ($f = 0.55$) for ABL2 at $\alpha = 15°$ and $W/H = 1.5$ in street 2.

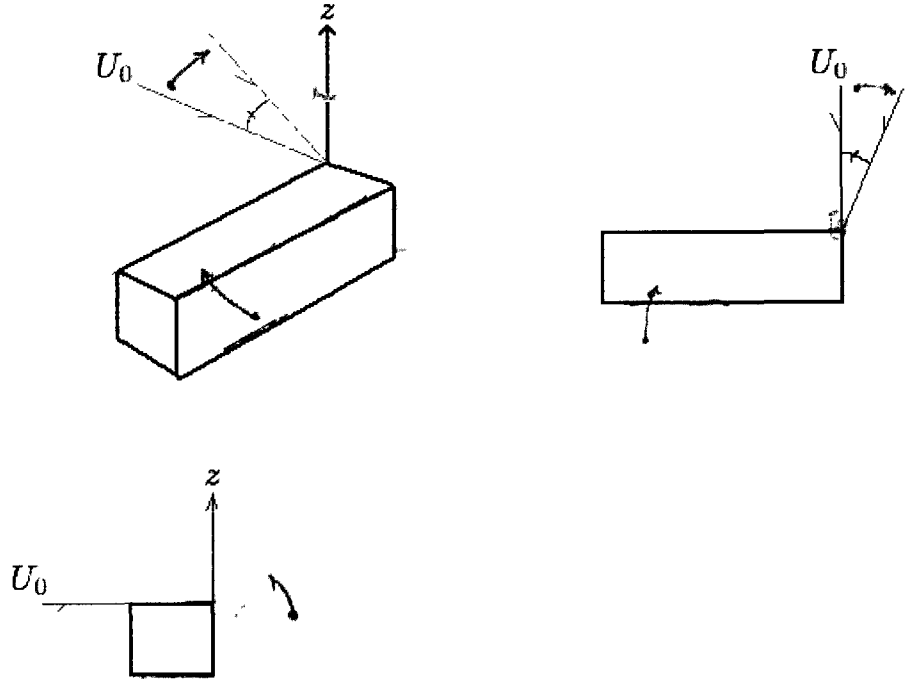

Figure 3.21. A schematic depicting the dependence of the arch vortex on incidence angle based on Becker et al. (2002).

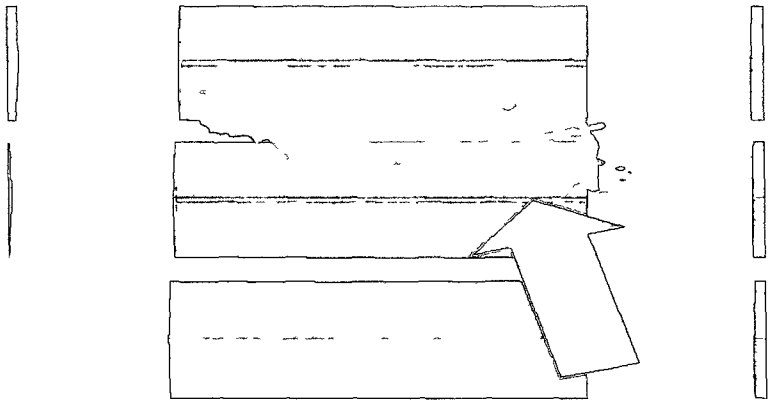

Figure 3.22. Isocontour of normalized Q-criterion ($Q/ < Q >= 1$) for ABL2 at $\alpha = 15°$ and $W/H = 1.5$ in street 2.

the Q-criterion.

3.3.2 **Incidence angle effect from street-to-street.** At the urban scale, the incidence angle effect can be characterized from street to street using our data set ABL2 for the incidence angle of $\alpha = 15°$. Figure 3.23 presents the general view of representative streamlines within the array for $\alpha = 15°$ and should be compared with Figure 3.3 for $\alpha = 0°$.

As expected from the study of the incidence angle effect in street 2 discussed above, the whole flow field in the urban array is strongly modified by the $\alpha = 15°$ incidence angle. Figures 3.24 and 3.25 present an isocontour of the Q-criterion and an isocontour of the NAM, respectively, for this incidence angle. The arch vortex in street 1 is almost aligned with the diagonal of the street, while a large portion of the arch vortices in streets 2 and 3 are aligned with the street axis. To illustrate the strong displacement of the second leg of the arch vortex near $y/ = 0.5$, Figure 3.26 presents a different view (from a downstream position) of the same isocontour

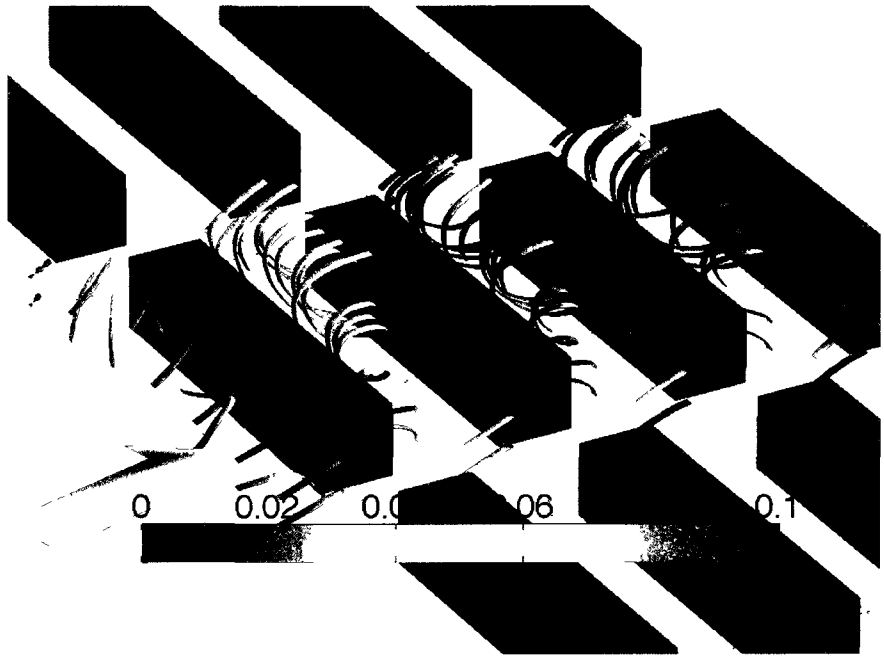

Figure 3.23. Representative mean streamlines for the ABL2 at $\alpha = 15°$. The starting locations for the streamlines are given in Table 3.3 and displayed as red dots. Color represents local TKE_H.

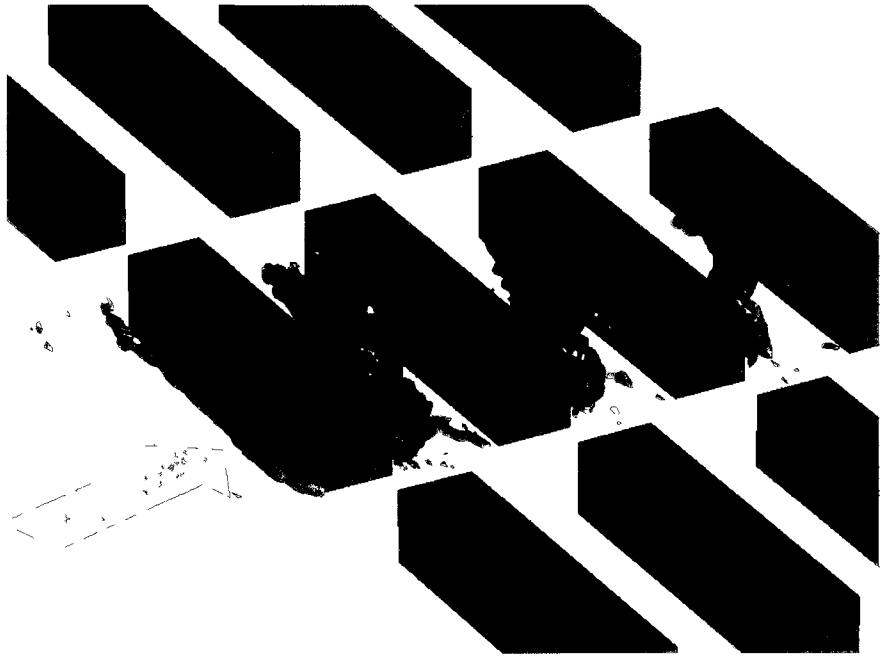

Figure 3.24. Isocontour of normalized Q-criterion ($Q/ < Q >= 2$) for ABL2 at $\alpha = 15°$ and $W/H = 1.5$ in street 2.

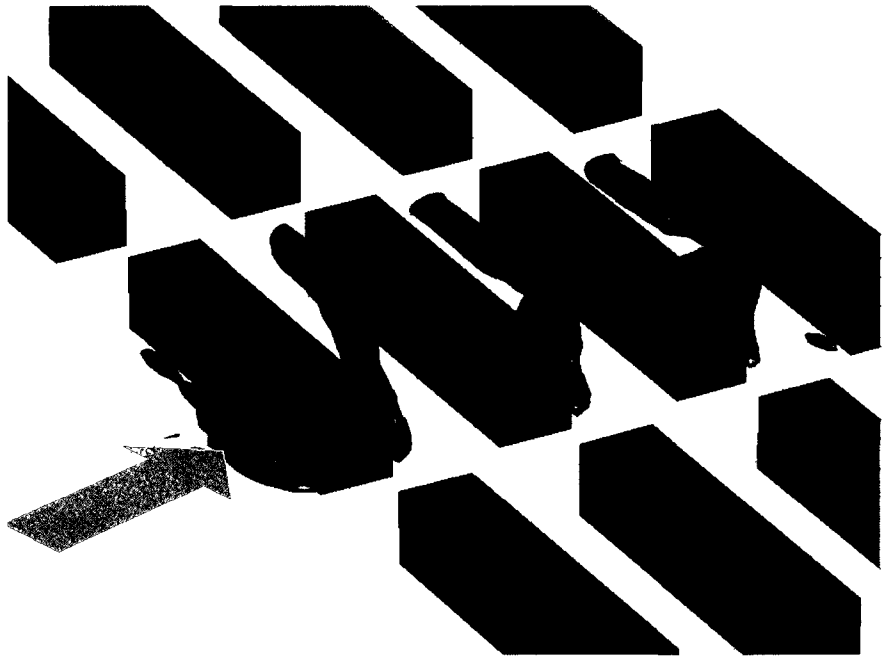

Figure 3.25. Isocontour of NAM ($f = 0.35$) for ABL2 at $\alpha = 15°$ and $W/H = 1.5$ in street 2.

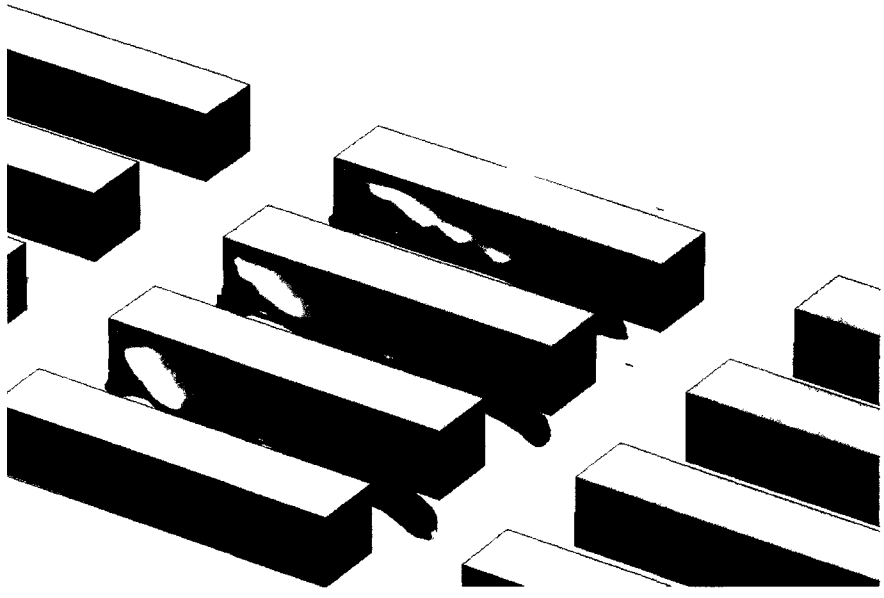

Figure 3.26. Isocontour of NAM (f=0.35) for ABL2 at $\alpha = 15°$ viewed from a downstream position.

displayed in Figure 3.25.

3.4 Effect of streamwise spacing on flow regime at the street scale

In this section, we focus our interest on street 2 for the ABL1 data set to compare the $W/H = 1.5$ results previously discussed with results for $W/H = 4$. According to the work by Oke (1988) and Martinuzzi and Havel (2000), the streamwise spacing W/H is an important parameter that defines the flow field observed in urban environments. As discussed in Section 3.2, a streamwise spacing of $W/H = 1.5$ yields a single recirculation region, referred to as the skimming flow regime by Oke (1988). The larger streamwise spacing investigated, $W/H = 4$, is associated with a different flow regime, the so-called wake interference regime. For this larger W/H spacing, incidence angles of $-4.5°$, $0°$ and $4.5°$ were investigated. Table 3.4 summarizes the location of the starting points for the calculation of the mean streamlines (again colored with TKE_H) presented in this section.

Table 3.4. Starting locations for mean streamlines at an $\alpha = 0°$ incidence angle for both $W/H = 1.5$ and 4.

Figure	W/H	x/W	y/L	z/H
3.27	1.5	0.15	0, $\pm$0.22, $\pm$0.44, $\pm$0.66	0.20, 0.60
3.28(a)	4	0.40, 0.85	0.07	0.10, 0.45
3.28(b)	4	0.10	$-$0.47, $-$0.55, $-$0.62	0.23, 0.35

3.4.1 Flow regimes associated with the two different streamwise spacings.

In Figure 3.27, the mean streamlines for a streamwise spacing of $W/H = 4$ are shown. Two distinct recirculation regions within the street are observed with the largest being downstream of the upstream block, while a secondary recirculation region is

formed upstream of the downstream block. This is better seen in Figure 3.28(a) where streamlines starting only on the center plane ($y/L \approx 0$) are shown.

The wake created by the upstream block interacts with the secondary recirculation upstream of the downstream block, hence its name of the wake interference regime as given by Oke (1988). As argued by Oke, upon further increase of the streamwise spacing, this interaction would weaken and finally disappear for a very large streamwise spacing. The flow would enter the isolated roughness flow regime, where the second recirculation region would turn into a classic horseshoe vortex structure.

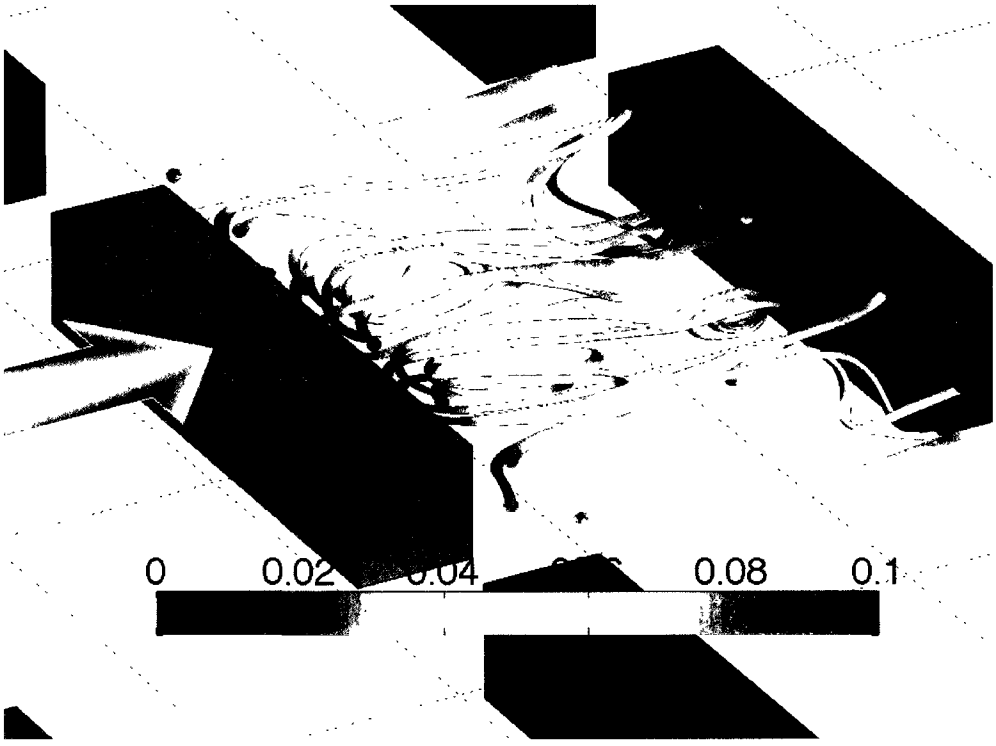

Figure 3.27. Representative mean streamlines for the ABL1 at $W/H = 4$ and $\alpha = 0°$. The starting locations for the streamlines are given in Table 3.4 and displayed as red dots. Color represents local TKE_H.

A comparison of the streamlines near the intersections ($y/L \approx -0.5$ for example) for the two flow regimes shows a more complex flow structure for the larger

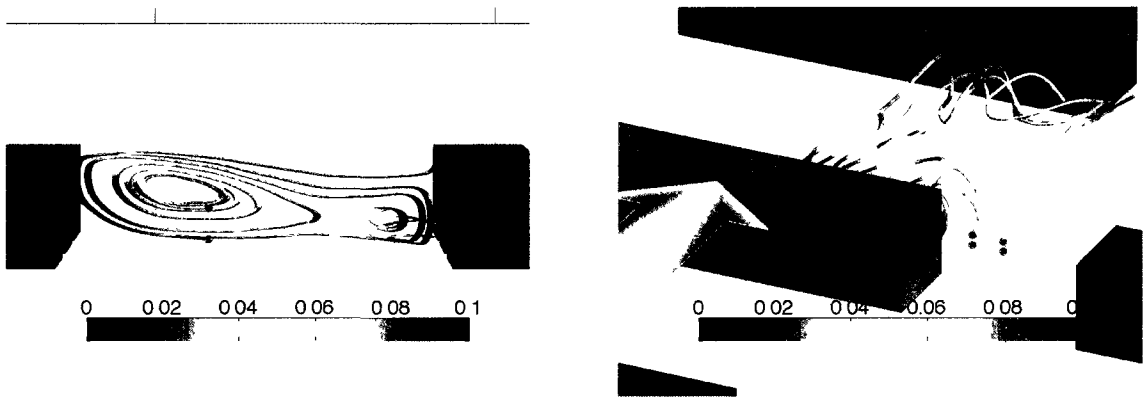

(a) In the center plane.

(b) Near the side of the streets.

Figure 3.28. Representative mean streamlines for the ABL1 at $W/H = 4$ and $\alpha = 0°$. The starting locations for the streamlines are given in Table 3.4 and displayed as red dots. Color represents local TKE_H.

aspect ratio $W/H = 4$ than for the $W/H = 1.5$ case. For example, by comparing Figures 3.15 with 3.27 and 3.28, it is observed that the wider side yields a more three-dimensional flow structure. However, there are similarities between the two flow regimes, especially directly downstream of the upstream block. For both flow regimes, the streamlines starting near the intersections tend to spiral up around a vertical axis and then tend to tilt to align their axis of rotation with the spanwise direction. These streamlines tend to converge towards the center of the street. The shape formed by these streamlines can be compared with the arch vortex observed earlier for $W/H = 1.5$. The streamline topology of the wake interference regime ($W/H = 4$) is largely different from the skimming flow regime ($W/H = 1.5$) close to the downstream block. In Figure 3.28(b), the streamlines, that were described as being part of the arch vortex, get in the secondary recirculation region and finally exit the street along a helicoidal path in the spanwise direction.

In terms of three-dimensionality, the data suggest that the skimming flow regime is less three-dimensional over a region centered about the mid-street than the

wake interference regime. This is argued when comparing Figure 3.15 and 3.27. The streamlines seem more 2D capturing the single recirculation region over about 60% of the street length L for $W/H = 1.5$. This quasi 2D region is not as developed for the wake interference regime, where only about 40% of the large recirculation region is quasi 2D.

It can be seen by comparing the TKE_H levels (color of streamlines) in Figures 3.15 with 3.27 that overall turbulence levels are larger for the wake interference regime. The largest levels of TKE_H are located near the shear layer for both flow regimes at $z/H \approx 1$ and about the center of the street near $y/L \approx 0$. These high levels of TKE_H at $z/H \approx 1$ suggest that there is a strong exchange of fluid between the street and the mean flow above the urban array. In the wake interference regime, $W/H = 4$, it is also interesting to note that large levels of TKE_H are observed within the core of the secondary recirculation region, near the downstream block (Figure 3.28(a)). This phenomenon can be directly linked to the strong three-dimensionality of the flow field in this region. The flow enters the secondary recirculation region from above, near the windward wall of the street, and then follows helicoidal paths, symmetric about mid-street, along the street axis, as seen in Figure 3.27. This spiraling motion carries the fluid quickly out of the street. The secondary recirculation region exhibits similarities with the horseshoe vortex that was observed upstream of the urban array but is much more turbulent due to its interaction with the large recirculation region sitting directly upstream.

3.4.2 Effect of incidence angle on the flow regimes. In this section, we investigate the effect of the small incidence angle $\alpha = -4.5°$ on the flow regime associated with the $W/H = 4$ streamwise spacing. Table 3.5 summarizes the location of the starting points for the mean streamlines presented in this section.

Figure 3.29 presents the mean streamline pattern for the wake interference

Table 3.5. Starting locations for mean streamlines at an $\alpha = -4.5°$ incidence angle for both $W/H = 4$ and 1.5.

Figure	W/H	x/W	y/L	z/H
3 29	4	0.20, 0.30, 0.40, 0.50, 0.60, 0.80	0.47	0.10, 0.50
3.30(a)	4	0.63	0.46, 0.49	0.10, 0.20
3.30(b)	4	0.92	0.34, 0.22, 0.10, 0, −0.13, −0.25, −0.37, −0.49	0.31

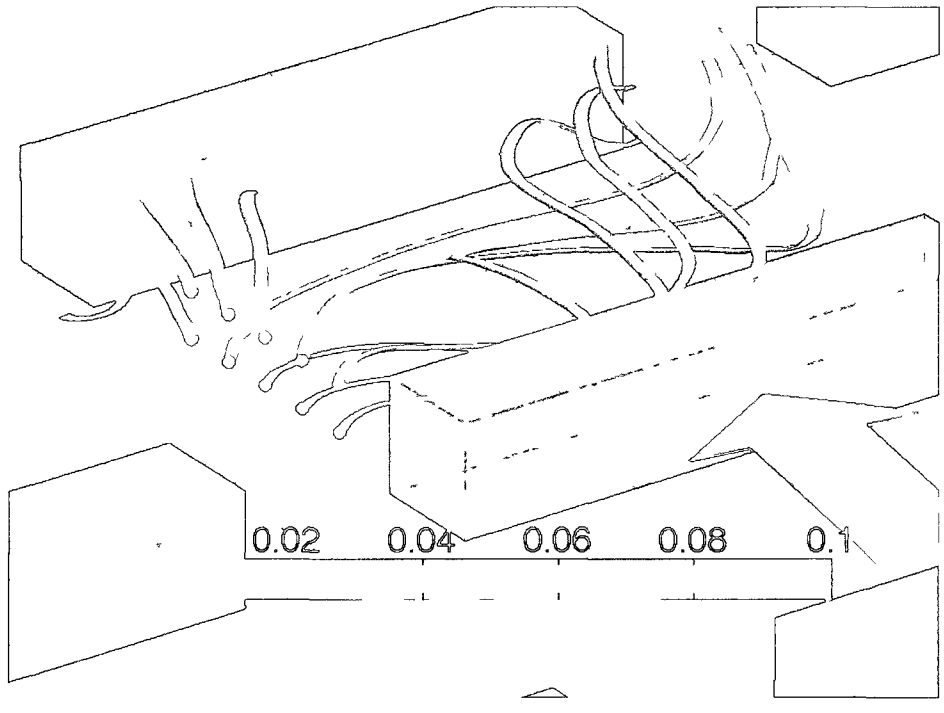

Figure 3 29. Representative mean streamlines for $W/H = 4$ for $\alpha = -4.5°$ incidence angle, colored with local TKE_H. Starting locations for streamlines shown as red dots and given in Table 3.5.

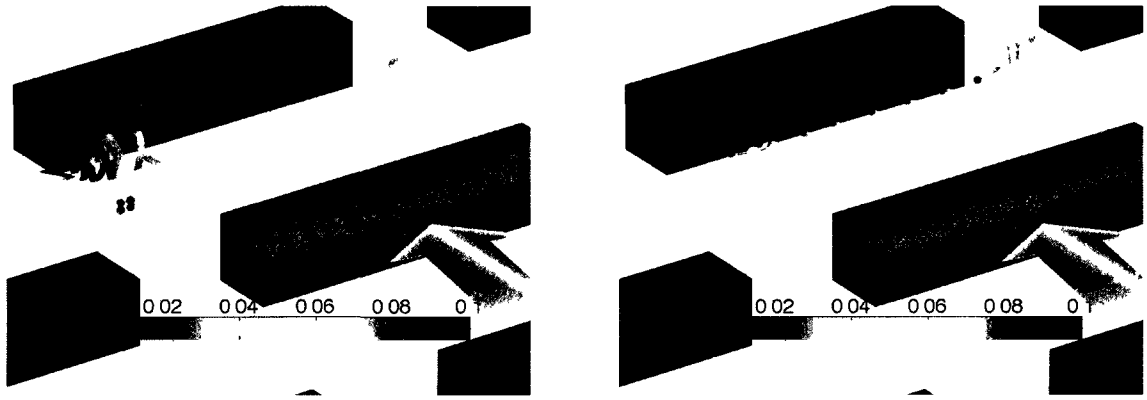

(a) Stagnation point.

(b) Corkscrew vortex.

Figure 3.30. Representative mean streamlines for the ABL1 at $W/H = 4$ at $\alpha = -4.5°$ to highlight features in the secondary recirculation region. The starting locations for the streamlines are given in Table 3.5 and displayed as red dots. Color represents local TKE_H.

regime at an incidence angle of $-4.5°$. It can be compared to the $W/H = 1.5$ streamwise spacing case presented earlier in Figure 3.16. It is seen by this comparison that for the skimming flow regime the mean streamlines are not as affected by the incidence angle of $-4.5°$ as for the $W/H = 4$ case, which reinforces the idea that the larger streamwise spacing case is more subject to three-dimensionality. In order to resolve the main structures in the mean streamlines of the wake interference regime (Fig. 3.29), the starting points are located along the streamwise direction close to the left intersection of street 2 ($y/L = 0.47$) for two different wall-normal positions. Even for this small incidence angle, these mean streamlines are observed moving along the street between the two blocks, nearly parallel to the street axis.

Figure 3.29 also highlights the effect of the incidence angle on the largest recirculation region. It is still observable for $\alpha = -4.5°$, but it is now tilted, driven by the incoming flow directly above roof level. The secondary recirculation region observed for the 0° incidence angle just upstream of the downstream block is also

present, but shows different features. Figures 3.30(a) and 3.30(b) focus on two main aspects of the secondary recirculation region. First, Figure 3.30(a) shows the presence of a stagnation point near the left end of the street, using four streamlines starting from very nearby locations. It can be seen that they have a very different behavior from each other; the secondary recirculation region separates into two regions going in opposite spanwise directions. Second, there is essentially a single helicoidal structure to the right of the stagnation point spanning the remaining length of the street and this structure can be better seen in Figure 3.30(b). It is important to note that the TKE_H levels are higher near the stagnation point, indicating that the location of the stagnation point may vary strongly in time.

3.4.3 Coherent structures. Figure 3.31 shows isosurfaces of the Q-criterion for the wake interference regime at a 0° incidence angle. Four different levels of the Q-criterion are displayed to highlight the shape and extent of the structures as a function of the strength of the vortical structures. For the largest threshold, see Figure 3.31(a), only the secondary recirculation is captured indicating that the vorticity in this region is large as compared with the larger primary recirculation region. As the threshold is lowered, the size of the isocontour characterizing the secondary recirculation increases slightly and features characterizing the large primary recirculation region begin to appear. When comparing this figure with the streamlines in Figures 3.27 and 3.28, it can be seen that the isocontour of the Q-criterion can give a good indication of the shape and extent of the recirculation regions.

When considering the effect of the small incidence angle $\alpha = -4.5°$ on the Q-criterion for the $W/H = 4$ case, Figure 3.32 shows that the tilting of the largest recirculation region. Similarly to the $\alpha = 0°$ incidence angle, an investigation for a range of thresholds indicates that the secondary recirculation presents stronger vorticity than the largest recirculation region.

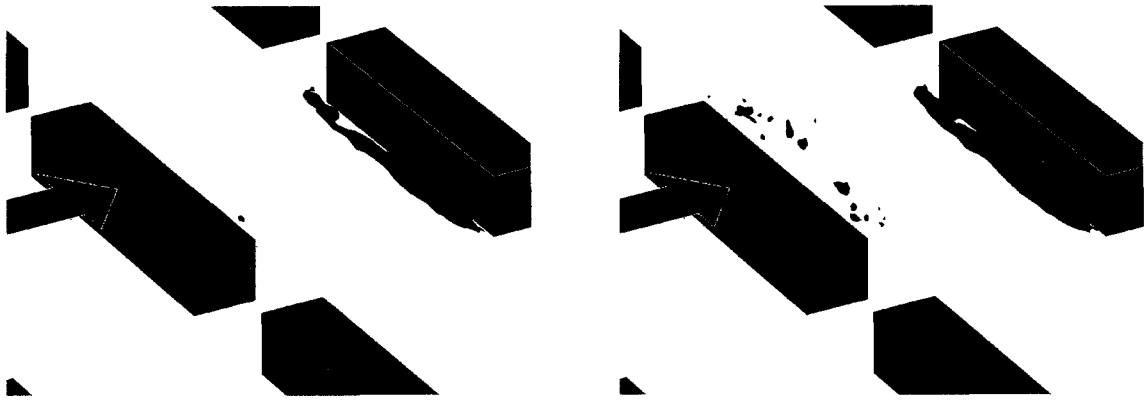

(a) $Q/ < Q >= 4$

(b) $Q/ < Q >= 3$

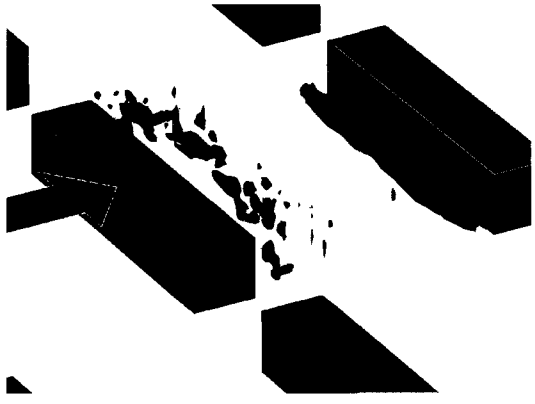

(c) $Q/ < Q >= 2$

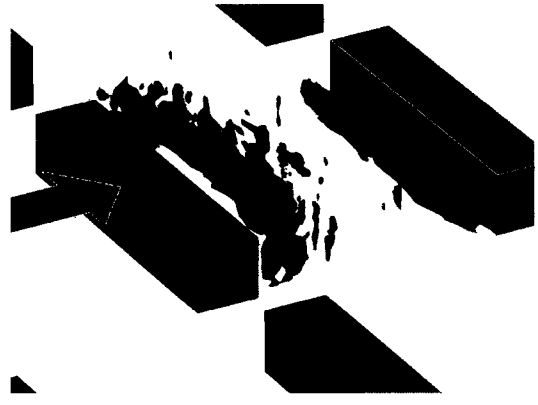

(d) $Q/ < Q >= 1$

Figure 3.31. Isocontours of Q-criterion normalized by $< Q >$ for ABL1 at $\alpha = 0°$ and $W/H = 4$ for four threshold levels.

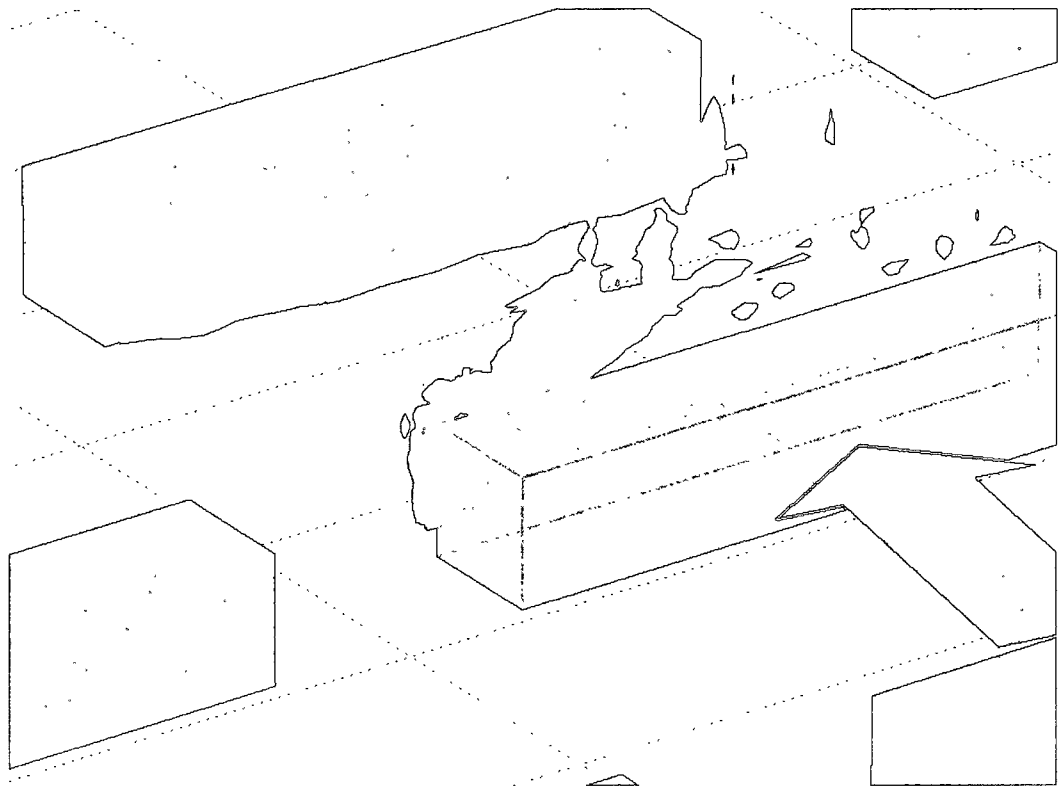

Figure 3.32. Isocontour of normalized Q-criterion ($Q/ < Q >= 2$) for ABL1 at $\alpha = -4.5°$ and $W/H = 4$.

In Figure 3.33, we present NAM iscontours for $W/H = 4$ at an incidence angle of $\alpha = 0°$. As the threshold value is decreased from 0.8 to 0.35 in increments of 0.15, more details begin to appear. For larger values of the threshold, only the largest recirculation region is captured. This is different from the results obtained with the Q-criterion and is due to the fact that the NAM does not measure the strength of the vortical structure, but rather its core location. As the NAM threshold is decreased to 0.50, both recirculation regions associated with the $W/H = 4$ streamwise spacing appear. Finally, upon further decrease of this threshold to $f = 0.35$, the isocontour connects the two recirculation regions, emphasizing the interaction between the two main vortical structures. Lastly, Figure 3.34 presents the effect of the incidence angle $\alpha = -4.5°$ on the flow field for this $W/H = 4$ case. The effect of the incidence angle is especially noticeable in the largest recirculation which appears to be strongly tilted, almost following the diagonal of the street.

3.5 Summary

A better understanding of the spatial distribution of flow structures in an urban environment as a function of wind direction and streamwise spacing was gained from this study. The "channeling effect" observed by others at large incidence angles was also observed in this study for the much smaller incidence angles investigated here and appears to be a major phenomenon driving the flow field in urban environments. The streamwise spacing of the streets was investigated and found to change the flow characteristics. Two flow regimes (skimming flow regime and wake interference regime) were studied in this urban configuration. The knowledge of the flow behavior in the street near the intersections is invaluable in the understanding of the dependence of the coherent structures on the characteristics of the approach flow. Wider streets appeared to be more prone to exchange with the upper layer and even more sensitive to wind direction. In the following chapter, the focus will be on pro-

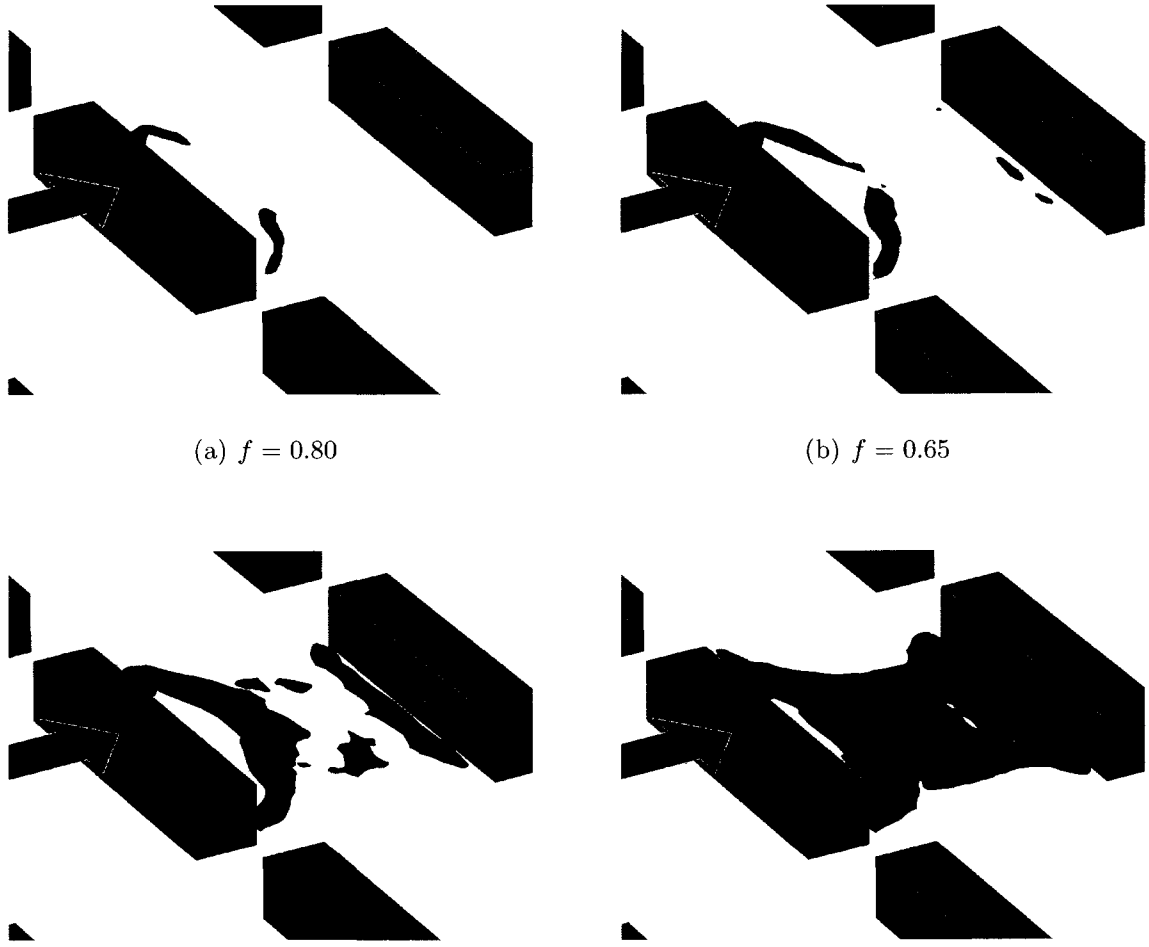

(a) $f = 0.80$ (b) $f = 0.65$

(c) $f = 0.50$ (d) $f = 0.35$

Figure 3.33. Isocontours of NAM for ABL1 at $\alpha = 0°$ for $W/H = 4$ for four threshold levels.

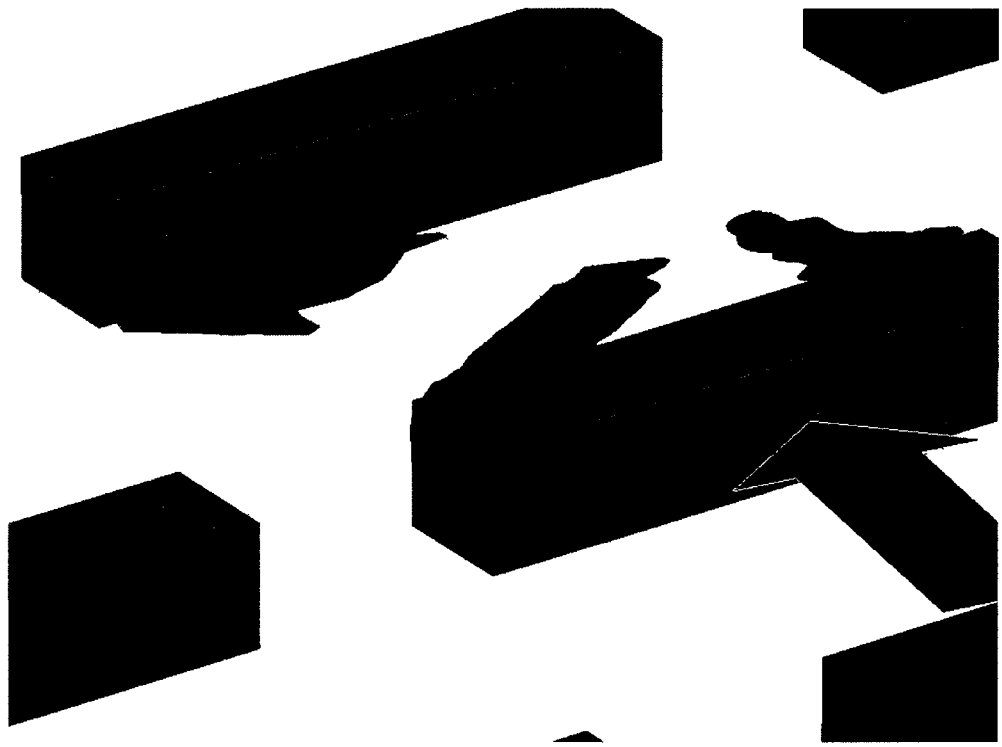

Figure 3.34. Isocontour of NAM ($f = 0.35$) for ABL1 at $\alpha = -4.5°$ and $W/H = 4$.

viding a better description of the turbulence distribution and a better understanding of the different mechanisms creating the turbulence in the urban environment.

CHAPTER 4

SPATIAL DESCRIPTION OF TURBULENCE CHARACTERISTICS

4.1 Introduction

In this chapter, the 3D data provided by the SPIV planes are presented in two different slices across the three-dimensional data sets. The first slice, denoted as S_y, is a vertical slice at mid-span ($y/L = 0$). The second slice, denoted as S_z, is a horizontal slice at $z/H = 0.2$ as depicted in Figure 4.1. These two slices provide a simple way to present the turbulence characteristics of the flow field under consideration. The color mapping used in the various figures presented in this chapter will indicate the magnitude of various turbulence statistics of interest.

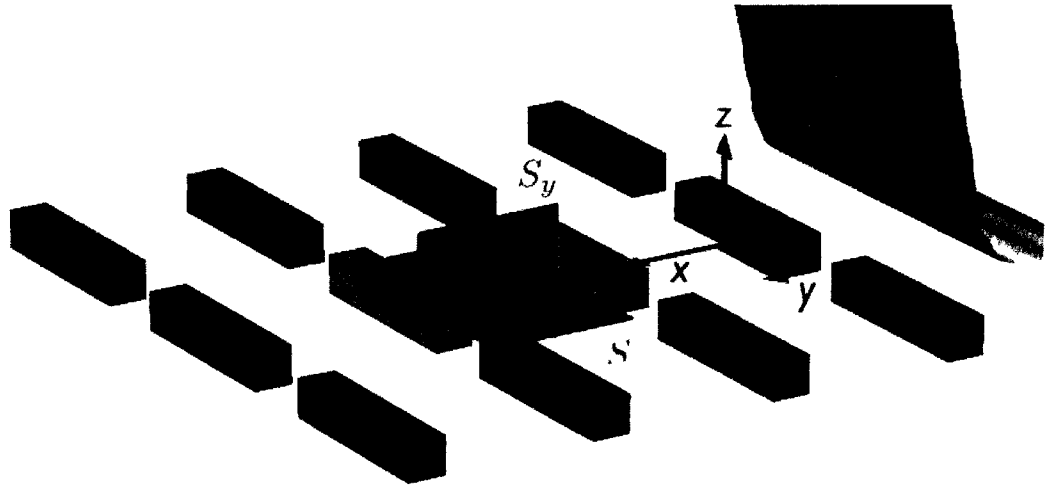

Figure 4.1. Schematic of the array, coordinate system and location of the slices S_y (in blue) and S_z (in green) for street 2.

The important terms in the turbulent kinetic energy (TKE) equation will be the main focus of this chapter. Since we have access to all components of velocity in the urban array over a large spatial domain, we are able to investigate many terms in the TKE equation:

$$\left(\frac{\partial}{\partial t} + U_j \frac{\partial}{\partial x_j}\right) k = \frac{\partial}{\partial x_j}\left(-\frac{1}{\rho}\overline{p u_i'}\delta_{ij} - \frac{1}{2}\overline{u_i' u_i' u_j'} + 2\nu \overline{s_{ij} u_i'}\right) - \overline{u_i' u_j'}\frac{\partial U_i}{\partial x_j} - 2\nu \overline{s_{ij} s_{ij}}. \quad (4.1)$$

The Einstein notation is used for convenience, u_i' corresponds to the fluctuating components of the velocity field, U_i corresponds to the mean components of the velocity field, and s_{ij} is the symmetric part of the fluctuating velocity gradient tensor. The left hand side (LHS) of this equation is composed of the temporal rate of change of turbulent kinetic energy per unit mass and the rate of change of turbulent kinetic energy per unit mass due to convection by the mean flow. The first terms on the right hand side (RHS) of this equation represent the transport of turbulent kinetic energy by three mechanisms: the pressure fluctuations, the turbulence itself, and the viscous stresses. The second to last term on the RHS are the rate of production of turbulent kinetic energy and the rate of dissipation of turbulent kinetic energy per unit mass due to viscous stresses. From our experimental SPIV data, the turbulent kinetic energy TKE and its rate of production, P_k, are computed. The other terms in the turbulent kinetic energy equation involving derivatives of fluctuating components of the velocity field are more difficult to estimate because of the limited spatial resolution. The transport of turbulent kinetic energy due to the pressure fluctuations cannot be estimated as no pressure measurements within the flow are available.

Table 4.1 presents the characteristics of the incoming boundary layers under investigation. The velocity U_H used to normalize TKE is obtained directly from the boundary layer profiles upstream of the urban array at a wall normal location of $z/H = 1$.

4.2 Street-to-street evolution of turbulence characteristics for a fixed streamwise spacing of $W/H = 1.5$ at an incidence angle $\alpha = 0°$

4.2.1 Spatial description of the turbulence kinetic energy TKE_H. We first present the spatial distribution of TKE_H within the urban array for the baseline data set ABL2 at an incidence angle of $\alpha = 0°$ in a vertical $x-z$ slice at midspan, $y/L = 0$, depicted as S_y in Figure 4.2. It can be seen that the TKE_H is first increasing as the

Table 4.1. Incoming flow characteristics.

ABL #	U_0	δ	n	U_H
ABL1	3.1 m/s	500 mm	0.20	2.0 m/s
ABL2	2.2 m/s	400 mm	0.14	1.6 m/s
ABL3	3.4 m/s	450 mm	0.17	2.2 m/s

flow moves from upstream of the array to street 1. It reaches its maximal value directly above street 1 as initially observed from the color mapping of the mean streamlines presented in Chapter 3. The region of the boundary layer directly above the mean height of the blocks is referred to as the "wake layer" while the region beneath is called the urban canopy (Stull, 1988). This region of large initial turbulence in the wake layer of the urban array is mostly due to the flow separation occurring at the leading edge of the upstream block (Martinuzzi & Havel, 2000). In street 1, near the ground, a secondary region of large TKE_H is observed with magnitudes comparable to those found in the shear layer. As the flow evolves to street 2, TKE_H is decaying strongly in the wake layer as compared with street 1. It is well documented that the flow does not separate on top of the second row of obstacles (Martinuzzi & Havel, 2000) and this is an explanation for the large drop in TKE_H. Finally, street 3 exhibits very similar features to street 2. As expected, the strongest transition is observed in the beginning region of the urban array and then slowly converges towards an equilibrium state.

In order to isolate different phenomena driving the distribution of TKE_H, it is insightful to decompose it into its individual components: $\frac{1}{2}\overline{u'^2}$, $\frac{1}{2}\overline{v'^2}$ and $\frac{1}{2}\overline{w'^2}$. Figure 4.3 displays these three components. It is directly apparent that there are two dominant contributions to the total TKE_H, namely, $\frac{1}{2}\overline{u'^2}$ (the streamwise component)

Figure 4.2. TKE_H in a vertical slice, S_y, at $y/L = 0$ for ABL2 at $\alpha = 0°$.

and $\frac{1}{2}\overline{v'^2}$ (the spanwise component), while $\frac{1}{2}\overline{w'^2}$ (the wall normal component) seems to play a minor role in the overall TKE_H.

The streamwise contribution $\frac{1}{2}\overline{u'^2}$ to TKE_H is dominant in the wake layer, while the spanwise contribution $\frac{1}{2}\overline{v'^2}$ is dominant near the floor within the streets. There is a contribution from the vertical component $\frac{1}{2}\overline{w'^2}$, but it is much weaker and mostly located in the wake layer and near the windward wall of each street, where the bulk flow is actually penetrating the streets. From this decomposition, it can be seen that there are most likely two different phenomena driving the turbulence in the urban environment, one acting in the wake layer and the other within the urban canopy.

We now investigate the spatial distribution of TKE_H in an $x - y$ slice parallel to the floor at $z/H = 0.2$, depicted as S_z in Figure 4.2. Figures 4.4 to 4.7 present the spatial distribution of TKE_H, $\frac{1}{2}\overline{u'^2}$, $\frac{1}{2}\overline{v'^2}$ and $\frac{1}{2}\overline{w'^2}$, respectively, in the horizontal slice S_z for the ABL2 data set at an incidence angle of $\alpha = 0°$. The wall normal height of this slice was selected so as to cross the regions of large TKE_H near the ground as seen in Figure 4.3(b). Figure 4.4 provides valuable information about the spanwise extent of the central region of large TKE_H near the ground. This region extends from $y/L \approx -0.25$ to $y/L \approx 0.25$ for street 1. Similarly to TKE_H in the wake layer above the block, TKE_H in the urban canopy is decaying noticeably from

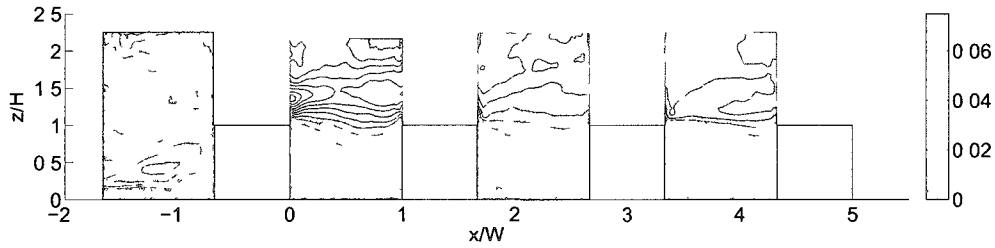

(a) $\frac{1}{2}\overline{u'^2}$ normalized by U_H^2

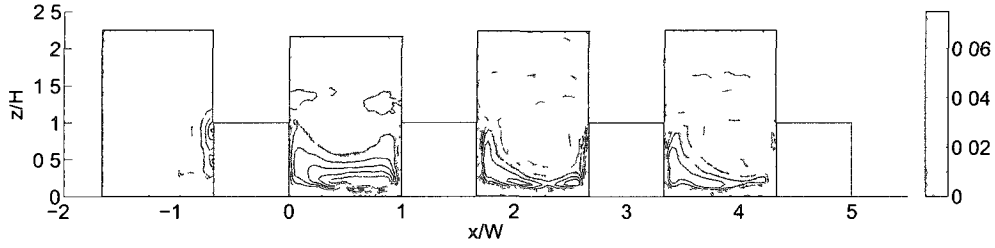

(b) $\frac{1}{2}\overline{v'^2}$ normalized by U_H^2

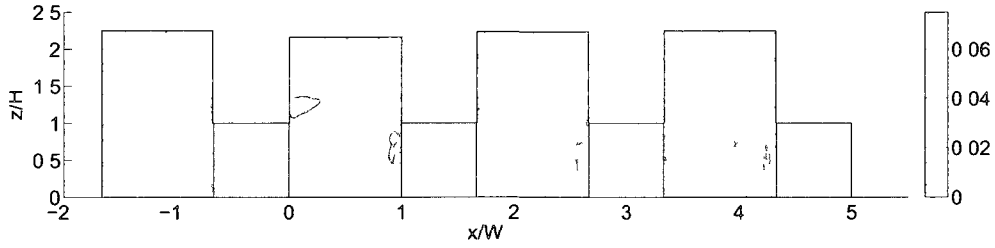

(c) $\frac{1}{2}\overline{w'^2}$ normalized by U_H^2

Figure 4.3. TKE_H components in a vertical slice, S_y, at $y/L = 0$ for ABL2 at $\alpha = 0°$.

street 1 to street 2. The extent of the region of large TKE_H appears to be reduced in street 3. In addition to the central region of TKE_H, we observe two regions of large TKE_H at the ends of the streets, associated with the shear layers formed off the sides of the blocks, which are especially strong in street 1. But overall, their intensity also decays as the flow evolves downstream from street to street. The following three

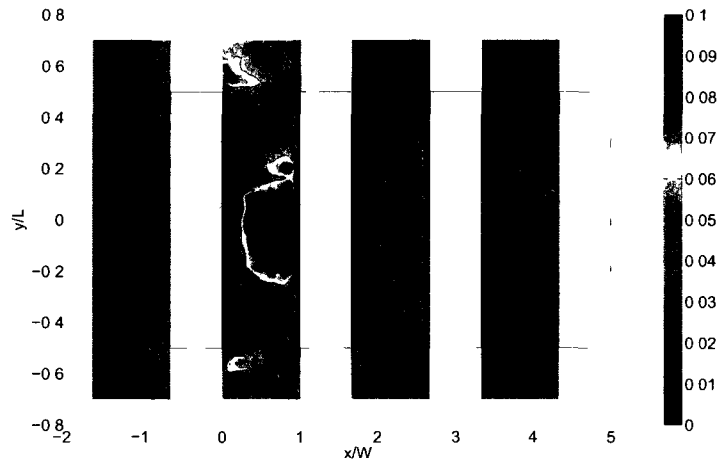

Figure 4.4. TKE_H in a horizontal slice, S_z, at $z/H = 0.2$ for ABL2 at $\alpha = 0°$.

Figures (4.5 to 4.7) present the individual components of TKE_H and let us identify the relative contributions to TKE_H. It can again be observed clearly that the central region of large TKE_H is directly linked to the spanwise component, $\frac{1}{2}\overline{v'^2}$, of the turbulent kinetic energy. The regions of large TKE_H near the ends of the streets are dominated by the streamwise fluctuations, $\frac{1}{2}\overline{u'^2}$, of the turbulent kinetic energy. The vertical component, $\frac{1}{2}\overline{w'^2}$, of TKE_H does not appear to have a dominant role in the TKE_H distribution at this z/H location which is similar in conclusion to that for the dominant mechanisms in the wake layer.

4.2.2 Relation to the rate of production of TKE. The SPIV data allows us to compute the rate of production of turbulent kinetic energy, $P_k = -\overline{u_i' u_j'} \frac{\partial U_i}{\partial U_j}$ term in the TKE equation. This is especially useful to determine more accurately the

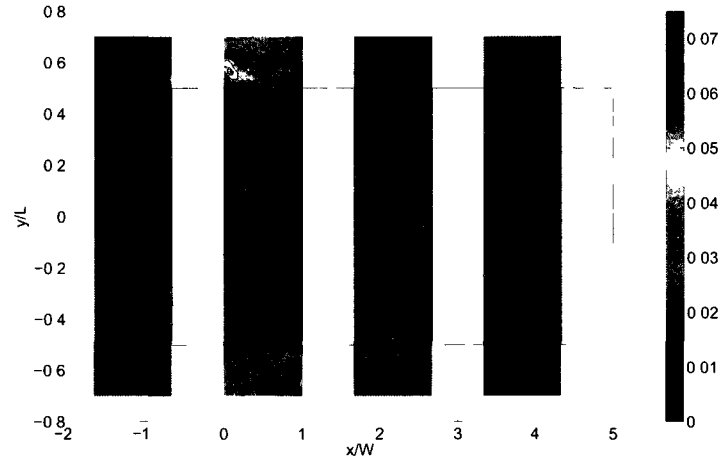

Figure 4.5. Streamwise component of the TKE_H , $\frac{1}{2}\overline{u'^2}/U_H^2$, in a horizontal slice, S_z, at $z/H = 0.2$ for ABL2 at $\alpha = 0°$.

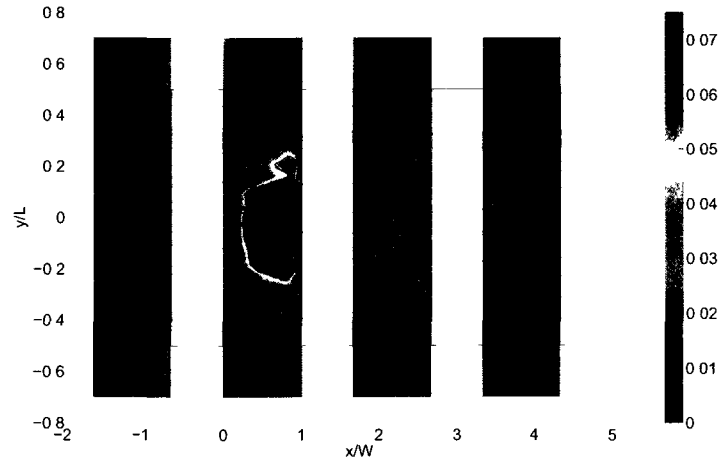

Figure 4.6. Spanwise component of the TKE_H , $\frac{1}{2}\overline{v'^2}/U_H^2$, in a horizontal slice, S_z, at $z/H = 0.2$ for ABL2 at $\alpha = 0°$.

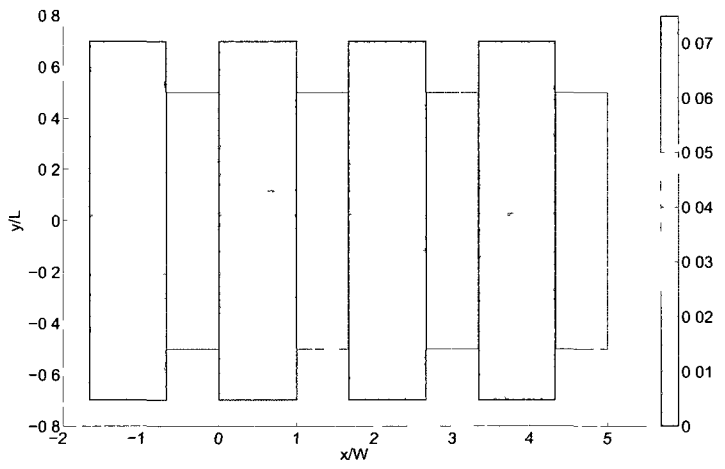

Figure 4.7. Wall normal component of the TKE_H , $\frac{1}{2}\overline{w'^2}/U_H^2$, in a horizontal slice, S_z, at $z/H = 0.2$ for ABL2 at $\alpha = 0°$.

sources of turbulence in the urban environment. The rate of production of turbulent kinetic energy is normalized by U_H^3/H in the figures presented in this chapter. It is interesting to decompose P_k into six individual components:

$$P_{u^2} = -\overline{u'^2}\frac{\partial U}{\partial x} \tag{4.2}$$

$$P_{v^2} = -\overline{v'^2}\frac{\partial V}{\partial y} \tag{4.3}$$

$$P_{w^2} = -\overline{w'^2}\frac{\partial W}{\partial z} \tag{4.4}$$

$$P_{uv} = -\overline{u'v'}\left(\frac{\partial U}{\partial y} + \frac{\partial V}{\partial x}\right) \tag{4.5}$$

$$P_{uw} = -\overline{u'w'}\left(\frac{\partial U}{\partial z} + \frac{\partial W}{\partial x}\right) \tag{4.6}$$

$$P_{vw} = -\overline{v'w'}\left(\frac{\partial V}{\partial z} + \frac{\partial W}{\partial y}\right) \tag{4.7}$$

Figure 4.8 presents the normalized P_k for the data set ABL2 in the vertical slice S_y at mid-span for an incidence angle of $\alpha = 0°$. It can be observed in this figure that there is a moderate level of production of TKE directly upstream of the urban array in the region around the location of the horseshoe vortex structure.

Relatively large values of TKE production are observed just above street 1 in the wake layer which agrees with the large TKE_H values found there. Also consistent are the relatively large values of production of TKE occurring in a region of the urban canopy near the floor of street 1. The production rate is diminishing as the flow evolves from street 1 to streets 2 and 3, but the regions producing TKE are still directly linked to the wake layer and the region near the ground. Figure 4.9 shows that the dominant term in the production rate, P_k, in the wake layer is the $P_{uw} = -\overline{u'w'}\left(\frac{\partial U}{\partial z} + \frac{\partial W}{\partial x}\right)$ term. It is also of interest to see that within the street the contribution of P_{uw} is not large, but rather the $P_{v^2} = -\overline{v'^2}\frac{\partial V}{\partial y}$ term is dominant as provided by Figure 4.10. P_{v^2} is large mostly in the center of the street and closer to the windward wall of the street. The next largest term is $P_{w^2} = -\overline{w'^2}\frac{\partial W}{\partial z}$ shown in Figure 4.11; however, the magnitudes are relatively low with the contribution very close to the windward wall and in the wake layer.

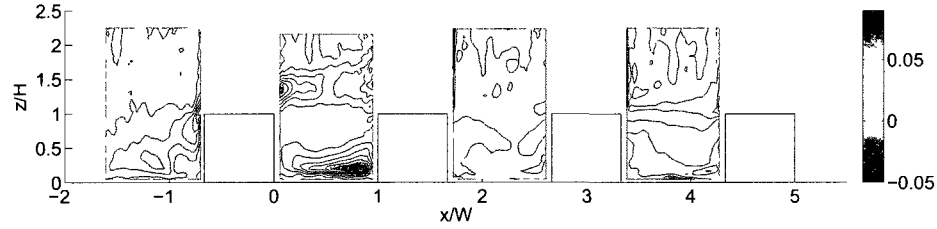

Figure 4.8. Production of TKE, P_k, normalized by U_H^3/H in a vertical slice S_y at $y/L = 0$ for ABL2 at $\alpha = 0°$.

Investigating the rate of production, P_k, in the horizontal slice, S_z, provides very similar information to the TKE_H distribution. That is, the extent of regions of large production are well correlated with the regions of large TKE_H and the data is therefore not shown here. In addition to the center region within the streets near the ground driven by the P_{v^2} term, the shear layers on the sides are driven by the P_{uv} term shown in Figure 4.12.

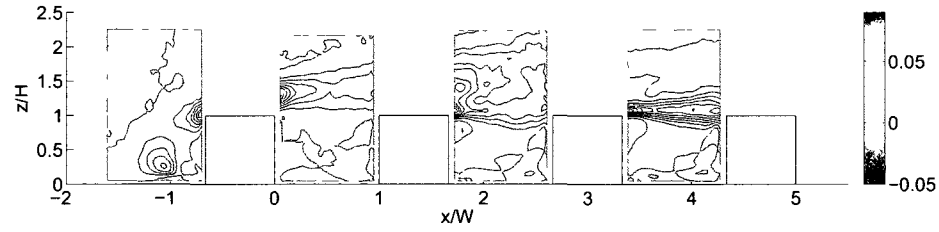

Figure 4.9. Production of TKE, P_{uw}, normalized by U_H^3/H in a vertical slice S_y at $y/L = 0$ for ABL2 at $\alpha = 0°$.

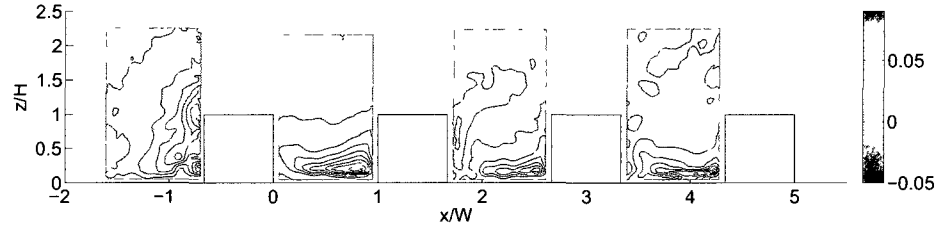

Figure 4.10. Production of TKE, P_{v^2}, normalized by U_H^3/H in a vertical slice S_y at $y/L = 0$ for ABL2 at $\alpha = 0°$.

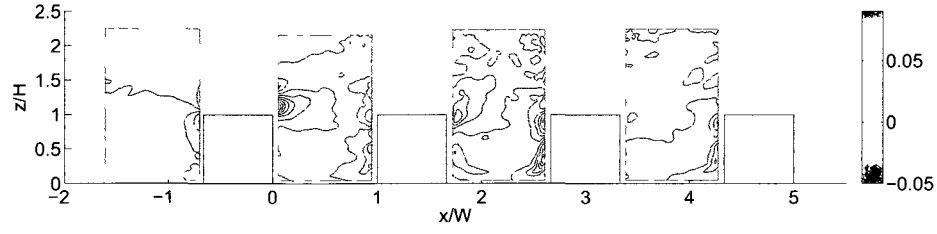

Figure 4.11. Production of TKE, P_{w^2}, normalized by U_H^3/H in a vertical slice S_y at $y/L = 0$ for ABL2 at $\alpha = 0°$.

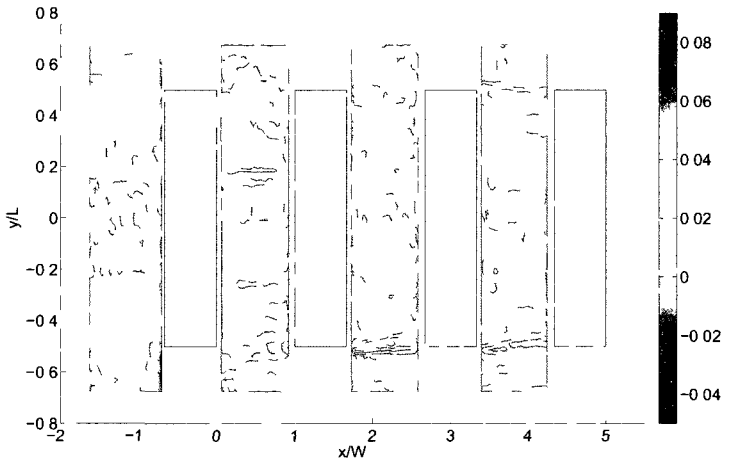

Figure 4.12. Production of TKE, P_{uv}, normalized by U_H^3/H in a vertical slice, S_y, at $y/L = 0$ for ABL2 at $\alpha = 0°$.

4.3 Effect of the incidence angle on the turbulence characteristics

4.3.1 Incidence angle effect in street 2. We will investigate here three incidence angles (0°, −4.5° and 15°) for the $W/H = 1.5$ case in street 2 as defined in Figure 3.1. The incidence angle −4.5° was obtained for the ABL1 data set while the incidence angle 15° was obtained from the ABL2 data set. So we will also present the differences between ABL1 and ABL2 for the 0° incidence angle. This is done so as to explain the differences in magnitude observed in the TKE_H distributions. The scaling of TKE is a non-trivial problem in such a complex setting, and a single velocity scale will not characterize the entire region of interest.

Figure 4.13 presents a vertical slice, S_y, at mid-span for both the ABL1 and ABL2 data sets. A direct comparison of the magnitude of TKE_H can be made by looking at Figures 4.13(a) and 4.13(c) which present the 0° incidence angle case for ABL1 and ABL2, respectively. Figure 4.13(b) presents the ABL1 case at an incidence angle of $\alpha = -4.5°$, while Figure 4.13(d) presents the ABL2 case at an incidence angle of $\alpha = 15°$. It can be observed from these figures that the effect of the small inci-

dence angle ($-4.5°$) is significant within the street. The region of moderately large TKE_H near the ground has shifted considerably nearer to the windward wall. The effect of the larger incidence angle (15°) is shown in Figure 4.13(d), for the same vertical slice, S_y, at mid-span for the ABL2 data set. The shift near the ground region of the moderately large TKE_H is amplified. This is in agreement with field experiments (e.g. S. Xie et al., 2003), showing that the maximum turbulent kinetic energy levels within the street are found nearer to the windward wall and are associated with lower levels of pollutant concentration. Note that the flow in field experiments is most often at a non-zero incidence angle.

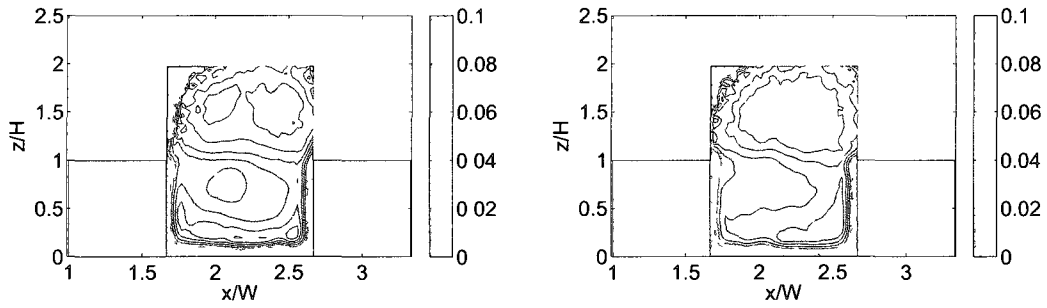

(a) ABL1 at $\alpha = 0°$

(b) ABL1 at $\alpha = -4.5°$

(c) ABL2 at $\alpha = 0°$

(d) ABL2 at $\alpha = 15°$

Figure 4.13. TKE_H in a vertical slice, S_y, at $y/L = 0$ for ABL1 and ABL2 at $\alpha = 0°$ in street 2.

In the horizontal slice, S_z, crossing the region of large TKE_H near the ground at $z/H = 0.2$, we perform the same comparison to assess the incidence angle effect in the spanwise direction. Figures 4.14(a) and 4.14(b) display the TKE_H results for $\alpha = 0°$ and $-4.5°$, respectively. Note that the arrows in each figure qualitatively represent the incoming flow direction and the angle of the arrows is exaggerated in order to show the wind direction. The region of relatively large TKE_H is somewhat shifted in the street and the overall levels of TKE have reduced when comparing the 0° incidence angle case with the non-zero incidence angle cases. This is most noticeable for the larger incidence angle of $\alpha = 15°$ case. The overall TKE levels have reduced to quite low levels. This noticeable change between incidence angles $\alpha = -4.5°$ and 15° indicates that there is a strong transition in the turbulence distribution for an incidence angle contained in this range. Work by Crowther et al. (2002) using Computational Fluid Dynamics (CFD) simulations actually suggests that the pollutant concentration in a street is very sensitive to the incidence angle in the range 0° to 20°. Beyond a 20° incidence angle, the contaminant concentration spatial distribution stays relatively constant, indicating that the turbulence also remains fairly constant. The strong transition observed by Crowther et al. (2002) is in good agreement with the data presented here.

4.3.2 Incidence angle effect on the turbulence characteristics. Figure 4.15 shows a vertical slice of TKE_H at $y/L = 0$ at $\alpha = 15°$ for the ABL2 data set. It is observed that in each street, the maximal levels of TKE_H are found very near the windward wall, as opposed to the data shown in Figure 4.2 for $\alpha = 0°$. Figure 4.16 displays the TKE_H in the horizontal slice, S_z, for the same data set at $\alpha = 15°$. It is found that for this incidence angle, the TKE_H distribution within the street is very much altered in the spanwise direction as compared with the zero-incidence case shown in Figure 4.4, especially from street 1 to 2. In street 1, the region of large TKE_H observed at mid-span for the $\alpha = 0°$ case is now shifted towards the

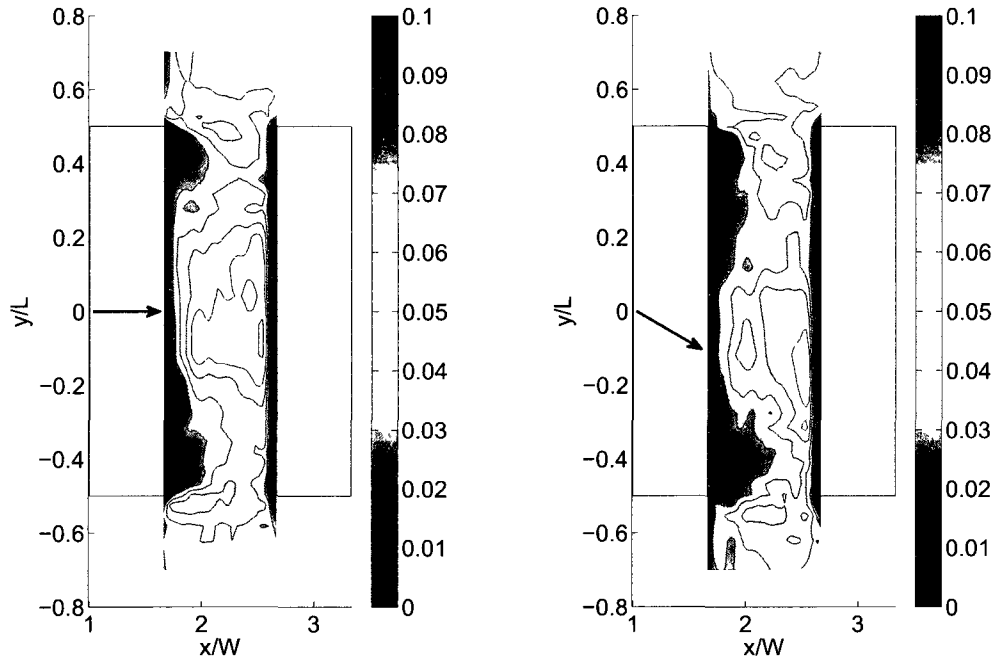

(a) ABL1 at $\alpha = 0°$

(b) ABL1 at $\alpha = -4.5°$

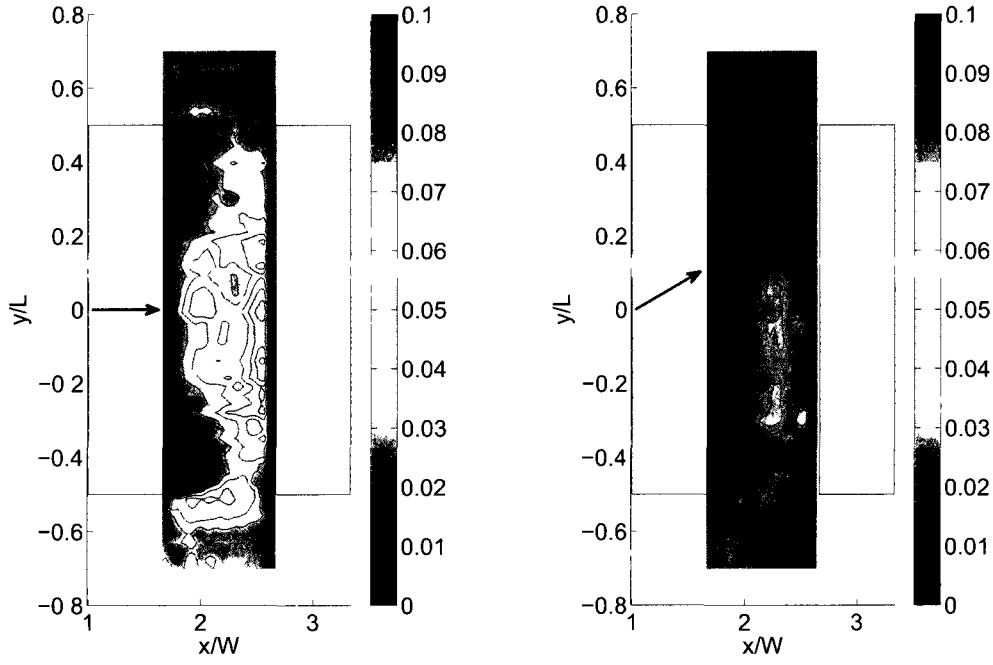

(c) ABL2 at $\alpha = 0°$

(d) ABL2 at $\alpha = 15°$

Figure 4.14. TKE_H in a horizontal slice, S_z, at $z/H = 0.2$ for ABL1 and ABL2 at $\alpha = 0°$ in street 2.

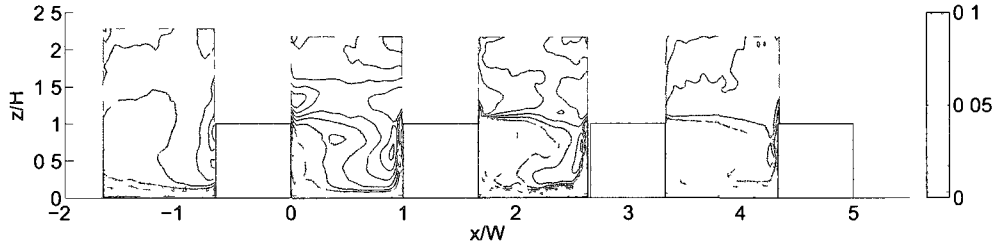

Figure 4.15. TKE_H in a vertical slice, S_y, at $y/L = 0$ for ABL2 at $\alpha = 15°$.

far end of the street near $y/L = 0.25$ for $\alpha = 15°$. Streets 2 and 3 present a very similar distribution of TKE_H to each other for $\alpha = 15°$, and the levels of TKE have decreased with increasing street # in the array. Especially near $y/L = 0.25$, the TKE_H levels appear to be at their lowest for streets 2 and 3. The region showing a maximum TKE_H for these two streets is actually located on the opposite side of the street ($-0.5 < y/L < 0$) and near the windward walls.

We investigate now the mechanisms coming into play in the production of TKE_H for a non-zero incidence angle. Figure 4.17 presents a vertical slice, S_y, of production of TKE for data set ABL2 at an $\alpha = 15°$ and is very similar to the TKE_H distribution shown in Figure 4.15. Turbulent kinetic energy is produced upstream of the array and in the wake layer just above roof level. Similarly to the 0° incidence case studied earlier, the dominant term in the production of TKE in this region is P_{uw}.

There is also production within the streets, near the windward walls. In order to assess which terms are dominating the production in this region, we present in Figures 4.18, 4.19 and 4.20 the total production P_k and the individual components P_{v^2} and P_{w^2}, respectively, in a horizontal slice at $z/H = 0.2$. The total production rate, P_k, displayed in Figure 4.18 shows high production near the windward wall.

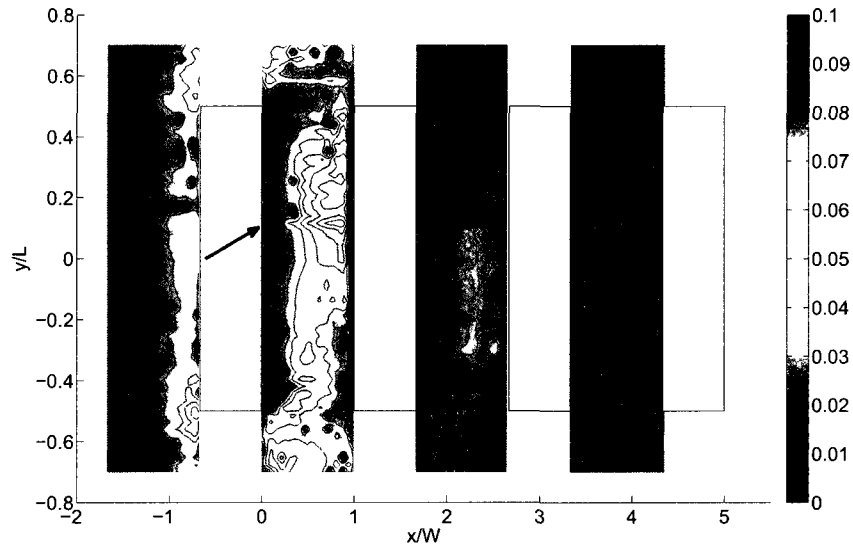

Figure 4.16. TKE_H in a horizontal slice, S_z, at $z/H = 0.2$ for ABL2 at $\alpha = 15°$.

Within the street, both P_{v^2} and P_{w^2} are contributing to the total production as can be seen from Figures 4.19 and 4.20. The P_{v^2} term presents a magnitude of about twice that of the P_{w^2} term, but is no longer the only significantly large term in the total TKE production within the street as compared with the 0° incidence angle case.

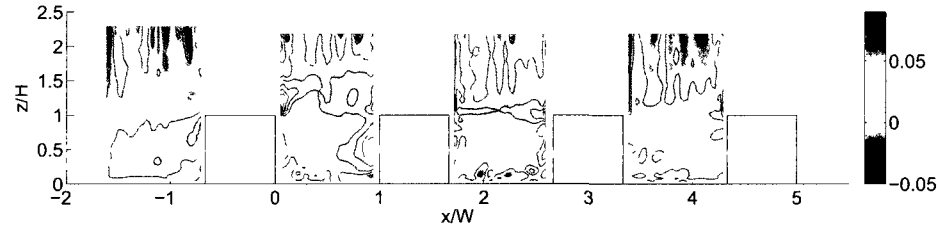

Figure 4.17. Production of TKE, P_k, normalized by U_H^3/H in a vertical slice S_y at $y/L = 0$ for ABL2 at $\alpha = 15°$.

4.4 Effect of streamwise spacing on turbulence characteristics

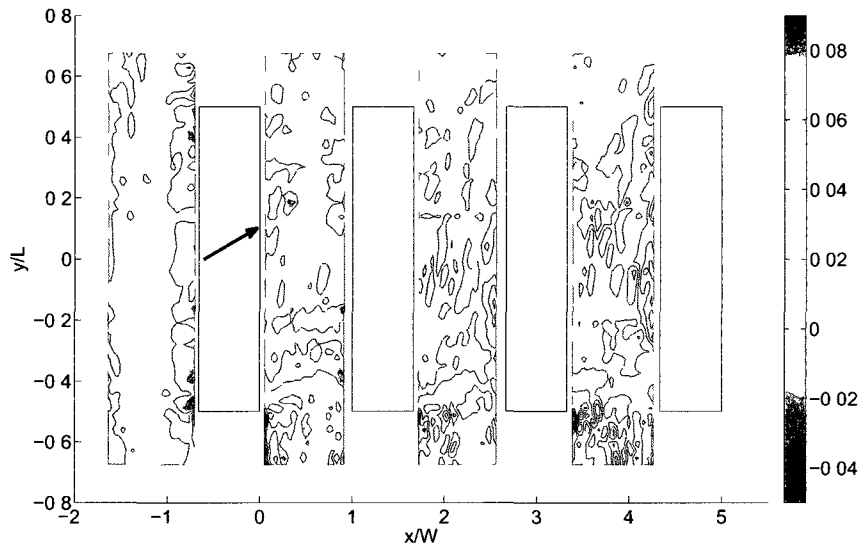

Figure 4.18. Production of TKE, P_k, normalized by U_H^3/H in a horizontal slice at $z/H = 0.2$ for ABL2 at $\alpha = 15°$.

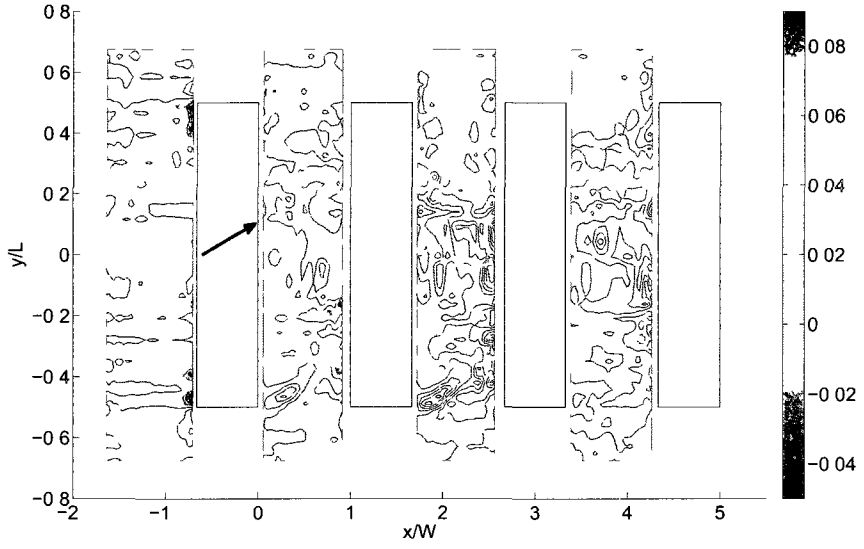

Figure 4.19. Production of TKE, P_{v^2}, normalized by U_H^3/H in a horizontal slice at $z/H = 0.2$ for ABL2 at $\alpha = 15°$.

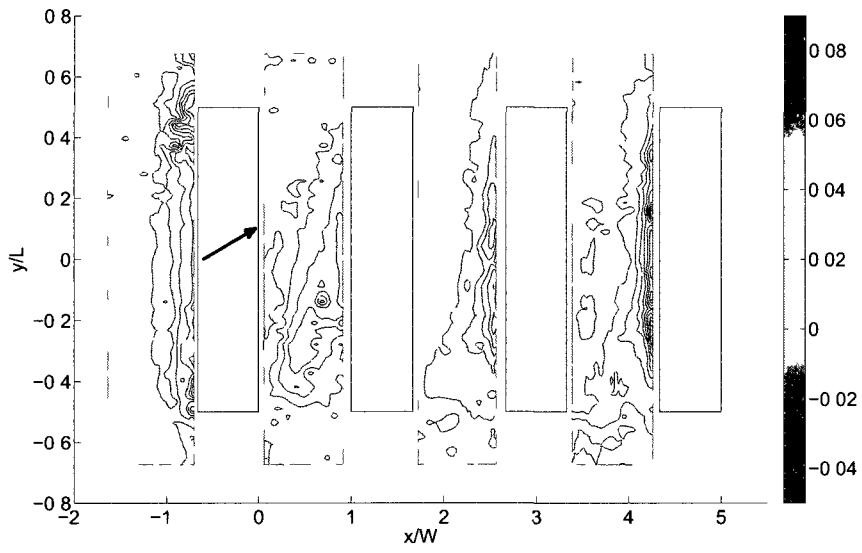

Figure 4.20. Production of TKE, P_{w^2}, normalized by U_H^3/H in a horizontal slice at $z/H = 0.2$ for ABL2 at $\alpha = 15°$.

In the first part of this section, we will investigate the effect of a wider streamwise spacing ($W/H = 4$) on the turbulence characteristics in street 2. This will be followed by the effect of a small incidence angle on the turbulence in this wider street.

4.4.1 TKE_H and production. From our data set ABL1, we can compare the streamwise spacing effect on the TKE_H distribution at the street scale in street 2. Figure 4.21 presents a vertical slice of TKE_H for the $W/H = 4$ streamwise spacing at mid-span. Note that there are three planes of SPIV data acquired for each spanwise location for this $W/H = 4$ case, which was necessitated by our interest in achieving adequate spatial resolution with our measurements. The TKE_H distribution is clearly distinct from that for the $W/H = 1.5$ case shown in Figure 4.13(a). This is expected since the $W/H = 4$ streamwise spacing is associated with the wake interference flow regime (Oke, 1988). However, similarly to the $W/H = 1.5$ case, the individual components of TKE_H for the $W/H = 4$ presented in Figure 4.22 still reflect the fact that the streamwise fluctuating component of velocity in the wake layer is mainly

responsible for the TKE_H levels. Also shown by the results in Figure 4.22 is the fact that the spanwise fluctuating component of velocity is driving the TKE_H distribution upstream of the downstream block. It is observed in Figure 4.22(b) that the TKE_H associated with the spanwise fluctuations $\overline{v'^2}$ is essentially located very near the windward wall for the $W/H = 4$ case as opposed to the $W/H = 1.5$ case where the region of large $\overline{v'^2}$ was observed near the ground at about mid-street in the streamwise direction (Figure 4.3).

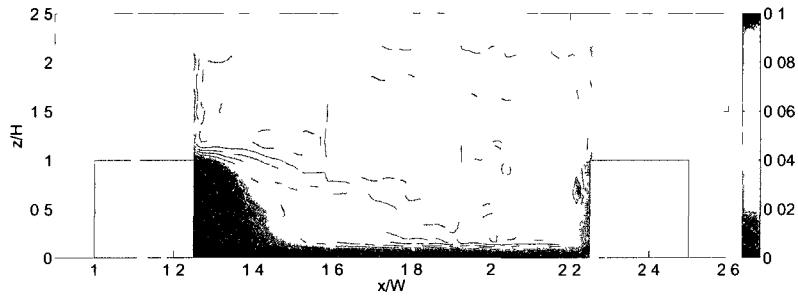

Figure 4.21. TKE_H in a vertical slice, S_y, at $y/L = 0$ for ABL1 at $\alpha = 0°$ and $W/H = 4$ in street 2.

As was done for the $W/H = 1.5$ case, an investigation of the turbulence production mechanisms for this $W/H = 4$ streamwise spacing is carried out. The results for the normalized production rate of TKE are provided in Figure 4.23. A striking difference of this $W/H = 4$ case is the absence of the large production of turbulent kinetic energy near the ground as compared with the $W/H = 1.5$ case shown in Figure 4.8. Although the turbulent kinetic energy distribution for the $W/H = 4$ case exhibits a region of large intensity near the windward wall (Fig. 4.21), its production is not occurring there. Interestingly in the $W/H = 4$ case, the turbulent production is dominated by the P_{uw} term only, as shown in Figure 4.24, where the P_{uw}

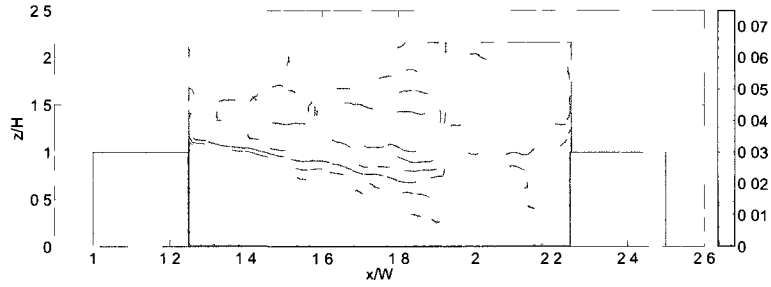

(a) $\frac{1}{2}\overline{u'^2}$ normalized by U_H^2

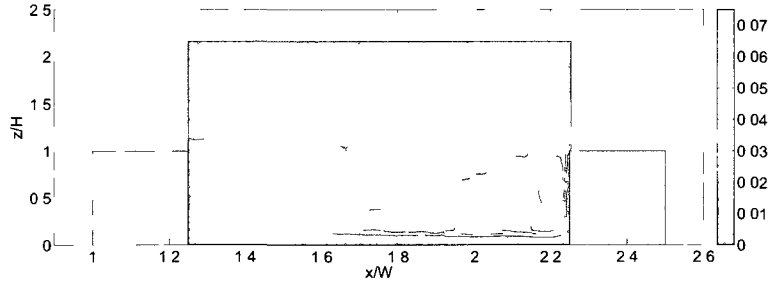

(b) $\frac{1}{2}\overline{v'^2}$ normalized by U_H^2

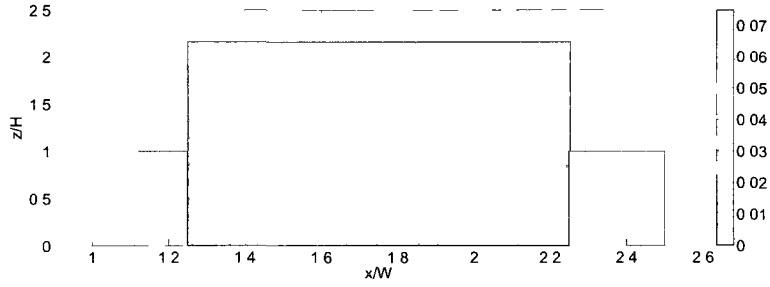

(c) $\frac{1}{2}\overline{w'^2}$ normalized by U_H^2

Figure 4 22 Individual components of TKE_H in a vertical slice, S_y, at $y/L = 0$ for ABL1 at $\alpha = 0°$ and $W/H = 4$ in street 2

term is very similar in shape to the total production of TKE. This is in contrast to the $W/H = 1.5$ case where both P_{uw} and P_{v^2} were observed to contribute (Figures 4.9 and 4.10). This indicates that the spanwise fluctuations observed near the windward wall in the TKE_H distribution for $W/H = 4$ may in fact be generated by this P_{uw} term and transported to the windward wall region. Figures 4.25 and 4.26 provide the results for the P_{v^2} and P_{w^2} terms for easy comparison and to illustrate that they are much smaller than the P_{uw} term. An investigation of the transport term due to the turbulent kinetic energy itself and the convection term in the turbulent kinetic equation did not provide conclusive answers as to what mechanisms are redistributing the turbulence in the windward wall region. The two other terms in the transport term, due to pressure and viscous effects, can not be determined with the measurement tools and the spatial resolution available for this study.

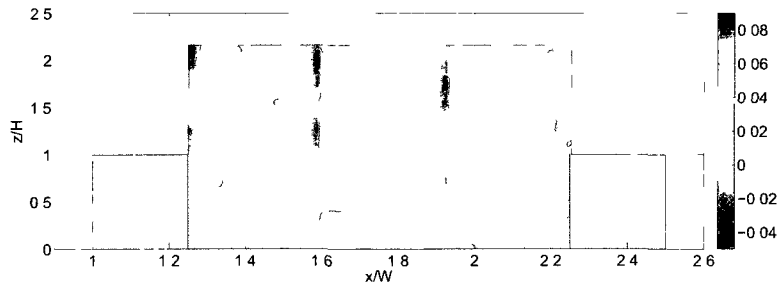

Figure 4.23. Production of TKE, P_k normalized by U_H^3/H in a vertical slice, S_y, at $y/L = 0$ for ABL1 at $\alpha = 0°$ and $W/H = 4$ in street 2.

4.4.2 Effect of incidence angle of the incoming flow on TKE_H as a function of streamwise spacing. Figure 4.27 presents results for a vertical slice, S_y, at $y/L = 0$ for $W/H = 4$. As suggested by our previous discussion of the incidence angle effect in Section 4.3, we note a region of high TKE_H near the windward wall for this small $-4.5°$ incidence angle. One noticeable difference compared with the $0°$

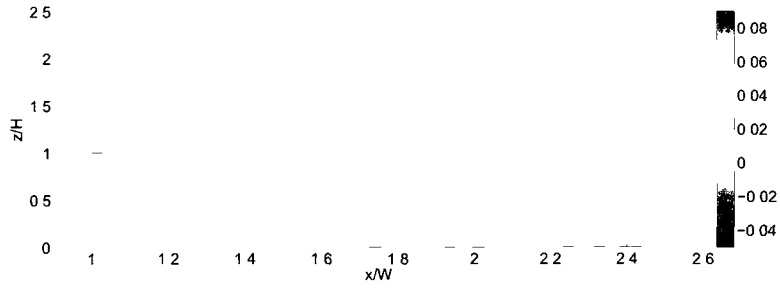

Figure 4.24. Production of TKE, P_{uw} normalized by U_H^3/H in a vertical slice, S_y, at $y/L = 0$ for ABL1 at $\alpha = 0°$ and $W/H = 4$ in street 2.

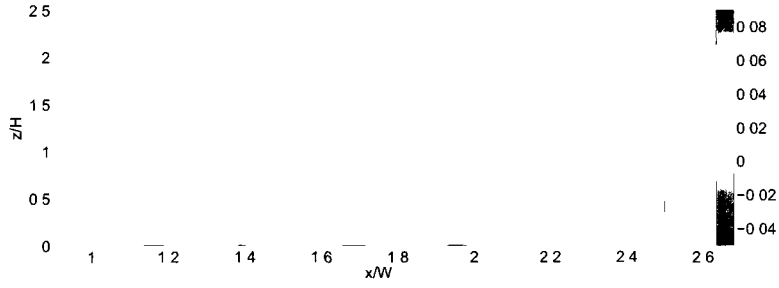

Figure 4.25. Production of TKE, P_{v^2} normalized by U_H^3/H in a vertical slice, S_y, at $y/L = 0$ for ABL1 at $\alpha = 0°$ and $W/H = 4$ in street 2.

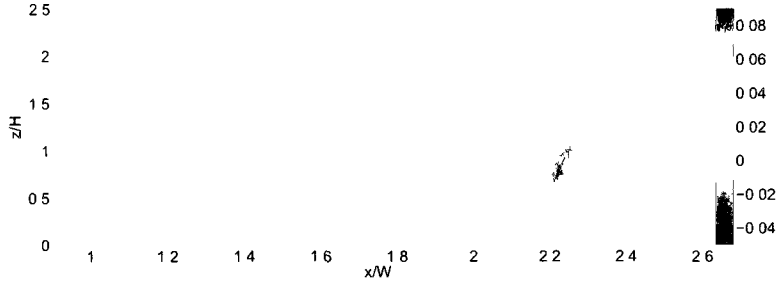

Figure 4.26. Production of TKE, P_{w^2} normalized by U_H^3/H in a vertical slice, S_y, at $y/L = 0$ for ABL1 at $\alpha = 0°$ and $W/H = 4$ in street 2.

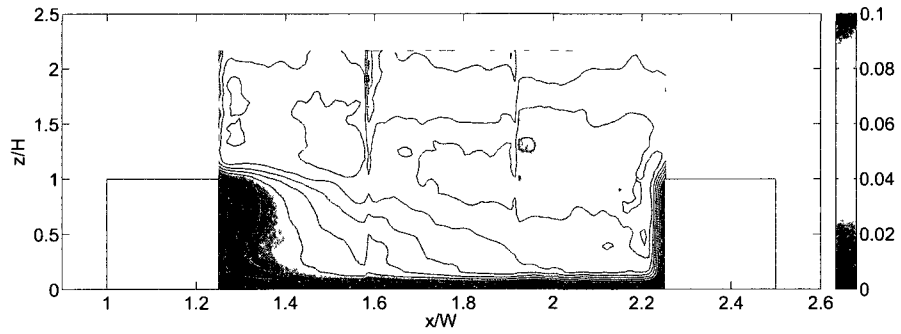

Figure 4.27. TKE_H in a vertical slice, S_y, at $y/L = 0$ for ABL1 at $\alpha = -4.5°$ and $W/H = 4$.

incidence angle shown in Figure 4.21 is that the downstream extent of the relatively large TKE_H values has grown.

Figures 4.28 and 4.29 present the $W/H = 4$ results for incidence angles of $\alpha = 0°$ and $-4.5°$ for a horizontal slice at $z/H = 0.2$. The effect of the incidence angle for the wake interference regime is to increase the TKE_H near the intersection of the street at $y/L \approx 0.5$ and $x/W \approx 2$, and is associated with the stagnation point observed in the streamlines pattern shown in Figure 3.30(a). This enhanced TKE_H is not observed in the $W/H = 1.5$ case shown in Figure 4.16. As discussed before, the channeling effect has an even more significant effect on wider streets; therefore, this difference between the $W/H = 1.5$ and 4 cases is not unexpected.

4.5 Summary

Insight on the mechanisms producing the turbulence in an urban environment was gained from this study. The production of turbulence was found to occur at various locations within the urban array. The wake layer directly above the array

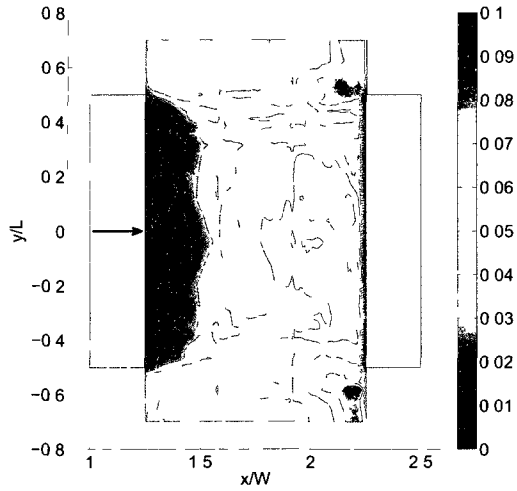

Figure 4.28. TKE_H in a horizontal slice, S_z, at $z/H = 0.2$ for ABL1 at $\alpha = 0°$ and $W/H = 4$ in street 2.

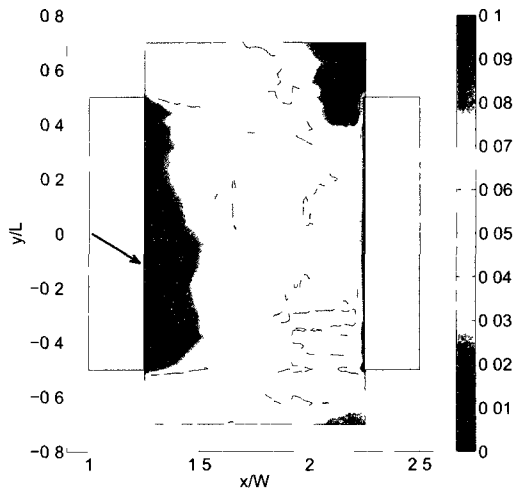

Figure 4.29. TKE_H in a horizontal slice, S_z, at $z/H = 0.2$ for ABL1 at $\alpha = -4.5°$ and $W/H = 4$ in street 2.

is responsible for the largest production of turbulent kinetic energy with the shear layers near the intersections also contributing noticeably. A coupling of vertical and spanwise velocity fluctuations within the street is responsible for a relatively large contribution to the turbulence production at the street scale for narrow streets. For wider streets, no evidence of turbulence production near the windward wall was found which may imply that turbulence is transported to the windward wall region from the shear layer where most of the production was found.

CHAPTER 5

STEPS TOWARDS A TEMPORALLY RESOLVED FLOW THROUGH COMPLEX ENVIRONMENTS

5.1 Introduction

The estimation of a full velocity field based on sparse measurements is a relatively recent topic. Most of the work has been carried out in the past 15 years and the studies have most often focused on estimating the temporal evolution of a low-dimensional flow or a reduced-order representation of a higher-dimensional flow. The dimensionality of the flow is a measure of its complexity. It can be characterized by the number of flow features that are contained in the flow field. In that sense, the urban flow field is very high-dimensional. However, the driving flow features associated with contaminant dispersion in an urban environment are the largest scales of motion and could possibly be captured by a tractable reduced-order representation of the flow field. To obtain this reduced-order representation, we will use Proper Orthogonal Decomposition (POD).

5.2 Reduced-order representation of the velocity field and energy content

Proper Orthogonal Decomposition is a technique that allows us to decompose a velocity field into a set of N basis functions, $\boldsymbol{\psi}_i(\boldsymbol{x})$, associated with a specific set of N POD coefficients, $\zeta_i(t)$:

$$\boldsymbol{u}'(\boldsymbol{x},t) = \sum_{i=1}^{N} \zeta_i(t)\boldsymbol{\psi}_i(\boldsymbol{x}). \tag{5.1}$$

Recall that we used the Reynolds decomposition to write the instantaneous velocity field as $\boldsymbol{u}(\boldsymbol{x},t) = \boldsymbol{U}(\boldsymbol{x}) + \boldsymbol{u}'(\boldsymbol{x},t)$. Note that this decomposition is applied to the fluctuating component of the velocity field, $\boldsymbol{u}'(\boldsymbol{x},t)$, since we are interested in investigating the temporal evolution of the flow field. The method of snapshot POD is used here as introduced by Sirovich (1987). It is particularly well suited to PIV

measurements and was used by many (e.g. Kostas, Soria, & Chong, 2005; Graftieaux, Michard, & Grosjean, 2001; Mokhasi et al., 2009). The advantage of POD over other techniques is that it is built so as to maximize the turbulent kinetic energy in the modes providing an optimal representation of the flow field. Mathematically speaking, the basis functions are selected such that the mean squared error over all possible basis functions is minimized. Another key advantage of this decomposition is that it can be performed so that the POD coefficients, ζ_i, depend only on time, while the basis functions, ψ_i, depend only on space. The modes are ordered so that the lower-order modes contain the maximum amount of energy. The energy is captured by the eigenvalues, $\lambda_i = \overline{\zeta_i(t)^2}$, associated with each mode and is directly related to the spatial scales captured by the basis functions. Larger spatial scales contain more energy than the smaller scales. Finally, the spatial basis functions need to be computed only once from an ensemble that accurately represents the flow field. This is especially useful since we can store the basis functions and perform the temporal analysis on the POD coefficients to study the temporal evolution of the complete flow field.

In this work, the SPIV fluctuation velocity data discussed in previous chapters are input to the LHS of Equation 5.1. Specifically for each plane of SPIV data, a set of spatial basic functions, ψ_i, and corresponding POD coefficients, ζ_i, can be obtained. Equation 5.1 provides the complete representation of the true fluctuating velocity field. To make this problem tractable, we will truncate the number of modes used for the POD analysis. To do this, we look at the energy content as a function of POD mode number. Figure 5.1 presents the energy spectrum for a single vertical plane at roughly mid-span for one of our data sets, ABL2, at an incidence angle of $\alpha = 0°$. One of the most important pieces of information provided by this energy spectrum is the rate of decay of the energy as a function of mode number. This provides a measure of the dimensionality of the flow field. Typically, one can look at the number

of modes that needs to be included to recover 99% of the turbulent kinetic energy in the flow. Urban type flows require about 400 modes to recover 99% of the turbulent kinetic energy, which makes them very high-dimensional. However, by only retaining the first six modes, it is possible to recover about 50% of the turbulent kinetic energy. In order to have a tractable problem, we only want to keep a few modes; therefore, our reduced-order representation of the velocity field will be based on the truncation of the POD representation, including only these first six modes.

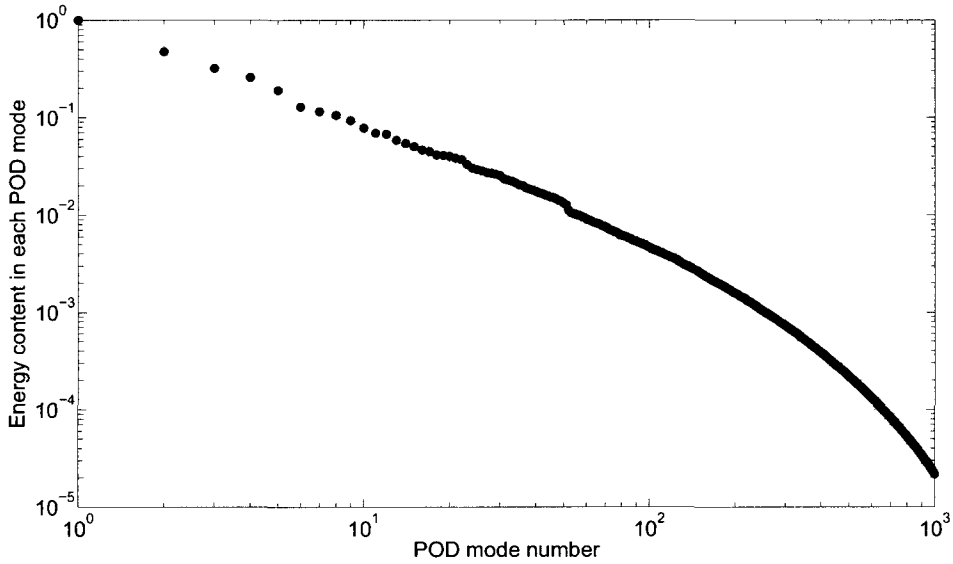

Figure 5.1. Energy content from a single plane at $y/L \approx -0.15$ as a function of POD mode number for ABL2 at $\alpha = 0°$ and $W/H = 1.5$.

5.2.1 Determination of the spatial basis functions ψ_i. Recall that we have 1218 SPIV snapshots per plane for the ABL2 case at 0° incidence angle and $W/H = 1.4$. For each of these planes, we split the ensemble into a "training ensemble" comprised of the first 1000 SPIV snapshots and a "testing ensemble" containing the remaining 218 SPIV snapshots. We use only the training ensemble to characterize the flow field. The "testing ensemble" will come into use at a later stage for the purpose of verification. Figure 5.2 presents the first six basis functions associated with the same

vertical plane of SPIV data used as an example for the energy spectrum plot shown in Figure 5.1 and was computed from the training ensemble. The color mapping here corresponds to vorticity associated with the basis functions vector field also displayed on the plots. This is done so as to highlight the typical spatial scales found in these basis functions, which range from about $1H$ to about $1/5H$. It can also be seen from Figure 5.2 that modes 1 and 2 essentially capture features associated with the large recirculation region within street 2, while higher-order modes successively capture features associated with the wake layer and smaller scales. A similar POD analysis is performed independently on the training ensemble of each of the 37 remaining vertical planes of SPIV data, yielding a total of 38 sets of basis functions, $\boldsymbol{\psi}_i^p(\boldsymbol{x})$, where the superscript p denotes the p^{th} SPIV vertical plane.

5.2.2 Determination of the temporal POD coefficients ζ_i. For each vertical plane p, we obtain the POD coefficients, ζ_i^p, by projecting the fluctuating velocity field onto the spatial basis functions, $\boldsymbol{\psi}_i^p(\boldsymbol{x})$:

$$\zeta_i^p(t) = \boldsymbol{\psi}_i^p(\boldsymbol{x})\boldsymbol{u}'^p(\boldsymbol{x}, t). \tag{5.2}$$

For each vertical plane p, the training ensemble of the fluctuating velocity data is used. Therefore, the time series of the POD coefficients, $\zeta_i^p(t)$ are obtained for the first 1000 SPIV snapshots.

Figure 5.3 shows the energy content captured by the first six modes as a function of the vertical plane number p. Also provided by the top abscissa is the correspondence between plane number p and its physical location in the array, y/L. The energy content for each plane is directly obtained from the eigenvalues, $\lambda_i^p = \overline{\zeta_i^p(t)^2}$. As can be seen from Figure 5.3, the average energy content is about 50% of the total energy for all the planes spanning the street length L. A slight asymmetry in the energy content can be observed on one side of the street, which is likely due to the asymmetry of the flow itself. This phenomenon was observed in Chapters 3 and

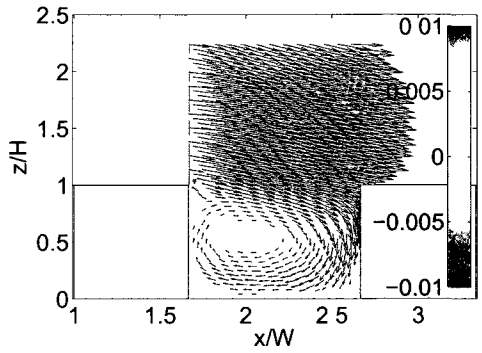

(a) ψ_1

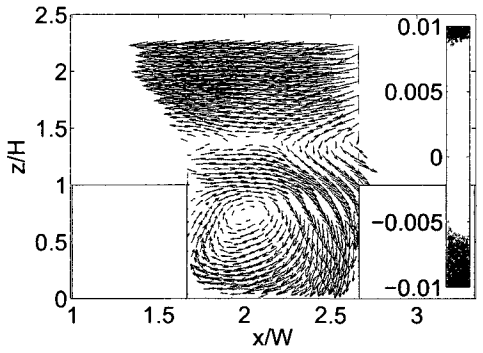

(b) ψ_2

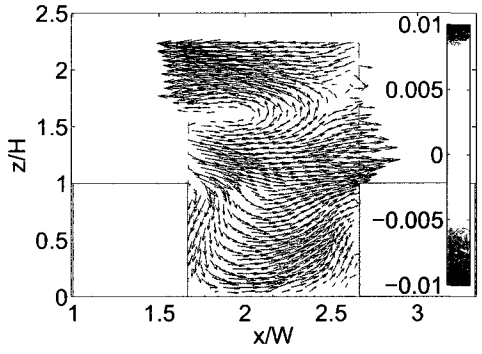

(c) ψ_3

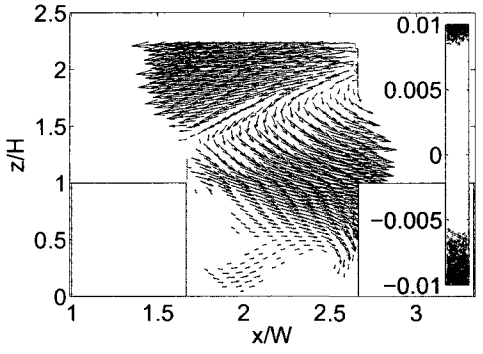

(d) ψ_4

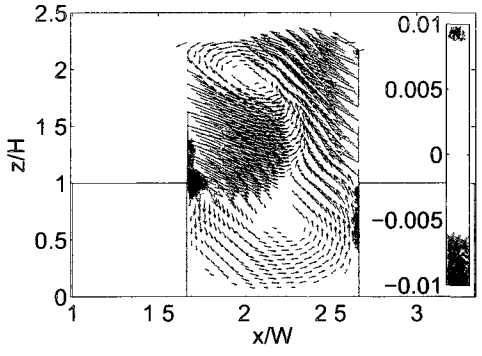

(e) ψ_5

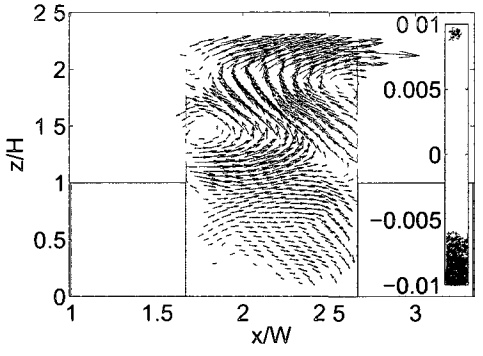

(f) ψ_6

Figure 5.2. Basis Functions, ψ_i, for a vertical plane located at $y/L \approx -0.15$. Color mapping refers to vorticity as derived from the vector maps.

4, where a slight asymmetry in the model or in the incoming flow field could yield asymmetries in the mean streamlines and turbulence distribution.

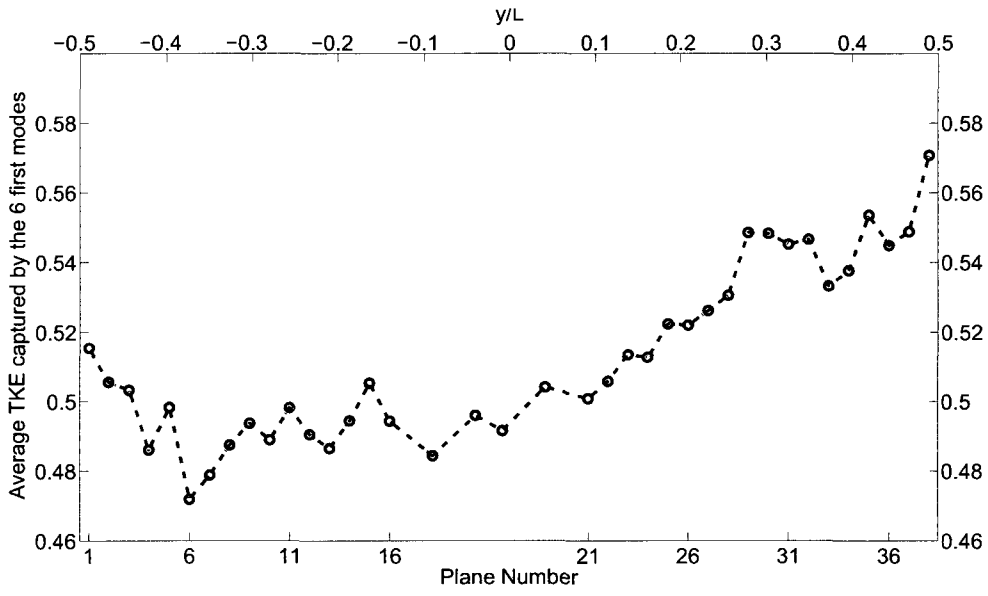

Figure 5.3. Average Turbulent Kinetic Energy contained in the first six modes as a function of spanwise location.

5.3 Temporal estimation of the flow field and sparse measurements

All of the temporal information for the flow field is contained in the POD coefficients. From our decomposition, we have the POD coefficients associated with each independent vertical SPIV plane. The planes were acquired independently from each other, so the POD coefficients are not correlated in time from plane to plane. Our goal is to estimate the temporal evolution of the flow field everywhere simultaneously which translates to estimating the POD coefficients everywhere in the flow field simultaneously.

To this end, one could perform a regression between the known independent POD coefficients and the entire SPIV velocity field. That would presumably give very good accuracy. However, in practice, we are interested in temporally resolving the

velocity field through a complex environment based on sparsely distributed sensors. These sparse measurements could be pressure, temperature, velocity measurements, etc. So the goal of this work is to investigate the use of sparse measurements to predict the flow field in a complex environment.

Our sparse measurements are selected to be only two components of the velocity at 39 streamwise locations for each SPIV plane at a constant z/H location instead of the entire 39 by 56 array of all three velocity components in each plane. Figure 5.4 presents the location of the "sparse training sensors" with respect to a single vertical plane. Two z/H positions will be investigated, $z/H = 0.5$ and $z/H = 1.75$. The regression will therefore be performed in each vertical plane p independently between the sparse measurements at one z/H location and the POD coefficients, $\zeta_i^p(t)$, for the 1000 realizations of the training ensemble. For the regression, we will need to construct measurement models; the two that we have chosen for this study are the Kernel Ridge Regression (KRR) model and the Linear Stochastic Estimation (LSE) model.

5.3.1 Construction of the KRR model. The Kernel Ridge Regression model is a non-linear regression model. For this investigation, radial basis functions (RBFs) are chosen for the kernel (Fasshauer, 2007). The inputs to the model are the "sparse measurements," $\boldsymbol{u}_s'(\boldsymbol{x}', t)$, obtained from the sparse sensors. The model takes the form:

$$\tilde{\zeta}_i(t) = \sum_{k=1}^{M} w_{ik} h_k(\boldsymbol{u}_s'(\boldsymbol{x}', t)) \tag{5.3}$$

where $\tilde{\zeta}_i(t)$ is the approximation to the temporal POD coefficient, $\zeta_i(t)$, w_{ik}'s are weights and h_k are the radial basis functions applied to $\boldsymbol{u}_s'(\boldsymbol{x}', t)$, and M is the number of basis functions. The weights, w_{ik}, need to be found to construct the KRR model. This is done by minimizing the following cost function, $C_i(\boldsymbol{w})$, (Mokhasi et al., 2009;

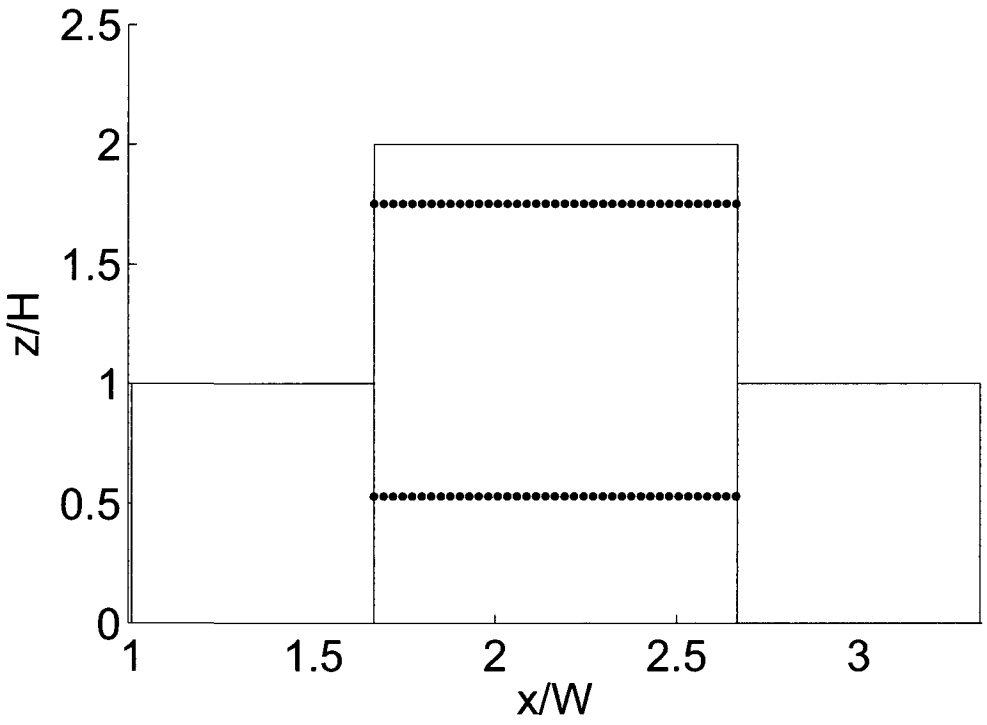

Figure 5.4. Schematic of a single vertical SPIV plane, the black dots represent the location of the "sparse training sensors."

Mokhasi, 2009b) using the training ensemble described earlier:

$$C_i(\boldsymbol{w}) = \sum_{n=1}^{L} (\zeta_i(t_n) - \tilde{\zeta}_i(t_n))^2 + \beta \sum_{k=1}^{M} w_{ik}^2 \tag{5.4}$$

where β is a regularization parameter, taken to be small (its value needs to be optimized using a technique such as "leave one out cross validation") and L is the number of snapshots in the training ensemble (1000 snapshots). The radial basis functions, h_k, used in this study are Gaussian and take the form:

$$h_k(\boldsymbol{x}) = e^{-\epsilon^2 \|\boldsymbol{x} - \boldsymbol{c}_k\|_2^2} \tag{5.5}$$

where ϵ is the scaling parameter (also needs to be optimized using "leave one out cross validation") and controls the width of the radial basis function, and $\boldsymbol{c}_k$ are the "centers," which correspond here to the measurements from the "sparse training sensors" $\boldsymbol{u}'_s(\boldsymbol{x}', t)$. The reader is referred to Fasshauer (2007) for a more detailed study of RBFs. Figure 5.5 shows a diagram of the procedure to build the kernel ridge regression for a single vertical plane p.

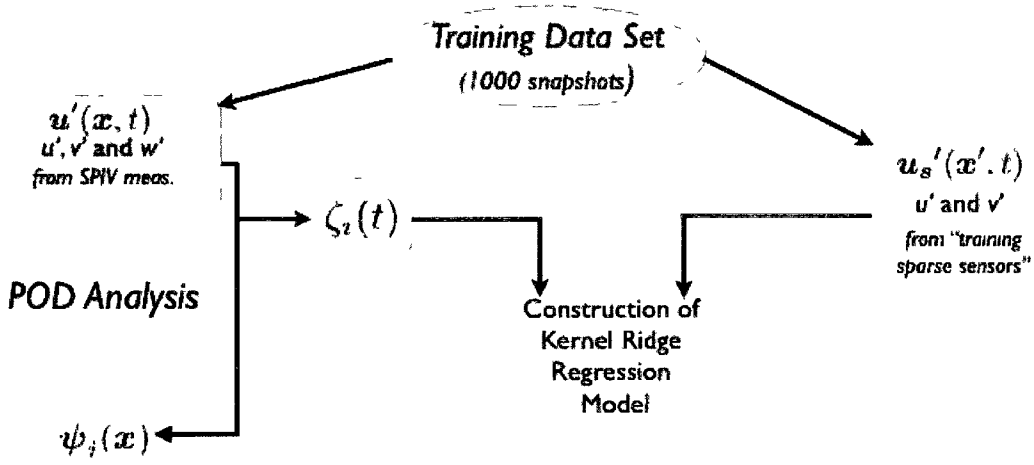

Figure 5.5. Construction of the KRR measurement model with sparse velocity measurements.

5.3.2 Construction of the LSE model. The Linear Stochastic Estimation formulation used in this work is a variation of the standard LSE used in Adrian and

Moin (1988). LSE seeks an estimate of $\boldsymbol{u}'(\boldsymbol{x},t)$ in the form:

$$\boldsymbol{u}'(\boldsymbol{x},t) = A(\boldsymbol{x},\boldsymbol{x}')\ \boldsymbol{u}'_s(\boldsymbol{x}',t), \tag{5.6}$$

where $\boldsymbol{u}'_s(\boldsymbol{x}',t)$ are the measurements at the location of the sparse sensors. By solving the variational problem, one can show that the kernel $A(\boldsymbol{x},\boldsymbol{x}')$ is the two-point correlation function suitably normalized. The kernel A is given by:

$$A(\boldsymbol{x},\boldsymbol{x}') = \frac{\langle \boldsymbol{u}'(\boldsymbol{x})\boldsymbol{u}'_s(\boldsymbol{x}')\rangle}{\langle \boldsymbol{u}'_s(\boldsymbol{x}')\boldsymbol{u}'_s(\boldsymbol{x}')\rangle}. \tag{5.7}$$

In replacing the velocity fields in this equation with their POD formulation, it can be shown (Mokhasi, 2009a) that the POD coefficient $\zeta_i(t)$ can be approximated directly using the following equation written in matrix-vector format:

$$\tilde{\zeta}_i(t) = \left(L_{im}\boldsymbol{\psi}_{mj}\right)\left(\boldsymbol{\psi}^T_{nj}L_{nm}\boldsymbol{\psi}_{mj}\right)^{-1}\boldsymbol{u}'_s(\boldsymbol{x}_j), \tag{5.8}$$

where L is a diagonal matrix with its elements being the eigenvalues λ_i, $\boldsymbol{u}'_s(\boldsymbol{x}_j)$ are the measurements from the sparse sensors and $\boldsymbol{\psi}$ are the basis functions at their spatial location. Specifically, the first index in the matrix-vector format formulation of the basis functions, $\boldsymbol{\psi}_{mj}$, corresponds to the POD mode number, while the second index refers to the spatial location. Here, this variant of LSE model relies solely on the knowledge of the basis functions at the locations of the "sparse training sensors" and on the eigenvalues, λ_i, associated with these basis functions. The accuracy of the model depends directly on the computed basis functions and on the amount and location of "sparse training sensors."

5.3.3 Testing and validation of the KRR and LSE models. In order to test and validate both measurement models, we use the testing ensemble which contains the remaining 218 SPIV snapshots per vertical plane that were not included in the training ensemble. The velocity data from each SPIV vertical plane, $\boldsymbol{u}'^p(\boldsymbol{x},t)$, in the testing ensemble serve as a reference. By projecting $\boldsymbol{u}'(\boldsymbol{x},t)$ onto the basis functions,

$\psi_i(\boldsymbol{x})$, computed from the training ensemble, we obtain the actual POD coefficients, $\zeta_i(t)$. Then the estimated POD coefficients, $\tilde{\zeta}_i(t)$, are obtained by providing the measurements from the sparse sensors, $\boldsymbol{u}'_s(\boldsymbol{x}', t)$, in the testing ensemble and hereafter referred to as "sparse testing sensors," either at $z/H = 0.5$ or $z/H = 1.75$, to the measurement models. Figure 5.6 presents a diagram summarizing the testing procedure that is carried out. The performance of the temporal estimation is measured by

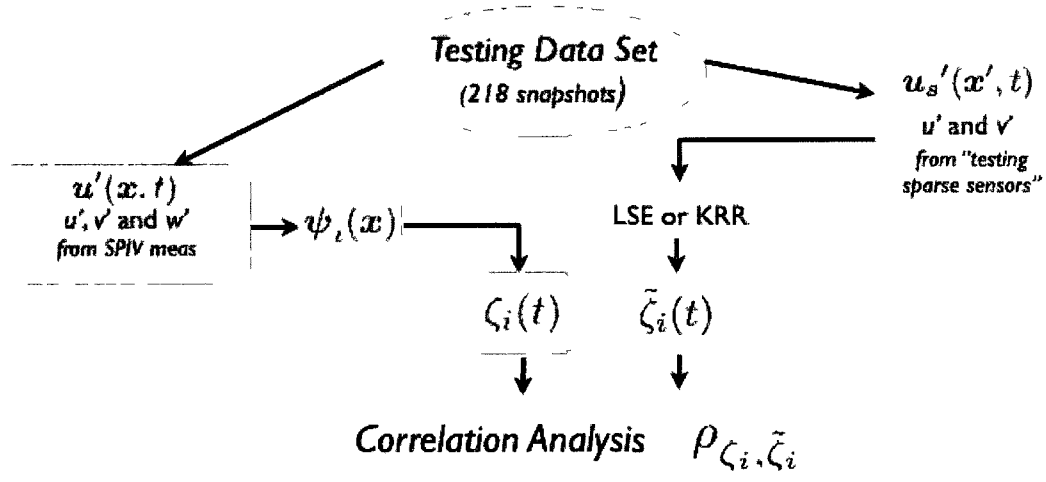

Figure 5.6. Testing of the KRR and LSE measurement models with sparse velocity measurements.

computing the correlation coefficient, $\rho_{\zeta_i,\tilde{\zeta}_i}$, for each mode between the actual POD coefficients, $\zeta_i(t)$, and the estimated POD coefficients, $\tilde{\zeta}_i(t)$. The correlation coefficient, $\rho_{\zeta_i,\tilde{\zeta}_i}$, is defined as the covariance of ζ_i and $\tilde{\zeta}_i$ divided by the product of their standard deviations:

$$\rho_{\zeta_i,\tilde{\zeta}_i} = \frac{\mathrm{cov}(\zeta_i, \tilde{\zeta}_i)}{\sigma_{\zeta_i}\sigma_{\tilde{\zeta}_i}}. \tag{5.9}$$

Figure 5.7 presents the correlation coefficient, $\rho_{\zeta_i,\tilde{\zeta}_i}$, as a function of the mode number (from 1 to 6) and the plane number (from 1 to 38) for the KRR model using the "sparse testing sensors" at $z/H = 0.5$ or $z/H = 1.75$. For those sensors at $z/H = 0.5$, it can be observed that the largest correlation coefficients are obtained

for mode 2 in a region centered about mid-span of the street. Mode 2 is essentially capturing information about the recirculation region within the street. The other modes are not very well resolved. However, for "sparse testing sensors" at $z/H = 1.75$, the picture is almost inverted. The correlation coefficients are much larger for nearly every mode but mode 2 in the region centered about mid-span. Recall that in Chapter 4 it was shown that the spanwise velocity fluctuations lower in the street were the main component to the overall TKE at that location. In the shear layer above the blocks, it was shown that the streamwise velocity fluctuations were the main component of the TKE. Therefore, it is suggested that the temporal evolution of mode 2 is strongly influenced by the spanwise velocity fluctuations lower in the street which are not well correlated with the streamwise velocity fluctuations above the street. So in summary, if sensors were located in the wake layer regions above the blocks, the temporal evolution would be well resolved for most modes at many locations within the street except for mode 2 in the mid-span region within the street. To accurately predict that mode, additional sensors within that region would be required.

The fact that the other modes are much better captured with sensors placed in the wake layer illustrates the power of the POD technique. Each of the first six modes captures information on the recirculation region trapped in the street. Being able to estimate a large portion of the temporal evolution of these six modes from sparse measurements in the wake layer indicates that there is a good correlation between the temporal evolution of the wake layer and the temporal evolution of the recirculation region.

The same correlation coefficient maps are shown for the LSE model in Figure 5.8. The conclusions are identical and the correlation coefficients almost match those obtained for the KRR model.

Figure 5.9 summarizes the average correlation coefficient over the first six

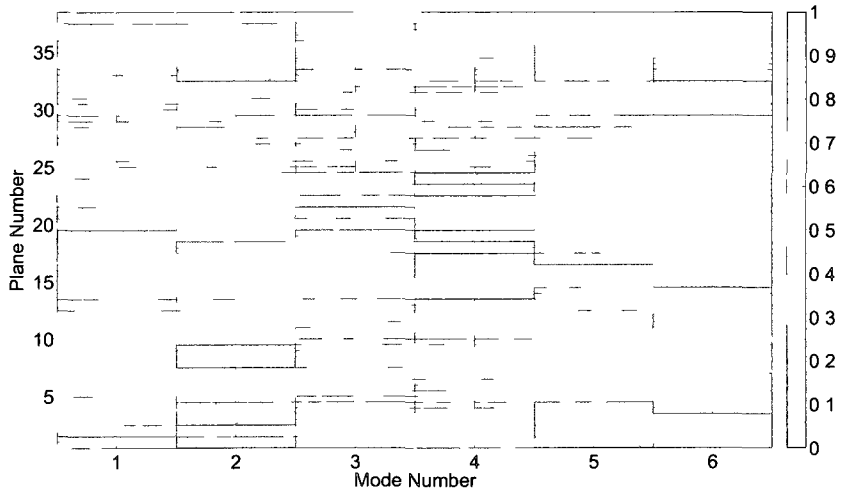

(a) Testing sensors at $z/H = 0\ 5$

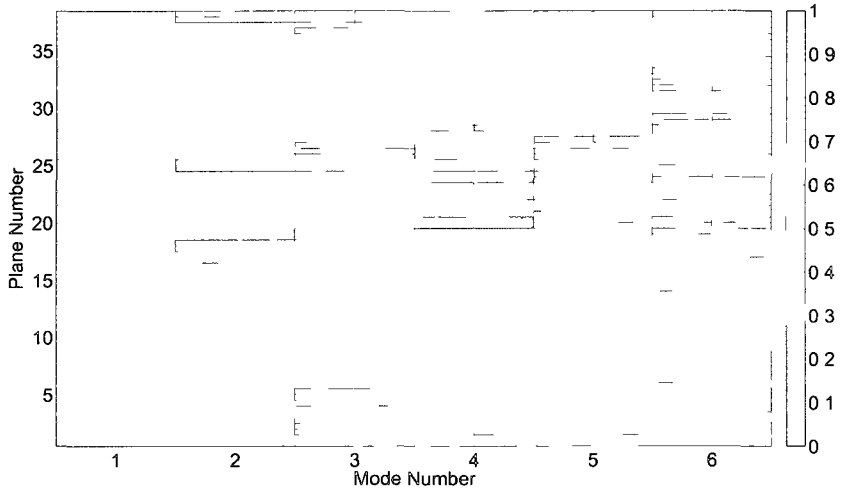

(b) Testing sensors at $z/H = 1\ 75$

Figure 5 7 Correlation coefficient maps for the KRR model for sensors at the two different z/H wall normal locations The color indicates the magnitude of the correlation coefficient, $\rho_{\zeta_i\,\tilde{\zeta}_i}$

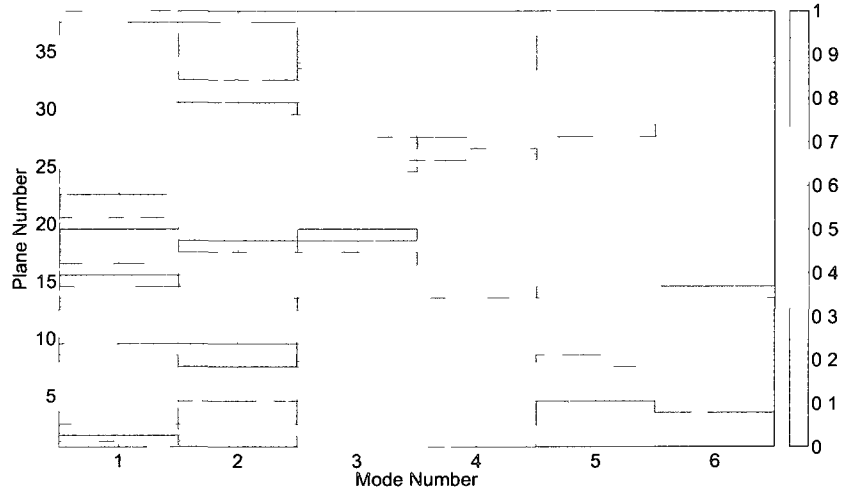

(a) Testing sensors at $z/H = 0\,5$

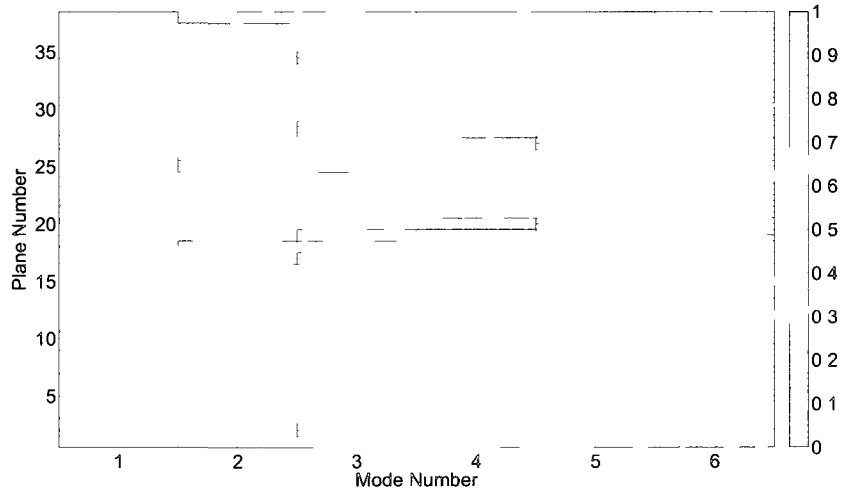

(b) Testing sensors at $z/H = 1\,75$

Figure 5 8 Correlation coefficient maps for the LSE model for sensors at the two different z/H wall normal locations The color indicates the magnitude of the correlation coefficient, $\rho_{\zeta_i\,\zeta_i}$

modes as a function of plane number both for the KRR and LSE models using the "sparse testing sensors" at $z/H = 0.5$ or $z/H = 1.75$. This shows how closely the two models perform. Taking the average over the plane number, the KRR model is found to give correlation coefficients of 37% and 62% for the temporal evolution of the first six modes for $z/H = 0.5$ and 1.75, respectively. The LSE model gives correlation coefficients of 34% and 60% for the temporal evolution.

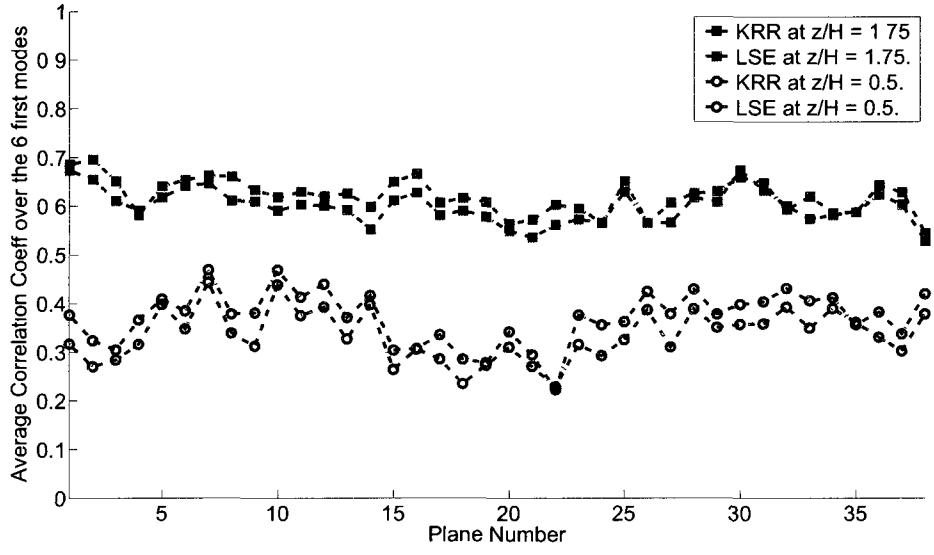

Figure 5.9. Average correlation coefficient over the first six modes versus spanwise plane number for "sparse testing sensors" at $z/H = 0.5$ and 1.75. The KRR model is depicted in blue and the LSE model in red.

From a comparison of the time series of the actual and estimated POD coefficients, it is observed that the energy content of the modes under consideration is not correctly resolved. We illustrate this in Figure 5.10, displaying the energy content of the actual POD coefficients, shown for reference, and both the energy content captured by the LSE and KRR models using sparse sensors at $z/H = 1.75$. This energy content for all three sets of POD coefficients is normalized by their respective energy content in mode 1. Recall that the energy is contained in the eigenvalues that

can be computed for the estimated POD coefficients as $\tilde{\lambda}_i = \overline{\tilde{\zeta}_i(t)^2}$. This damping of the energy content obtained from the estimation can be lessened by using the known eigenvalues obtained from the initial POD analysis, λ_i, and normalizing the estimated POD coefficients to match the expected energy content according to:

$$\tilde{\zeta}_i(t)_{\text{corrected}} = \tilde{\zeta}_i \frac{\lambda_i}{\tilde{\lambda}_i}. \tag{5.10}$$

Figure 5.11 presents a comparison between the "uncorrected" estimated POD coefficients as obtained from the KRR model for a single vertical plane (5.11(a)) and its "corrected" counterpart (5.11(b)). Also, since both the KRR and LSE models provide similar results, we only use the KRR model for the remainder of this chapter.

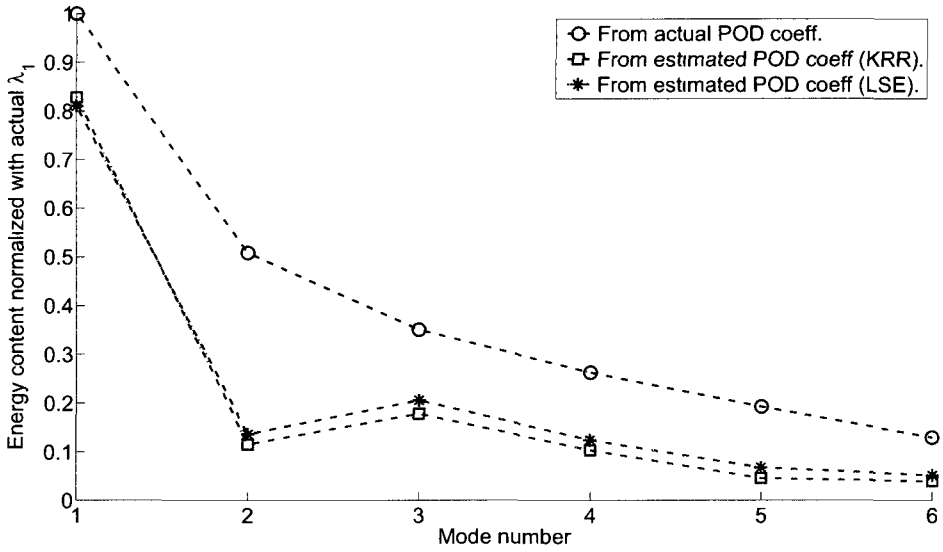

Figure 5.10. "Uncorrected" normalized energy content as a function of mode number for both the KRR and LSE models based on "sparse testing sensors" at $z/H = 1.75$, for a single plane at $y/L \approx -0.15$.

Finally, using the "corrected" results obtained from the KRR model, we provide a measure of the accuracy of the estimation in terms of the spatially averaged TKE, denoted as $<$ TKE $>$. We calculate the percentage error per vertical plane, Err, between the spatially averaged TKE obtained from the estimation, $<$ TKE$_e$ $>$,

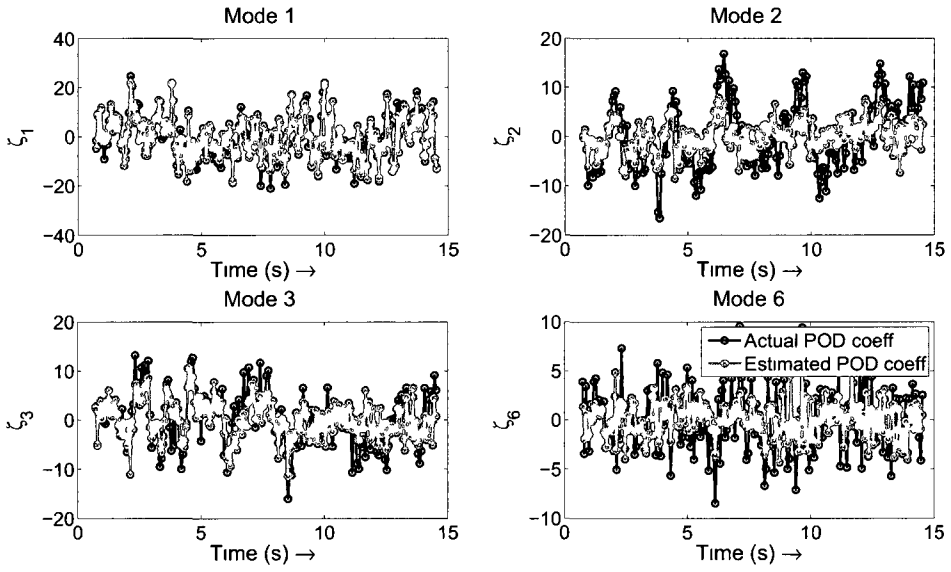

(a) Uncorrected

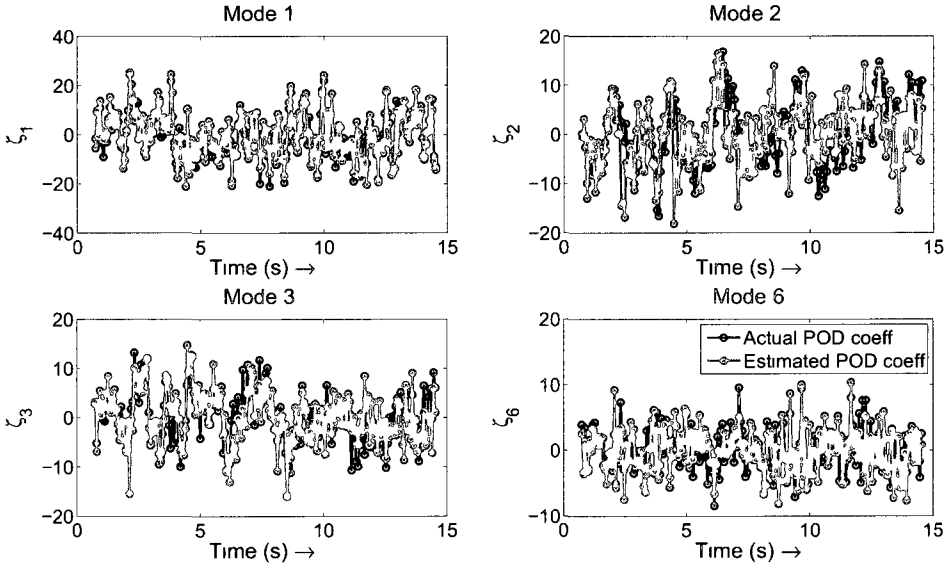

(b) Corrected

Figure 5.11. The estimated time series of the POD coefficients for modes 1, 2, 3 and 6 as obtained from the KRR model with "sparse testing sensors" at $z/H = 1.75$.

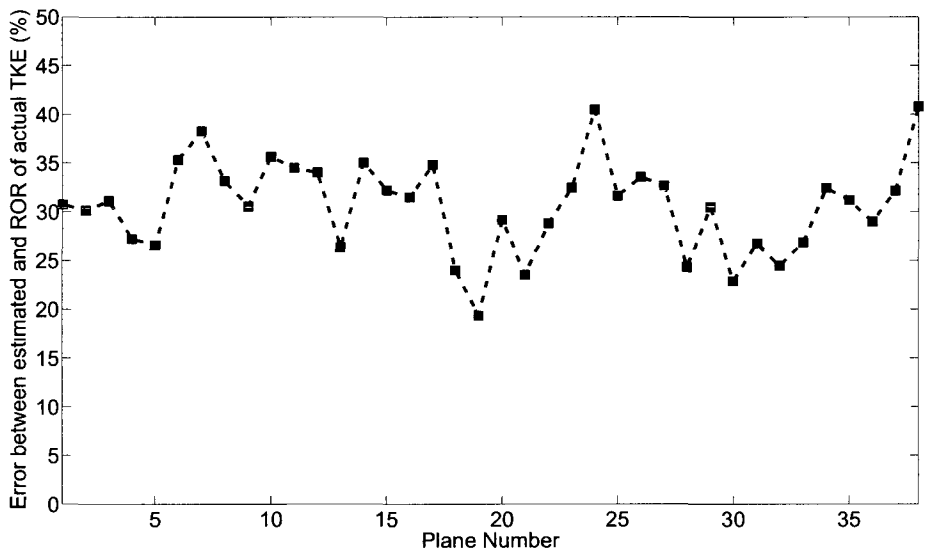

Figure 5.12. Percentage error between the actual and estimated $< \text{TKE} >$ as a function of plane number.

and the spatially averaged TKE obtained from the reduced-order representation of the actual testing data, $< \text{TKE}_a >$, set as follows:

$$\text{Err} = \sqrt{\frac{< (\text{TKE}_e - \text{TKE}_a)^2 >}{< \text{TKE}_a^2 >}} \tag{5.11}$$

Figure 5.12 presents this percentage error as a function of plane number. The average error over the planes is found to be about 30%. Even though this seems to be a large difference in terms of magnitude, this has to be put in perspective of the typical accuracy expected for turbulence estimation where differences of up to one order of magnitude are common (Patnaik et al., 2007). More importantly, our estimation captures well the spatial distribution of the TKE. This is shown in Figure 5.13 that presents a comparison at mid-span of the estimated TKE with respect to the reduced-order representation of the actual TKE using the first six modes. The different regions of large TKE are indeed well represented in the estimation.

5.4 Estimation of the reduced-order representation of the 3D velocity field

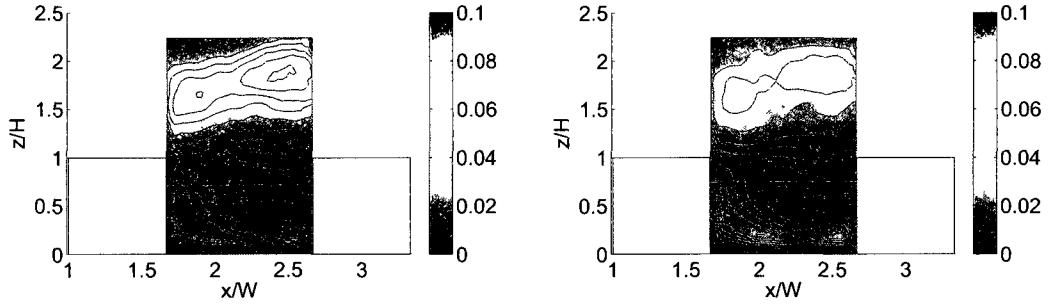

(a) KRR estimation.

(b) Reduced-order representation of actual data from SPIV measurements.

Figure 5.13. Vertical slice of TKE_H at mid-span based on the estimation in street 2 for the ABL2 at 0° incidence angle and $W/H = 1.5$.

In order to obtain the temporal evolution of the reduced-order representation of the 3D velocity field in the entire street 2, we now need to provide simultaneous sparse measurements distributed across the street that will serve as input to the constructed measurement models. We have determined that the performance of the temporal estimation of the velocity field was best for sparse sensors at $z/H = 1.75$. Therefore, a horizontal plane of 2DPIV data was collected at $z/H = 1.75$ to serve as the actual sparse sensor measurements, $\boldsymbol{u}'_s(\boldsymbol{x}', t)$. Note that this 2DPIV data plane was acquired independently of the 38 SPIV data planes. Figure 5.14 presents this horizontal plane with respect to the urban array and also the spatial location of the actual sensors (denoted as black dots) that are going to be used to estimate the instantaneous velocity field in and above street 2. Once again, only a few sensors are displayed for clarity. In reality, we use 39 sensors along the intersection of each SPIV vertical plane with the 2DPIV horizontal plane.

The 2DPIV data set is composed of 406 snapshots acquired at 15 Hz. The streamwise and spanwise components of the fluctuating velocity field are extracted

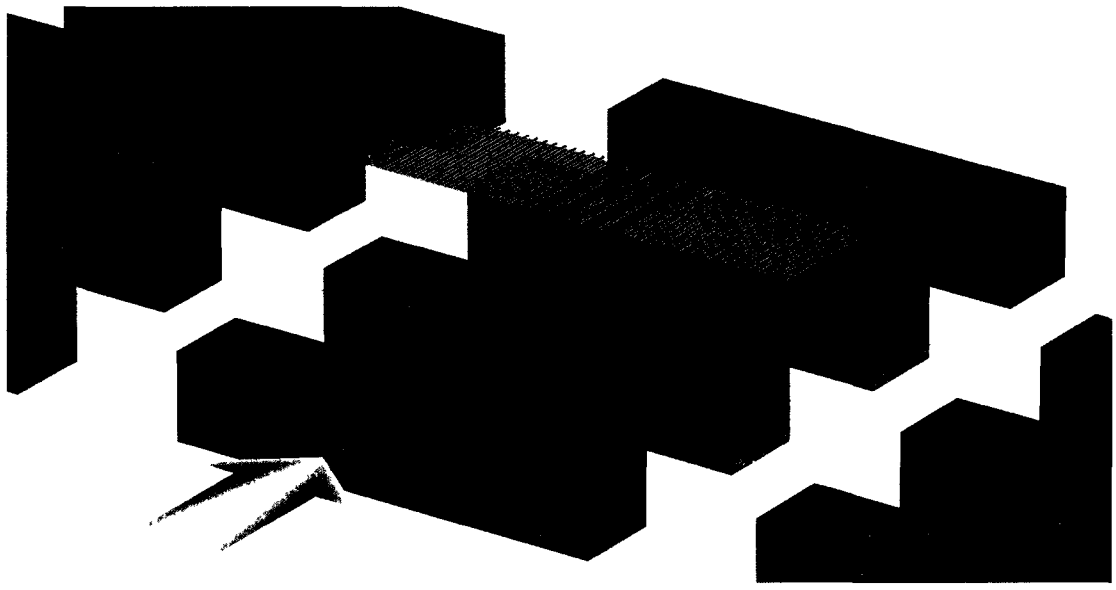

Figure 5.14. Schematic of the horizontal 2DPIV plane (in red) at $z/H = 1.75$. The black dots represent the location of the actual sparse sensors.

from these 2DPIV snapshots at the actual sensor locations. The sensor measurements, $\boldsymbol{u}'_s(\boldsymbol{x}', t)$, are then provided to the 38 KRR measurement models constructed earlier to give an estimation of the POD coefficients, $\zeta_i^p(t)$, associated with each vertical plane p. The estimated reduced-order representation of the 3D fluctuating velocity field, $\tilde{\boldsymbol{u}}'(\boldsymbol{x}, t)$, is therefore obtained by concatenating the results from each vertical plane to yield:

$$\tilde{\boldsymbol{u}}'(\boldsymbol{x}, t) = \left[\sum_{i=1}^{6} \tilde{\zeta}_i^1(t) \boldsymbol{\psi}_i^1(\boldsymbol{x}); \sum_{i=1}^{6} \tilde{\zeta}_i^2(t) \boldsymbol{\psi}_i^2(\boldsymbol{x}); \ldots; \sum_{i=1}^{6} \tilde{\zeta}_i^{38}(t) \boldsymbol{\psi}_i^{38}(\boldsymbol{x}) \right]. \tag{5.12}$$

By adding the mean velocity field component, $\boldsymbol{U}(\boldsymbol{x})$, to this fluctuating velocity field, we now have a fully 3D data set, $\tilde{\boldsymbol{u}}(\boldsymbol{x}, t) = \boldsymbol{U}(\boldsymbol{x}) + \tilde{\boldsymbol{u}}'(\boldsymbol{x}, t)$, describing the reduced-order representation of the velocity at 406 instants in time.

Similarly to the study performed with the testing ensemble on the energy content of the eigenvalues associated with the first six modes, we investigate the energy content of the "uncorrected" estimated POD coefficients obtained from the actual sparse sensors. Figure 5.15 presents the energy content captured by the estimation

using the actual sensors. It can be seen that the picture is similar to the one shown in Figure 5.10 earlier when using the testing ensemble. Therefore, we can correct the energy content by normalizing the estimated POD coefficients using the eigenvalues obtained from the training ensemble introduced earlier. The corrected energy content of the estimated POD coefficients is also displayed in Figure 5.15. The remainder of the results presented in this chapter takes into account the corrected energy content.

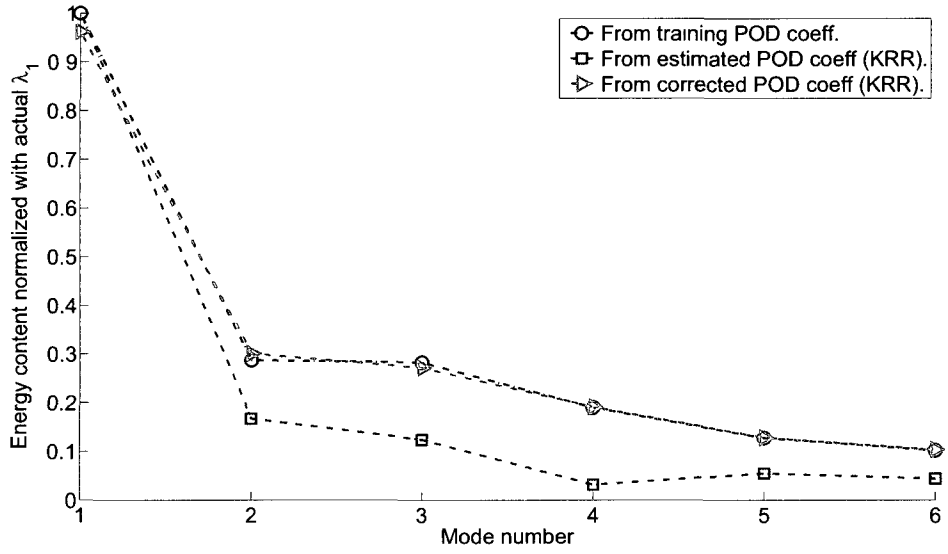

Figure 5.15. Normalized energy content as a function of mode number for the KRR model based on the actual sparse sensors at $z/H = 1.75$, for a single plane at $y/L \approx -0.15$.

From the corrected estimation of the reduced-order representation of the velocity field, $\tilde{\boldsymbol{u}}(\boldsymbol{x}, t)$, we compute the TKE_H in a vertical plane at mid-span and compare it to the results shown in Chapter 4. For convenience, Figure 5.16 presents the data from the estimation, the actual data as obtained from direct SPIV measurements and a reduced-order representation of the SPIV measurements based on the first six modes. As expected, the TKE_H levels found in the estimated data are about half the

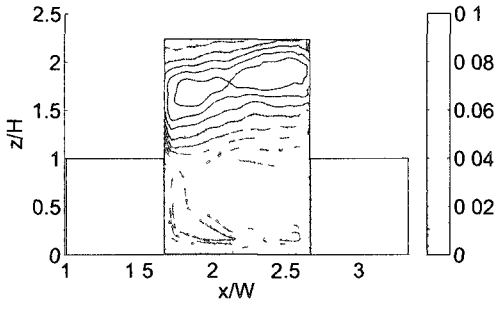

(a) KRR estimation.

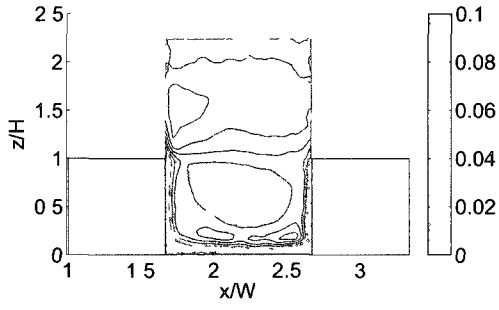

(b) Actual data from SPIV measurements.

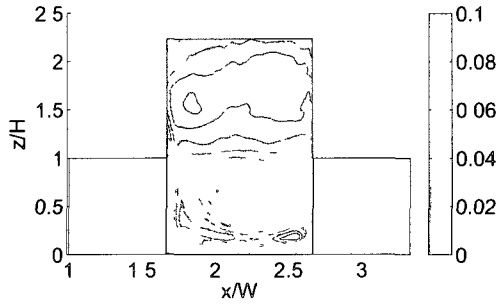

(c) Reduced-order representation of actual data from SPIV measurements.

Figure 5.16. Vertical slice of TKE_H at mid-span based on the estimation in street 2 for the ABL2 at 0° incidence angle and $W/H = 1.5$.

actual levels since the first six modes used to describe the velocity capture about 50% of the total TKE. Strong similarities in the spatial distribution of TKE_H are also observed between the estimated and actual data. The two most dominant regions are the wake layer and the region within the street close to the ground which indicates that the measurement models provide physical results. A comparison of the estimation with the reduced-order representation of the actual data shows a good agreement in TKE_H levels and spatial distribution.

We can now present results for instantaneous streamlines and isosurfaces of instantaneous normalized angular momentum from the reduced-order representation of the velocity field, $\tilde{\boldsymbol{u}}(\boldsymbol{x},t) = \boldsymbol{U}(\boldsymbol{x}) + \tilde{\boldsymbol{u}}'(\boldsymbol{x},t)$, in street 2. Figure 5.17 shows an example of instantaneous streamlines colored with TKE_H. Again, the TKE color levels are about 50% of the actual levels. It can be seen from this figure that features associated with the mean streamlines can clearly be observed in this instantaneous representation. A large portion of the recirculation region is still apparent. The starting points of the displayed streamlines are shown as red dots and are identical to the ones presented in Chapter 3, see for example Figure 3.3. But since the streamline description is sensitive to the location of the starting points, a better way to look at an instantaneous snapshot is to compute the instantaneous normalized angular momentum. Figure 5.18 presents this description at that same instant in time. As expected from the streamlines plot, the vortical structure captured by the NAM is very similar to the mean distribution, see Figure 3.13(d) for comparison. This is an important result that reinforces the importance of studying the mean characteristics of this complex flow. Looking at the spatial displacement of the vortical structures as a function of time can provide complementary information on the range of locations that could be used to place sensors in the street to optimize the estimation. This will be presented in Chapter 6.

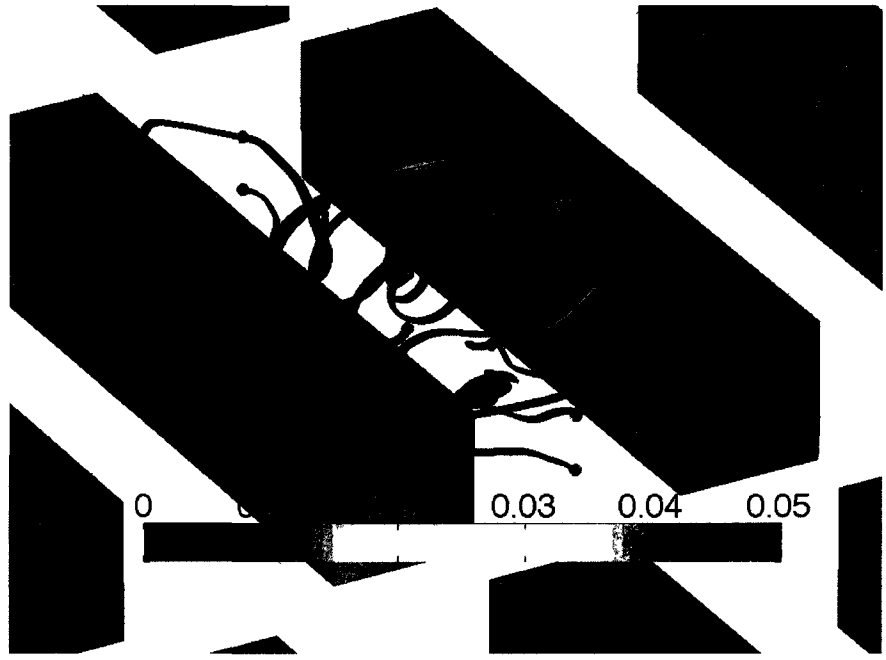

Figure 5.17. Instantaneous streamlines as calculated from the KRR estimation colored with local turbulent kinetic energy for the ABL2 at 0° incidence angle and $W/H = 1.5$.

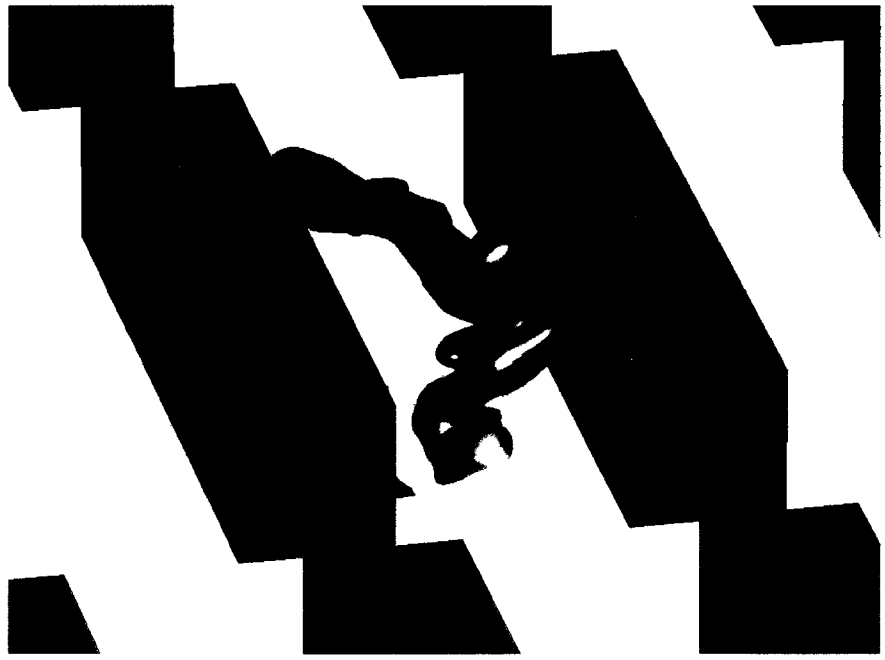

Figure 5.18. Instantaneous NAM in street 2, $f = 0.35$ for the ABL2 at 0° incidence angle and $W/H = 1.5$.

5.5 Continuous description of the reduced-order representation of the velocity field using a linear state space model

The temporal resolution of the estimated 3D data set, $\tilde{\boldsymbol{u}}(\boldsymbol{x}, t)$, presented above is only as good as the temporal resolution of the sparse sensors, i.e. the frequency of the 2DPIV acquisition set to 15 Hz. In this section, we construct a dynamical model that describes the continuous evolution of the estimated velocity field, $\tilde{\boldsymbol{u}}(\boldsymbol{x}, t)$. Since we are interested in the temporal evolution, we can perform a new POD analysis of this estimated velocity field. This provides us with a set of POD spatial basis functions, $\boldsymbol{\phi}_i(\boldsymbol{x})$, and a corresponding set of POD coefficients, $\xi_i(t)$. Therefore, the dynamical model needs to describe the temporal evolution of the POD coefficients, $\xi_i(t)$.

A linear state-space model is chosen for the dynamical model. We are seeking the matrix $\mathbf{A}$ such that:

$$\frac{d\boldsymbol{\xi}(t)}{dt} = \mathbf{A}\boldsymbol{\xi}(t), \tag{5.13}$$

where $\boldsymbol{\xi}(t)$ is a vector containing the time series of each POD mode. This equation can be solved analytically and the solution reads:

$$\boldsymbol{\xi}(t + \delta t) = e^{\mathbf{A}\delta t}\boldsymbol{\xi}(t). \tag{5.14}$$

From the instantaneous realizations of the reduced-order representation of the velocity field, we can find the matrix $\mathbf{M}$ such that:

$$\boldsymbol{\xi}^{k+1} = \mathbf{M}\boldsymbol{\xi}^{k}, \tag{5.15}$$

where the index k represents the k^{th} time step. By simply recognizing that:

$$e^{\mathbf{A}\delta t} = \mathbf{M}, \tag{5.16}$$

we can find the matrix $\mathbf{A}$ using:

$$\mathbf{A} = \frac{\mathrm{logm}(\mathbf{M})}{\delta t}. \tag{5.17}$$

We carry out a simple test to assess if the temporal resolution of the estimated velocity field, $\tilde{\boldsymbol{u}}(\boldsymbol{x}, t)$, is sufficient to rely on the continuous description provided by such a linear state-space model. Figure 5.19 presents the discrete map of POD coefficients available to us. From the set of POD coefficients obtained from the measurement model (sampled at 15 Hz), we also extract a subset of POD coefficients, skipping every other time step (similar to sampling at 7.5 Hz) in order to perform a comparison between a linear state-space model constructed using each of these two sets of POD coefficients. The down-sampled version of the original discrete map of POD coefficients is shown in blue in the discrete map presented in Figure 5.19. Figure 5.20 presents the results for the continuous description of these two data

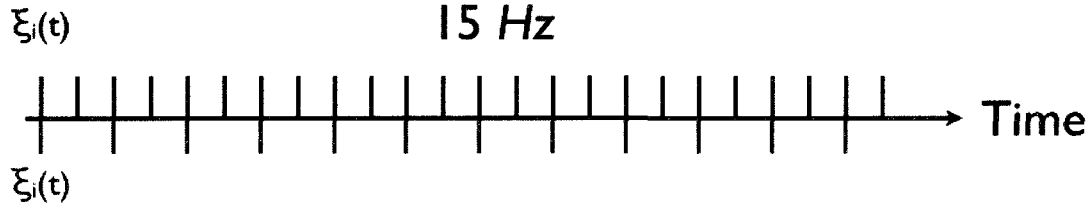

Figure 5.19. Schematic illustrating the downsampling used to test the temporal resolution of the estimation.

sets. It is very interesting to note that both continuous models agree fairly well even though they are based on two different sampling frequencies. This indicates that the continuous models do capture the temporal evolution of the POD coefficients and that we can rely on the estimation between two consecutive discrete values of the POD coefficients, therefore providing a realistic continuous temporal evolution of the reduced-order representation of the velocity field. The correlation coefficients between the two models are given in Table 5.1 for modes 1 to 6. They show a strong correlation between the two models, especially for modes 1 and 2, indicating that the largest scales of motion are also the slowest in this flow field.

Based on the linear state-space model that was constructed using every time

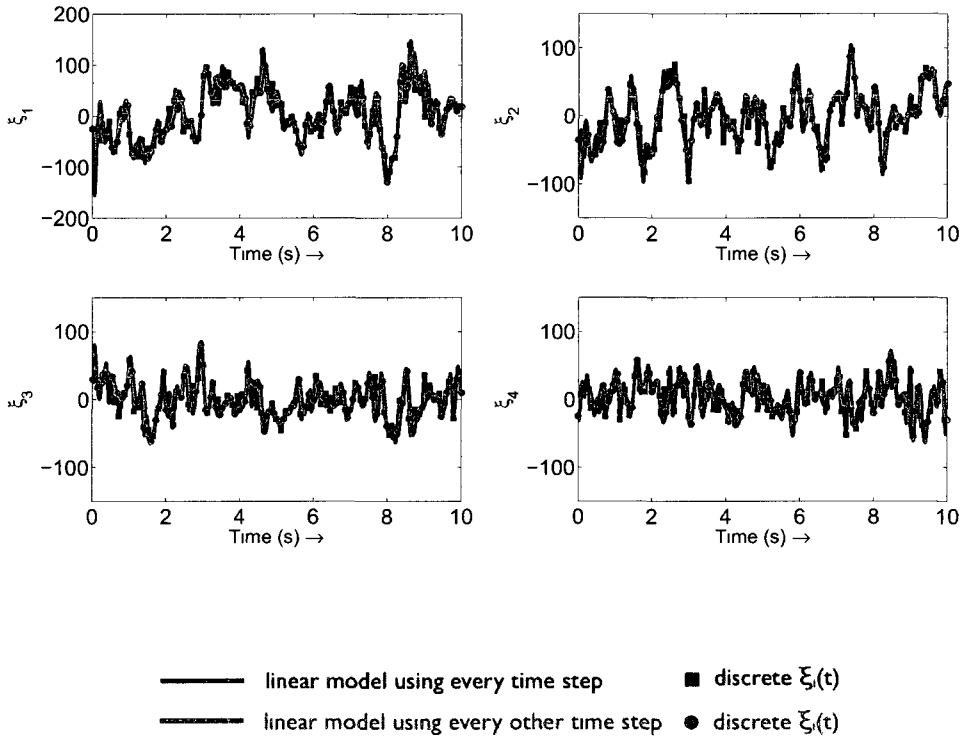

Figure 5.20. Solutions to linear state-space models for modes 1 to 4.

Table 5.1. Correlation coefficients between the POD coefficient time series obtained from each linear state-space model.

Mode number	1	2	3	4	5	6
Correlation coefficient	0.89	0.89	0.73	0.68	0.67	0.55

step available, we can now compute the temporal evolution of the POD coefficients, $\xi_i(t)$, at any desired frequency. Figure 5.21 presents snapshots extracted from a time evolution of the normalized angular momentum sampled at 37.5 Hz. Animations of

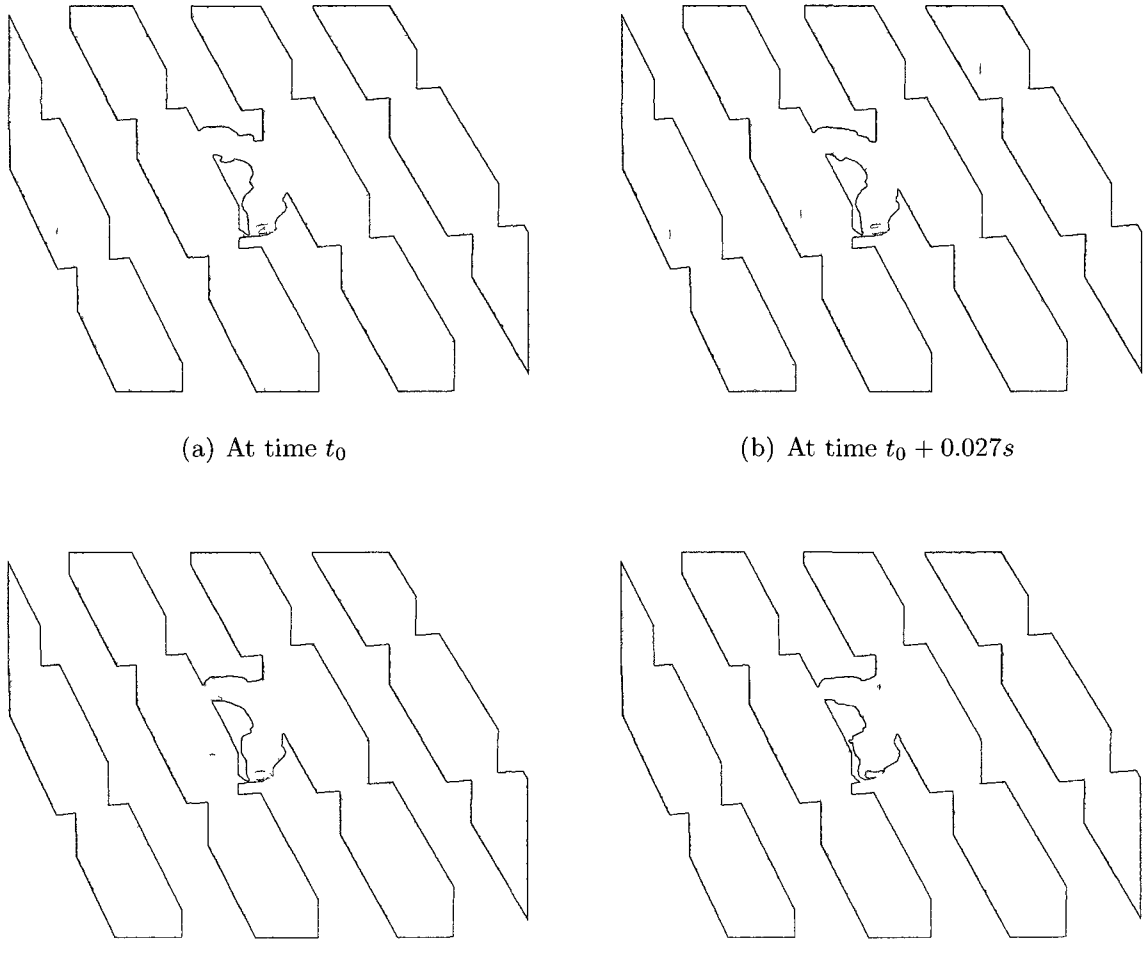

(a) At time t_0

(b) At time $t_0 + 0.027s$

(c) At time $t_0 + 0.053s$

(d) At time $t_0 + 0.080s$

Figure 5.21. Time sequence at 37.5 Hz of the arch vortex as calculated using the Normalized Angular Momentum ($f = 0.35$).

the temporal evolution of the reduced-order representation of the velocity field have been constructed. They highlight the streamwise and wall normal oscillations of the arch vortex within the street.

CHAPTER 6
DISCUSSION OF RESULTS

6.1 Alternative measure of the incidence angle

As described in Chapter 2, the incidence angle α was defined as the angle of the x-axis of the urban array with respect to the approach boundary layer mean flow direction. Experimentally, we rotated the urban array to simulate the three incidence angles investigated in this thesis, hereafter referred to as the nominal incidence angles. To set these angles, the side wall of the wind tunnel served as the reference streamwise direction. A grid defining the position of each block in the urban array was drawn on the glass sitting on the floor in the center of the test section. Instead of using a standard compass to determine the x-axis direction of our coordinate system, simple trigonometry was used and the large dimensions of the window allowed for drawing large triangles, providing an estimated uncertainty on the incidence angle of 0.05°. The blocks were then secured to the window glass with epoxy. However, as was determined in Chapters 3 and 4, slight asymmetries were observed in several of the mean and turbulence statistics that were presented for the $\alpha = 0°$ case. This suggests that the flow in this urban array is very sensitive to the setup and/or to any asymmetries in the incoming flow itself.

In the following sections, aspects linked to the incidence angle effects on the flow field will be investigated in greater detail. To do so, it is of interest to consider an alternative measure of the incidence angle as determined directly from the SPIV measurements. At a wall-normal position of $z/H >\approx 2$ over the span of the SPIV data domain ($-0.7 < y/L < 0.7$), we calculate an "effective incidence angle," α_e, between the mean streamline direction and the x-axis. Table 6.1 presents the resulting effective incidence angles for the different configurations studied in this work. Note that for a nominal incidence angle, α, the effective angle, α_e, is computed in each street where

SPIV data are available.

From this table, for the cases where the nominal incidence angle is 0°, it can be observed that the effective incidence angle, α_e, is offset by a small amount ranging from 0.1° to 1°. We believe that these effective incidence angles contribute to the slight asymmetries that are observed in the results presented earlier for a nominal incidence angle of 0°.

For the non-zero nominal incidence angles, it is interesting to study the ABL2 data set at $\alpha = 15°$, as it provides data for all streets. Directly upstream of the urban array, the agreement between the nominal and effective incidence angles is fairly good. As the flow moves to street 1, a redirection of the flow just above the urban array by as much as 2.5° is observed. Then, the effective angle remains fairly constant in streets 2 and 3. Considering now the non-zero nominal incidence angle for ABL1 ($\alpha = -4.5°$), the SPIV data show a difference of about one degree with the effective angle obtained in street 2, which could either be due to a slight misalignment or to a redirection of the flow by the urban array. So in summary, these non-zero effective incidence angles are thought to be the cause of the asymmetries observed in the results presented in Chapters 3 and 4.

6.2 Arch vortex location and incidence angle effects

6.2.1 Arch vortex in street 2. In Chapter 3, recall that we used the normalized angular momentum (NAM) and the Q-criterion to characterize the location, shape and extent of the arch vortex in the streets. More specifically, the NAM is a good tool for identifying the core of the arch vortices while the Q-criterion is useful in measuring their strength, shape and extent. Being able to locate the arch vortex is of importance as it is believed by many to be a driving factor in contaminant dispersion within an urban environment (Grinstein, Bos, & Dey, 2009; Boris, 2005).

Table 6.1. Nominal (α) and effective (α_e) incidence angles for each ABL configuration

ABL #	W/H	α	α_e			
			Upstream	Street 1	Street 2	Street 3
ABL1	1.5	0°			1°	
		−4.5°			−4.2°	
ABL1	4	0°			0.7°	
		−4.5°			−3.4°	
ABL2	1.5	0°	0.2°	0.5°	0.5°	0.4°
		15°	15.1°	12.3°	12.4°	12.5°
ABL3	1.5	0°	0.1°	−0.1°	0°	−0.1°

For example, the effect of the arch vortex is to move contaminants from the ground level to the top of buildings along their leeward side. Some of the contaminants remain trapped in the arch vortex, while some are released into the wake layer and transported quickly to another street. Therefore, being able to locate the arch vortex in the streets is of importance. We have determined in Chapter 3 that the NAM was effective in locating the core of the arch vortex. We will now study further the distribution of NAM in an x-z slice at mid-span for the ABL2 data set in street 2. The results in Figure 6.1 provide a fairly clear picture of the location of the core of the arch vortex as being associated with the maximal intensity of the contour. In

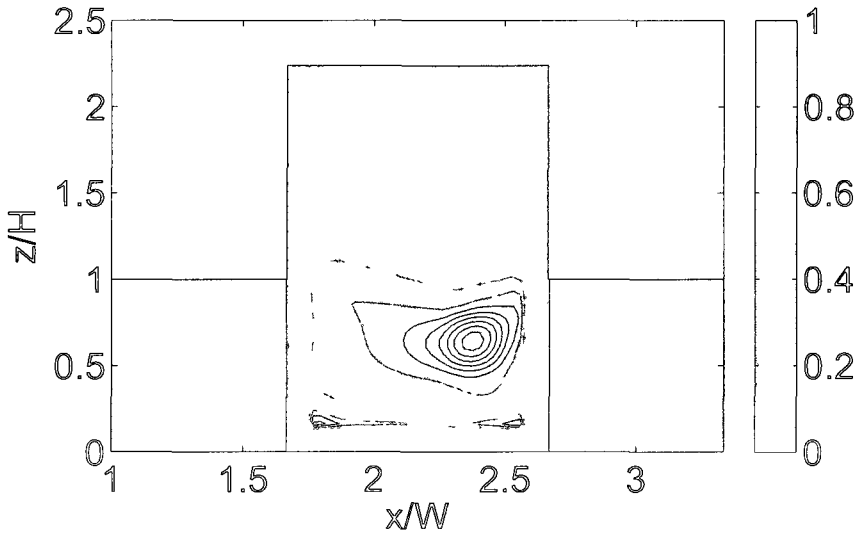

Figure 6.1. Vertical slice of NAM for ABL2 at mid-span in street 2 at $\alpha = 0°$. Color represents the levels of f.

order to extract the core location of the arch vortex structures, we therefore find the coordinates of the maximum of the NAM distribution along the street. We apply this on the data in street 2 for ABL1 at both $\alpha = 0°$ and $-4.5°$ and for ABL2 at $\alpha = 15°$ to compare the three incidence angles investigated in this study. Figure 6.2

presents the streamwise coordinate of the arch vortex as a function of its spanwise coordinate, for these three data sets. The baseline case is taken to be the ABL1 data set at 0° incidence angle and is shown in red on the figure. The core of the arch vortex appears to be fairly symmetric about mid-span for this $\alpha = 0°$ incidence angle case. Its maximal streamwise position is found in the center of the street while near the intersections, the core is located closer to the leeward wall. Upon increase of the incidence angle to $\alpha = -4.5°$, the streamwise location of the arch vortex core as a function of its spanwise location is significantly modified. From a spanwise position of $y/L = 0.5$ to about about mid-span, the core of the arch vortex is closer to the leeward wall as compared with the 0° incidence case. However, for $y/L < -0.1$, the core location remains fairly constant at a streamwise position of $x/W \approx 0.66$. This nearly straight portion of the arch vortex is the direct consequence of the channeling effect observed in the mean streamlines presented in Chapter 3, see for example Figure 3.16.

Considering the largest incidence angle of $\alpha = 15°$ studied in this work, we see a very similar behavior. Note that the results for $-4.5°$ and 15° have different signs so the approach flow direction is shown as arrows on the figure: the black arrow is for $-4.5°$ and the blue arrow is for 15°. These arrows are displayed for indicating the incoming flow direction and do not represent the true incidence angles. In order to make the comparison between the $-4.5°$ and 15° results easier to show, we simply reverse the $-4.5°$ case so as to "simulate" a $+4.5°$ incidence angle. This is shown in Figure 6.2(b). The similarity of the arch vortex position for both 4.5° and 15° is striking. This indicates that the channeling effect begins to occur at very small incidence angles. The transition from a symmetrical shape of the arch vortex to a channeling configuration clearly happens for incidence angles less than 4.5°.

The same comparison is performed for the wall-normal position of the arch

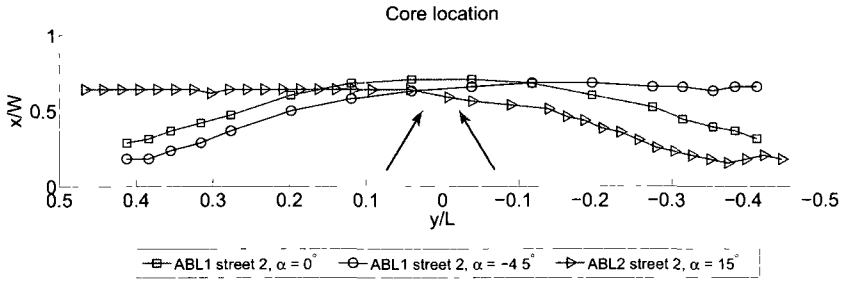

(a) $\alpha = 0°$, $-4.5°$ and $15°$ ($\alpha_e = 1°$, $-4.2°$ and $12.4°$)

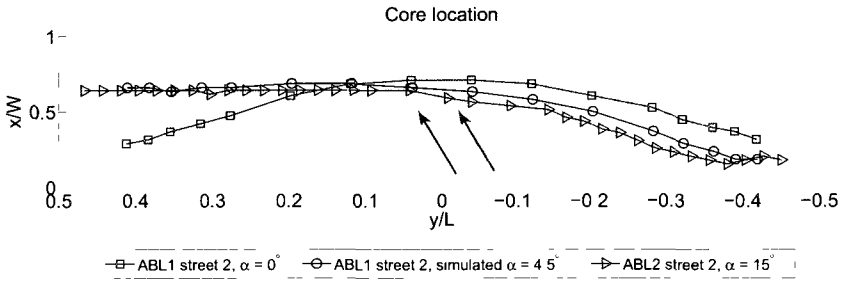

(b) $\alpha = 0°$, $4.5°$ and $15°$ ($\alpha_e = 1°$, $-4.2°$ and $12.4°$)

Figure 6.2. Streamwise location of the core of the arch vortex as a function of spanwise direction in street 2 for three incidence angles.

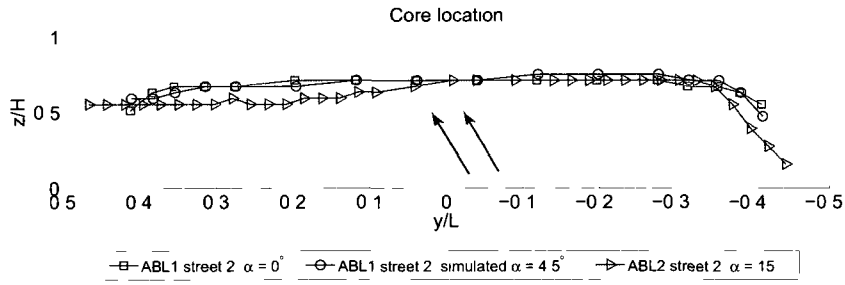

Figure 6.3. Wall-normal location of the core of the arch vortex as a function of spanwise direction in street 2 for three incidence angles.

vortex in the street and the results are shown in Figure 6.3. Again, the $-4.5°$ results have been symmetrically shifted about mid-span to "simulate" a 4.5° incidence angle so as to compare with the 15° incidence angle more easily. The wall-normal position of the core of the arch vortex does not seem to be very affected by the incidence angle once the channeling effect occurs. There is a difference in wall-normal position between the two non-zero incidence angles under investigation. The larger incidence angle displays a lower arch vortex position in the street along the wall-normal direction which could also be due to the different ABL considered in this case.

As mentioned earlier in Chapter 3, a shift of one of the legs of the arch vortex was clearly observed for non-zero incidence angles. For the $-4.5°$, one leg moved closer to the intersection while for the 15°, this shift was amplified such that one leg left our field of view. We have seen that this shifting phenomenon was different from the one observed in Becker et al. (2002) for a single obstacle, where they proposed a shift of the leg on the top of the single obstacle as the incidence angle was increased. However, Kim and Baik (2004) performed a three-dimensional numerical simulation

of a flow around a regular array of cubes. In this investigation, they varied the incidence angle of the ambient wind and also found a significant shift in the position of one leg of the arch vortex for an incidence angle of 15°. Their simulation covered a domain large enough that they could determine that the shifted leg was actually moving upwind in the intersection. Even though our data do not provide information about the location of the shifted leg, the significant shift observed by Kim and Baik (2004) is much more consistent with our results than the results by Becker et al. (2002).

From the temporal estimation of the reduced-order representation of the velocity field discussed in Chapter 5, we can determine features associated with the temporal evolution of the arch vortex in the array. In terms of contaminant dispersion, we are most interested in determining the spatial scales associated with the unsteadiness of the arch vortex. Recall that from the temporal estimation we were able to obtain a time series of 406 snapshots of the velocity field in the entire street at a 15 Hz temporal resolution. In order to locate the arch vortex in time, we can calculate the NAM at each instant and find its core location as a function of time. Figure 6.4 presents the streamwise and wall-normal coordinates of the core of the arch vortex as a function of its spanwise coordinate. The black line corresponds to the core location as determined from the mean flow field as discussed in Section 6.2. The gray envelopes correspond to the spatial range occupied 90% of the time by the arch vortex core over the duration of the temporal estimation. Using Figure 6.4, it can be seen that both for the streamwise and wall-normal position of the arch vortex core, the spatial range is about 20% of the street width and height giving a measure of the spatial unsteadiness of the arch vortex in our urban environment.

6.2.2 Street-to-street evolution of the arch vortex. We will now present a street-to-street evolution of the arch vortex location as a function of ABL2 and ABL3

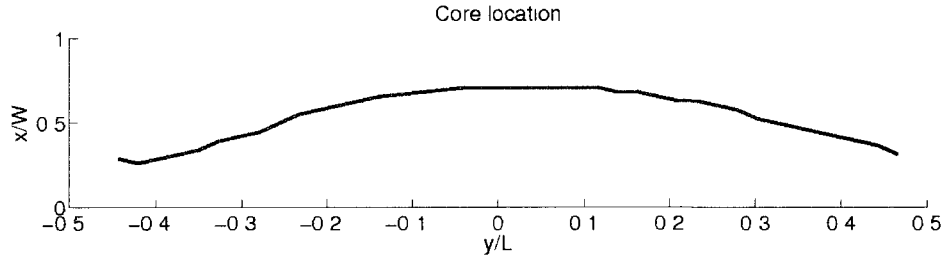

(a) Streamwise location

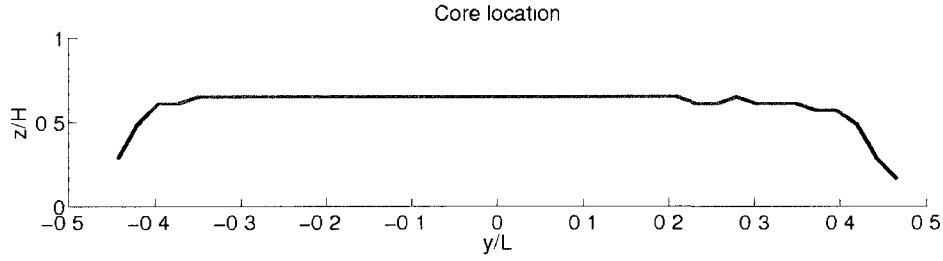

(b) Wall-normal location

Figure 6.4. Core location of the arch vortex along the spanwise direction in street 2, 90% of the realizations are within the gray envelope.

for a nominal 0° incidence angle. We present in Figure 6.5 the streamwise location of the core of the arch vortex as a function of its spanwise location both for ABL2 and ABL3 in each street so that a direct comparison between ABL2 and ABL3 can be made. For a given street, the core location for ABL2 is very similar as compared with ABL3. For example, in street 3, the maximum difference in streamwise position of the arch vortex between ABL2 and ABL3 is 1 mm, which is equal to the streamwise spatial resolution of the SPIV data. Therefore, it is found that the effect of the two mean free stream speeds with different power-law exponents associated with ABL2 and ABL3 on the location of the arch vortex is minimal.

Looking at a single ABL, for example ABL2, we find that the arch vortices in streets 1 and 2 are located at roughly the same streamwise location and are approximately within 2 mm of each other. However, for street 3, we observe that the core is located about 6 mm farther downstream in the central region as compared with streets 1 and 2. This result could be due to a couple of reasons: first, the arch vortex could become more curved as the flow evolves from street to street, and secondly, it could be due to a growing asymmetry in the flow field. As seen from the previous study of the incidence angle effect, the flow field is very sensitive to asymmetries. The arch vortex in street 1 is nearly symmetric, but starting from street 2, the asymmetry grows. This is in agreement with the measure of the effective incidence angle going from $\alpha_e = 0.2°$ to $\alpha_e = 0.5°$ from upstream of the array to streets 1 and 2 given in Table 6.1. We propose that a small asymmetry is generated in the flow field in street 1 due to the small effective incidence angle ($\alpha_e = 0.2°$) found directly upstream. The asymmetry in street 1 will then condition the flow field in street 2 and we expect the asymmetry to grow as the flow evolves from street to street through a cascade effect until a sufficiently large effective angle is reached at which the channeling effect takes place. In Figure 6.5, it can be observed near the intersection at $y/L = 0.4$ that as the flow evolves from street to street, the streamwise location of the arch vortex

is consistently decreasing. This observation is consistent with the transition from a nearly 0° to a −4.5° incidence angle presented earlier in Figure 6.2.

Similarly, Figure 6.6 presents the wall-normal location of the core of the arch vortex as a function of its spanwise location both for ABL2 and ABL3 in each street. As expected from the streamwise representation of the arch vortex, the agreement between ABL2 and ABL3 is again clear in terms of the wall-normal core position. No major change in core location for a given street is observed when comparing ABL2 with ABL3. Focusing now on a single ABL, it can be seen that the wall-normal location of the arch vortex drops from street 1 to 2 and the differences observed between streets 2 and 3 are less. In addition, the asymmetry observed in the streamwise position in Figure 6.5 is also seen in the wall-normal position of the core in street 3.

We consider now the effect of the 15° incidence angle on the flow field associated with ABL2 in each street. Figure 6.7 presents the streamwise position of the arch vortex core as a function of its spanwise position. In street 1, the arch vortex is clearly seen to have a quasi linear distribution, roughly following the diagonal of the street. A transition is observed as the flow moves to street 2. Near $y/L = -0.5$, the core location is similar to that in street 1, but moves downstream more quickly with increasing span until reaching a plateau at roughly mid-span. The same behavior is observed in street 3 with an even steeper increase in the $-0.5 < y/L < -0.1$ region.

Figure 6.8 presents the wall-normal position of the arch vortex as a function of its spanwise position for the same ABL2 data set at 15°. Similarly to its 0° incidence angle counterpart (Fig. 6.6), the arch vortex is located higher in street 1 as compared to the other streets. In the region $-0.5 < y/L < -0.2$, all three streets present a very similar arch vortex core position, but as we move closer to mid-span, differences appear between street 1 and the other streets. Both for streets 2 and 3, the arch vortex core is found lower in the canopy of the street until it plateaus at a

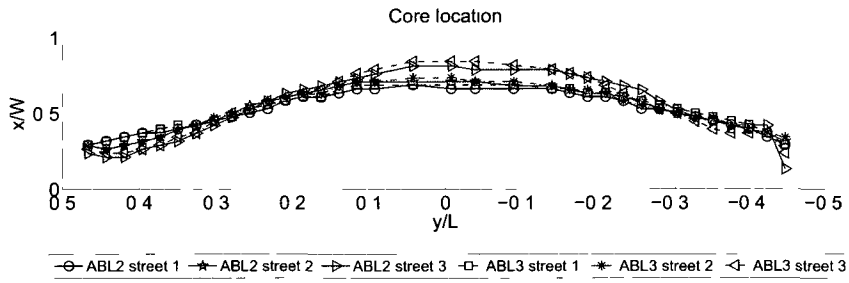

Figure 6.5. Streamwise location of the core of the arch vortex as a function of spanwise direction for each street at $\alpha = 0°$.

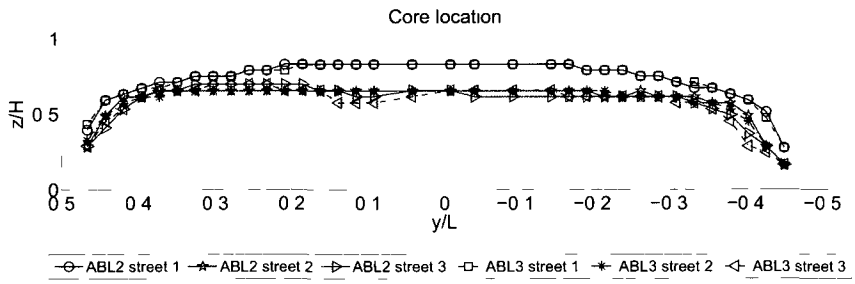

Figure 6.6. Wall-normal location of the core of the arch vortex as a function of spanwise direction for each street at $\alpha = 0°$.

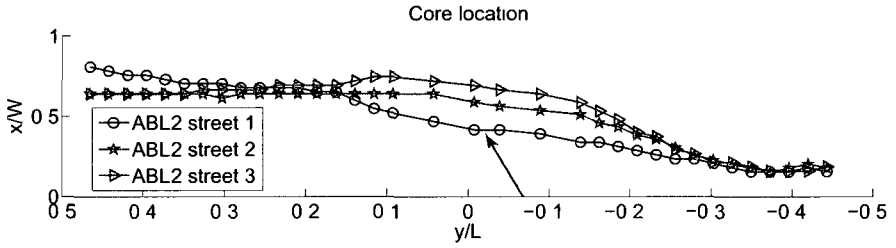

Figure 6.7. Streamwise location of the core of the arch vortex as a function of spanwise direction for each street at $\alpha = 15°$.

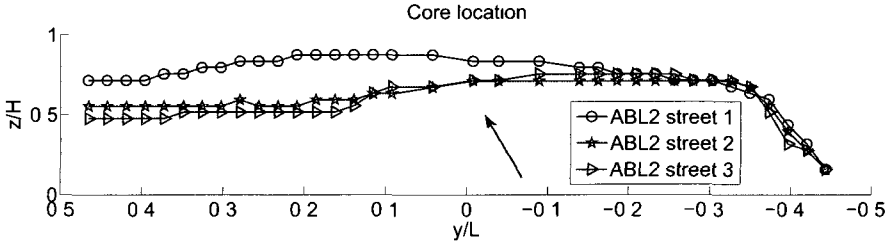

Figure 6.8. Wall-normal location of the core of the arch vortex as a function of spanwise direction for each street at $\alpha = 15°$.

wall-normal position of $z/H \approx 0.5$ for spanwise locations $y/L > 0.1$.

The transition of the flow as it moves from street 1 to 2 is observed in both the streamwise and wall-normal positions of the arch vortex for a non-zero incidence angle as opposed to only in the wall-normal position for a zero-incidence angle. Between streets 2 and 3, only small differences in the streamwise and wall-normal positions of the arch vortex core, are observed indicating that the flow is not changing significantly in terms of structures. This seemed to be independent of incidence angles for $0° < \alpha < 15°$.

In summary, the incidence angle effect was found to be very similar for $-4.5°$ and $15°$, suggesting that the channeling effect occurs at very small incidence angles. The unsteadiness of the arch vortex was characterized by looking at the spatial range occupied by the arch vortex core using the temporal estimation of the flow field obtained in Chapter 5. The street-to-street evolution of the flow structures, namely the arch vortices, highlighted a convergence towards equilibrium after the strong transition observed in the beginning of the array, which is consistent with other investigations, suggesting that the flow reaches an equilibrium state fairly quickly in urban environments.

6.3 Ventilation and channeling

A quantity of interest to modelers and environmentalists is the air exchange rate at the street level, which provides a measure of the ventilation of the street, (e.g. X. Xie et al., 2006) and, therefore, a measure of the channeling effect. This type of information can be very valuable in numerical models and provides more insight on the dominant effects on the street ventilation. Since we have 3D data available, it is possible to compute this quantity for the various data sets.

Figure 6.9 presents a sketch of the slices used to delineate the boundaries of

each street. Similarly to the study in Section 6.2, we first focus on a single street (street 2) and then extend our analysis to the street-to-street evolution.

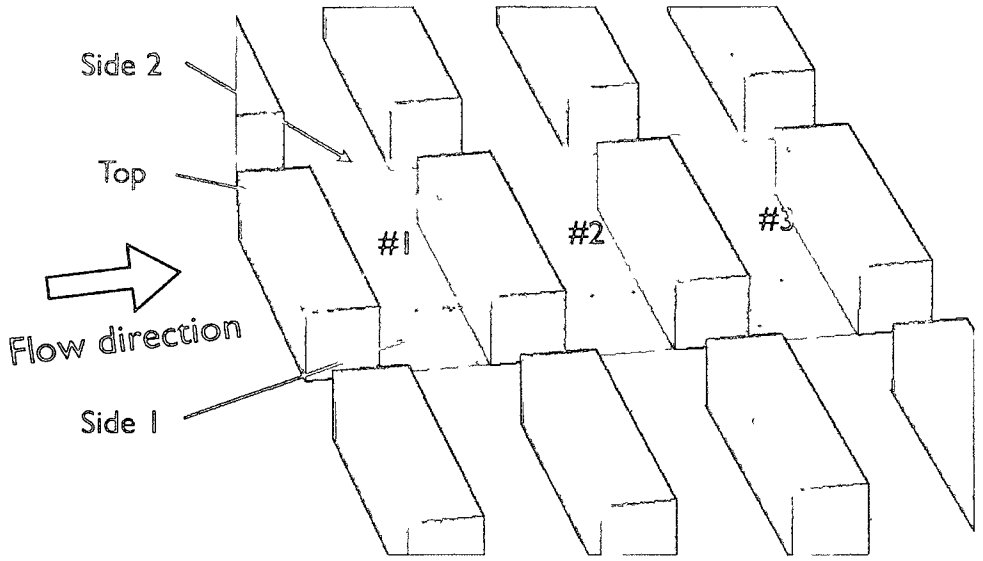

Figure 6.9. Schematic of the spatial domain used for computing the ventilation ratio.

The ventilation ratio, VR, is used to estimate the ratio of the flow that is entering and exiting the streets through the domain boundaries (side 1, side 2 and top) and is computed by integrating the velocity field over these sides. In order to isolate the flow entering or exiting the street through each side, we decompose the velocity field into its positive and negative components. Therefore, the VR associated with the flow entering a street through side 1 is the integral of the positive component of velocity in the spanwise direction, denoted V_+, over side 1.

$$\mathrm{VR}_{in} = \int_{\text{side 1}} V_+ dA \tag{6.1}$$

And, VR associated with the flow exiting the street through side 1 is the integral of the negative component of velocity in the spanwise direction, denoted V_-, over side 1. The same decomposition is applied to side 2 and the top.

The ventilation ratios presented in Tables 6.2 and 6.3 are all normalized so as

to represent a percentage of the total flow entering or exiting the street through each side. Therefore, the sum of VR_{in} over the three sides is 100%. VR_{out} is normalized in the same manner. Finally, we also present the total ventilation ratio, i.e. the sum of the ventilation ratios of the flow entering and exiting each side, in order to quantify the dominant effects of ventilation of the street. For example, the total VR through side 1 is defined as:

$$\mathrm{VR}_{tot_{\mathrm{side\ 1}}} = \mathrm{VR}_{in_{\mathrm{side\ 1}}} + \mathrm{VR}_{out_{\mathrm{side\ 1}}}, \tag{6.2}$$

and is normalized by $\mathrm{VR}_{tot_{\mathrm{side\ 1}}} + \mathrm{VR}_{tot_{\mathrm{side\ 2}}} + \mathrm{VR}_{tot_{\mathrm{top}}}$.

6.3.1 Ventilation ratios in street 2 for a nominal incidence angle of $\alpha = 0°$.

Table 6.2 presents a comparison of the ventilation ratios in street 2 for data sets ABL1, ABL2, and ABL3, in the case of a nominal incidence angle of $\alpha = 0°$. The effective incidence angle, α_e, is also presented so as to highlight its effect on the VR. As observed in Section 6.1, α_e indicated that the flow field was slightly off its nominal incidence angle. Therefore, we expect to see asymmetries between the flow entering and exiting the street from sides 1 and 2 for the nominal incidence angle of $\alpha = 0°$.

For a fixed streamwise spacing of $W/H = 1.5$, corresponding to cases 1, 3 and 4 in Table 6.2, it can be seen that there are strong similarities between all three ABLs. All three cases show that approximately 55% to 60% of the flow entering the street is doing so via the top while approximately 90% of the flow is exiting also through the top. This is another indication of the importance of the arch vortex with respect to contaminant transport. The flow exiting through the top is directly driven by the arch vortex described in Chapter 3 and in Section 6.2.

For a perfectly symmetric urban array and approach flow conditions, the VR would be identical for sides 1 and 2. As discussed earlier in this chapter, there are slight asymmetries in our urban array and/or the approach flow boundary layer; hence, we do expect to see differences in the values when comparing the VR of side

1 with that for side 2. The lowest effective incidence angle, α_e, for the four cases presented in Table 6.2 is for Case 4. For this case, the difference in the VR between side 1 and 2 is quite small. As the effective incidence angle increases to 0.5° for case 3 and 1.2° for case 2, the difference in the VR between sides 1 and 2 increases.

A comparison of cases 1 and 2 provides information on the streamwise spacing effect on the street ventilation. Case 2 is for the $W/H = 4$ configuration. It is interesting to see that the ventilation ratio for the flow entering this wider street from both sides and the top is fairly close to that for $W/H = 1.5$ (case 1). However, the ventilation ratios for the flow exiting the wider street are significantly different as compared to $W/H = 1.5$. The increase in the flow exiting the wider street through sides 1 and 2 can directly be related to the larger dimensions of the street and also to the secondary recirculation region sitting just upstream of the downstream block (see Fig. 3.27) which was observed to flush fluid from the street along spanwise helicoidal paths.

6.3.2 Ventilation ratios in street 2 for a non-zero nominal incidence angle α.

Table 6.3 shows the effect of a non-zero nominal incidence angle, α, on the ventilation ratio. For convenience, we present again in this table the ABL1 case at a nominal incidence angle of 0° for $W/H = 1.5$. Recall that for this case, we determined that an effective incidence angle of 1.2° generated a difference in the ventilation ratios for the flow entering the street through side 1 as compared to side 2 of 6%. Now considering case 5 with an effective incidence angle of $\alpha_e = -4.2°$, the difference in ventilation ratios for the flow entering the street through side 1 as compared to side 2 has jumped to 42%. Therefore, a very small incidence angle of merely a few degrees can generate a very large channeling effect. This channeling effect happens clearly for angles as low as about 4° and is therefore almost always present in a real urban setting. Increasing the incidence angle to $\alpha_e = 12.6°$, see case 7, reinforces the channeling, with half of

Table 6.2. Ventilation ratios in street 2 for nominal incidence angle $\alpha = 0°$.

Case	ABL #	W/H	α	α_e	VR_{side}	VR_{in} (%)	VR_{out} (%)	VR_{tot} (%)
1	ABL1	1.5	0°	1.2°	side 1	24	2	12
					side 2	18	4	10
					top	58	94	78
2	ABL1	4	0°	0.7°	side 1	23	17	20
					side 2	16	15	15
					top	61	68	65
3	ABL2	1.5	0°	0.5°	side 1	19	6	11
					side 2	24	6	13
					top	57	88	76
4	ABL3	1.5	0°	0.1°	side 1	23	4	11
					side 2	24	7	13
					top	53	89	76

the flow entering through one side and the other half through the top of the street for an $\alpha_e = -3.4°$. In terms of the exit flow, we observed that for $\alpha \approx 0°$, about 90% of the flow exited the street through the top. For these non-zeros incidence angles, we see that as α increases, the ventilation ratio out of the streets shifts more and more from the top to one side.

We have discussed in Chapter 3 that the wake interference regime ($W/H = 4$) was even more sensitive to variations in incidence angle of the incoming flow. Case 6 shows this very clearly, even though the effective incidence angle is only $\alpha_e = -3.4°$. The ventilation ratios are already reaching comparable levels to those obtained at the 12.6° effective incidence angle depicted in case 7 for the skimming flow regime ($W/H = 1.5$). Indeed, about half of the flow entering street 2 is entering through one side, the other half entering through the top of the street.

6.3.3 Street-to-street evolution of the ventilation ratios. In this section, we investigate the ventilation of the streets as the flow is evolving from street to street in the urban array. We present data for ABL2 at incidence angles of $\alpha = 0°$ and $\alpha = 15°$. Figure 6.10 presents the evolution of the ventilation ratios (VR_{in}, VR_{out} and VR_{tot}) as a function of the street number for the ABL2 data set at an incidence angle of $\alpha = 0°$. From Figure 6.10(a), it can be seen that the majority of the flow entering the streets is through the top. The asymmetry in the ventilation ratios for the flow entering through sides 1 and 2 is increased as the flow is evolving from street to street. This supports the cascade effect described in Section 6.2. Most of the flow exiting the streets is also through the top for all streets and is shown in Figure 6.10(b). This ventilation ratio is not significantly affected by the growing asymmetry of the flow field as sides 1 and 2 show very similar values.

Figure 6.11 presents the ventilation ratios for ABL2 at an incidence angle of $\alpha = 15°$. As observed previously for street 2, it can be seen in Figure 6.11(a) that

Table 6.3. Ventilation ratios in street 2 for non-zero nominal incidence angles.

Case	ABL #	W/H	α	α_s	VR_{side}	VR_{in} (%)	VR_{out} (%)	VR_{tot} (%)
1	ABL1	1.5	0°	1.2°	side 1	24	2	12
					side 2	18	4	10
					top	58	94	78
5	ABL1	1.5	−4.5°	−4.2°	side 1	1	20	10
					side 2	43	3	23
					top	56	77	67
6	ABL1	4	−4.5°	−3.4°	side 1	0.5	50	25
					side 2	50	0.5	25
					top	49.5	49.5	50
7	ABL2	1.5	15°	12.6°	side 1	51	0.5	24
					side 2	0	36	19
					top	49	63.5	57

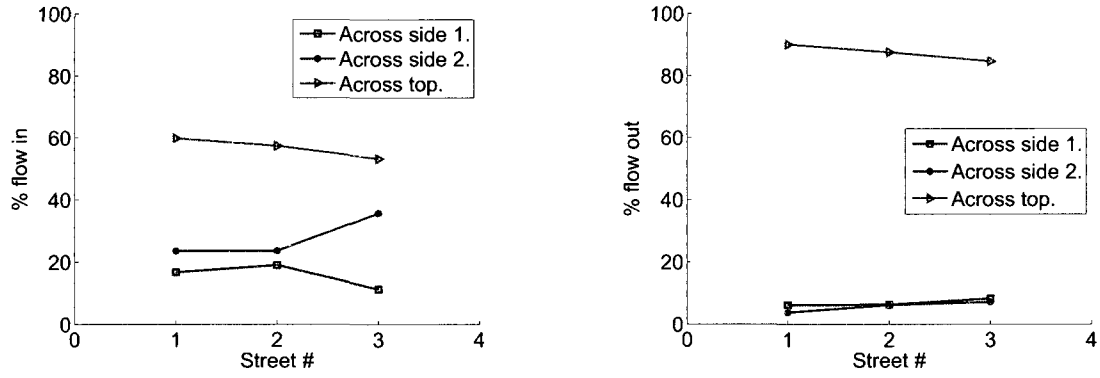

(a) VR_{in} (b) VR_{out}

Figure 6.10. Ventilation ratios for ABL2 for an effective incidence angle $\alpha_e = 0.2°$.

almost no flow is entering any street through side 2. Most of the flow is entering through side 1 and the top, with comparable levels in streets 1 and 2. In street 3, there is more flow entering through side 1 than through the top which could be related to a change in the effective incidence angle with increasing street #.

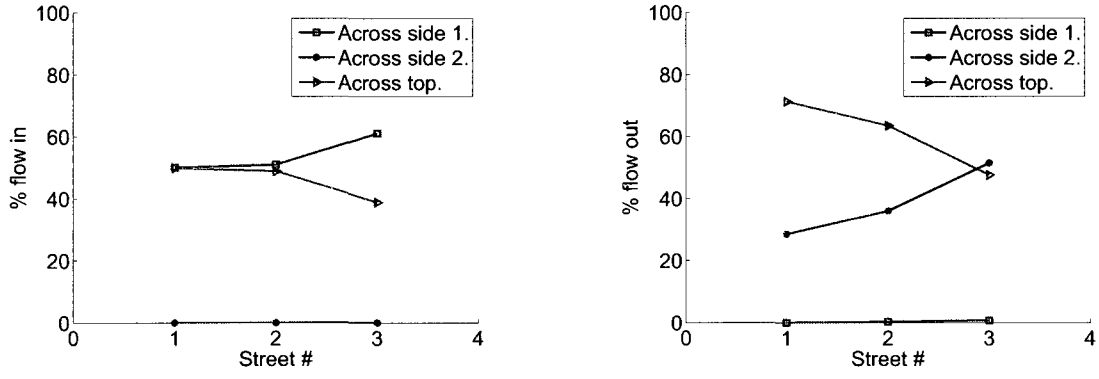

(a) VR_{in} (b) VR_{out}

Figure 6.11. Ventilation ratios for ABL2 for an effective incidence angle of $\alpha_e = 15.1°$.

In Figure 6.11(b) presenting the ventilation ratios for the flow out of the streets, we observe that almost no flow is exiting through side 1, the ventilation ratio associated with the flow exiting through side 2 is continuously increasing as the flow moves

from street to street, and, therefore, the ventilation out of the street through the top diminishes. This is very important in terms of contaminant transport. Knowing how much of a contaminant released in a street will be carried out via the intersections or over the street can be very useful in predicting the total spread of the contaminant plume at the urban scale.

The shear layer formed off the top surface of the blocks, driving the arch vortex, is responsible for the main portion of the ventilation which is true for all incidence angles studied. However, as the incidence angle is increased, the channeling of the flow plays an ever increasing role as the ventilation through the sides increases.

6.4 Convergence towards an equilibrium

Many have looked into characterizing the minimum distance, L_C, necessary for the flow to reach an equilibrium state in the urban environment (e.g. Belcher & Coceal, 2001; MacDonald et al., 2002; Bentham & Britter, 2003; Belcher, Jerram, & Hunt, 2003). Also, this length scale is important as it can be used for scaling both vertical and streamwise velocities in the canopy (Belcher, 2005). The approaching flow, for example from a rural environment, is affected by the larger roughness associated with an urban environment. It is decelerated by the obstacles and interacts with the streets by exchanging momentum with the canopy. After traveling a certain distance over the urban environment, a new equilibrium may be reached where the roughness associated with the urban environment characterizes the mean wind profiles. Belcher and Coceal (2001) describe the transition to this new equilibrium state as having three regions: an impact region, an adjustment region and a roughness change region. The impact region is just upstream of the urban environment, where the incoming flow impinges onto the first row of buildings. The adjustment region is where the transition from low roughness flow to higher roughness flow occurs. In the roughness change region, a new equilibrium state is finally reached. Bentham

and Britter (2003) have proposed a model to estimate the characteristic length, L_C, needed to reach this new equilibrium state. This model is based on the dynamical effects of the canopy by considering the equation for the spatially averaged momentum. A simplified variation of this model is found in Belcher (2005) and is used here to estimate the characteristic length, L_C, for our urban environment:

$$L_C \approx \frac{H(1-\lambda_p)}{\lambda_f}, \tag{6.3}$$

where H is the mean height of the obstacles, λ_p and λ_f are shape parameters defined in Britter and Hanna (2003) which characterize the aspect ratio of the urban environment. For an urban environment covering a total area, A_t, with N buildings of the same dimensions with a frontal area, A_f, and a plan area, A_p, λ_p and λ_f can be estimated by:

$$\lambda_p = \frac{NA_p}{A_t}, \tag{6.4}$$

$$\lambda_f = \frac{NA_f}{A_t}. \tag{6.5}$$

Using the dimensions of our urban environment for the $W/H = 1.5$ configuration, we obtain $\lambda_p = \lambda_f \approx 0.29$, which is typical of the skimming flow regime (MacDonald et al., 2002). For the $W/H = 4$ case, we find $\lambda_p = \lambda_f \approx 0.14$, which is again typical of the wake interference regime. These values of λ_p and λ_f yield an $L_C = 2.5H$ for our $W/H = 1.5$ case and an $L_C = 6H$ for the $W/H = 4$ case. These characteristic lengths appear to be relatively short and would suggest that the incoming wind profile is near equilibrium by the time it reaches street 2. However, Belcher et al. (2003) and Coceal and Belcher (2004) show that the adjustment of a rural boundary layer to an urban canopy occurs over a distance of 3 L_C. We can conclude from these considerations that the flow field studied in this thesis is at least very near an equilibrium state by street 3. We have already argued in Chapter 3 that this could be the case, where we discussed the evolution of flow structures from street to street

and observed similarities between streets 2 and 3. Bentham and Britter (2003) have also derived a characteristic velocity scale, U_C, from their model of the form:

$$U_C = \left(\frac{L_C}{H}\right)^{1/2} u_*, \tag{6.6}$$

where u_* is calculated as $u_* = \sqrt{\tau_*/\rho}$. Here, τ_* is the turbulent momentum flux in the inertial sublayer above the buildings. In order to estimate u_*, MacDonald et al. (2002) looked for a constant stress region in the wake layer of a flow over a regular array of cubes. We present in Figure 6.12 a comparison between a spatially averaged $-\overline{u'w'}$ profile from their study (including measurements in the wake of the cube as well as in the streamwise gaps between the cubes) and similar spatially averaged $-\overline{u'w'}$ profiles obtained from our SPIV measurements in streets 2 and 3 for ABL2 and ABL3. These profiles are normalized by the mean streamwise component of velocity measured upstream of the array at $z/H = 1$. MacDonald et al. (2002) could not find a constant stress layer in the $-\overline{u'w'}$ profile and therefore averaged $-\overline{u'w'}$ between $z/H = 1$ and $z/H = 2$ to obtain u_*. However, our $-\overline{u'w'}$ profiles obtained from the SPIV measurements exhibit a relatively constant stress region in the range $1 < z/H < 1.5$, shown in Figure 6.12. We therefore use these results to estimate u_* in our work. Table 6.4 summarizes the values obtained for the friction velocity u_* and also the characteristic velocity scale U_C defined above. From Table

Table 6.4. Velocity scales u_* and U_C.

ABL #	W/H	α	u_* in street 2	u_* in street 3	averaged U_C
ABL2	1.5	0°	0.14	0.13	0.22
ABL3	1.5	0°	0.19	0.17	0.30

6.4, it can be seen that u_* does not vary significantly from street 2 to 3, indicating again that the flow is near equilibrium.

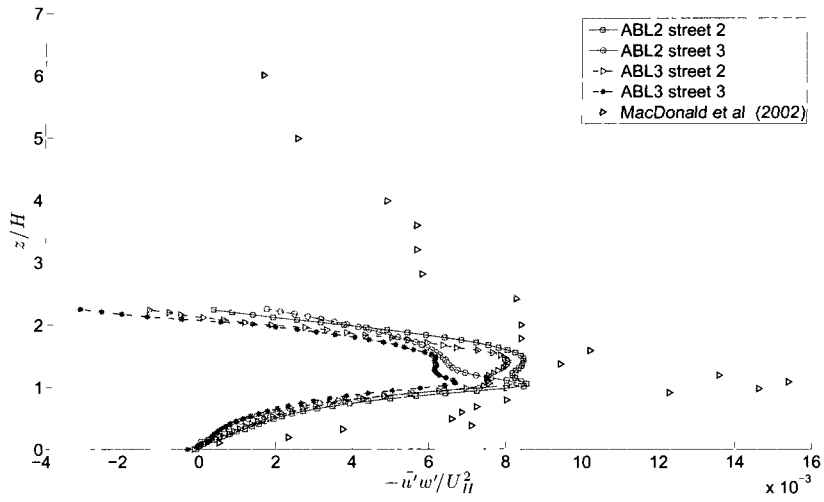

Figure 6.12. Reynolds shear stress $-\overline{u'w'}$ profiles normalized by U_H^2.

We will now compare Reynolds stresses obtained in this study with those obtained in the work done by Castro et al. (2006). In their work, they focused on the flow over a long fetch of staggered cubes. Their measurements are performed far enough in the roughness fetch that the equilibrium region is well established. They used a combination of hot-wire and LDA measurements to document the flow. The locations of their point measurements are shown in Figure 6.13 and were determined to adequately represent the turbulence characteristics over the entire equilibrium region. Clearly, the geometry studied in Castro et al. (2006) is very different from the one examined in this work as theirs is a staggered array of cubes and ours is a regular array of rectangular obstacles. However, measurements at location 1 may provide a meaningful comparison as the profiles are obtained in the middle of the wake of a cube. In order to make the comparison more relevant, we only compare our profiles of Reynolds stresses in street 3 of ABL2 to those of Castro et al. (2006), as we have assessed that this was our best "near equilibrium case." Similarly to Castro et al. (2006), we focus on a mid-span location in our street 3 and we extract our profiles in the center of the street.

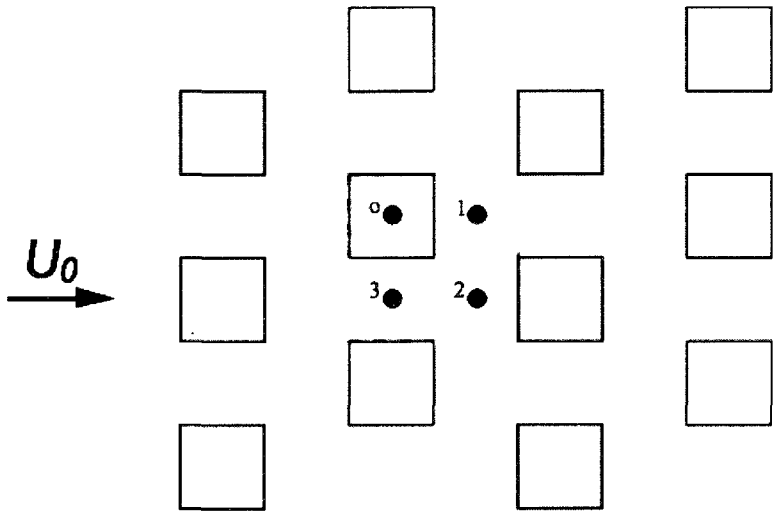

Figure 6.13. Spatial location of measurements performed by Castro et al. (2006).

In their work, they used U_0 as the velocity scale to normalize the turbulence statistics. In comparing our turbulence statistics using this velocity scale with their results, the differences in magnitudes for the various turbulence quantities were observed to be quite large. A better comparison was obtained when using a velocity scale based on the mean streamwise velocity at $z/H = 1$ where the turbulence profiles were obtained, U_{Hs}. As mentioned earlier in Section 3.2, scaling the turbulence in an urban environment is challenging and is not the focus of this study. However, U_H is providing a reasonable scaling for the turbulence within the wake layer and is used here. We present first a comparison for the $\overline{u'^2}$ component of the Reynolds stress tensor in Figure 6.14. A fairly good agreement is observed between the two experiments. Our measurements (shown in red) in the wake layer display a non-monotonic variation of $\overline{u'^2}$ with wall-normal location for $z/H > 1$. This could be due to the wakes of the upstream blocks from streets 1 and 2 and would be expected to be reduced for

full equilibrium state. The same phenomenon may also appear in Castro et al. (2006) to a lesser degree; however, the scatter in their results make this inconclusive.

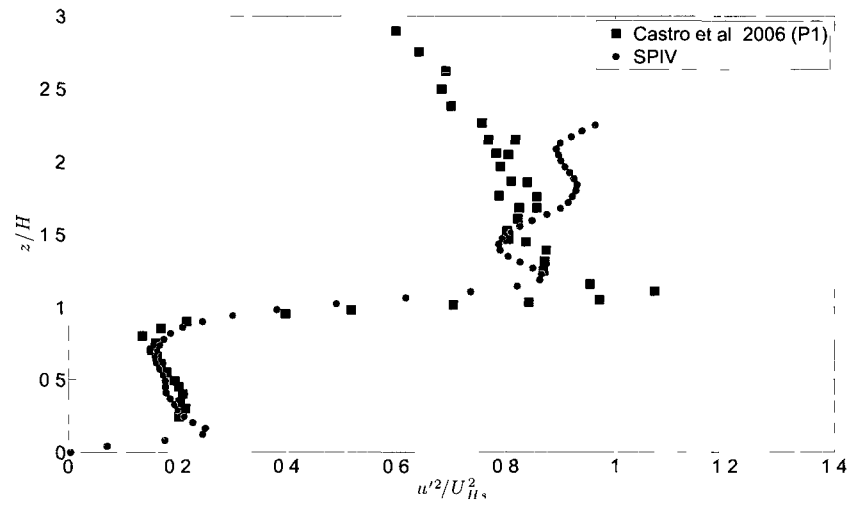

Figure 6.14. Reynolds stress $\overline{u'^2}$ profiles normalized by U_{Hs}^2.

Figure 6.15 presents the spanwise, $\overline{v'^2}$, component of the Reynolds stress tensor. A relatively similar shape between the two profiles is seen, which is somewhat surprising considering that the geometry of the two is quite different (staggered array of cubes versus regular array and different aspect ratios). The data of Castro et al. (2006) display a secondary peak of $\overline{v'^2}$ within the street with different magnitude and wall-normal position from our SPIV measurements. Plate (1995) described the challenges associated with parameterizing the urban canopy layer due to highly variable geometries, so the differences are expected. However, a general agreement in the shape of the profiles is an indication that a proper scaling may be found in future work.

The $\overline{w'^2}$ component of the Reynolds stress tensor is investigated in Figure 6.16. Large differences are observed and are likely due to the location of the measurements. As described in Figure 6.13, the measurement station of Castro et al. (2006) is located

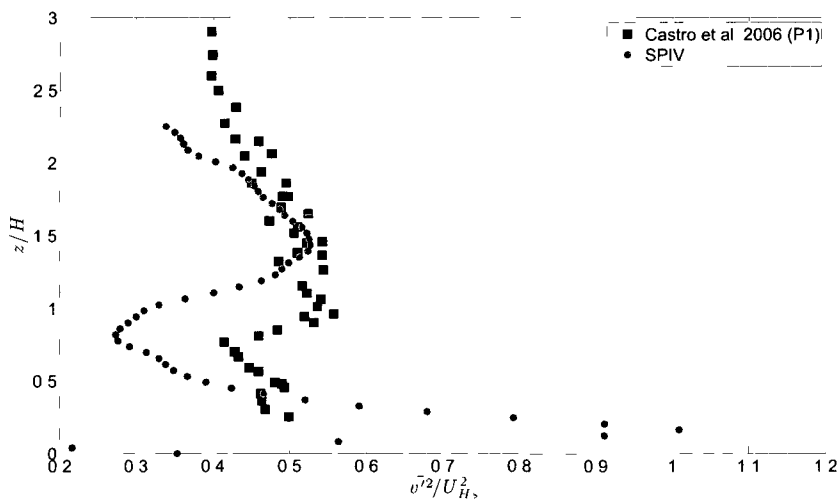

Figure 6.15. Reynolds stress $\overline{v'^2}$ profiles normalized by U_{Hs}^2.

near the leeward wall of the cube and the aspect ratio chosen in their study is $W/H = 3$. Our measurement station is taken at the center of street for a $W/H = 1.5$. Differences in the flow regime must be expected and the effect of these differences on the wall-normal component of the Reynolds stress tensor are most likely significant.

Finally, Figure 6.17 presents a comparison of the $-\overline{u'w'}$ component of the Reynolds stress tensor. Similarly to the $\overline{u'^2}$ component, we observe a good agreement in the overall shape, with difference in the magnitudes.

In Chapter 4, we observed a noticeable decay in the turbulent kinetic energy levels as the flow moved from street 1 to streets 2 and 3. In order to quantify this decay of TKE as the flow is moving from street to street, we calculate the spatial rms of TKE, $<$ TKE $>$, over the entire SPIV data available in each street so as to capture the turbulence found in the wake layer, the side shear layers and within the street. Table 6.5 summarizes the values found for the drop in $<$ TKE $>$ from street 1 to 2 normalized by $<$ TKE $>$ in street 1 and the drop in $<$ TKE $>$ from street 2 to 3 normalized by $<$ TKE $>$ in street 2. For both incidence angles under consideration in

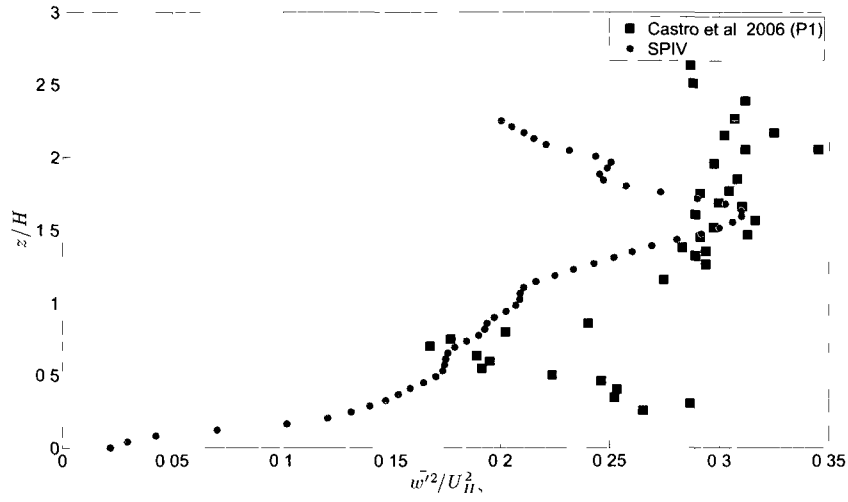

Figure 6.16. Reynolds stress $\overline{w'^2}$ profiles normalized by U_{Hs}^2.

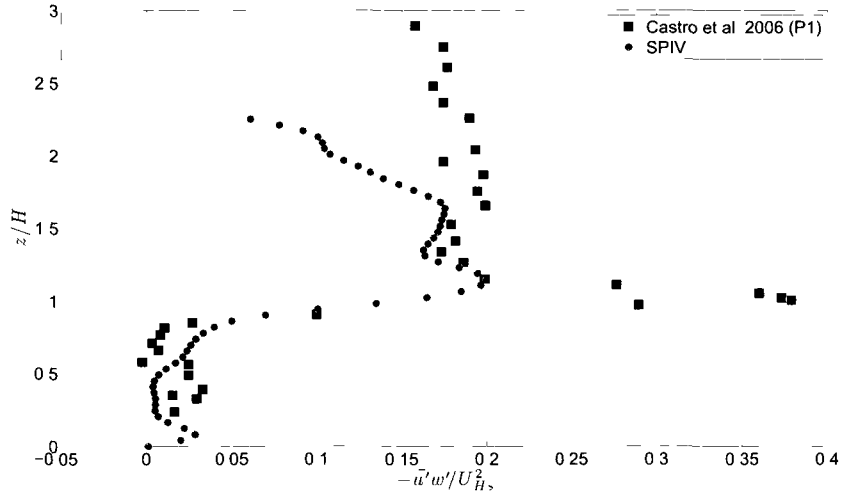

Figure 6.17. Reynolds stress $-\overline{u'w'}$ profiles normalized by U_{Hs}^2.

the ABL2 data set, the drop in TKE is found to be larger from street 1 to 2 ($\approx 25\%$) as compared with the drop in TKE from street 2 to 3 ($\approx 10\%$). This supports a convergence towards an equilibrium since the drop between streets 2 and 3 becomes smaller. However, for the ABL3 data set, we observe a larger drop from street 2 to 3 ($\approx 17\%$) as compared with the drop from street 1 to 2 ($\approx 12\%$) which indicates that a longer characteristic distance, L_C, might be required in that case to reach the equilibrium as compared with the ABL2 data. The simple model shown earlier for L_C does not take into account the incoming flow characteristics and therefore only provides an estimate of that characteristic length.

Table 6.5. Normalized drop in $<$ TKE $>$ from street to street.

ABL #	W/H	α	From street 1 to 2	From street 2 to 3
ABL2	1.5	0°	24%	11%
ABL2	1.5	−4.5°	23%	7%
ABL3	1.5	0°	12%	17%

6.5 Turbulence distribution and relation to the arch vortex

Recall that in Chapter 4 we discussed the regions of relatively large TKE production. The wake layer directly above the array is responsible for the largest production of turbulent kinetic energy with the shear layers near the intersections also contributing noticeably. The main component of this production was the $-\overline{u'w'}\left(\frac{\partial U}{\partial z}+\frac{\partial W}{\partial x}\right)$ term. Another region nearer to the ground within the street was also observed to have relatively large values of TKE production and those were found to be due to a combination of vertical and spanwise velocity fluctuations within the street

We are now interested in relating the arch vortex to the turbulence distribution

studied in Chapter 4. Figures 6.18 and 6.19 present a vertical slice of TKE_H across the array at mid-span for the ABL2 data set at a nominal incidence angle of $\alpha = 0°$ and 15°, respectively. The core location of the arch vortices as computed in Section 6.2 is superimposed on these figures (represented by red stars) to provide a more in-depth description of the main features of this flow field. From both Figures 6.18 and 6.19, we can see that the cores of the arch vortices are sitting in relatively low turbulence regions. These plots also provide more evidence that the flow is approaching an equilibrium state as the changes in TKE and vortex location are more similar when comparing street 3 with street 2 than when comparing street 2 with street 1. A

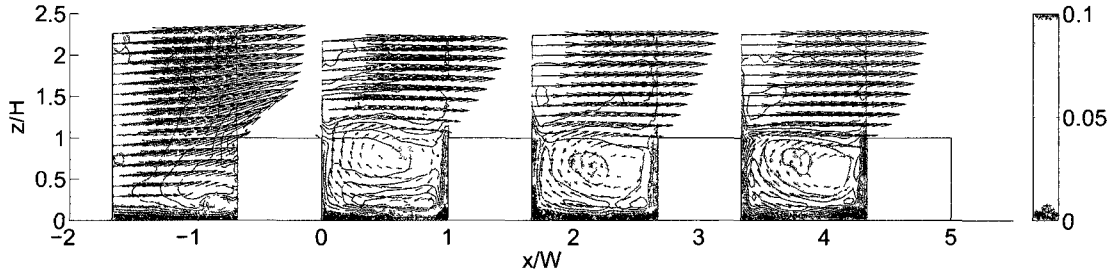

Figure 6.18. Vertical slice, S_y, of TKE_H at $y/L = 0$, for ABL2 at $\alpha = 0°$. The red stars represent the core of the arch vortices and the black arrows correspond to the mean velocity components U and W.

comparison with the work by Brown, Lawson, Decroix, and Lee (2000) can be made here. They investigated experimentally the mean flow and turbulence characteristics in a 2D array of buildings (ribs spanning the wind tunnel width). In their work[1], they present a vertical slice of TKE at mid-span upstream and in the first two streets of the 2D urban array. Strong similarities are observed in the velocity vector maps obtained by Brown et al. (2000) and those presented in Figure 6.18 and Figure 6.19. Namely, both experiments show that the recirculation region associated with the arch vortex

[1]http://library.lanl.gov/cgi-bin/getfile?00460036.pdf

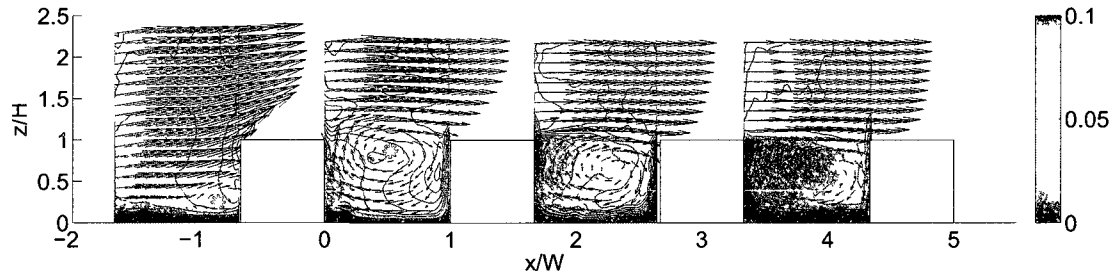

Figure 6.19. Vertical slice, S_y, of TKE_H at $y/L = 0$, for ABL2 at $\alpha = 15°$. The red stars represent the core of the arch vortices and the black arrows correspond to the mean velocity components U and W.

is located lower in the second street than in the first street. The flow separation occurring at the leading edge of the upstream block is clearly observed in the data of Brown et al. (2000) and no region of large spanwise fluctuations is observed which can be explained by the 2D configuration under investigation in Brown et al. (2000).

In addition, we present in Figure 6.20, a zoomed-in version of Figure 6.18 for street 1 and for street 3. In order to provide information about the size of the arch vortex, a velocity vector map for the U and W components is superimposed. The arch vortices are observed to be "trapped" between the wake layer and the region of relatively large TKE_H seen near the ground level within the street. The velocity vector map is in good agreement with other experimental studies (e.g. Martinuzzi & Havel, 2000) and also with field experiments (e.g. DePaul & Sheih, 1986; Eliasson et al., 2006, where mean velocities were found in a street by tracing the motion of balloons). Figure 6.21 presents the corresponding horizontal slice across street 1 at $z/H = 0.2$. Figure 6.21(a) displays the total TKE_H with the velocity vector map superimposed. The location of the legs of the arch vortex is also represented as red stars. Figure 6.21(b) presents the $\overline{v'^2}$ contribution to the TKE_H. Again, the arch vortex is defined by the core location of its legs and the velocity vector map now

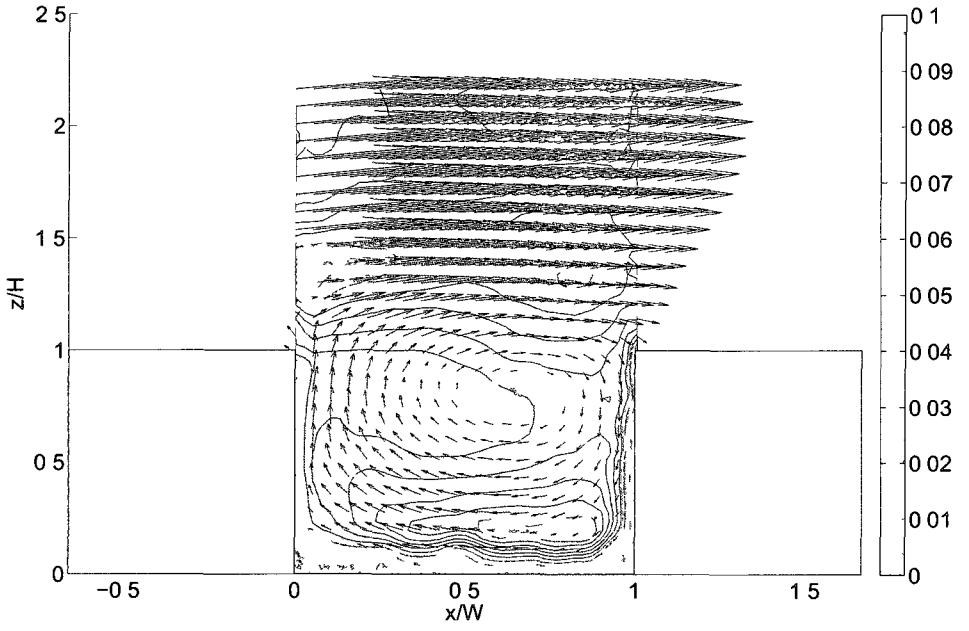

(a) Street 1

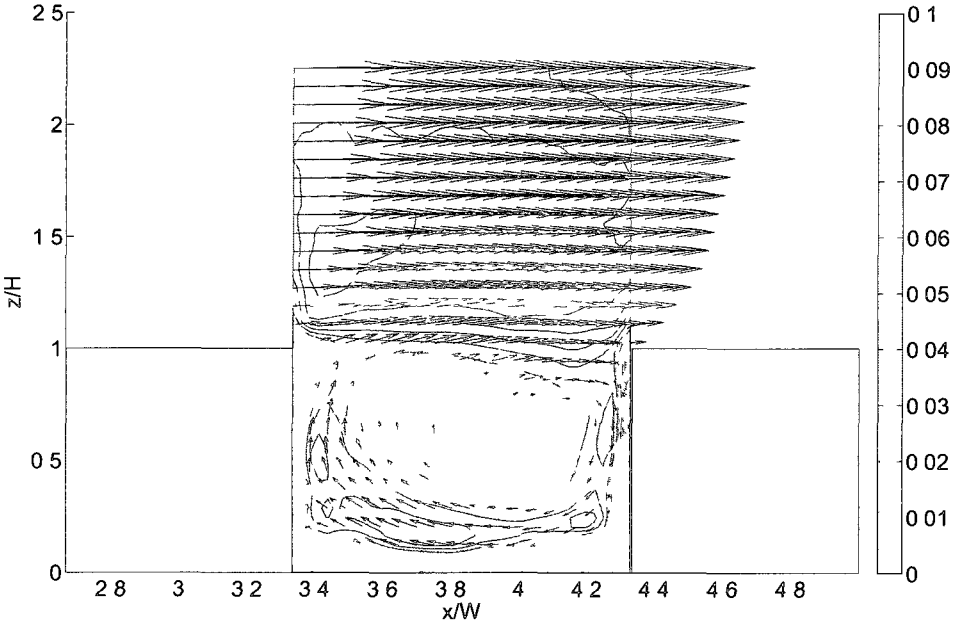

(b) Street 3

Figure 6 20 Vertical slice, S_y, of TKE_H at $y/L = 0$, for ABL2 at $\alpha = 0°$ The red stars represent the core of the arch vortices and the black arrows correspond to the mean velocity components U and W

provides the U and V components of the mean velocity field.

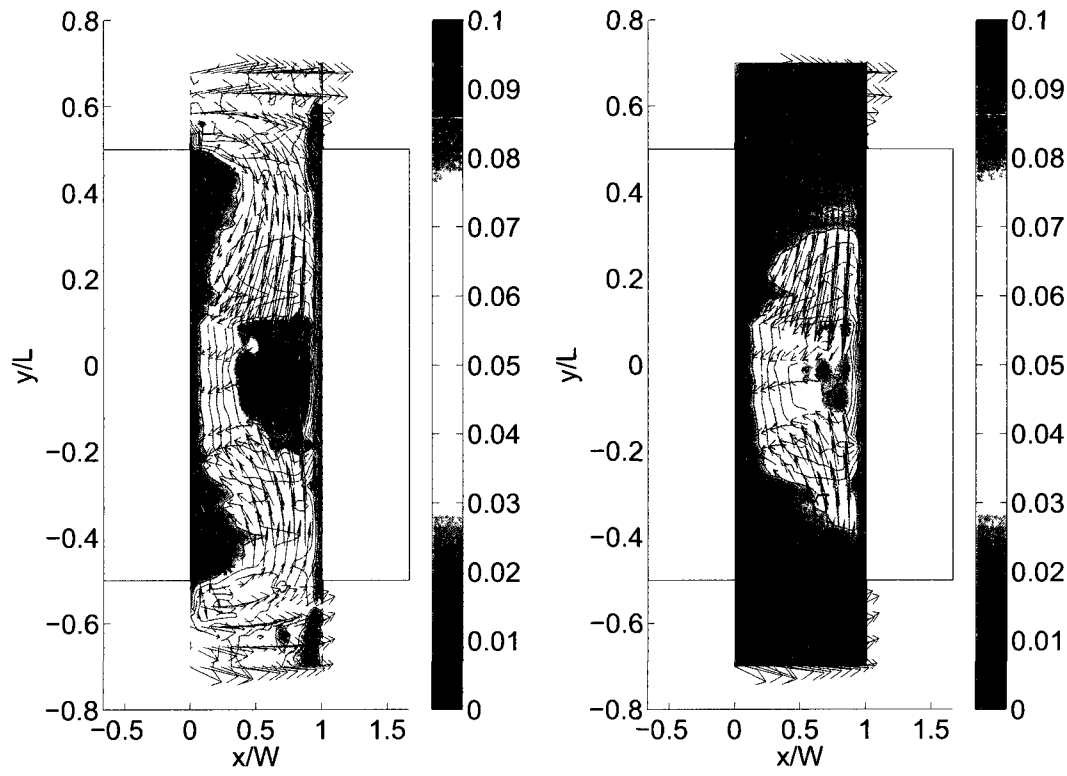

(a) TKE_H in street 1

(b) $\overline{v'^2}$ in street 1

Figure 6.21. Horizontal slice, S_z, at $z/H = 0.2$, for ABL2 at $\alpha = 0°$. The red stars represent the core of the arch vortex legs and the black arrows correspond to the mean velocity components U and V

For the sake of completeness, we also present in Figure 6.22, a zoomed-in version of Figure 6.19 in street 1 A vertical slice of TKE_H across street 1 at mid-span for the incidence angle of $\alpha = 15°$ for the ABL2 data set is shown. The location of the arch vortex core is represented by a red star and the velocity vector field is superimposed. It is observed that the arch vortex is again next to the region of relatively large TKE_H, this time near the windward wall. Finally, in Figure 6.23, we present a horizontal slice of TKE_H at $z/H = 0.5$ for this same incidence angle in the

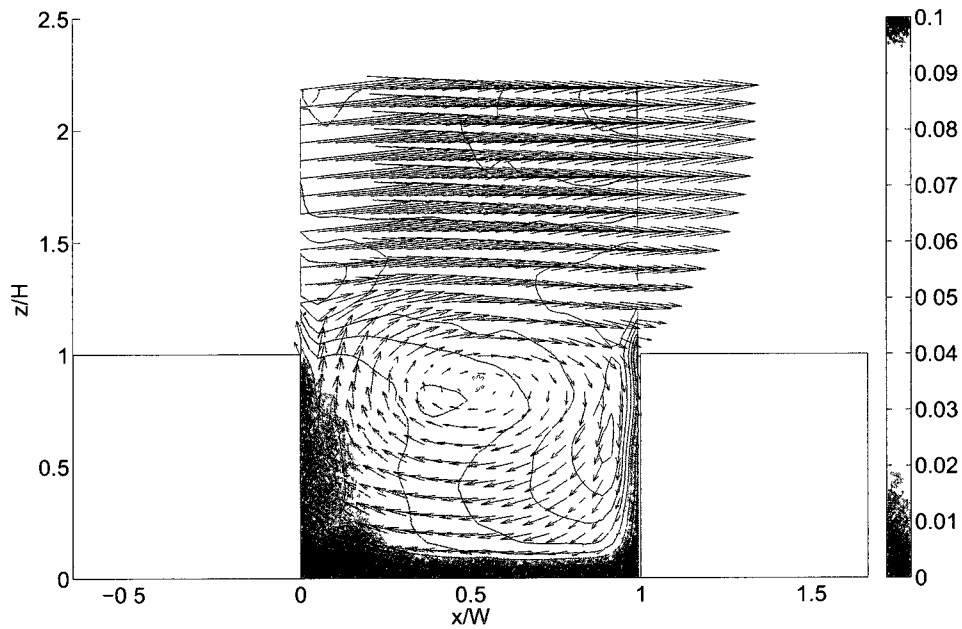

Figure 6.22. Vertical slice, S_y, of TKE_H at $y/L = 0$, for ABL2 at $\alpha = 15°$. The red star represents the core of the arch vortex and the black arrows correspond to the mean velocity components (U and W).

ABL2 data set. Note that this slice is taken at $z/H = 0.5$ so as to cross the region of large TKE_H seen in Figure 6.22. The red star denotes again the core of the arch vortex, here a single leg because of the channeling effect which is observed clearly from the velocity vector map.

Returning to one of our motivations for this work, namely that of contaminant transport, the driving parameters are the following: the arch vortex is the main factor in the direct transport of the contaminants from one region to another whereas the wake layer, the shear layers near the intersections, and the high turbulence region found within the street near the ground for $\alpha = 0°$ or next to the windward wall for higher incidence angles are responsible for the dispersion of contaminants. Both phenomena are therefore strongly coupled with respect to contaminant transport. The turbulence will affect the size of a contaminant plume while the arch vortex will carry it to other streets via channeling and ejection from the street.

The equation for the conservation of a passive scalar, here a contaminant is given by (Stull, 1988):

$$\frac{\partial C}{\partial t} + u_j \frac{\partial C}{\partial x_j} = \nu_C \frac{\partial^2 C}{\partial^2 x_j} + S_C, \tag{6.7}$$

where the first and second terms on the LHS are the temporal rate of change of the passive scalar C and the transport by both the mean and the fluctuating velocity components. Respectively, on the RHS, there is the molecular diffusion and a source term. Typically, in urban flows, the molecular diffusion term is small and if we only focus on the transport part by assuming that the release of contaminant was sudden, we see that the equation reduces to:

$$\frac{\partial C}{\partial t} + u_j \frac{\partial C}{\partial x_j} = 0. \tag{6.8}$$

By using the Reynolds decomposition, we can write $u_j = U_j + u'_j$ and then argue that the U_j term would be dominated by the arch vortex at the street scale, while the u_j

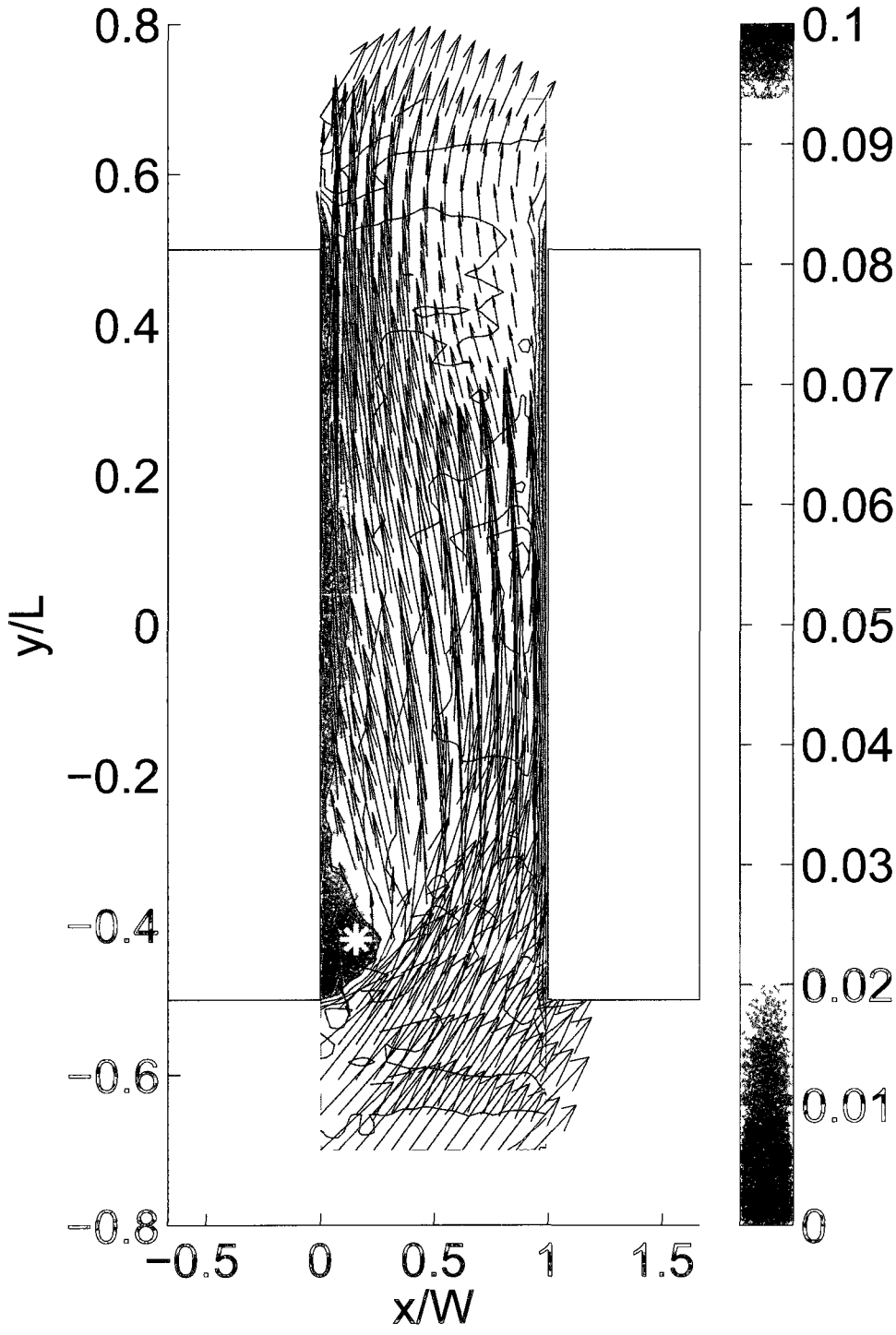

Figure 6.23. Horizontal slice, S_z, of TKE_H at $z/H = 0.5$, for ABL2 at $\alpha = 15°$. The red star represents the core of the arch vortex leg and the black arrows correspond to the mean velocity components U and V.

would be largest in the regions of large TKE. We can now see how the arch vortex will transport a contaminant, while the TKE will dominate with regard to mixing.

For example, in Figure 6.20(a), if a contaminant were to be released in the center of the street near the ground in the region of large TKE, which was shown to be primarily dominated due to spanwise fluctuations, the turbulence would mix it in the spanwise direction while the arch vortex would carry it to the leeward wall. A portion of the mixed contaminant would stay in the recirculation region while another would be released in the wake layer above the street.

A three-dimensional visualization of this mechanism is presented in Figure 6.24 for the ABL2 data set at a 0° incidence angle. An isocontour of NAM depicting the location of the arch vortex (light red), an isocontour of $\overline{u'^2}$ (light blue), and an isocontour of $\overline{v'^2}$ (light purple) are displayed. The $\overline{u'^2}$ and $\overline{v'^2}$ isocontours can be seen wrapping around the arch vortex as expected from the slices presented earlier. Figure 6.24 emphasizes the distinct regions of influence of the $\overline{u'^2}$ and $\overline{v'^2}$ components of the TKE. The $\overline{u'^2}$ component is observed to be in the vicinity of the head of the arch vortex, in the wake layer, and also in the side shear layers in the vicinity of the arch vortex legs. The $\overline{v'^2}$ component is seen to occupy a large portion of the street centered about mid-span and interacting with the legs and the lower part of the arch vortex.

In Figure 6.25, we present another combination of isocontours for the ABL2 data set at a 15° incidence angle. An isocontour of NAM (light red), an isocontour of $\overline{u'^2}$ (light blue) and an isocontour of the sum of the $\overline{v'^2}$ and $\overline{w'^2}$ components of the TKE (light purple) are displayed. The $\overline{v'^2}$ component of the isocontour shown in light purple accounts for about twice the contribution of the $\overline{w'^2}$ component. This $\overline{w'^2}$ term is included as it is not negligible any longer for a non-zero incidence angle. The general picture provided by Figure 6.25 for a 15° incidence angle presents similarities with the 0° incidence angle shown in Figure 6.24 in the wake layer. The streamwise

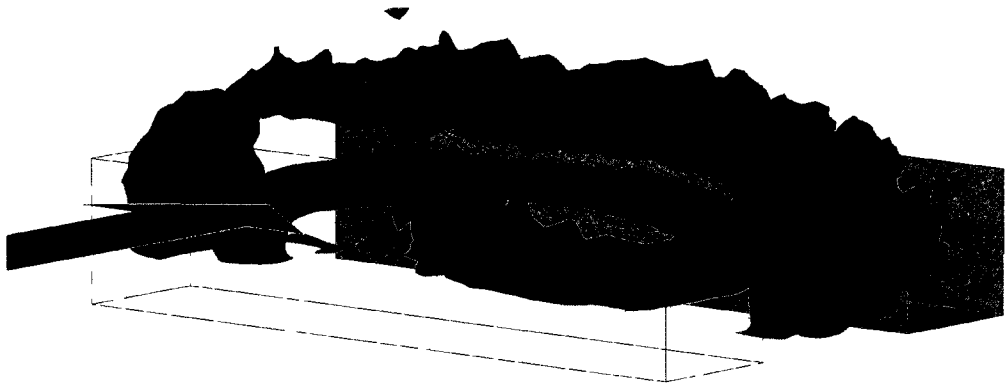

Figure 6.24. Isocontours of NAM (in light red, $f = 0.45$), $\overline{u'^2}$ (in light blue, $= 0.04$) and $\overline{v'^2}$ (in light purple, $= 0.04$) in street 1 for ABL2 at $\alpha = 0°$.

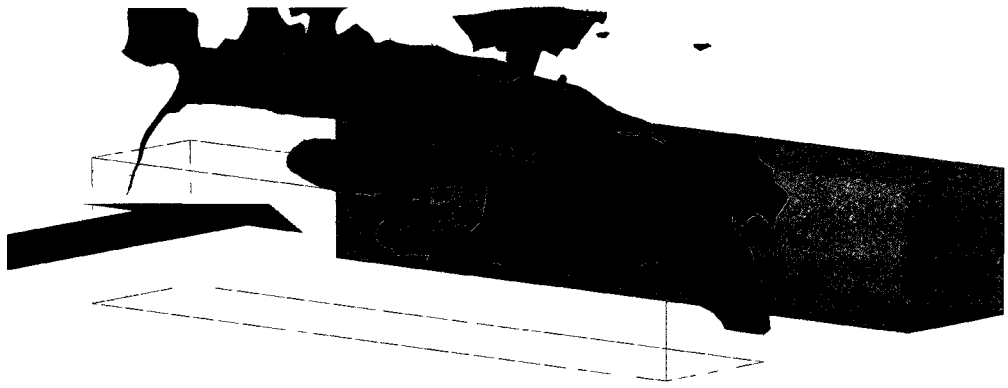

Figure 6.25. Isocontours of NAM (in light red, $f = 0.45$), $\overline{u'^2}$ (in light blue, $= 0.03$) and $\overline{v'^2}$ (in light purple, $= 0.045$) in street 1 for ABL2 at $\alpha = 15°$.

fluctuations term $\overline{u'^2}$ is again dominant in that region. The side shear layers are not as turbulent as the blocks are more sheltered from the incoming flow. Finally, the relation between the $\overline{v'^2}$ term and the arch vortex is not evident as illustrated in Figures 6.24 and 6.25. We argue that the $\overline{v'^2}$ term is the result of the channeling effects. The relation between the $\overline{v'^2}$ term and the channeling effects is more evident as seen in Figures 6.21(b) and 6.23. For the 0° incidence angle case, the high levels of $\overline{v'^2}$ near the center of the street are due to the symmetry of the flow field. For the 15° incidence angle case shown in Figure 6.23, the channeling effect is responsible for the larger levels of $\overline{v'^2}$ near the windward wall.

6.6 Towards a temporally resolved flow

Steps have been taken towards achieving a temporally resolved flow. First, a spatial description of the flow structures and turbulence mechanisms were obtained over a large domain. This study provided valuable knowledge about specific regions of the flow field that present the dominant characteristics, i.e. high levels of turbulence, arch vortices, etc.

In order to obtain a temporally resolved flow field in the entire domain, measurement models were constructed using the SPIV data. This is one of the primary steps needed to obtain a temporally resolved flow field. The measurement model can provide information on the current instantaneous state of the flow based on sparse measurements. The KRR and LSE measurement models were calculated and discussed in Chapter 5. No significant differences between the two models were found. However, the KRR model was used as it is more advantageous in its ability to handle various types of inputs (velocity, pressure, temperature, etc.).

If one desires a temporally resolved flow, then temporally resolved sparse measurements must be obtained and serve as the input to the measurement model. If

in addition, the state of the flow at future times is desired, then a dynamical model is required. This was not achievable in this investigation because we did not have a means to obtain temporally resolved velocity measurements at multiple discrete locations within the flow field simultaneously with the SPIV data, which are required to construct an accurate dynamical model.

For example, if multiple Laser Doppler Velocimetry measurements could have been performed along with the SPIV measurements, then we could have predicted the temporal evolution of this flow field. Nevertheless, this study is a necessary step towards the determination of this temporal evolution because it now provides the background regarding the spatial structures and turbulence mechanisms dominating the flow field, which will be invaluable in determining where such temporal measurements should be performed. For example, sensors could be placed at the windward wall to capture the spanwise fluctuations of the velocity field characterizing the wind fluctuations at the street scale. In the shear layers at the top and at the sides, another set of sensors could be used to determine the turbulence levels around the arch vortex. These measurements would fully characterize the dominant features of the flow field and aid in the temporal prediction of transport and dispersion of contaminants at the urban scale.

6.7 Towards the prediction of contaminant transport and dispersion using a reduced-order representation of the urban flow field

The results presented in Chapter 5 are a direct application of some of the tools developed by Mokhasi et al. (2009) and Mokhasi (2009b). The use of a reduced-order representation for a high-dimensional flow field proved to be beneficial in capturing a large amount of the TKE while providing a computationally tractable description of the flow field (6 modes).

However, a practical application of these tools to a real urban setting is likely

ways away, since there are questions that still need to be addressed, such as: i). How do we obtain the spatial basis functions for a real urban environment? and ii), Do we need to recompute these basis functions for each specific geometry?

The problem of contaminant transport and dispersion is incredibly complex and currently, it appears that all approaches have advantages that could be combined to improve the current status of the predictive tools. It is difficult to imagine obtaining both spatially and temporally resolved data in an urban setting via field measurements. With the ever increasing computational power and sophistication of CFD simulations, one could envision simulating beforehand, for a specific geometry, a vast range of flow scenarios corresponding to different boundary conditions such as wind direction, speed, gustiness, etc. For each scenario, a POD analysis could be performed to extract the corresponding spatial basis functions. The CFD simulations could also serve as a powerful tool to determine the optimal location of sensors that would be required in the urban environment to characterize the range of flow scenarios and correctly identify the boundary conditions. Measurement models and dynamical models could also be derived from these numerical simulations and be readily available when the need arises.

The attractiveness of this approach lies in the amount of information that can be computed beforehand; specifically obtaining the spatial basis functions requires the most processing power. Predicting the transport and dispersion of contaminants in an urban environment for some scenarios would want to be done as quickly as possible. Using the dynamical model in conjunction with measurement models is efficient in the sense that only the POD coefficients need to be estimated once a contaminant is released.

It is of critical importance to characterize the spatial basis functions accurately. This means that CFD simulations need to be validated against complex flow fields

that represent urban flows well, both in space and time. To do so, well-controlled experiments that provide both space and time dependence of urban-like flow fields have to be performed. *The reduced-order representation of the flow field obtained in this study could be regarded as a first data set that provides spatial and temporal evolution of the flow field in a complex geometry.* It will therefore be made available upon request.[2] This data set could be used to validate and compare the accuracy of the different predictive tools available today. More data sets with good spatial and temporal resolution are needed to characterize the very wide range of situations encountered in urban areas. The combination of simultaneous SPIV and multiple LDV measurements seems to be a promising approach. Nevertheless, field experiments are still a necessary step to further validate both laboratory and numerical simulations. Indeed, the current state of predictive models is that they will need to continue to require site-specific information in order to confirm their prediction.

Regarding the second question, the spatial basis functions will change from specific location to specific location and from boundary condition to boundary condition, which is why CFD simulations should be performed for each case. This is already common practice for evolved predictive tools such as MILES (Patnaik et al., 2007). New numerical simulations need to be run for different parameters. We could, however, envision computing spatial basis functions that take into account a range of wind directions in their direct computation also requiring experimental models to benchmark them. Further investigation is needed as the cost may be a reduced accuracy of the temporal prediction.

---

[2]bmonnier@iit.edu, wark@iit.edu

CHAPTER 7

CONCLUSIONS

7.1 Summary

This work represents a major contribution to the understanding of complex urban flow fields. A fully three-dimensional characterization of the flow field for various parameters allows for the complete spatial description of the dominant scales and turbulence mechanisms within the urban environment. An innovative approach was employed to estimate the temporal evolution of the primary scales responsible for the transport and dispersion mechanisms within a complex environment. This approach provides a temporal resolution, equal to the temporal resolution of the sparse measurements, of a reduced-order representation of a fully three-dimensional flow. *This is the first time that such an approach has been applied to a high-dimensional, spatially-resolved flow, representative of complex urban conditions.* The temporal evolution of this 3D flow can serve as a validation data set for predictive tools. The effect of the incidence angle on the flow structures and turbulence mechanisms was found to be important. *Even for incidence angles as small as* 4.5°, *a significant channeling effect was observed.* This channeling effect is a crucial factor in the transport mechanism and could be occurring for angles less than 4.5°. The dependence of the channeling effect on incidence angles was found to be a function of street spacing; specifically, the channeling effect is more acute for wider streets.

Two scales were studied in this work: a street scale where such effects as incidence angles, streamwise spacing, and incoming flow characteristics were investigated, and an urban scale where a transition towards an equilibrium state was observed.

7.1.1 At the street scale. By comparing a narrow street to a wider street, two flow regimes were studied. For the narrow street, a single primary recirculation region was

identified as the classic arch vortex. For the wider street, a secondary recirculation region was found upstream of the downstream side of the street in addition to the primary recirculation region associated with the arch vortex. In the wake layer of both the narrow and wider streets, the turbulence levels were found to be dominated by the streamwise fluctuations of the velocity field. The production of turbulence was found to be well correlated to these high levels of TKE and strongly dominated by the $-\overline{u'w'}\left(\frac{\partial U}{\partial z}+\frac{\partial W}{\partial x}\right)$ term. For the narrower street at a zero-incidence angle, the region of high TKE near the ground, dominated by the spanwise fluctuations of the velocity field, was found to coincide with the $-\overline{v'^2}\frac{\partial V}{\partial y}$ term in the production rate. However, a region of high turbulence located near the windward wall of the wider street was found to not coincide with turbulent kinetic energy production in that region. It was proposed that the turbulence was transported to the windward wall from the wake layer.

Through the channeling effect that was described at length in this work, both the arch vortex and the region of high turbulence within the street were observed to be strongly modified. The non-zero incidence angle effect on the arch vortex location was found to be very similar for the $-4.5°$ and $15°$ incidence angle cases where a shift of one of the arch vortex legs towards the intersection was observed. The production of turbulence was also seen to be affected in the canopy with a shift of the region of production associated with spanwise fluctuations in a region near the ground for $\alpha = 0°$ to a region next to the windward wall for the non-zero incidence angle cases. This shift of the region of large TKE in the street to the windward wall was also found to coincide with a region of high production of turbulence dominated by both $-\overline{v'^2}\frac{\partial V}{\partial y}$ and $-\overline{w'^2}\frac{\partial W}{\partial z}$ with a ratio of about two to one. Similar to the $0°$ incidence angle case, in the wake layer above the urban canopy, the streamwise fluctuations were found to be the dominant contribution to the TKE for incidence angles of $\alpha = -4.5°$ and $15°$, and the production of TKE was again found to be strongly dominated by the

$-\overline{u'w'}\left(\frac{\partial U}{\partial z}+\frac{\partial W}{\partial x}\right)$ term.

The results for three different approach boundary layers were presented for the middle street within the urban array. The effects of these three different ABLs, with mean free-stream speeds ranging from about 2 m/s to 3 m/s, were found to be minimal in terms of flow structures. The arch vortices were found to remain at approximately the same location with respect to the street and the dominant mechanisms producing the turbulence were found to be consistent for all three incoming flows. However, differences were observed in the TKE levels and a proper scaling was not determined; therefore, it is suggested to be a focus of a future investigation.

A ventilation ratio was used to measure the strength of the channeling effect. For all incidence angles, it was found that the largest contribution to the total ventilation occurred through the roof of the street. As the incidence angle α was increased, the channeling effect became stronger and more and more of the ventilation occurred through the sides of the street as compared with the $\alpha = 0°$ case. The wider street was observed to yield larger ventilation ratios through the sides and this was believed to be due to both the geometry and the effect of the secondary recirculation region.

7.1.2 At the urban scale. For the investigation of the street-to-street evolution of the flow, two different cases were presented corresponding to free-stream speeds of 2 m/s and 3 m/s. For both cases, a strong transition in the flow field was observed from the beginning of the urban array to street 1. The flow field then appeared to converge towards an equilibrium state both in terms of flow structures and turbulence characteristics. More specifically, the spatial location of the arch vortex within streets 2 and 3 was found to be very similar to each other. A significant drop in TKE from street 1 to streets 2 and 3 was observed for both atmospheric boundary layers investigated with the decrease in TKE more evident for the slower ABL results. This indicated a dependence of the equilibrium on the incoming flow field characteristics.

The convergence towards an equilibrium state was found to be in rough agreement with other works and a simple model was employed to estimate the minimum length required to reach a full equilibrium state. However, this model had no dependence on incoming flow parameters and therefore lacked the ability to predict the difference observed in the present results between the two ABLs.

7.1.3 Three-dimensional interaction of the arch vortex with regions of large TKE. As known, spatial structures in a flow can transport contaminants from one location to another. The contaminants will be dispersed more in regions where there are higher levels of TKE. The present work has provided the dependence of the spatial structures responsible for this transport on the incidence angle, street spacing, and unsteadiness of the flow.

7.1.4 Towards temporal estimation and prediction. The temporal study presented provided a framework for furthering estimation techniques based on a reduced-order representation of the flow field. In practice, one wants to estimate the temporal evolution of flow fields over spatial domains as large as possible with a minimum number and complexity of sensors. Two measurement models, Linear Stochastic Estimation and Kernel Ridge Regression, were constructed to play the role of flow field estimators using sparse information taken from the entire velocity field. They were found to provide very similar results even though they were based on different approaches. The reliability of the measurement models was investigated and found to be dependent on the location of the sparse sensors. Therefore, the results of a spatially resolved velocity field would be a very good tool to use to determine the optimal location of sparse sensors needed to predict a temporally resolved flow field. The temporal estimation of the reduced-order representation of the flow field obtained using the measurement model could serve as a valuable tool to validate various prediction tools.

7.2 Recommendations

Understanding and controlling the dispersion of pollutants and contaminants in urban areas is a complex problem that requires the combination of field experiments, laboratory experiments, and numerical simulations. Through laboratory experiments, one can understand the effects of well controlled parameters on the flow field within increasingly more complex environments. But this needs to be validated in situ with measurements in the urban environment. In addition, with the ever increasing computational power and accuracy of numerical models, one can envision constructing accurate models that also need to be validated against field and laboratory experiments.

Parameterizing the urban canopy layer is of primary interest as it can provide simple models of transport and dispersion at the street scale. As observed in our study and in many other works, the scaling is non trivial. The urban flow involves a variety of phenomena and has a wide range of scales. Further work is needed in this branch via systematic studies of driving parameters such as geometry of the urban environment, incoming flow characteristics, etc. Especially, the sensitivity to incoming flow appeared to be challenging and a proper scaling of the TKE would be of major interest.

Using the understanding of the interactions between the dominant flow structures, i.e. the arch vortices, and the regions of large TKE, an optimization on sensor placement should be performed to assess the accuracy of various measurement models. The reduced-order representation of the velocity field is especially attractive for such complex urban flow fields. Experiments combining temporally resolved sparse measurements distributed optimally along with SPIV measurements could provide relevant data to construct dynamical models able to predict the flow-field behavior. This would of course be of primary interest for contaminant transport and dispersion

in an urban environment.

More work has to be done to assess if resolving building blocks of flows in urban areas could be enough to validate CFD codes and use them in order to build the spatial basis functions that are needed to describe the flow field. The spatial study was done with a relatively dense resolution. In the interest of time and cost, experiments could be performed with about half the amount of vertical planes and still provide a good picture of the flow field. However, if one wants to resolve more details about the other terms in the TKE equation, a better spatial resolution would be required, especially in the spanwise direction.

APPENDIX A

GAPPY-POD AS A MEANS TO CLEAN PIV DATA

A.1 Proper Orthogonal Decomposition Given an ensemble of velocity field realizations, the method of POD seeks a representation of the ensemble velocity fields in the form:

$$\boldsymbol{u}(\boldsymbol{x}, t; N) = \sum_{k=1}^{N} \zeta_k(t)\ \boldsymbol{\psi}_k(\boldsymbol{x}). \tag{A.1}$$

The above series solution provides an approximation of the members of the ensemble by selecting a set of basis functions such that the mean squared error is minimized over all possible function bases of the same dimension N. The mathematical formulation of finding the optimal set of basis functions $\boldsymbol{\psi}(\boldsymbol{x})$ can be addressed as a maximization problem given by:

$$J(\boldsymbol{\psi}) = \frac{\langle\ |(\boldsymbol{u}, \boldsymbol{\psi})|^2 \rangle}{\|\boldsymbol{\psi}\|^2} \stackrel{!}{=} \max_{\boldsymbol{\psi} \in \mathcal{L}^2}, \tag{A.2}$$

which leads to a Fredholm integral eigenvalue problem:

$$\int_{\Omega} \mathbf{R}(\boldsymbol{x}, \boldsymbol{x}')\, \boldsymbol{\psi}(\boldsymbol{x}')\, \mathrm{d}\boldsymbol{x}' = \lambda\, \boldsymbol{\psi}(\boldsymbol{x}). \tag{A.3}$$

The kernel $\mathbf{R}(\boldsymbol{x}, \boldsymbol{x}')$, a symmetric positive definite kernel, is called the two-point correlation tensor and is given by:

$$\mathbf{R}(\boldsymbol{x}, \boldsymbol{x}') = \left\langle\ \boldsymbol{u}(\boldsymbol{x}, t) \bigotimes \boldsymbol{u}(\boldsymbol{x}', t)\ \right\rangle. \tag{A.4}$$

where, $\langle\ \cdot\ \rangle$ denotes an ensemble averaging operation and $\bigotimes$ denotes diadic product. An alternate formulation was developed by Sirovich (1987) to alleviate the large computational costs associated with solving the standard POD eigenvalue problem (A.3). The method of snapshots relies on the ergodic hypothesis which states that for statistically stationary signals the time average and the ensemble average are the same, the eigenvalue problem in (A.3) can be reformulated to a smaller problem. The ergodic hypothesis can be written mathematically as:

$$\begin{aligned} \mathbf{R}(\boldsymbol{x}, \boldsymbol{x}') &= \left\langle\ \boldsymbol{u}(\boldsymbol{x}, t) \bigotimes \boldsymbol{u}(\boldsymbol{x}', t)\ \right\rangle \\ &= \frac{1}{T} \int \boldsymbol{u}(\boldsymbol{x}, t) \boldsymbol{u}(\boldsymbol{x}', t)\, \mathrm{d}t \end{aligned} \tag{A.5}$$

and converts the spatial integral problem into a temporal problem. In the above equation, T represents a suitably long time. A correlation matrix is computed as:

$$C_{ij} = \frac{1}{M} \int_D \boldsymbol{u}^{EN}(\boldsymbol{x}, t_i) \cdot \boldsymbol{u}^{EN}(\boldsymbol{x}, t_j)\, \mathrm{d}\boldsymbol{x}, \tag{A.6}$$

where M is the number of snapshots available in the original ensemble of data and $\boldsymbol{u}^{EN}$ represents the velocity snapshots that form the ensemble. Let v_i^k be the i^{th} element of the eigenvector $\boldsymbol{v}^k$ corresponding to the eigenvalue λ_k, $k = 1, 2, 3 \ldots, M$ of the correlation matrix $\mathbf{C}$. Let us define α_{ki} as:

$$\alpha_{ki} := \frac{v_i^k}{\sqrt{M \sum_{m,r} v_m^k \, v_r^k \, C_{mr}}}. \tag{A.7}$$

Based on the above equations, one can then compute the POD basis functions as:

$$\boldsymbol{\psi}_k(\boldsymbol{x}) = \sum_{i=1}^{M} \alpha_{ki} \, \boldsymbol{u}^{EN}(\boldsymbol{x}, t_i), \tag{A.8}$$

and the temporal coefficients as:

$$\zeta_k(t_p) = \int_D \boldsymbol{u}(\boldsymbol{x}, t_p) \, \boldsymbol{\psi}_k(\boldsymbol{x}) \, \mathrm{d}\boldsymbol{x}. \tag{A.9}$$

From the decomposition, the following property also holds:

$$\int_D \boldsymbol{\psi}_i(\boldsymbol{x}) \boldsymbol{\psi}_j(\boldsymbol{x}) \mathrm{d}\boldsymbol{x} = \delta_{ij}, \tag{A.10}$$

$$\frac{1}{T} \int_0^T \zeta_i(t) \zeta_j(t) \mathrm{d}t = \langle \zeta_i(t) \zeta_j(t) \rangle = \lambda_i \, \delta_{ij}, \tag{A.11}$$

where λ_i are the eigenvalues associated with the eigenvectors $\boldsymbol{v}$. The properties (A.10) and (A.11) prompted the use of the term "bi-orthogonal decomposition" by Aubry, Guyonnet, and Lima (1992). The method of snapshots reduces the computational complexity significantly. The spectral convergence properties ensure that the basis functions are optimal and converge faster than any other set of functions that could be constructed in the Hilbert space. In addition, as seen in Equation (A.8), all the basis functions are constructed as linear superpositions of the ensemble snapshots.

Therefore, the basis functions automatically satisfy the continuity equation, no-slip, and periodic boundary conditions (if such conditions apply). The conditions of mass conservation and no-slip at solid walls are of particular importance when dealing with flows around complex geometries, such as the ones typical for an urban setting.

At this point, it becomes apparent that a good set of POD basis functions is one that captures a variety of flow phenomena with sufficient accuracy. In order to achieve this, a common practice is to obtain sample snapshots of the velocity fields that span a variety of flow states, or span a large interval of time. When one is dealing with flow cases that exhibit diverse flow phenomena, it becomes important that the POD decomposition be able to capture all of them. To ensure this, the initial ensemble of velocity snapshots should contain velocity fields that correspond to different conditions. The general rule of thumb is to select snapshots that span the range of several integral time scales of the flow.

A.2 Gappy-POD In this section, we first introduce the concept of Gappy-POD used to compute the complete velocity fields based on measurements taken at sparse locations within the domain. We consider the POD expansion of the velocity field given by:

$$\boldsymbol{u}(\boldsymbol{x},t) = \sum_{k=1} \zeta_k(t)\, \boldsymbol{\psi}_k(\boldsymbol{x}).$$

For a given domain, the POD basis functions describe the spatial variations associated with the flow. In order to determine the velocity field at a certain instance in time, one must find the correct POD coefficients, $\boldsymbol{\zeta}(t)$, for the corresponding modes at that specific instance in time. It has been observed for a variety of applications that the number of POD modes required for an accurate reconstruction is quite small. It is therefore no surprise that one could envision a method that enables one to compute the POD coefficients using information from the domain (for example in the form of sensor measurements). Linear stochastic estimation (LSE) is a method based directly

on POD analysis that constructs such a model. The method of LSE seeks an estimate of the velocity field $\boldsymbol{u}(\boldsymbol{x},t)$ in the form:

$$\boldsymbol{u}(\boldsymbol{x},t) = \mathbf{A}(\boldsymbol{x},\boldsymbol{x}')\ \boldsymbol{u}(\boldsymbol{x}',t), \tag{A.12}$$

where $\boldsymbol{u}(\boldsymbol{x}',t)$ are the sensor measurements. By solving the variational problem, one can show that the kernel $\mathbf{A}(\boldsymbol{x},\boldsymbol{x}')$ is the two-point correlation function suitably normalized. The kernel $\mathbf{A}$ is given by:

$$\mathbf{A}(\boldsymbol{x},\boldsymbol{x}') = \frac{\mathbf{R}(\boldsymbol{x},\boldsymbol{x}')}{\langle \boldsymbol{u}(\boldsymbol{x}') \bigotimes \boldsymbol{u}(\boldsymbol{x}') \rangle}, \tag{A.13}$$

where $\langle . \rangle$ denotes ensemble averages and $\bigotimes$ denotes diadic product. It was shown in the work of Adrian (1977) that the inclusion of quadratic terms into the estimation equations added very little information and could effectively be neglected, at least for homogenous turbulence. Following the development of LSE, the method has found widespread application in the experiments associated with fluid mechanics. Examples of this can be found in the work of Glauser and George (1992), Hudy et al. (2007), Murray and Ukeiley (2003) and Taylor and Glauser (2004) who have used LSE in combination with scalar pressure measurements to obtain a complete description of the velocity fields for different geometries like backward facing steps, axi-symmetric jets, and cavities. Various extensions of LSE have been explored in the work of Hudy et al. (2007); Tinney et al. (2006); Borée (2003); Bonnet and Delville (2001); Picard and Delville (2000) and others. It is also noted at this point that an extension of POD called Extended POD was developed by Glezer, Kadioglu, and Pearlstein (1989). E-POD, as termed by the authors, developed the idea that the POD coefficients of the velocity field, as obtained by regular POD analysis, could be used as expansion coefficients for measurements (or any scalar/vector variable other than the velocity). By invoking this constraint, it was shown that one could obtain a set of new basis functions for the measurements. Since measurements always constituted a complete snapshot, one could then use the decomposition of the measurements to

directly compute the POD coefficients. It was also shown that E-POD could be closely related to the idea of modified-LSE approach as developed by Taylor and Glauser (2004) where surface pressure measurements were used to compute the velocity POD coefficients.

The LSE relies on the original eigenvalue formulation of POD, as given in (A.3) to construct the model. Gappy-POD can be viewed as the "method of snapshots" equivalent to LSE, i.e., rather than relying on the two-point correlation matrix (which can be rather large at times), the gappy-POD relies directly on the POD velocity expansion to construct its reconstruction model. To develop the equations associated with gappy-POD, we first start with the computation of the POD coefficients as given by:

$$\zeta_k(t) = \int \boldsymbol{u}(\boldsymbol{x}, t)\, \boldsymbol{\psi}_k(\boldsymbol{x})\, \mathrm{d}\boldsymbol{x}. \tag{A.14}$$

To simplify the analysis, we assume that all spatial integrations performed during the POD analysis and hence-forth are Monte-Carlo integrations; i.e.,

$$\int_D \boldsymbol{u}(\boldsymbol{x}, t)\, \mathrm{d}\boldsymbol{x} \equiv V_0 \sum_{n=1}^{N} \boldsymbol{u}(\boldsymbol{x}_n, t), \tag{A.15}$$

where $V_0 = \frac{V}{N}$. V is the volume of the domain and N is the number of points in the domain. It can be shown that the Monte-Carlo approximation converges as $\frac{1}{\sqrt{N}}$. It should be noted that the use of a Monte-Carlo approximation does not change the POD analysis in any way. The main convergence properties associated with the POD analysis remain unaffected. Therefore, the computation of the POD coefficients can be written as:

$$\zeta_k(t) = V_0 \sum_{n=1} \boldsymbol{u}(\boldsymbol{x}_n, t)\, \boldsymbol{\psi}_k(\boldsymbol{x}_n). \tag{A.16}$$

Now, consider that velocity is available at location $\boldsymbol{x}_j$, i. e., we are given the velocities at certain locations $\boldsymbol{x}_j$ in our domain. Then we can decompose the right side of the

above equation into known and unknown parts as:

$$\zeta_k(t) = V_0 \left(\sum_j \boldsymbol{\psi}_k(\boldsymbol{x}_j)\boldsymbol{u}(\boldsymbol{x}_j,t) + \sum_{r=1} \boldsymbol{\psi}_k(x_r)\,\boldsymbol{u}(\boldsymbol{x}_r,t) \right), \quad k = 1, 2, \cdots N, \tag{A.17}$$

where $\boldsymbol{u}(\boldsymbol{x}_j, t)$ represents the velocity measurements at different j locations and M represents the total number of available POD modes (note that technically we require $M \to \infty$, but we always have a finite ensemble of snapshots). Writing the unknown velocities at location $\boldsymbol{x}_r$ in terms of the POD expansion gives:

$$\begin{aligned} \zeta_k(t) &= V_0 \left(\sum_j \boldsymbol{\psi}_k(\boldsymbol{x}_j)\boldsymbol{u}(\boldsymbol{x}_j,t) \right) \\ &\quad + V_0 \left(\sum_r \sum_{p=1}^{N} \boldsymbol{\psi}_k(\boldsymbol{x}_r)\boldsymbol{\psi}_p(\boldsymbol{x}_r)\zeta_p(t) \right). \end{aligned} \tag{A.18}$$

Rearranging the terms in (A.18) such that all terms containing the POD coefficients $\zeta(t)$ are moved to the left hand side and writing in the matrix-vector format. we have:

$$\zeta_p(t) = V_0 \left[I_{kp} - V_0\, \boldsymbol{\psi}_{kr}\boldsymbol{\psi}_{pr}^T \right]^{-1} \boldsymbol{\psi}_{kj}\boldsymbol{u}(\boldsymbol{x}_j,t). \tag{A.19}$$

The term in the bracket is a square matrix and symmetric. The term $\boldsymbol{\psi}_{kr}$ represents the value of the k^{th} basis function at location $\boldsymbol{x}_r$. The superscript T in the above equations indicates the transpose of the matrix. In order to compute the velocity field directly from velocity sensors at locations $\boldsymbol{x}_j$, we can multiply (A.19) by the value of POD basis functions at different $\boldsymbol{x}_r$ locations. This gives:

$$\begin{aligned} \boldsymbol{\psi}_{pr}^T\zeta_p(t) &= V_0\, \boldsymbol{\psi}_{pr}^T \left[I_{kp} - V_0\, \boldsymbol{\psi}_{kr}\boldsymbol{\psi}_{pr}^T \right]^{-1} \\ &\quad \boldsymbol{\psi}_{kj}\boldsymbol{u}(\boldsymbol{x}_j,t), \end{aligned} \tag{A.20}$$

$$\begin{aligned} \boldsymbol{u}(\boldsymbol{x}_r,t) &= V_0 \left(\boldsymbol{\psi}_{pr}^T \left[I_{kp} - V_0\, \boldsymbol{\psi}_{kr}\boldsymbol{\psi}_{pr}^T \right]^{-1} \boldsymbol{\psi}_{kj} \right) \\ &\quad \boldsymbol{u}(\boldsymbol{x}_j,t). \end{aligned} \tag{A.21}$$

The gappy-POD Equation (A.21) shows that, if one has a complete set of basis functions, then one can get an approximation of the velocity field in an entire domain

using a few sensor measurements at different locations in space. However, if the initial velocity snapshots that are used to construct the POD basis functions as in (A.8) have missing information at various spatial locations, then an iterative process must be carried out to fill the "gaps" which leads to the iterative gappy-POD procedure.

A.3 Iterative Gappy-POD Iterative gappy-POD deals with cases when the velocity field in the original ensemble is itself incomplete. In order to describe the iterative procedure, we first make the following assumptions:

1. The velocity fields at different instances in time have *information missing* at different locations. Let $\boldsymbol{x}_r$ represent the spatial locations where the velocity field information is missing, then $\boldsymbol{x}_r = \boldsymbol{x}_r(t)$.

2. Let R represent the total number of spatial points where velocity information is missing, and let N represent the total number of spatial points in the domain, then $\left\langle \frac{R(t)}{N-R(t)} \right\rangle < 1$.

3. Let M denote the number of snapshots in the ensemble. The velocity fields $\boldsymbol{u}(\boldsymbol{x}, t)$ are represented as:

$$\boldsymbol{u}(\boldsymbol{x}, t) = \sum_{k=1}^{K} \zeta_k(t) \boldsymbol{\psi}_k(\boldsymbol{x}),$$

such that $K < M$. This observation is of vital consequence for the iterative procedure to succeed.

As an initial step, the missing information or *gaps* in the velocity snapshots are filled as:

$$\boldsymbol{u}(\boldsymbol{x}_r, t) = \frac{1}{N-R} \sum_{\substack{n=1 \\ n \neq r}}^{N} \boldsymbol{u}(\boldsymbol{x}_n, t). \tag{A.22}$$

The above step fills the gaps in the velocity snapshot with the spatial mean of the velocity snapshot. We now have the complete velocity field available to us. Let us represent this new ensemble as $\boldsymbol{U}^{(0)}$. The iterative procedure is now as follows:

1. Specify the number of POD modes K ($K < M$) that will be used during the iteration and a tolerance ϵ required to stop the iteration. Set iteration $s = 0$.

2. Perform POD analysis using method of snapshots on the velocity ensemble $\boldsymbol{U}^{(s)}$ and extract the first K dominant POD modes. Let $\lambda^{(s)}$ represent the eigenvalues associated with the POD modes $\boldsymbol{\psi}^{(s)}$ at iteration s.

3. Use (A.21) to construct new approximations to the velocities at locations $\boldsymbol{x}_r$ as:

$$\boldsymbol{u}^{(s)}(\boldsymbol{x}_r, t) = V_0 \left(\left(\boldsymbol{\psi}_{pr}^{(s)} \right)^T \left[I_{kp} - V_0 \, \boldsymbol{\psi}_{kr}^{(s)} \left(\boldsymbol{\psi}_{pr}^{(s)} \right)^T \right]^{-1} \boldsymbol{\psi}_{kj}^{(s)} \right) \boldsymbol{u}(\boldsymbol{x}_j, t).$$

   It is important to note that the above equation changes from one PIV snapshot to the next because the location of the missing data changes, i.e. $\boldsymbol{x}_r$ changes.

4. Update the velocity gaps at location $\boldsymbol{x}_r$ with the ones obtained at step 2 as:

$$\boldsymbol{u}(\boldsymbol{x}_r, t) = \boldsymbol{u}^{(s)}(\boldsymbol{x}_r, t).$$

   We now have a new velocity ensemble with no gaps, $\boldsymbol{U}^{(s+1)}$.

5. Repeat Step 2-4 until $\|\lambda^{(s+1)} - \lambda^{(s)}\|_2 < \epsilon$.

A.3.1 Validation of the algorithm with PIV data. The commercial software used in the experimental study to process the raw PIV images is ProVision-XS by Integrated Design Tools (IDT) and lets us store a "flag matrix" that contains the status of each computed velocity vector. Namely, we know if the computation of the vector is successful; that is, a valid vector is one where all conditions to obtain an accurate estimation of the velocity are met. Conversely, a spurious vector is one where all conditions are not met. The spurious vectors can be replaced with interpolated vectors using a least square estimation based on the nearest neighbors approximation which is a common approach. We are presenting a different approach, one that uses iterative gappy-POD to replace the spurious vectors. In order to test the technique,

we use a "clean" set of PIV data, in the sense that a large amount of the vectors is valid. The testing case is generated by considering 2DPIV data as obtained in the wake of a rib sitting in a turbulent boundary layer, with a mean free stream speed $U_0 = 10$ m/s. The flow is highly turbulent even for such a simplified case and presents strong similarities to more complex flow fields, for example the flow through an array of blocks (Monnier et al., 2010) where iterative gappy-POD was used. The main advantage of our testing case is that the iterative gappy-POD technique is not actually required to recover missing data. The overall percentage of spurious vectors is under 1%. By artificially adding gaps into this set of data, we recreate a situation similar to that obtained for the flow field studied in Monnier et al. (2010). We can then perform the iterative gappy-POD procedure and compare the post-processed velocity vectors with the originally available data.

The validation test ensemble is composed of 406 velocity snapshots (60×60 vectors each). Gaps are introduced in a random manner throughout the 406 snapshots so that their size is comparable to typical gaps found in PIV data. It is important to note that both the U (streamwise) and W (vertical) components of the velocity field were considered missing. Figures A.1(a) and A.1(b) show one of the instantaneous snapshots that have been flagged as valid vectors (yellow contours) or spurious vectors (green contours). Figure A.1(a) is extracted from the original data set where approximately 1% of the vectors are spurious. It has been selected because it presents a larger gap in the top left area of the region of interest. This particular snapshot has about 2% of missing data. Figure A.1(b) is the same snapshot after the artificial gaps are being introduced and contains a little over 3% of missing data.

Figures A.2(a) and A.2(b) are presenting actual PIV snapshots before and after introducing the gaps. In Figure A.2(a), the yellow circle indicates a typical gap found in PIV data that is due to lack of seeding and non-uniform mixing. In Figure

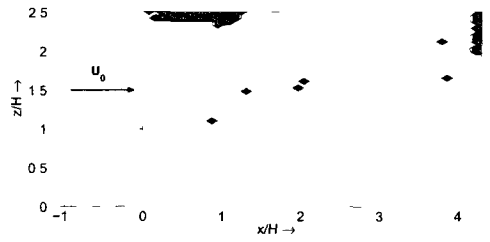

(a) Instantaneous Flag matrix for 1% of spurious vectors (original data).

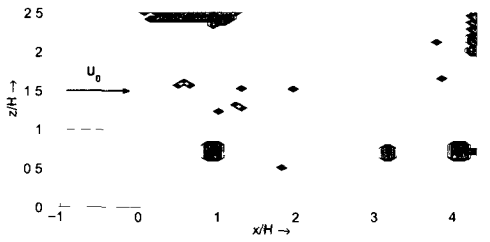

(b) Instantaneous Flag matrix for 3% of spurious vectors.

Figure A.1. Instantaneous Flag matrices, yellow corresponds to valid vectors, green to spurious vectors.

A.2(b) the artificial gaps are circled in green and their size is selected so it is about the same as the typical gaps encountered in PIV data. The gaps are added at random locations throughout the test ensemble.

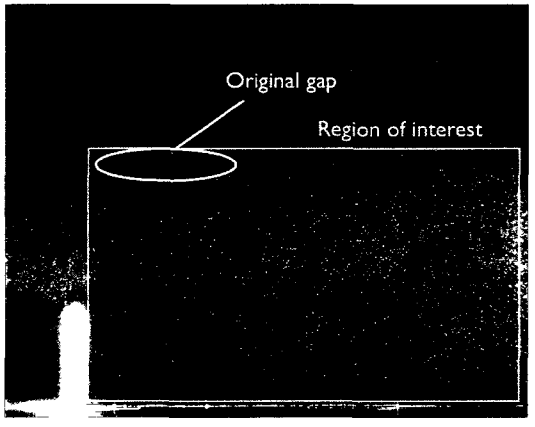

(a) Original PIV data, instantaneous snapshot.

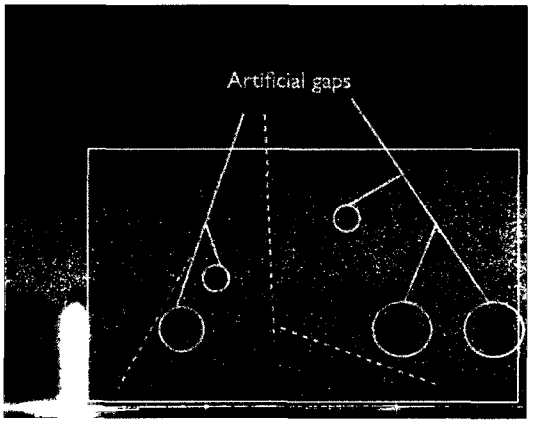

(b) Same snapshot with artificially added gaps.

Figure A.2. Instantaneous PIV snapshot, yellow circle indicates non-artificial gap due to lack of seeding, green circles indicate added artificial gaps.

Iterative gappy-POD is used here as an alternative to the standard post-processing PIV data algorithm and shows its advantage when large gaps are found

in the PIV snapshot. Figure A.3 presents a comparison between the raw PIV data (Fig A.3(a)), the nearest neighbors interpolation (A.3(b)) and the gappy-POD post-processed data (A.3(c)) for the case where only 1% of the vectors are spurious. The "dots" in Figure A.3 indicate the presence of missing data. The missing data are seen to be more prominent in the upper left and upper right regions of the domain in Figure A.3. For this case, the nearest neighbors interpolation is capable of correcting the few spurious vectors as long as the gaps are small enough. The iterative gappy-POD on the other hand is able to estimate the velocity field at *all* the missing locations. To demonstrate the gappy-POD capability further, we present the same comparison for the same snapshot when the artificial gaps are introduced as shown in Figure A.4 . The artificial gaps in Figure A.4 are again indicated as red dots in the domain. For this case it becomes apparent that the nearest neighbors interpolation fails at recovering the velocity field in the large gaps while the iterative gappy-POD performs very well in estimating the velocity vectors and filling in those gaps. The orange rectangles indicate the zoomed in regions displayed in Figure A.5 for an easier comparison. It can be clearly seen that the nearest neighbors interpolation (A.5(b)) successfully estimates the two missing vectors in the upper part of the zoomed in region while it fails at estimating the larger gap near the bottom, as opposed to the iterative gappy-POD technique that succeeds in both cases.

In order to perform a meaningful comparison between the gappy POD post-processed velocity field, the standard PIV interpolation and the original one, we need to measure how similar they are to each other. To do so, a POD analysis of the original data set is carried out, yielding a set of spatial basis functions ψ_k associated with a set of temporal POD coefficients ζ_k. By projecting the post-processed gappy data set onto the same set of basis functions, we obtain a new set of temporal POD coefficients that we can compare to the original ones. We use the same technique to generate the temporal POD coefficients associated with the standard PIV inter-

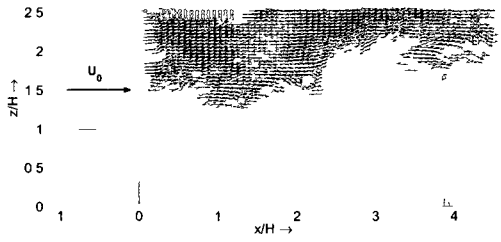

(a) Instantaneous 2D vector field as obtained with PIV processing, showing only valid data in black

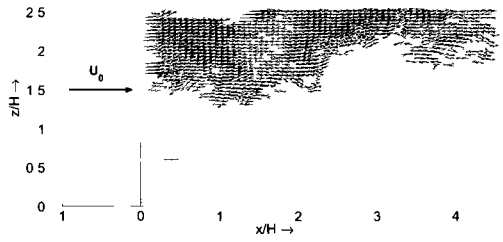

(b) Instantaneous 2D vector field as obtained with nearest neighbors interpolation

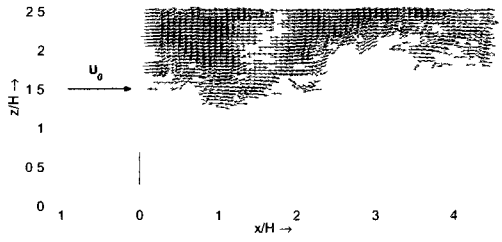

(c) Instantaneous 2D vector field as obtained after iterative gappy-POD processing

Figure A 3 Comparison of raw PIV velocity field (a), velocity field after nearest neighbor interpolation (b) and after gappy-POD processing (c) Note that the empty spaces in (a) and (b) are recovered by gappy-POD as shown in (c)

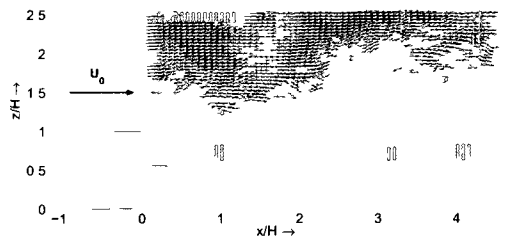

(a) Instantaneous 2D vector field as obtained with PIV processing, showing valid data in black, spurious data in red

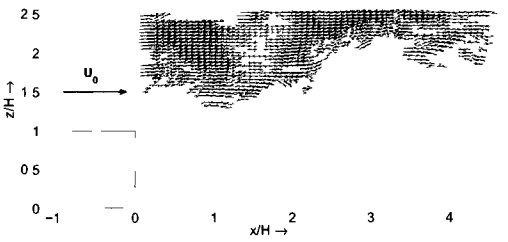

(b) Instantaneous 2D vector field as obtained with nearest neighbors interpolation

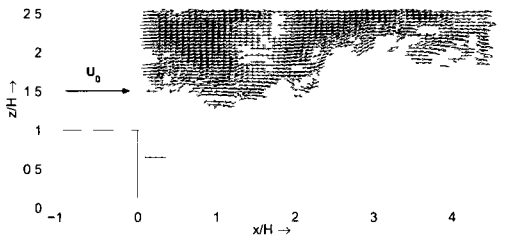

(c) Instantaneous 2D vector field as obtained after iterative gappy-POD processing

Figure A 4 Comparison of raw PIV velocity field (a), velocity field after nearest neighbor interpolation (b) and after gappy-POD processing (c) Artificial gaps are introduced at various locations in the domain

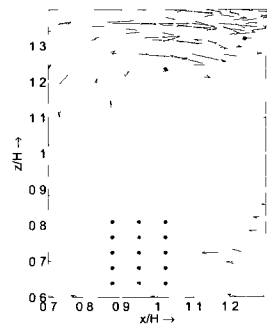

(a) Instantaneous 2D vector field as obtained with PIV processing, showing valid data in black, spurious data in red.

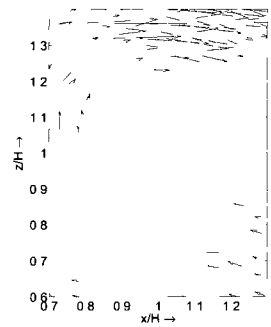

(b) Instantaneous 2D vector field as obtained with nearest neighbors interpolation.

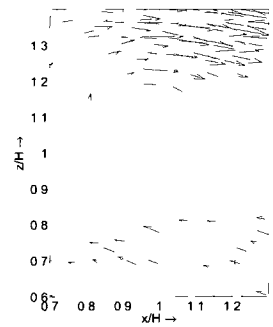

(c) Instantaneous 2D vector field as obtained after iterative gappy-POD processing.

Figure A.5. Zoomed in instantaneous 2D vector fields for the gappy data set.

polation technique. The advantages here are that it is straightforward to compare time series and the information about both velocity components is included. We simply look at the correlation coefficient between each pair of POD coefficients for the different POD mode number. An example of such a comparison is shown in Figure A.6. It can be clearly seen that the iterative gappy-POD algorithm outperforms the nearest neighbors interpolation algorithm for all modes. The accuracy degrades as higher order modes are considered. However, the recovery of the gaps is very good, with a correlation of nearly 95% up to the 50th mode in our example. This implies that most of the details in the flow are well captured even though the gaps are large and this suggests that turbulence statistics can be resolved correctly as well.

The Reynolds stress $-\overline{u'w'}$ normalized by U_o^2 is presented in Figure A.7 with the colormap indicating the magnitude of the Reynolds stress. Figure A.7(a) presents the nearest neighbors interpolated PIV data when no gaps are artificially added, Figure A.7(b) presents the nearest neighbors interpolated data when gaps are introduced

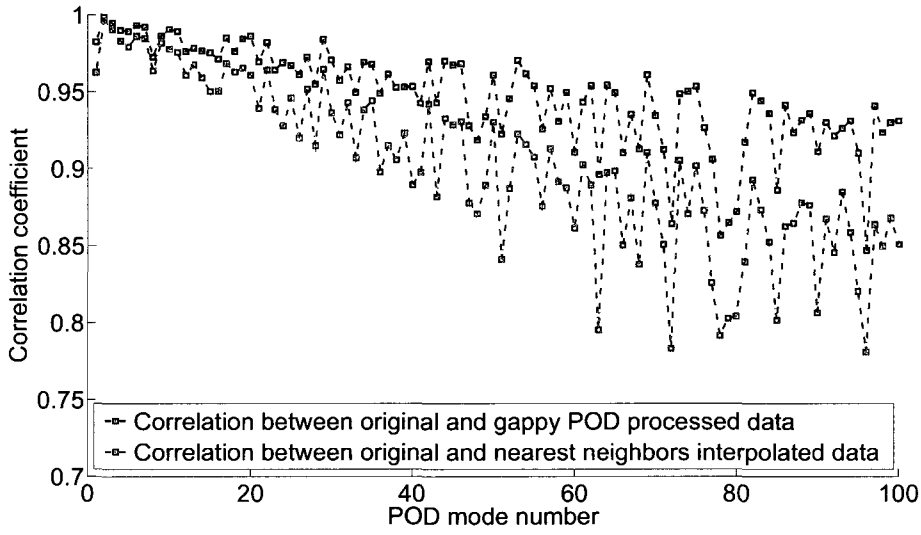

Figure A.6. Correlation coefficients between actual POD coefficients and the ones obtained for both standard nearest neighbors interpolation and iterative gappy-POD vs POD mode number.

and finally Figure A.7(c) displays the iterative gappy-POD processed data when the gaps are present. As expected the iterative gappy-POD technique provides a good approximation of the turbulence statistics.

Another way of checking the accuracy of the iterative gappy-POD procedure is to investigate the convergence of the eigenvalues with the number of iterations. Figure A.8(a) presents the eigenvalues associated with 100 POD modes for four different number of iterations. It can be seen from this plot that the eigenvalues are already converging towards a final value for 20 iterations (20, 100 and 150 iterations are quasi identical). Lastly, an alternative way to look at the convergence of the method is by plotting the error $E(r)$ (defined as the difference between the updated minimal eigenvalue and its previous occurrence, normalized by the updated one, see Equation A.23) as a function of the iteration number r, see Figure A.8(b). The decrease of the error magnitude is almost linear up to the 100th mode in this logarithmic plot.

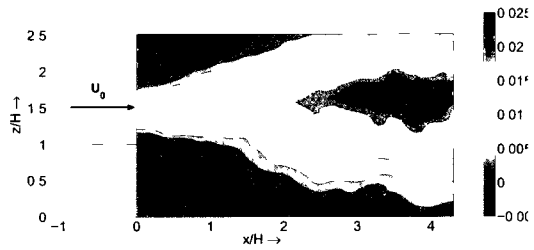

(a) Reynolds stress -$\overline{u'w'}$ normalized by U_0^2 as obtained with clean data set PIV (1% spurious vectors).

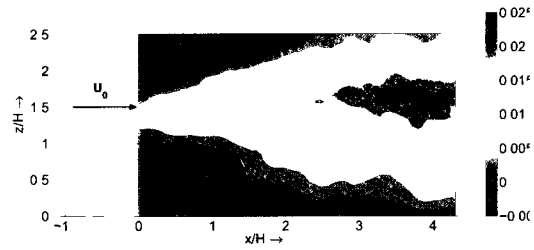

(b) Reynolds stress -$\overline{u'w'}$ normalized by U_0^2 as obtained with nearest neighbors interpolated data set for artificial gappy data (3% spurious vectors).

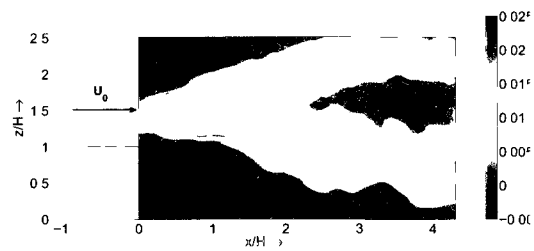

(c) Reynolds stress -$\overline{u'w'}$ normalized by U_0^2 as obtained after iterative gappy-POD processing of gappy data (3 % spurious vectors).

Figure A.7. Vertical slice of Reynolds stress -$\overline{u'w'}$ normalized by U_0^2.

$$E(r) = \frac{\left|\lambda_N^{(r+1)} - \lambda_N^{(r)}\right|}{\left|\lambda_N^{(r+1)}\right|}, \tag{A.23}$$

where λ_N denotes the N^{th} eigenvalue. Since the eigenvalues are arranged in descending order, λ_N denotes the smallest eigenvalue.

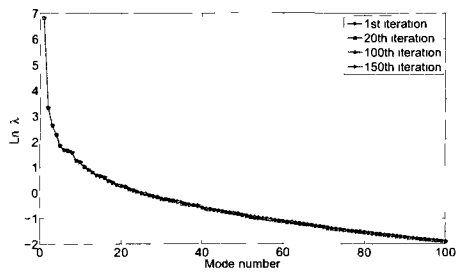

(a) Convergence of the eigenvalues.

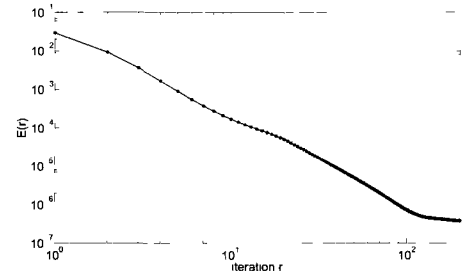

(b) Error vs iteration.

Figure A.8. Convergence of eigenvalues and error evolution as number of iterations increases.

APPENDIX B

COMPLEMENTARY DATA FOR THREE DIMENSIONAL DESCRIPTION OF MEAN FLOW AND COHERENT STRUCTURES

B.1 Q-criterion

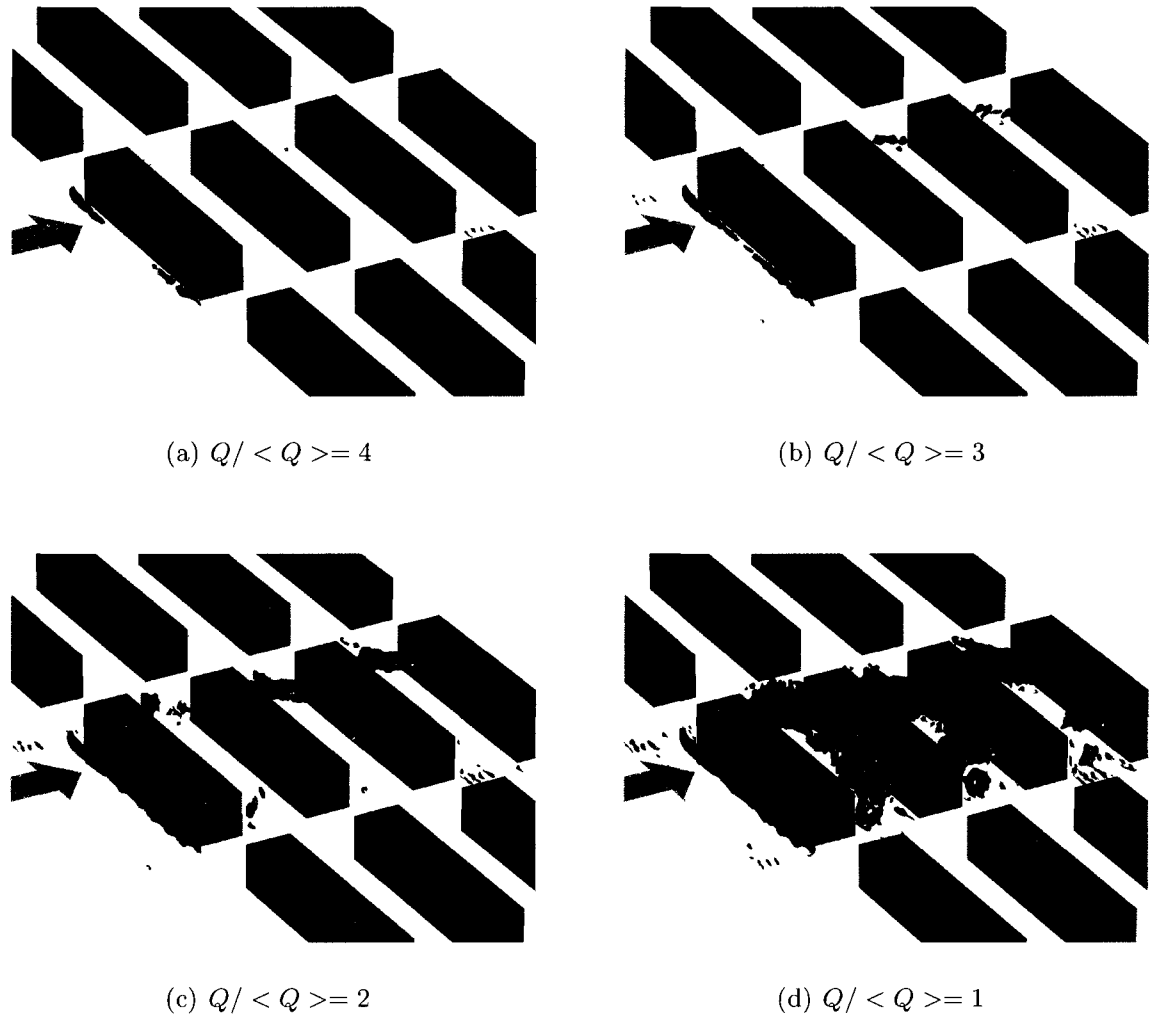

(a) $Q/ < Q >= 4$ (b) $Q/ < Q >= 3$

(c) $Q/ < Q >= 2$ (d) $Q/ < Q >= 1$

Figure B.1. Isocontours of Q-criterion normalized by $< Q >$ for ABL3 at $\alpha = 0°$ for four threshold levels.

B.2 λ_2 criterion and λ_{ci}^2 criterion Both λ_2 and λ_{ci}^2 were investigated. The results are shown here as they do not provide complementary information on the flow field. The isosurfaces of Q are also compared with the λ_2 method described in Jeong, Hussain, Schoppa, and Kim (1997) used to identify pressure minima. λ_2 is the second largest eigenvalue of the $S_{ik}S_{kj} + \Omega_{ik}\Omega_{kj}$ tensor and was computed for every data point of our domain. The information provided by this quantity is very similar to the Q isosurfaces, as shown by comparing Figure B.2 for λ_2 and Figure 3.12 for Q,

where isocontours are shown for the ABL2 data set at an incidence angle $\alpha = 0°$. Even though the iso-λ_2 results are shown to be noisier, especially close to the walls, the main structures of interest are captured in a very similar manner. Therefore, we will not show results for the other data sets, as there is no additional information to gain from these plots.

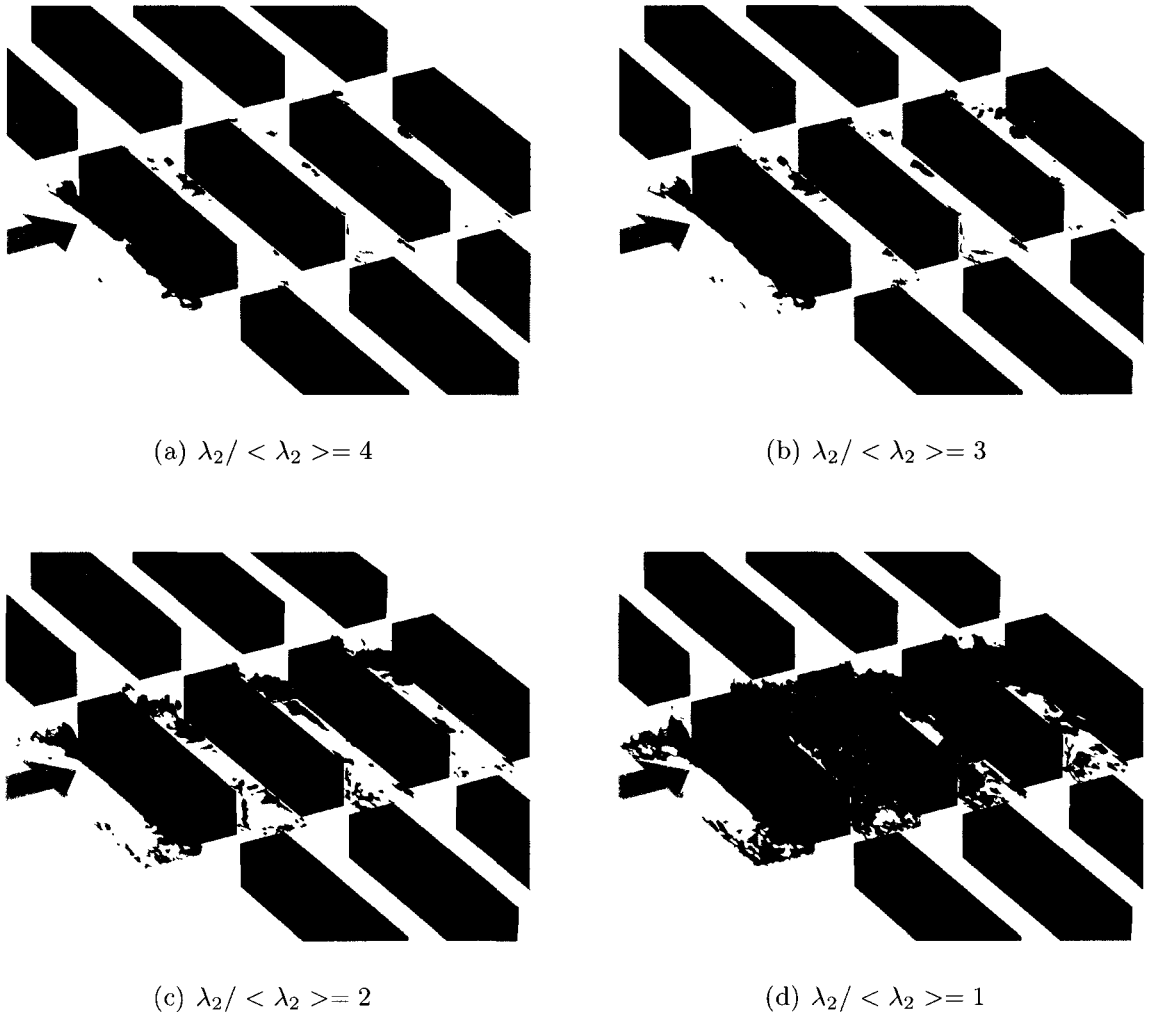

(a) $\lambda_2 / < \lambda_2 >= 4$

(b) $\lambda_2 / < \lambda_2 >= 3$

(c) $\lambda_2 / < \lambda_2 >= 2$

(d) $\lambda_2 / < \lambda_2 >= 1$

Figure B.2. Isocontours of λ_2-criterion normalized by $< \lambda_2 >$ for ABL2 at $\alpha = 0°$ for four threshold levels.

The swirling strength is the squared imaginary part of the complex eigenvalues of the velocity gradient tensor. The complex eigenvalues indicate locally spiraling streamlines. According to Sousa (2002), this technique provides an improvement in

the identification of large-scale vortical structures over vorticity magnitude because it better separates structures affected by local swirling motion from structures affected by high shear alone. Similarly to the λ_2 technique, there is no additional information to gain over the Q-criterion. The λ_{ci}^2 proves to be also noisier than the Q-criterion and captures the same features. Figure B.3 presents isocontours of λ_{ci}^2 for the ABL2 data set at an incidence angle $\alpha = 0°$. Barely any differences between the three techniques can be spotted, see Figures 3.12, B.2 and B.3.

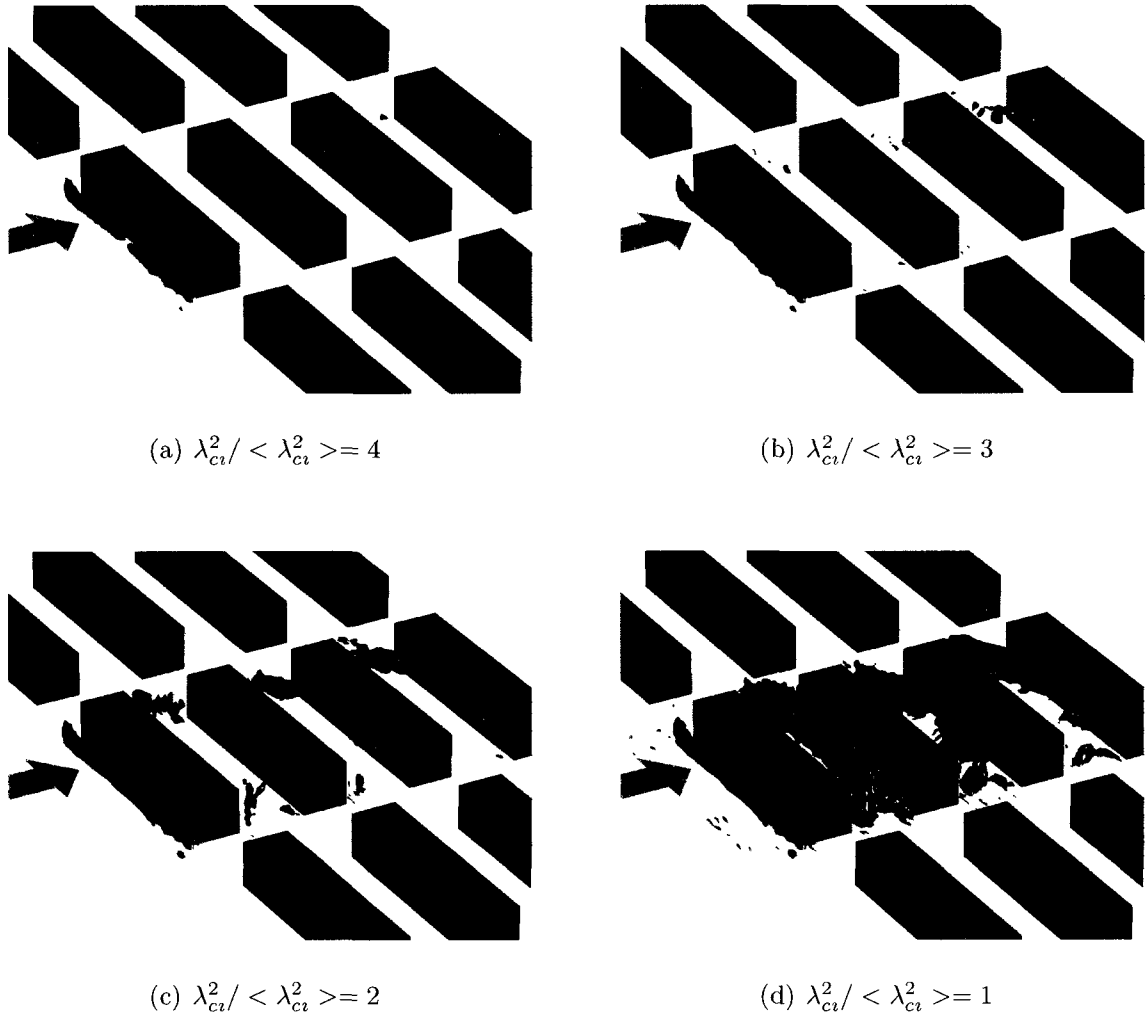

(a) $\lambda_{ci}^2 / < \lambda_{ci}^2 >= 4$

(b) $\lambda_{ci}^2 / < \lambda_{ci}^2 >= 3$

(c) $\lambda_{ci}^2 / < \lambda_{ci}^2 >= 2$

(d) $\lambda_{ci}^2 / < \lambda_{ci}^2 >= 1$

Figure B.3. Isocontours of λ_{ci}^2-criterion normalized by $< \lambda_{ci}^2 >$ for ABL2 at $\alpha = 0°$ for four threshold levels.

B.3 Vorticity contours Figures B.4 to B.6 present the evolution of the vorticity

components as the incoming flow is varied to ABL3 with an incidence angle $\alpha = 0°$. The conclusions are very similar to the ABL2 case. All features of the horseshoe vortex vorticity associated to the shear layers are still present. And similarly to the ABL2 case, one can see an asymmetry in the distribution of the vortical regions.

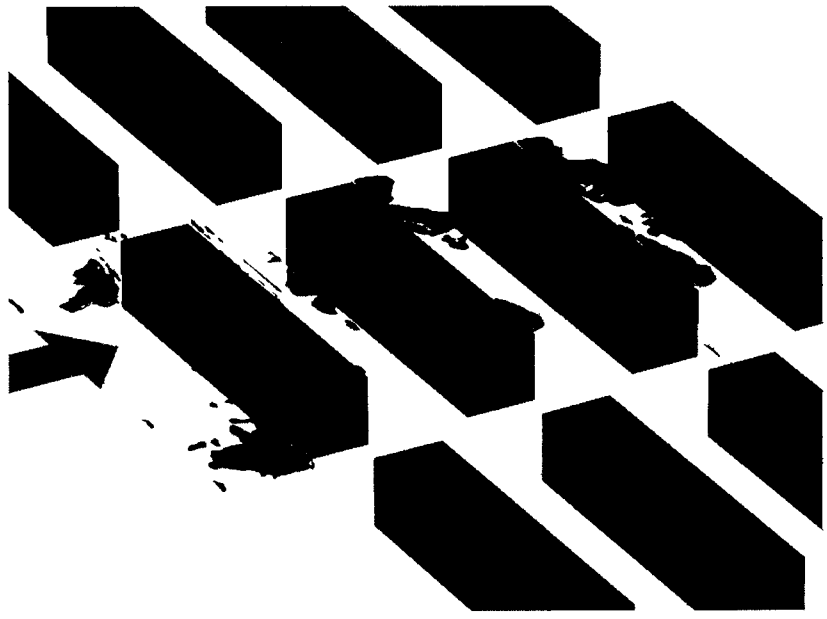

Figure B.4. Isocontour of $\frac{|\omega_x|}{<\omega>} = 1$ for ABL3 at $\alpha = 0°$ and $W/H = 1.5$.

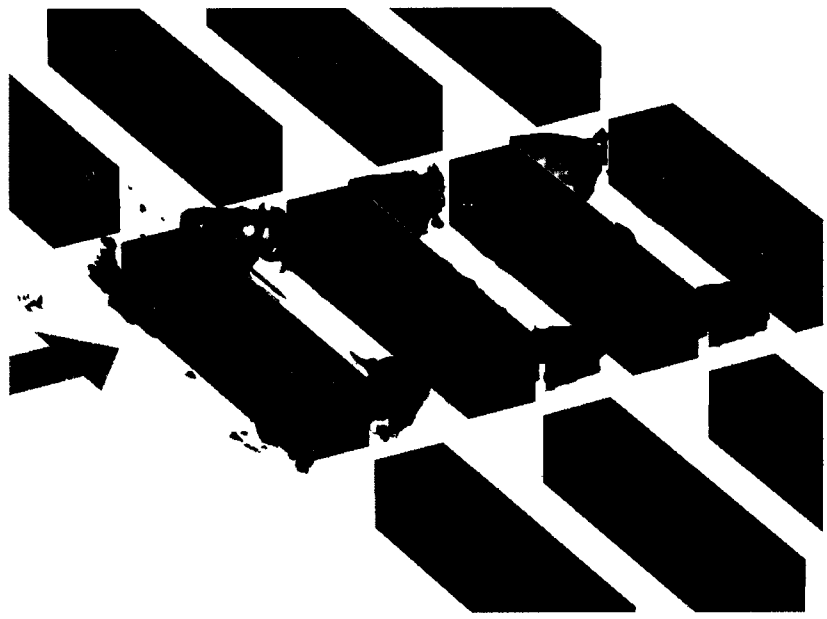

Figure B.5. Isocontour of $\frac{|\omega_z|}{<\omega>} = 1$ for ABL3 at $\alpha = 0°$ and $W/H = 1.5$.

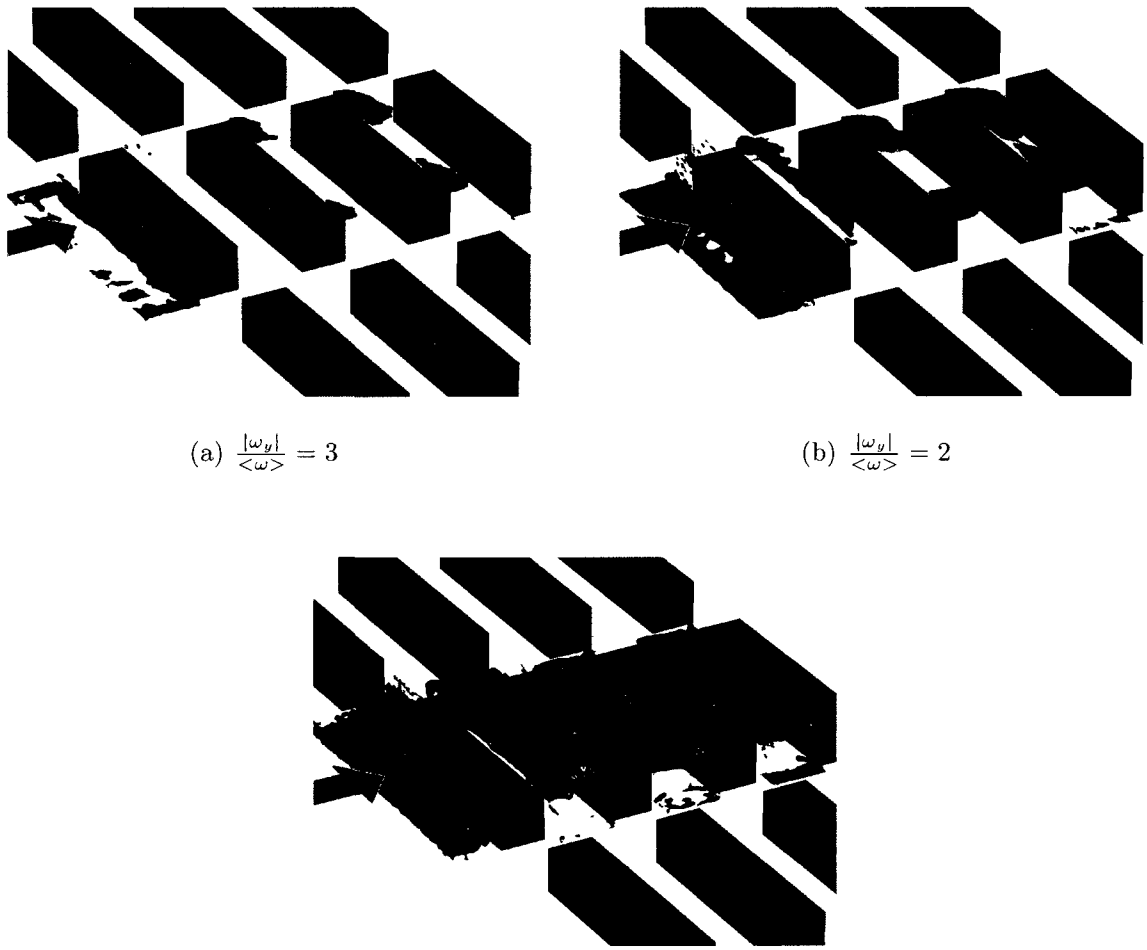

(a) $\frac{|\omega_y|}{<\omega>} = 3$

(b) $\frac{|\omega_y|}{<\omega>} = 2$

(c) $\frac{|\omega_y|}{<\omega>} = 1$

Figure B.6. Isocontour of $\frac{|\omega_y|}{<\omega>}$ for ABL3 at $\alpha = 0°$ and $W/H = 1.5$ for three threshold levels.

BIBLIOGRAPHY

Adrian, R. (1977). On the role of conditional averages in turbulence theory. *In: Proceedings of the 4th biennial symposium on turbulence in liquids.*

Adrian, R. (2005). Twenty years of particle image velocimetry. *Experiments in Fluids, 39*, 159–169.

Adrian, R., & Moin, P. (1988). Stochastic estimation of organized turbulent structure: homogeneous shear flow. *Journal of Fluid Mechanics, 190*, 531–559.

Adrian, R., & Yao, C. (1985). Pulsed laser technique application to liquid and gaseous flows and the scattering power of seed materials. *Applied optics, 24*(1), 44–52.

Ahmad, K., Khare, M., & Chaudhry, K. (2002). Model vehicle movement system in wind tunnels for exhaust dispersion studies under various urban street configurations. *Journal of Wind Engineering and Industrial Aerodynamics, 90*, 1051–1064.

Aliabadi, S., & Watts, M. (2002). Contaminant propagation in battlespace environments and urban areas. *AHPCRC Bulletin, 12.*

Aubry, N., Guyonnet, R., & Lima, R. (1992). Spatio-temporal symmetries and bifurcations via bi-orthogonal decompositions. *Journal of Nonlinear Sciences, 2*, 183-215.

Baik, J., & Kim, J. (1999). A numerical study of flow and pollutant dispersion characteristics in urban street canyons. *Journal of Applied Meteorology, 38*, 1576–1589.

Becker, S., Lienhart, H., & Durst, F. (2002). Flow around three-dimensional obstacles in boundary layers. *Journal of Wind Engineering and Industrial Aerodynamics, 90*, 265–279.

Belcher, S. (2005). Mixing and transport in urban areas. *Royal Society of London Transactions Series A, 363*, 2947–2968.

Belcher, S., & Coceal, O. (2001). Scaling the urban boundary layer. *COST 715 Workshop on Urban Boundary Layer Parameterisations, Zurich, 10 pp.*

Belcher, S., Jerram, N., & Hunt, J. (2003). Adjustment of a turbulent boundary layer to a canopy of roughness elements. *Journal of Fluid Mechanics, 488*, 369–398.

Bentham, T., & Britter, R. (2003). Spatially averaged flow within obstacle arrays. *Atmospheric Environment, 37*, 2037–2043.

Biltoft, C. A. (2001). Customer report for Mock Urban Setting Test. *DPG Document No. WDTC- FR-01-121, West Desert Test Center, U.S. Army Dugway Proving Ground, Dugway, Utah, 58 pp.*

Blackwelder, R., & Haritonidis, J. (1983). Scaling of the bursting frequency in turbulent boundary layers. *Journal of Fluid Mechanics, 132*, 87–103.

Bonnet, J., & Delville, J. (2001). Review of coherent structures in turbulent free shear flows and their possible influence on computational methods. *Flow, Turbulence and Combustion, 66*, 333–353.

Borée, J. (2003). Extended proper orthogonal decomposition: a tool to analyse correlated events in turbulent flows. *Experiments in Fluids, 35*, 188–192.

Boris, J. (2005). Dust in the wind: challenges for urban aerodynamics. *AIAA Paper 2005-5393.*

Britter, R., & Hanna, S. R. (2003). Flow and dispersion in urban areas. *Annual Review of Fluid Mechanics, 35*, 469–96.

Brown, M., Lawson, R., Decroix, D., & Lee, R. (2000). Mean flow and turbulence measurements around a 2-D array of buildings in a wind tunnel. *11th Joint AMS/AWMA Conference on the Applications of Air Pollution Meteorology.*

Brown, M., Pardyjak, E., Zajic, D., Princevac, M., Streit, G., & Biltoft, C. (2002). The MUST field experiment: mean and turbulent wind fields at the upstream edge of a building array, 3 pp. *AMS 4th Symposium on the Urban Environment.*

Calluaud, D., & David, L. (2004). Stereoscopic particle image velocimetry measurements of the flow around a surface-mounted block. *Experiments in Fluids, 36*, 53–61.

Camelli, F., Lohner, R., & Hanna, S. (2006). VLES study of flow and dispersion patterns in heterogeneous urban areas, 14 pp. *44th AIAA Aerospace Sciences Meeting and Exhibit.*

Castro, I., Cheng, H., & Reynolds, R. (2006). Turbulence over urban-type roughness: Deductions from wind-tunnel measurements. *Boundary-Layer Meteorology, 118*, 109–131.

Castro, I., & Robins, G. (1977). The flow around a surface-mounted cube in uniform and turbulent streams. *Journal of Fluid Mechanics, 79*, 307–335.

Cheng, H., & Castro, I. (2002). Near wall flow over urban-like roughness. *Boundary-Layer Meteorology, 104*(2), 229–259.

Chong, M., Perry, A., & Cantwell, B. (1990). A general classification of three-dimensional flow fields. *Physics of Fluids A: Fluid Dynamics, 2*(5), 765–777.

Christen, A., Vogt, R., & Rotach, M. (2003). Profile measurements of selected turbulence characteristics over different urban surfaces. *Fourth International Conference on Urban Air Quality, Prague, 25–27*, 408–411.

Coceal, O., & Belcher, S. (2004). A canopy model of mean winds through urban areas. *Quarterly Journal of the Royal Meteorological Society, 130*, 1349–1372.

Coceal, O., Thomas, T., Castro, I. P., & Belcher, S. E. (2006). Mean flow and turbulence statistics over groups of urban like cubical obstacles. *Boundary-Layer Meteorology, 121*, 491–519.

Crowther, J., Galeil, A., & Hassan, A. (2002). Three-dimensional numerical simulation of air pollutant dispersion in street canyons. *Water, Air, and Soil Pollution: Focus, 2*, 279–295.

Davenport, A. G. (1965). The relationship of wind structures to wind loading. *Wind Effects on Buildings and Structures, Proceedings of the Conference held at the National Physical Laboratory, Symposium No. 16, Teddington, Middlesex*, 54–102.

Delville, J., Ukeiley, L., Cordier, L., & Bonnet, J. (1999). Examination of large-scale structures in a turbulent plane mixing layer. Part 1. Proper orthogonal decomposition. *Journal of Fluid Mechanics, 391*, 91–122.

DePaul, F., & Sheih, C. (1986). Measurements of wind velocities in a street canyon. *Atmospheric Environment, 20*(3), 455–459.

Dobre, A., Arnold, S., Smalley, R., Boddy, J., Barlow, J. F., Tomlin, A. S., et al. (2005). Flow field measurements in the proximity of an urban intersection in London, UK. *Atmospheric Environment, 39*, 4647–4657.

Drubka, R., Tan-atichat, J., & Nagib, H. (1977). Analysis of temperature compensating circuit for hot-wires and hot-films. *DISA information, 22*, 5–14.

Eliasson, I., Offerle, B., & Grimmond, C. (2006). Wind fields and turbulence statistics in an urban street canyon. *Atmospheric Environment, 40*, 1–16.

Eskridge, R., & Rao, S. T. (1986). Turbulent diffusion behind vehicles: experimentally determined turbulence mixing parameters. *Atmospheric Environment (1967), 20*(5), 851–860.

Fang, C., & Sill, B. (1992). Aerodynamic roughness length: correlation with roughness elements. *Journal of Wind Engineering and Industrial Aerodynamics, 41-44*, 449–460.

Fasshauer, G. E. (2007). *Meshfree approximation methods with MATLAB* (Vol. 6). Illinois institute of Technology, Chicago, IL: Interdisciplinary Mathematical Sciences.

Gailis, R. (2004). Wind tunnel simulations of the Mock Urban Setting Test - experiment procedures and data analysis, 63 pp. *Australian Government - Department of Defence, DSTOTR1532.*

Garbero, V., Salizzoni, P., & Soulhac, L. (2010). Experimental study of pollutant dispersion within a network of streets. *Boundary-Layer Meteorology, 136*(3), 457–487.

Gayev, Y., & Savory, E. (1999). Influence of street obstructions on flow processes within urban canyons. *Journal of Wind Engineering and Industrial Aerodynamics, 82*, 89–103.

Glauser, M., & George, W. (1992). Application of multipoint measurements for flow characterization. *Experimental Thermal and Fluid Science, 5*, 617–632.

Glezer, A., Kadioglu, Z., & Pearlstein, A. J. (1989). Development of an extended proper orthogonal decomposition and its application to a time periodically forced plane mixing layer. *Physics of Fluids A: Fluid Dynamics, 1*(8), 1363-1373.

Graftieaux, L., Michard, M., & Grosjean, N. (2001). Combining PIV, POD and vortex identification algorithms for the study of unsteady turbulent swirling flows. *Measurement Science and Technology, 12*, 1422–1429.

Green, M. A., Rowley, C., & Haller, G. (2007). Detection of Lagrangian coherent structures in three-dimensional turbulence. *Journal of Fluid Mechanics, 572*, 111–120.

Grinstein, F., Bos, R., & Dey, T. (2009). LES based urban dispersal predictions for consequence management. *ERCOFTAC bulletin, 78*, 11–14.

Gromke, C., Buccolieri, R., Sabatino, S. D., & Ruck, B. (2008). Dispersion study in a street canyon with tree planting by means of wind tunnel and numerical investigations-evaluation of CFD data with experimental data. *Atmospheric Environment, 42*, 8640–8650.

Gromke, C., & Ruck, B. (2007). Influence of trees on the dispersion of pollutants in an urban street canyon–experimental investigation of the flow and concentration field. *Atmospheric Environment, 41*, 3287–3302.

Gromke, C., & Ruck, B. (2009). On the impact of trees on dispersion processes of traffic emissions in street canyons. *Boundary-Layer Meteorology, 131*, 19–34.

Gunes, H., Sirisup, S., & Karniadakis, G. (2006). Gappy data: To krig or not to krig? *Journal of Computational Physics, 212*, 358–382.

Gunnarsson, T. (1974). *Implementation of the counter-jet technique for modeling of atmospheric surface layers in the IIT environmental wind tunnel.* Master's thesis, Illinois Institute of Technology, Chicago, IL.

Haller, G. (2001). Distinguished material surfaces and coherent structures in three-dimensional fluid flows. *Physica D: Nonlinear Phenomena, 149*, 248–277.

Haller, G. (2005). An objective definition of a vortex. *Journal of Fluid Mechanics, 525*, 1–26.

Hudy, L., Naguib, A., & Humphreys, W. (2007). Stochastic estimation of a separated-flow field using wall-pressure-array measurements. *Physics of Fluids, 19*, 1–18.

Hunt, J., Wray, A., & Moin, P. (1988). Eddies, streams, and convergence zones in turbulent flows. *In its Studying Turbulence Using Numerical Simulation Databases, 2. Proceedings of the 1988 Summer Program pp 193-208 (SEE N89-24538 18-34).*

Hussein, H., & Martinuzzi, R. (1996). Energy balance for turbulent flow around a surface mounted cube placed in a channel. *Physics of Fluids, 8*, 764–780.

Jeong, J., Hussain, F., Schoppa, W., & Kim, J. (1997). Coherent structures near the wall in a turbulent channel flow. *Journal of Fluid Mechanics, 332*, 185–214.

Kastner-Klein, P., Berkowicz, R., & Plate, E. J. (2000). Modelling of vehicle-induced turbulence in air pollution studies for streets. *International Journal of Environment and Pollution, 14*(1-6), 496–507.

Kastner-Klein, P., Fedorovich, E., & Rotach, M. (2001). A wind tunnel study of organised and turbulent air motions in urban street canyons. *Journal of Wind Engineering and Industrial Aerodynamics, 89*, 849–861.

Kastner-Klein, P., & Rotach, M. (2004). Mean flow and turbulence characteristics in an urban roughness sublayer. *Boundary-Layer Meteorology, 111*, 55–84.

Kim, J., & Baik, J. (2001). Urban street-canyon flows with bottom heating. *Atmospheric Environment, 35*, 3395–3404.

Kim, J., & Baik, J. (2003). Effects of inflow turbulence intensity on flow and pollutant dispersion in an urban street canyon. *Journal of Wind Engineering and Industrial Aerodynamics, 91*, 309–329.

Kim, J., & Baik, J. (2004). A numerical study of the effects of ambient wind direction on flow and dispersion in urban street canyons using the RNG k-epsilon turbulence model. *Atmospheric Environment, 38*, 3039–3048.

Kostas, J., Soria, J., & Chong, M. S. (2005). A comparison between snapshot POD analysis of PIV velocity and vorticity data. *Experiments in Fluids, 38*, 146.

Kovar-Panskus, A., Louka, P., Sini, J., Savory, E., Czech, M., Abdelqari, A., et al. (2002). Influence of geometry on the mean flow within urban street canyons–a comparison of wind tunnel experiments and numerical simulations. *Water, Air, and Soil Pollution: Focus, 2*, 365–380.

Kovar-Panskus, A., Moulinneuf, L., Savory, E., Abdelqari, A., J, F. S., J, M. R., et al. (2002). A wind tunnel investigation of the influence of solar-induced wall-

heating on the flow regime within a simulated urban street canyon. *Water, Air, and Soil Pollution: Focus*, *2*, 555–571.

Krajnovic, S., & Davidson, L. (2000). Flow around a three-dimensional bluff body. *9th International Symposium on Flow Visualization, Heriot-Watt University, Edinburgh, 10 pp.*

Lecerf, A., Renou, B., Allano, D., Boukhalfa, A., & Trinit, M. (1999). Stereoscopic PIV: validation and application to an isotropic turbulent flow. *Experiments in Fluids*, *26*, 107–115.

Li, X., Leung, D., Liu, C., & Lam, K. (2008). Physical modeling of flow field inside urban street canyons. *Journal Of Applied Meteorology and Climatology*, *47*, 2058–2067.

Louhichi, H., Fournel, T., Lavest, J., & Aissia, H. B. (2006). Camera self-calibration in Scheimpflug condition for air flow investigation. *Advances in Visual Computing, LCNS*, *4292*, 891–900.

Louka, P., Belcher, S., & Harrison, R. (1998). Modified street canyon flow. *Journal of Wind Engineering and Industrial Aerodynamics*, *74-76*, 485–493.

Louka, P., Belcher, S., & Harrison, R. (2000). Coupling between air flow in streets and the well-developed boundary layer aloft. *Atmospheric Environment*, *34*, 2613–2621.

Louka, P., Vachon, G., Sini, J. F., Mestayer, P., & Rosant, J. M. (2002). Thermal effects on the airflow in a street canyon - Nantes'99 experimental results and model simulations. *Water, Air, and Soil Pollution: Focus*, *2*, 351–364.

MacDonald, R., Schofield, S. C., & Slawson, P. (2002). Physical modelling of urban roughness using arrays of regular roughness elements. *Water, Air and Soil Pollut: Focus*, *2*, 541–554.

Martinuzzi, R., & Havel, B. (2000). Turbulent flow around two interfering surface-mounted cubic obstacles in tandem arrangement. *Journal of Fluids Engineering*, *122*, 24–31.

Martinuzzi, R., & Tropea, C. (1993). The flow around surface-mounted, prismatic obstacles placed in a fully developed channel flow. *Journal of Fluids Engineering*, *115*, 85–92.

Mestayer, P., Sini, J. F., & Jobert, M. (1995). Simulation of the wall temperature influence on flows and dispersion within street canyons. *Transactions on Ecology and the Environment*, *6*, 109–116.

Mokhasi, P. (2009a). *Equivalence between gappy-POD and linear stochastic estimation.* Unpublished manuscript, Illinois Institute of Technology, MMAE Depart-

ment, Chicago, IL.

Mokhasi, P. (2009b). *Strategies for the real-time prediction of velocity fields.* PhD thesis, Illinois Institute of Technology, Chicago, IL.

Mokhasi, P., & Rempfer, D. (2004). Optimized sensor placement for urban flow measurement. *Physics of Fluids*, 1758–1764.

Mokhasi, P., Rempfer, D., & Kandala, S. (2009). Predictive flow-field estimation. *Physica D: Nonlinear Phenomena, 238*, 290–308.

Monnier, B., Neiswander, B., & Wark, C. (2010). Stereoscopic particle image velocimetry measurements in an urban-type boundary layer: Insight into flow regimes and incidence angle effect. *Boundary-Layer Meteorology, 135*, 243–268.

Murray, N., & Ukeiley, L. (2003). Estimation of flow field from surface pressure measurements in open cavity. *AIAA Journal, 41*(5), 969-972.

Murray, N., & Ukeiley, L. (2006). Flow field dynamics in open cavity flows. *12th AIAA/CEAS Aeroacoustics Conference, AIAA Paper 2006-2428*(May).

Murray, N., & Ukeiley, L. (2007). An application of Gappy POD. *Experiments in Fluids, 42*, 79—91.

Nagib, H., Morkovin, M., Yung, J., & Tan-atichat, J. (1974). On modeling of atmospheric surface layers by the counter-jet technique. *AIAA J, 14*(2), 185–190.

Naguib, A., Wark, C., & Juckenhoefel, O. (2001). Stochastic estimation and flow sources associated with surface pressure events in a turbulent boundary layer. *Physics of Fluids, 13*(9), 2611–2626.

Nakamura, H., Igarashi, T., & Tsutsui, T. (2003). Local heat transfer around a wall-mounted cube at 45 ° to flow in a turbulent boundary layer. *International Journal of Heat and Fluid Flow, 24*, 807–815.

Niachou, K., Livada, I., & Santamouris, M. (2008). Experimental study of temperature and airflow distribution inside an urban street canyon during hot summer weather conditions. Part II: Airflow analysis. *Building and environment, 43*, 1393–1403.

Nielsen, M. (2000). Turbulent ventilation of a street canyon. *Environmental Monitoring and Assessment, 65*, 389–396.

Oke, T. (1988). Street design and urban canopy layer climate. *Energy and Buildings, 11*, 103–113.

Patnaik, G., Grinstein, F., Boris, J., Young, T., & Parmhed, O. (2007). Large-scale urban simulations. In F. Grinstein, L. Margolin, & W. Rider (Eds.), *Implicit large eddy simulation: computing turbulent fluid dynamics.* New York, NY:

Cambridge.

Picard, C., & Delville, J. (2000). Pressure velocity coupling in a subsonic round jet. *International Journal of Heat and Fluid Flow, 21*, 359–364.

Plate, E. J. (1971). *Aerodynamic characteristics of atmospheric boundary layer.* Oak Ridge, TN: United States Atomic Energy Commission, 192 pp.

Plate, E. J. (1995). Urban climates and urban climate modelling: An introduction. In J. E. Cermak (Ed.), *Wind climate in cities* (pp. 23–39). Dordrecht, The Netherlands: Kluwer.

Prasad, A. (2000). Stereoscopic particle image velocimetry. *Experiments in Fluids, 29*, 103–116.

Rafailidis, S. (1997). Influence of building areal density and roof shape on the wind characteristics above a town. *Boundary-Layer Meteorology, 85*, 255–271.

Raffel, M., Willert, C. E., & Kompenhans, J. (1998). *Particle image velocimetry: A practical guide* (Third ed.). New York, NY: Springer-Verlag Berlin Heidelberg.

Reynolds, R. T., & Castro, I. (2008). Measurements in an urban-type boundary layer. *Experiments in Fluids, 45*(1), 141–156.

Richards, P. J., Hoxey, R. P., Connell, B. D., & Lander, D. P. (2007). Wind-tunnel modelling of the silsoe cube. *Journal of Wind Engineering & Industrial Aerodynamics, 95*, 1384–1399.

Richards, P. J., Hoxey, R. P., & Short, L. (2001). Wind pressures on a 6m cube. *Journal of Wind Engineering & Industrial Aerodynamics, 89*, 1553–1564.

Robins, A., & Castro, I. (1977). A wind tunnel investigation of plume dispersion in the vicinity of a surface mounted cube – II. the concentration field. *Atmospheric Environment (1967), 11*, 299–311.

Rotach, M. (1995). Profiles of turbulence statistics in and above an urban street canyon. *Atmospheric Environment, 29*(13), 1473–1486.

Sakamoto, H., & Arie, M. (1983). Vortex shedding from a rectangular prism and a circular cylinder placed vertically in a turbulent boundary layer. *Journal of Fluid Mechanics, 126*, 147–165.

Santiago, J., Dejoan, A., Martilli, A., Martín, F., & Pinelli, A. (2009). LES and RANS simulations of the MUST experiment. Study of incident wind direction effects on the flow and plume dispersion. *The seventh International Conference on Urban Climate, Yokohama, Japan*(July).

Shadden, S., Lekien, F., & Marsden, J. (2005). Definition and properties of Lagrangian coherent structures from finite-time Lyapunov exponents in two-

dimensional aperiodic flows. *Physica D: Nonlinear Phenomena, 212*, 271–304.

Sirovich, L. (1987). Turbulence and the dynamics of coherent structures, Part I: Coherent structures. *Quarterly of Applied Mathematics, 45*(3), 561-571.

Soloff, S., Adrian, R., & Liu, Z. (1997). Distortion compensation for generalized stereoscopic particle image velocimetry. *Measurement Science and Technology, 8*(12), 1441–1454.

Sousa, J. (2002). Turbulent flow around a surface-mounted obstacle using 2D-3C DPIV. *Experiments in Fluids, 33*, 854–862.

Stull, R. (1988). *An introduction to boundary layer meteorology* (First ed.). Dordrecht, The Netherlands: Kluwer Academic Publishers.

Sykes, R., Parker, S., Henn, D., & Gabruk, R. (1996). SCIPUFF- a generalized dispersion model. *NATO: Challenges of Modern Society, 21*, 425–432.

Tabatabai, M., Kawall, J., & Keffer, J. (1987). Flow visualization using hot-wire anemometry. *Dantec Information, 4*(Feb.), 11–12.

Taylor, J., & Glauser, M. (2004). Towards practical flow sensing and control via POD and LSE based low-dimensional tools. *Journal of Fluids Engineering, 126*, 337–345.

Tinney, C., Coiffet, F., Delville, J., Hall, A., Jordan, P., & Glauser, M. (2006). On spectral linear stochastic estimation. *Experiments in Fluids, 41*, 763–775.

Uehara, H., Murakami, S., Oikawa, S., & Wakamatsu, S. (2000). Wind tunnel experiments on how thermal stratification affects flow in and above urban street canyons. *Atmospheric Environment, 34*, 1553–1562.

Ukeiley, & Murray, N. (2005). Velocity and surface pressure measurements in an open cavity. *Experiments in Fluids, 38*, 656–671.

Wang, Z., Plate, E., Rau, M., & Keiser, R. (1996). Scale effects in wind tunnel modelling. *Journal of Wind Engineering and Industrial Aerodynamics, 61*, 113–130.

Watkins, S., Abdulrahim, M., Thompson, M., Shortis, M., Loxton, B., Segal, R., et al. (2009). An overview of experiments on the dynamic sensitivity of MAVs to turbulence. *AIAA Paper 2009-5906.*

Watkins, S., Ravi, S., & Loxton, B. (2010). The effect of turbulence on the aerodynamics of low reynolds number wings. *Engineering Letters, 18*, 6 pp.

Willert, C. (1997). Stereoscopic digital particle image velocimetry for application in wind tunnel flows. *Measurement Science and Technology, 8*(12), 1465–1479.

Xie, S., Zhang, Y., Qi, L., & Tang, X. (2003). Spatial distribution of traffic-related pollutant concentrations in street canyons. *Atmospheric Environment, 37*(23), 3213–3224.

Xie, X., Huang, Z., Wang, J., & Xie, Z. (2005). The impact of solar radiation and street layout on pollutant dispersion in street canyon. *Building and environment, 40*, 201–212.

Xie, X., Liu, C., Leung, D., & Leung, M. (2006). Characteristics of air exchange in a street canyon with ground heating. *Atmospheric Environment, 40*, 6396–6409.

Yee, E., & Biltoft, C. (2004). Concentration fluctuation measurements in a plume dispersing through a regular array of obstacles. *Boundary-Layer Meteorology, 111*, 363–415.

Yee, E., Gailis, R. M., Hill, A., Hilderman, T., & Kiel, D. (2006). Comparison of wind-tunnel and water-channel simulations of plume dispersion through a large array of obstacles with a scaled field experiment. *Boundary-Layer Meteorology, 121*, 389–432.

Zhou, Y., & Stathopoulos, T. (1997). A new technique for the numerical simulation of wind flow around buildings. *Journal of Wind Engineering & Industrial Aerodynamics, 72*, 137–147.